Programmable chiral nanocolloids

THÈSE N^{O} 7830 (2017)

PRÉSENTÉE LE 20 JUILLET 2017
À LA FACULTÉ DES SCIENCES ET TECHNIQUES DE L'INGÉNIEUR
UNITÉ DE RATTACHEMENT POUR SCIENTIFIQUES IMX
PROGRAMME DOCTORAL EN SCIENCE ET GÉNIE DES MATÉRIAUX

ÉCOLE POLYTECHNIQUE FÉDÉRALE DE LAUSANNE

POUR L'OBTENTION DU GRADE DE DOCTEUR ÈS SCIENCES

PAR

Hyeonho JEONG

acceptée sur proposition du jury:

Prof. D. Grundler, président du jury
Prof. P. Fischer, Prof. F. Stellacci, directeurs de thèse
Prof. K. Balasubramanian, rapporteur
Prof. V. Valev, rapporteur
Prof. H. Hofmann, rapporteur

ÉCOLE POLYTECHNIQUE
FÉDÉRALE DE LAUSANNE
Suisse
2017


MAX-PLANCK-GESELLSCHAFT

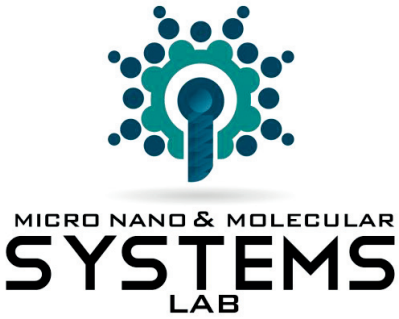
MICRO NANO & MOLECULAR
SYSTEMS
LAB

Acknowledgements

First and foremost, I would like to thank my thesis director Prof. Peer Fischer without whom this thesis would not have been possible. He has given me a great opportunity and guidance to conduct my Ph.D. with the world-class facilities. I of course thank to the Max Planck Society and the Max Planck–EPFL centre for molecular nanoscience and technology for the Ph.D. fellowship.

I would like to thank Prof. Francesco Stellacci for accepting me as his external Ph.D. student at EPFL. It is also my pleasure to thank Prof. Dirk Grundler, Prof. Heinrich Hofmann, Prof. Kannan Balasubramanian and Prof. Ventsislav K. Valev for serving on my Ph.D. exam committee. Thanks also the department, EDMX (Anne Kolly and Chrystelle Demierre), for the administrative managements and supports.

I am likewise grateful to all the former and present lab colleagues: Mariana Alarcón-Correa, Prof. John G. Gibbs, Cornelia Miksch, Prof. Ji-Tae Kim, Dr. Debora Walker, Dr. Dhruv Singh, Alejandro Posada, Dr. Tian Qiu, Udit Choudhury, Dr. Peter Oswald, Dr. Sahand Eslami, Insook Kim, Kai Melde, Dr. Stefano Palagi, Johannes Sachs, Prof. Zhiguang Wu, Jan-Philipp Guenther, Vincent Kadiri, Tingting Yu, Prof. Vijay Chikkadi, and Eunjin Choi – thank you for the invaluable support, assistance, and friendship. Most of all, my sincere thanks go to Jutta Hess for her constant background support, and Dr. Andrew G. Mark and Dr. Tung-Chun Lee for their rigorous and elaborate advices.

My thanks also go to collaborators: Dr. Klaus Kuhnke, Philippe Roelli, Prof. Christophe Galland, Debadrita Paria, Prof. Ambarish Ghosh, Prof. Junsuk Rho, Thomas Reindl, Ulike Waizmann, Prof. Lawrence D. Ziegler, Kwanghyo Son, and Dr. Soon Jung Jung – thank you for the fruitful collaborations. I am also grateful to all former and current Korean community in MPI-Stuttgart for their friendship and advices.

Finally, my most sincere thanks go to my family and fiancée. I dedicate this thesis to them.

"Your beginnings will seem humble, so prosperous will your future be." **Job 8:7**

Stuttgart, 30th May 2017

Hyeon-Ho Jeong (정현호)

Abstract

Nanoparticles promise a variety of application in energy, medicine, and biology. However, most nanoparticles' material composition and shape cannot be tuned and so functions have thus far been limited. Moreover they are often also chemically unstable in solution. Therefore, the overall goal of this thesis is to develop nanoparticles whose function and shape can be programmed and that can be corrosion protected, and to then apply these nanoparticles to sensing tasks in complex biological fluids. A special focus of this thesis is chiral nanostructures.

A promising technique to address this is physical vapour shadow growth, namely nano glancing angle deposition (nanoGLAD). This scheme allows the design of new three-dimensional (3D) hybrid nanoparticles as it permits the control over both the shape and material composition of the nanoparticles. Although this method offers the possibility to grow nanoparticles that are functionally programmed, it has so far not allowed the use of many materials that are chemically unstable in solution, which limits the scope of potential applications.

This thesis starts with describing the nanoGLAD growth procedure. A first application is the wafer-scale patterning of unconventional nanoshapes, e.g. tri-layer particles, holes, rings, and hollow domes, which are not possible using state of the art 3D nanofabrication methods (chapter 2). Then, in conjunction with atomic layer deposition (ALD), this thesis shows how the nanoGLAD scheme can be adapted for the fabrication of '3D core-shell nanoparticles and nanocolloids' using unstable and reactive materials. The key concept here is that the core consists of the unstable material which is grown such that the shell contains no voids or defects (chapter 3). Notably, the shapes that can be grown include symmetry-broken chiral nanoparticles, which possess unique spectral properties that make them useful for sensing applications. This thesis uses chiral nanocolloids to realise extremely sensitive plasmonic nanosensors and nanocolloids that can also be used as a nanomechanical probes for active nanorheology. By forming a composite of two materials during growth – one that gives a strong plasmonic response and the other to tune the composite's dielectric function – plasmonic nanoparticles are presented that show record local surface plasmon resonance (LSPR) sensitivities to date (chapter 4). With the same alloying principle a plasmonic and a ferromagnetic material are combined. The resulting 'chiral + plasmonic + ferromagnetic' particles can be actuated using a magnetic field and this is used to measure the viscosity of blood plasma in the presence of blood cells. The viscosity of blood serum is an important disease indicator, but the measurement using commercial rheometers requires the separation of the blood cells. This is not needed in the nanorheological measurements shown in this thesis (chapter 5).

Keywords

Nanoparticles, nanocolloids, physical vapour deposition, shadow growth, chiral plasmonics, corrosion protection, plasmonic sensing, nanorheology

Zusammenfassung

(translated in German by Vincent Kadiri and Tingting Yu)

Nanopartikel versprechen eine Vielzahl von Anwendungen in Bereichen der Energie, Medizin und Biologie. Allerdings können die Materialzusammensetzungen und -formen der meisten Nanopartikel nicht fein genug abgestimmt werden, sodass die bisherigen Funktionen bislang begrenzt waren. Darüber hinaus sind sie oft auch chemisch instabil in Lösungen. Das Ziel dieser Arbeit ist daher Nanopartikel zu entwickeln, deren Funktion und Form programmiert werden können und, die korrosionsgeschützt sind, damit diese Nanopartikel dann in komplexen biologischen Flüssigkeiten als Sensoren verwendet werden können. Ein besonderer Fokus dieser Arbeit sind chirale Nanostrukturen.

Eine vielversprechende Technik, um dies zu erreichen, ist das physikalische vapour shadow growth (Dampfschattenwachstum) Verfahren: die Nano glancing angle deposition (nanoGLAD). DieseMethode ermöglicht die Gestaltung neuer dreidimensionaler (3D) Hybrid-Nanopartikel, da sie die Kontrolle über die Form und die Materialzusammensetzung der Nanopartikel ermöglicht. Obwohl diese Methode die Möglichkeit bietet Nanopartikel, die funktional programmiert sind, herzustellen, war es bei vielen Materialien bisher nicht möglichsie zu verwenden, da sie in Lösungen chemisch instabil sind, was den Umfang der möglichen Anwendungen begrenzte.

Diese Arbeit beginnt mit der Beschreibung des nanoGLAD-Wachstumsverfahrens. Eine erste Anwendung ist dieStrukturierung von unkonventionellen Nanostrukturen auf Waferebene, z.B. Dreischichten-Partikel, Löcher, Ringe und Hohlkuppeln, die nach dem Stand der Technik konventioneller 3D-Nanofabrikationsverfahren nicht möglich sind (Kapitel 2). Dann zeigt diese Arbeit in Verbindung mit der Atomic Layer Deposition (ALD), wie das nanoGLAD-Schema für die Herstellung von "3D-Core-Shell-Nanopartikeln und -Nanokolloiden" für instabile und reaktive Materialien angepasst werden kann. Das Schlüsselkonzept besteht darin, dass der Kern aus dem instabilen Material besteht, das so gewachsen ist, dass die Schale keine Hohlräume oder Defekte enthält (Kapitel 3). Bemerkenswert ist, dass die gebildeten Formen symmetrie-gebrochene, chirale Nanopartikel beinhalten, die einzigartige spektrale Eigenschaften besitzen, die sie für Anwendungen als Sensoren attraktiv machen. Diese Arbeit verwendet chirale Nanokolloide, um extrem empfindliche plasmonische Nanosensoren und Nanokolloide zu verwirklichen, die auch als nanomechanische Sonden für aktive Nanorheologie verwendet werden können. Durch die Bildung eines Komposits aus zwei Materialien während des Wachstums - eines, das eine starke plasmonische Resonanz verursacht und einem zweiten, um die dielektrische Funktion des Komposits abzustimmen, werden plasmonische Nanopartikel hergestellt, die Rekorde lokaler Oberflächenplasmonresonanz (LSPR) Empfindlichkeiten darstellen (Kapitel 4). Mit dem gleichen Prinzip der Kompositbildung werden ein plasmonisches und ein ferromagnetisches Material kombiniert. Die resultierenden "chiralen + plasmonischen + ferromagnetischen" Partikel können mit einem Magnetfeld aktuiert werden. Dies wird verwendet, um die Viskosität des Blutplasmas in Gegenwart von Blutzellen zu messen. Die Viskosität des Blutserums ist ein wichtiger Krankheitsindikator, aber die Messung mit kommerziellen Rheometern erfordert die Trennung der Blutzellen. Dies ist bei den in dieser Arbeit gezeigten nanorheologischen Messungen nicht notwendig (Kapitel 5).

Schlüsselwörter

Nanopartikel, Nanocolloide, physikalische Dampfabscheidung, Schattenwachstum, chirale Plasmonik, Korrosionsschutz, plasmonische Erfassung, Nanorheologie

Contents

List of Figures

List of Tables

List of Symbols and Abbreviations

A	Optical absorption
$\mathbf{B}$	Applied magnetic field
c	Concentration
D	Diffusion coefficient
d	Diameter
E	Optical (plasmonic) extinction
E_{a}	Energy barrier in diffusion process

f	Frequency
g	Edge-to-edge gap
$\mathbf{H}$	Magnetic field strength
h	Height
k_{B}	Boltzmann constant
$\mathbf{k}$	Wave vector
L	Programmed length in deposition system
l	Length
$\mathbf{M}$	Magnetisation
$\mathbf{m}$	Magnetic moment
n	Refractive index
P	Power
R	Major radius of a nanohelix
r	Minor radius of a nanohelix
S	Proportion
S_n	Refractive index sensitivity
s	Center-to-center spacing
T	Temperature
t	Time
v	Volume fraction
w	Thickness of a layer deposited on QCM
α	Angle of an incident vapour flux
δ	Pojection angle
$\delta\chi$	Chiral shape factor
ε	Dielectric constant
φ	Azimuthal rotation rate
λ	Wavelength
$\bar{\chi}$	Achiral shape factor
σ	Instrumental resolution (in CD)
τ_r	Relaxation time (in DLS)
ϕ	Phase lag between $\mathbf{B}$ and $\mathbf{k}$
θ	Angle in SEM
$\theta_{\mathbf{B}}$	Angle between $\mathbf{B}$ and $\mathbf{k}$
$\theta_{\mathbf{m}}$	Angle between $\mathbf{m}$ and $\mathbf{k}$
$\boldsymbol{\omega}$	Angular velocity
η	Viscosity
χ	Hydrodynamic shape factor
$\boldsymbol{\tau}$	Torque
γ	Shear rate (rheometer)
3D	Three-dimensional
AR	Aspect ratio
ALD	Atomic layer deposition
BCML	Block-copolymer micelle nanolithography
BDMT	1,4-benzenedimethanethiol
CB	Circular birefringence
CD	Circular dichroism
CMOS	Complementary metal-oxide-semiconductor

DDSCAT	Discrete dipole scattering
DLS	Dynamic light scattering
DMSO	Dimethyl sulfoxide
EBL	Electron beam lithography
EDX	Energy dispersive X-ray spectroscopy
EELS	Electron energy loss spectroscopy
EF	Energy filtered
FD-CD	Fluorescence-detected circular dichroism
FOM	Figure of merit
FWHM	Full width at half maximum
GLAD	Glancing angle deposition
HADDF	high-angle annular dark-field imaging
HSQ	Hydrogen silsesquioxane
ICP	Inductively coupled plasma
IP	In-plane
IPS	Intermediate polymer stamps
LCP	Left-handed circularly polarised light
LH	Left-handed
LIA	Lock-in-amplifier
LN	Liquid nitrogen
LSPR	Local surface plasmon resonance
MEMS	Micro electro mechanical systems
MSD	Mean square displacement
NC	Nanocap
NIL	Nanoimprint lithography
NIR	Near-infrared
NP	Nanoparticle
NSL	Nanosphere lithography
NW	Nanowire
OD	Optical density
OES	Optical emission spectroscopy
OOP	Out-of-plane
ORD	Optical rotatory dispersion
PB	Phosphate buffer
PEG	Polyethylene glycol
PEM	Photoelastic modulator
PMT	Photomultiplier
PSPR	Propagating type surface plasmon resonance
PVP	polyvinylpyrrolidone
R6G	Rhodamine 6G
RCP	Right-handed circularly polarised light
RH	Right-handed
RIE	Reactive ion etching
RIU	Refractive index unit
ROA	Raman optical activity
SERS	Surface enhanced Raman spectroscopy
SEM	Scanning electron microscopy
SQUID	Superconducting quantum interference device
TEM	Transmission electron microscopy

TMA	Trimethylaluminum
QCM	Quartz crystal monitor
VIS	Visible
UV	Ultraviolet

Chapter 1 Introduction

1.1 Chirality at the nanoscale

1.1.1 Chirality

Chirality, which originates from the Greek word for 'hand', describes any object or group of points that are odd under parity (symmetry of space inversion). In 1894, Lord Kelvin defined chirality with the statement [1]:

"I call any geometrical figure, or any group of points, chiral, and say that it has chirality, if its image in a plane mirror, ideally realized, cannot be brought to coincide with itself."

For instance, if an object cannot be superimposed on its mirror image, it is said to be chiral and the two mirror image forms are called 'enantiomers'.[2] In nature, many structures and molecules are chiral, especially peptides, enzymes, proteins, and DNA (see figure 1:1). A major question in chemistry is the homochirality of life; the observation that most molecules of life only exist as one enantiomer, namely D-sugars and L-amino acids.[3]

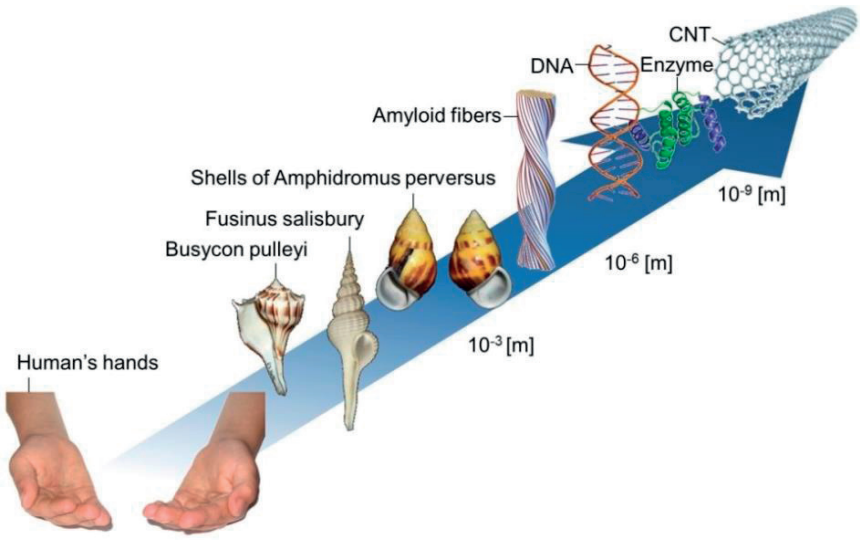

Figure 1:1 Chirality in nature at the small scale: Sinistral Busycon pulley,[4] dextral Fusinus salisbury,[4] shells of Amphidromus perversus,[4] DNA,[5] enzyme,[5], CNT,[6] and amyroid fibers.[7] Reprinted from Nature Publishing Group and Wiley-VCH publisher.

1.1.2 Circular dichroism (CD)

Two, left- and right-handed, enantiomers possess similar physical and chemical properties, so only under a chiral influence can their properties differ. Enantiomers for instance respond differently to left- and right-

circularly polarized light. Known as optical activity, this is the difference in the complex refractive index of a solution containing chiral molecules of one enantiomer in excess $\tilde{N} = \tilde{n}_0 \pm \delta\tilde{n}$ with $\delta\tilde{n} = \delta n + i\,\delta k$, where n is the refractive index and k is the extinction coefficient of the solution.[8] The differences in the real (δn) and imaginary parts (δk), respectively, give rise to circular birefringence (CB) and circular dichroism (CD), and measuring those features provides direct means of distinguishing the handedness of the chiral molecules. Several other related methods that probe the chirality of molecules have been developed including fluorescence-detected circular dichroism (FD-CD), optical rotatory dispersion (ORD), vibrational circular dichroism (VCD), and Raman optical activity (ROA).[3, 9-14] Among them, CD spectroscopy is convenient for the study of both colloids and nanostructured substrates that show some optical absorption, hence this thesis extensively uses CD to investigate novel chiral plasmonic nanoparticles (see figure 1:2a). [9] Figure 1:2b shows an example of CD spectra of a chiral molecule as a function of wavelength. Such chiroptical effects depend on the change of the electric field of the electromagnetic wave across the dimensions of the molecule, so that they are inherently weak.[15] However, in the case of nanostructures that approach the dimensions of visible light, these effects are therefore larger, and moreover they can show resonances in the visible range of the spectrum, thanks to the nanoparticles' unique optical properties that are discussed in the following sections.

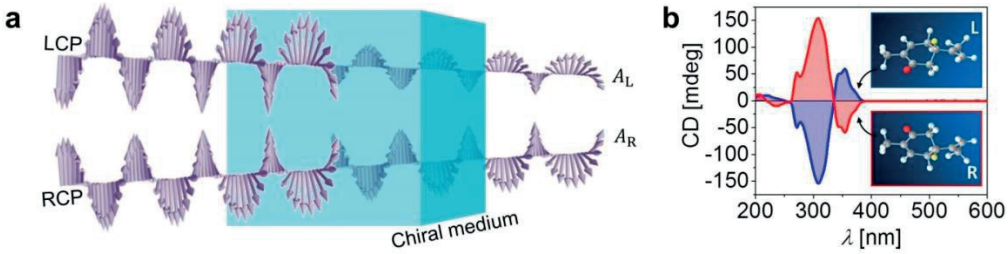

Figure 1:2 Circular dichroism (CD) spectroscopy. (a) Schematic view of CD spectroscopy. Left- and right-circularly polarised light interacts with a solution containing an isotropic chiral medium. The absorption difference depends on the handedness of the medium. (b) Example of CD spectra of chiral molecules as a function of wavelength, here 1% carvone (red: right-handed and blue: left-handed). Each inset shows the left- and right-handed carvone structures.

1.2 Chiral nanoparticles

In the range of 1 to 100 nm length scale, materials are typically defined as nanoparticles and possess unique properties that differ from those of the corresponding bulk materials.[16] Examples are quantum dots (c.f. semiconductors),[17] superpara-magnetism (c.f. ferri- or ferro-magnetic materials),[18] up-conversion of light (c.f. rare-earth materials),[19] and local plasmonics (c.f. metals).[20] Thanks to their small size nanoparticles are also of interest for applications in biology and in medicine for imaging,[21, 22] sensing,[23] therapy,[16] and actuation.[24] Moreover, the large surface to volume ratio of nanoparticles facilitates their use as catalysts.[25, 26] These diverse properties support technical advances in diverse areas such as nanochemistry,[16] nanolithography,[27] and nanofabrication.[28] The latter has also enabled the design and fabrication of 3D building blocks of new functional materials, namely "metamaterials" with properties that are not found in naturally occurring materials.[29] "Meta" originates from the Greek word for 'beyond', hence a metamaterial describes a material that is engineered to give rise to unusual properties not normally found in natural materials.[29-31] For instance, photonic and plasmonic metamaterials show many exciting optical properties: a magnetic response at optical frequencies, a negative refractive index, zero reflection through impedance matching, perfect absorption, giant circular dichroism,

and enhanced nonlinear optical properties.[27] Being able to make a suspension of such metamaterials, i.e. metafluid, would open up entirely new classes of functions and applications of meta-systems that currently cannot be demonstrated. However, this is challenging as the current methods cannot grow truly 3D chiral nanoparticles that are also chemically stable.[15, 18, 32] Therefore very limited functions and applications of chiral nanoparticles have been investigated so far. Detailed examples will be discussed in the following subsections, before the thesis presents means to grow as well as to protect chiral nanocolloids that can be used as sensors and nanoprobes.

1.2.1 Fabrication

1.2.1.1 Conventional methods

Chemical means permit the synthesis of a large number of nanocolloids made of various shapes and materials,[33] but energetically favourable configurations at the nanoscale generally show high symmetry and thus currently there is no method to synthesise multifunctional metallic nanoparticles having a defined chirality.[34] Exceptions are possible where symmetrical nanoparticles are either linked to chiral molecules (e.g. figure 1:3a)[32, 35-38] or arranged in a chiral order, figures 1:3b–d.[39] In these cases chiroptical effects are induced by the coupling of the chiral molecule to the nanoparticle or the interactions between the nanoparticles. The use of these arrangements have been proposed for chiral sensing,[32, 40] but have so far met with limited success due to the yields and reproducibility of the chiral nanostructures. Furthermore, since many chemically synthesised nanoparticles are not stable in biological-fluids,[18, 41, 42] they are not useful for bio-applications. On the other hand, physical methods, mostly electron-/ion-beam-based lithography, have also been used for the fabrication of diverse 2D and 3D chiral structures (figures 1:3e–h).[43-46] These methods can be used to make chiral structures with interesting chiroptical properties, but they often do not permit large (wafer-) scale processing.[47] On surfaces the structures can exhibit 2D chirality, but for applications in solution the chiral structures must be 3D and chiral, and this requires multiple lithography steps that require independent and thus time-consuming processing steps (figures 1:3g–h).

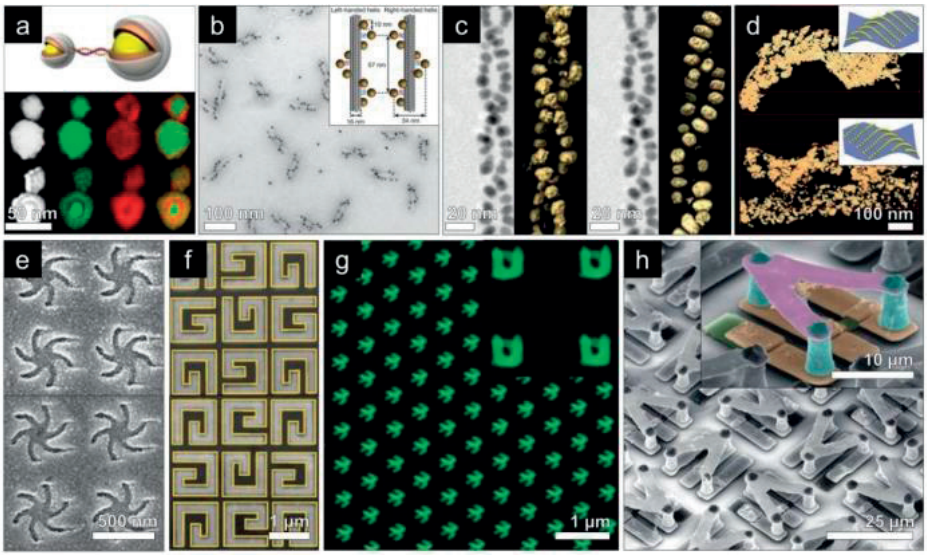

Figure 1:3 Collections of current chiral plasmonic nanostructures. (a)–(d) Self-assembly of plasmonic nanoparticles in a chiral order from the molecular to the macro scale.[32, 35, 38, 39] (e)–(f) 2D[43, 44] and (g)–(h) 3D chiral nanostructures[45, 46] fabricated by nanolithographic techniques. Reprinted from American Chemical Society, Nature Publishing Group, and Wiley-VCH publisher.

1.2.1.2 Nano glancing angle deposition

A promising method to grow chiral nanoparticles is nano glancing angle deposition (nanoGLAD), which is mainly used in this thesis, figure 1:4. Physical vapour deposition (PVD) is a well-established means to grow thin films from a number of materials, including metals, semiconductors, insulators, and magnetic materials. The vapours land on the target substrate where they nucleate with neighbouring adatoms. Depending on the adatom's dominant interfacial force between cohesion with the neighbouring adatom and adhesion on the substrate, a constant deposition follows one of three growth regimes (2D layer or Frank–van der Merwe growth, 3D island or Volmer-Weber growth, and layer-plus-island or Stranski-Krastanov growth).[48] A key point is that in ordinary (normal incidence) deposition the entire substrate is coated with a continuous film.[49] Meanwhile, when an angle of the vapour flux is not normal to the substrate, i.e. an oblique angle (figure 1:4a), the region behind each nucleus becomes 'self-shadowing' where the subsequent ballistic evaporant cannot land.[50, 51] For example, figure 1:4b shows, that at high angles of the vapour flux, the pre-formed nuclei serve as seeds and give rise to a shadowing area behind them. So additional adatoms are primarily deposited on top of the already existing seeds.[52] If the surface has many such seed particles that are suitably spaced together, then this process results in the growth of an array of slanted columnar structures, which was firstly investigated by König and Helwig in 1950.[50] Later, in 1959, Young and Kowal first proposed an azimuthal rotation of the target substrate during growth, leading to the change in the direction of the incident vapour flux relative to the substrate, figure 1:4c.[51] This process is known as glancing angle deposition (GLAD) coined by Robbie et al. and makes it possible to grow nanostructured 3D films. [53, 54] For example, a slow continuous rotation of the substrate during growth leads to the formation of helical columns, while a fast rotation yields vertical columns normal to the substrate.[55]

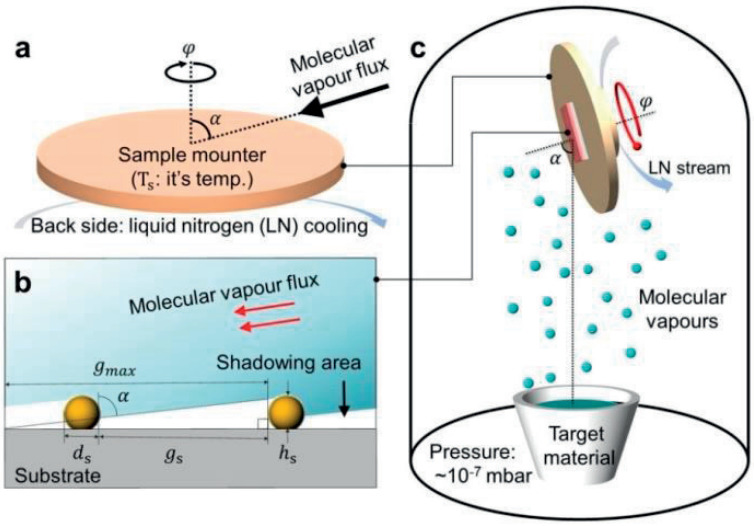

Figure 1:4 Nano glancing angle deposition (nanoGLAD). (a) Definition of the angle of molecular vapour flux and the azimuthal rotation of the substrate. (b) An illustration of the shadow effect in a periodic array of the BCML-grown seed particles. (c) A schematic view of the nanoGLAD apparatus with a substrate cooling.

As is also typical for PVD, multiple sources simultaneously or sequentially permit the control over the material composition.[54] However, at the nanoscale, surface diffusion of the adatoms is a significant factor in determining the shape of the resulting nanoparticle and, because of high surface diffusion of many (metal) adatoms, it is challenging to fabricate 3D (metallic) nanoparticles. In 2013 it has been nevertheless shown how 3D-shaped complex nanostructures (< 100 nm) including metallic ones can be fabricated.[56] In par-

ticular, the method combines the two techniques of block copolymer micelle nanolithography (BCML) [57] with GLAD. This "nanoGLAD" scheme allows the design of 3D hybrid nanomaterials and nanocolloids. Its key idea is the use of a "nano" shadow effect by means of (1) a wafer-level array of nanoseeds and (2) suppression of adatoms' surface diffusion by cooling the substrate. Firstly, BCML, which is a lithographic method developed by Glass et al.,[57] is used for the fabrication of the wafer-level array of metallic nanoparticles to be used as a seed layer (figure 1:5). In a nutshell, block-copolymer micelles, poly(styrene)-b-poly(2-vinylpyridine), are formed by self-assembly in a suitable solvent and each of their cores contains metallic salt (e.g. $HAuCl_4$), figure 1:5a. Then they are spin-coated onto a wafer, which results in a quasi-hexagonal ordered monolayer of the micelles spaced evenly apart over the entire surface of the wafer (figure 1:5b). By treating the coated wafer with a plasma, the block-copolymers are removed and at the same time the salts are reduced to form nanodots (figure 1:5c). Figure 1:5d shows an example of an array of 10 nm gold nanoparticles patterned by the BCML method. Note that the resultant nanodots' sizes and spacings can be precisely tuned by controlling, respectively, the loading amount of the salt in solution and the chain length of the block-copolymers.[58] In fact as those geometrical factors will dramatically affect the uniformity of the GLAD structures, it is essential to determine the optimal dimension of the seed layer, which is fully addressed in this thesis (see chapter 2 for the detailed effect of the arrangement of the seeds on the shadow growth process).[55, 59]

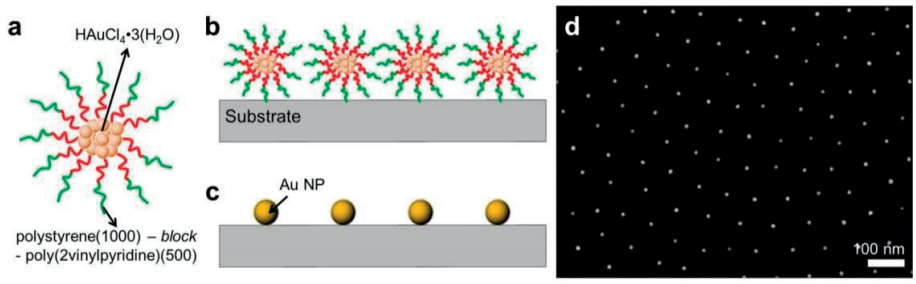

Figure 1:5 Block copolymer micelle nanolithography (BCML).[57] (a) A micelle whose core is metallic salt and encapsulated in self-assembled block copolymers when dispersed in solvent. (b) Formation of an extended monomicellar film by spin coating. (c) A subsequent plasma treatment that removes the block copolymers and reduces the metallic salt into the form of nanoparticles. (D) An SEM image of an array of ~10 nm gold nanoparticles patterned by BCML.

Reducing the substrate's temperature during growth will be effective to minimize the surface diffusion of the adatoms.[60] According to the structure zone model the morphology of a thin film is classified depending on the ratio between the substrate's temperature T_s and the melting temperature of target material T_m during growth, figure 1:6.[61, 62]

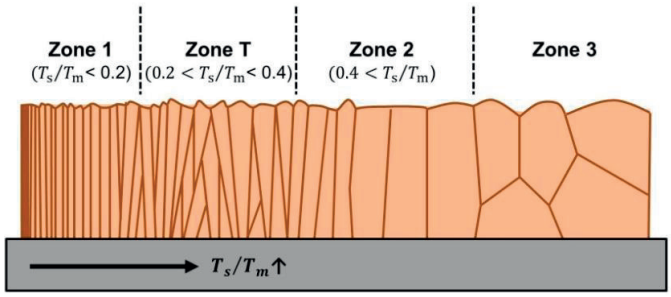

Figure 1:6 Structure zone model of a thin film grown by physical vapour deposition (PVD) as a function of temperature ratio, T_s/T_m. Reprinted from Elsevier Ref. 62.

For T_s/T_m < 0.2 the structural profile belongs to zone 1 where individual well separated columns grow. This is due to the suppressed surface diffusion of the evaporant and, by Fick's law, it can be considered as a thermally activated Arrhenius-type process where the diffusion coefficient D is given as,[52]

$$D \propto e^{-E_a/k_B T_s}, \tag{1:1}$$

where k_B is Boltzmann's constant, and E_a is the energy barrier of the diffusion process. It follows that the surface mobility can be reduced using cooling (figure 1:4c).[56] Contacting the substrate to a liquid nitrogen reservoir, for example, permits the growth of the small Ag-Cu metallic alloyed chiral nanoparticles (see figure 1:7a).[56] Figures 1:7b–e also shows more examples of chiral nanocolloids with different chirality and material composition, grown by nanoGLAD.[28, 63-65] However, especially challenging is the growth of metal nanoparticles using unstable materials such as Co, Cu, Ag, Mg, etc., which quickly oxidise and corrode in aqueous solution. Nanocolloids from these materials have thus far not been used for applications in solutions. This thesis presents a scheme to grow 3D hybrid nanoparticles with unstable materials and to protect them that they are chemically stable (see chapter 3), such that they can be used for chiral plasmonic sensing applications. These are described in the following section.

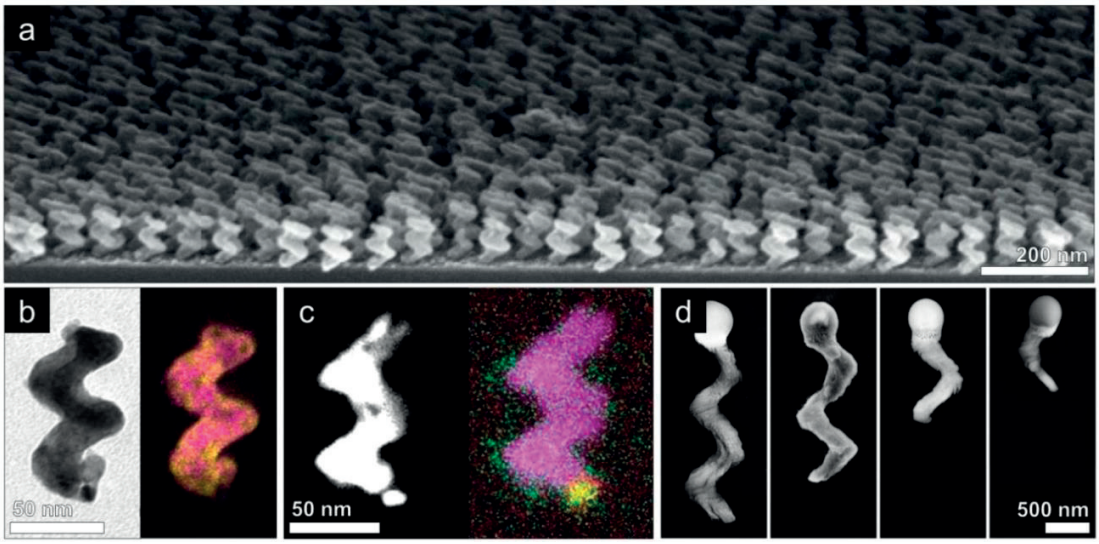

Figure 1:7 Chiral nanohelices grown by nanoGLAD. (a) The SEM image of Ag-Cu nanohelices as grown on a wafer before release.[56] (b) The TEM image of Ag-Cu nanohelix and its corresponding EDX mapping image (yellow: Ag, purple: Cu).[28] (c) The high-angle annular dark-field (HADDF)-TEM image of Ni nanohelix and its corresponding EDX mapping image (yellow: Au, red: Ti, purple: Ni, green: O).[63] (d) The SEM images of SiO_2 microhelices with different number of turns.[66] Reprinted from Nature Publishing Group, Royal Society of Chemistry, and American Chemical Society.

1.2.2 Chiral plasmonic applications

Metallic nanoparticles whose diameter is smaller than the wavelength of light can support coherent collective oscillations of delocalised electrons in response to electromagnetic radiation.[67] These are known as localised surface plasmons (LSPs) and their resonance (LSPR), figure 1:8a.[68] The LSPR accompanies a local electric field enhancement near the surface of the nanoparticle, and plasmonic nanostructures find use as optical antennas,[69, 70] for imaging or sensing of small particles,[68, 71-73] in photo-reactions,[74-76] as well as catalytic reactions,[77-79] and for local heating (thermal applications),[80] which can be useful in

nanolithography,[81-84] photothermal therapy,[85, 86] and the thermophoretic effect.[87] Moreover, since the LSPR provides a spectral resonance peak that shifts in response to changes of the refractive index of the medium surrounding the particle, many different types of sensing applications have been demonstrated, e.g. sensing biomolecules by tracking the LSPR peak according to the effective refractive index change caused by molecules adsorbed onto the surface of the nanoparticle.[73, 88] Consistent with the purpose of plasmonic function, material engineering promises the design of customised plasmonic features with the flexibility in tuning the position, bandwidth, and the number of the plasmonic resonant modes.[89-91] This can be achieved by controlling the geometry and material composition of the nanoparticle and some examples are shown in figure 1:8b.[92-97]

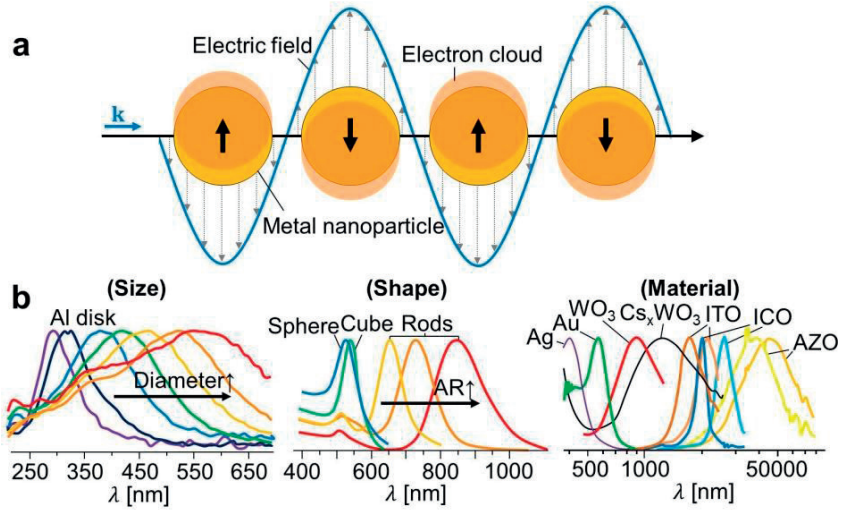

Figure 1:8 Local surface plasmon resonances (LSPR) of metal nanoparticles. (a) Schematic view of coherent collective oscillations of free electrons of metal nanoparticles in response to light when the diameter of the nanoparticle is smaller than the wavelength of light. (b) Plasmonic resonances engineered by size,[94] shape,[95] and material composition of nanomaterials.[96] Reprinted from the American Chemical Society.

When such metal nanoparticles are chiral, then their suspension can show an induced chiroptical effect near the frequency of the plasmon resonance: this is interesting as such chiroptical effects are typically weak in molecules. Chiral nanoparticles have already been grown using nanofabrication techniques [35, 56, 98-100] and their chiroptical effects are indeed stronger than what is observed in molecules,[64, 101, 102] which suggests new sensing capabilities.[15, 32] The scope of potential applications can be increased by tailoring the geometry of the nanostructure [103-105] or by growing nanostructures that incorporate several functionalities, i.e. that are also magnetic [106] or respond to electric fields.[76] It is therefore desirable to develop a way to tailor the chiral shape of the nanoparticle and to simultaneously incorporate several additional functionalities in the chiral nanoparticles. The following subsections introduce two key applications, plasmonic sensing and active plasmonics.

1.2.2.1 Plasmonic sensing

In bio-applications, it would be desirable to have a local sensor for use *in situ* or *in vivo*. The LSPR of nanostructures shifts in response to changes of the refractive index of the surrounding medium, figures 1:9a-b.[91] Since the electric field is highly localised on the particle it only has a small penetration depth into the surrounding medium, which makes for a localised sensor.[23, 107, 108] Crucially, it is also possible to apply chiral plasmonics to such LSPR sensing, by tracking the CD spectral peak positions in response to

refractive index changes (e.g. figure 1:10a).[109] The bipolar nature of CD gives richer spectral features and zero crossings that can be tracked resulting in a narrow effective full width at half maximum (FWHM) and features that are a function of the spectral resolution of the detector.[93] This translates into high FOMs. A similar approach has been demonstrated on a surface of structures that were magnetic and gave rise to a magnetic-dichroism spectrum. The achiral magnetic nanoantennas induced ellipticity in the transmitted beam.[110] In this case the choice of material was dictated by the requirement to induce a magneto-optical response, which significantly limits a range of potential materials. Conventional LSPR sensors rely only on pure metal nanoparticles (e.g. Au and Ag) whose sensitivities are typically below 1000 nm/RIU (see figure 1:9c), such that their sensitivities are still much lower than those found in propagating type surface plasmon resonance (SPR) biosensors (< 5000 nm/RIU). Hence such LSPR nanosensors require improved sensitivity and FOM for any practical use.[72, 73] This thesis shows how material engineering plays an important role and how it can – together with CD spectroscopy – be used to achieve record LSPR sensitivities and FOMs (figure 1:10a).[93] The surprising finding is that a chiral nanostructure is more sensitive than an ordinary achiral nanoparticles in detecting achiral properties (ordinary refractive index changes – see chapter 4).

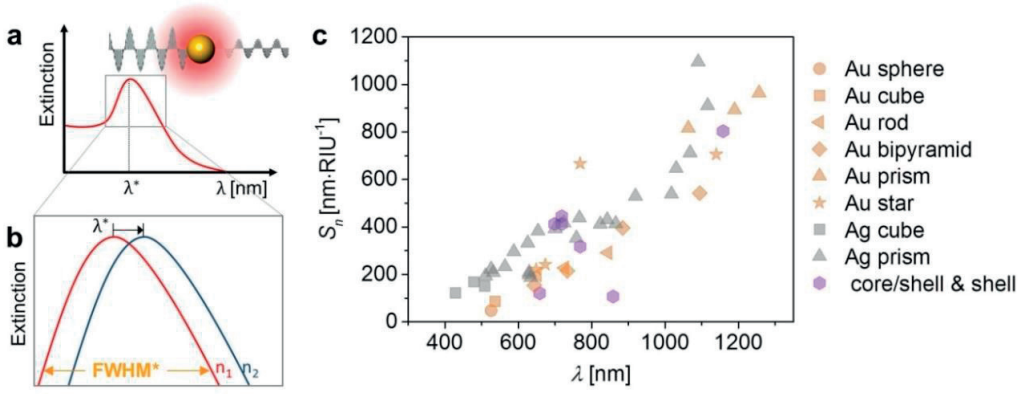

Figure 1:9 LSPR sensing. (a) Schematic view of the plasmonic resonance of metallic nanoparticles as a function of wavelength, λ. Inset shows a common plasmonic sensing system where a metallic nanoparticle (here a sphere) interacts with light and generates a detectable extinction peak at the plasmon resonance. (b) A zoomed-in region near the peak λ^* showing how it shifts in wavelength as the refractive index of the surrounding medium changes $n_1 < n_2$. (c) The LSPR sensitivities, S_n reported to date in the literature for metallic nanocolloids (Au sphere,[95] Au cube,[95] Au rod,[95] Au bipyramid,[95] Au prism,[111] Au star,[95, 112, 113] Ag sphere,[114, 115] Ag cube,[116, 117] Ag prism,[114, 118, 119] core-shell (or shell) [120-124]) as a function of λ at 1.333 RIU. The symbols and colours are different for the shapes and the material composition, respectively. Reprinted from American Chemical Society and Royal Society of Chemistry.

Chiral plasmonics also promises new sensing schemes that permit the detection of chiral molecules, figures 1:10b-c. The electromagnetic field near a nanostructure can give rise to an optical chirality surpassing that of circularly polarised light, which is known as a superchiral field and this could be useful in chiral detection figure 1:10b.[15, 125, 126] However, the underlying mechanism of how the chiral near-field may interact with the chiral molecule and affect the CD spectrum is still unclear. Another interesting scheme is the use of a Föster-type resonance energy transfer (FRET) with plasmons, figure 1:10c.[32, 40] At the plasmonic resonance the achiral nanoparticle generates a 'hot electron', which is the metastable state of excited electrons, but has no visible optical activity itself. Then if this plasmonic particle is in contact with a chiral molecule, energy can be transferred to the molecule such that the molecular optical activity can be stimulated. This could be a very flexible and sensitive sensing scheme, but it has to date not been realised.

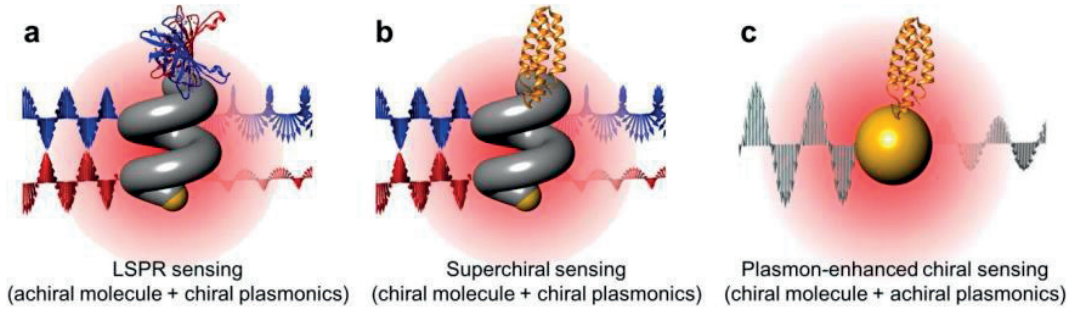

Figure 1:10 Chiral plasmonic sensing. (a) Refractive index sensing by the aid of chiral plasmonics.[93, 109, 110] (b) Superchiral sensing by using the superchiral optical field generated by the chiral plasmonic nanoparticle.[15, 125] (c) Plasmon-enhanced chiral sensing based on FRET with plasmons.[32, 40]

1.2.2.2 Active plasmonics

"Active" plasmonic systems have recently been developed by controlling either the applied electromagnetic radiation to the metallic nanostructure [46, 127-129] or the dynamics of the nanostructures. [130-134] Strictly, the structures here are "actuatable" and have nothing in common with "active matter". The first demonstration relies on strong electric fields to align a Au nanorod. The long axis of the Au nanorod is aligned along the direction of the external electric field due to a torque exerted by the electric field acting on the dominant axis of the rod's polarisability, so that its orientation and thus interaction with polarised light can be controlled, figures 1:11a.[130] Simpler schemes have been developed that facilitate alignment by a weak electric field [132, 134] or a magnetic field,[133] figures 1:11b-c. However, they still require complex fabrication schemes and show low yields. Recently, the chiroptical response has been tuned using a DNA origami decorated with Au nanoparticles, and the polarity of the chiroptical response was manipulated (figures 1:11d-e).[36, 37] Those systems, however, have low yield and show low optical activity (below 1×10^{9} °·M^{-1}·cm^{-1} of molar circular dichroism), slow transition times (approximately 15 min to complete), and low reproducibilities (only 4 cycles), and they are thus unsuitable for optical devices and systems. A continuous and reproducible way to actively drive particle dynamics and to modulate CD signals is therefore needed and demonstrated in this thesis (see chapter 5).

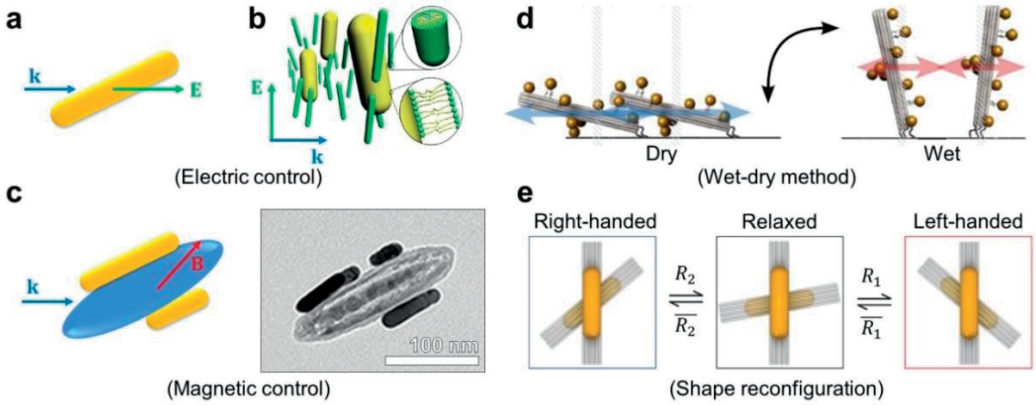

Figure 1:11 Plasmonic switching by particle dynamics. (a)–(c) Plasmonic switch: (a) An electric alignment of Au nanorods.[130] (b) An electric alignment of Au nanorods by the aid of liquid crystals.[132, 134] (c) A magnetic aliment of Au nanorods supported by a magnetic particle.[133] (d)–(e) Chiral plasmonic switch: (d) A control of suspension of chiral nanostructures in fluid.[36] (e) Shape deformation by DNA origami.[37] Images reprinted from Nature Publishing Group and American Chemical Society.

1.3 Objective and Outline

The overall goal of this thesis is to develop chiral plasmonic nanomaterials that are capable of sensing tasks in complex biological fluids. For this this thesis focuses on the following problems:

(1) Fabrication:
- How to fabricate and control 3D features at the nanoscale?
- How to achieve high chemical stability of various nanoparticles including chiral ones in solution?
- How to incorporate multiple functions and use these for sensing applications?

(2) Application :
- What practical applications can be achieved in biological fluids by the chiral nanomaterials developed in this thesis?
- What is the advantage of the chiral plasmonic spectroscopy for LSPR sensing and how to engineer the dielectric function of chiral plasmonic nanomaterials for enhanced LSPR sensing performance?
- How to realise switchable chiral plasmonics and how to use them for nanorheology?

To address the problems listed above, the aims of this thesis are:

Chapter 2: Nano glancing angle deposition
The aim of this chapter is to describe the nano physical shadow growth technique used throughout the thesis. In particular, the scalability of the nanoGLAD process, ranging from single 3D nanostructure to wafer-scale (unconventional) nanopatterns, is examined.

Chapter 3: Corrosion-protected hybrid nanoparticles
This chapter presents a substrate-based physical fabrication scheme that can nevertheless coat the entire surface of a nanoparticle. In conjunction with atomic layer deposition (ALD), the nanoGLAD scheme is used to design and fabricate core-shell hybrid nanocolloids that are coated such that they are (chemically) stable in physiological fluids as well as acidic and oxidising fluids.

Chapter 4: Chiral plasmonic nanosensors
The first aim to use chiral particles is as a refractive index nanosensor. The key idea is to use the extinction-based circular dichroism as a spectral signature by tracking its bipolar peaks (zero-crossing) that have a narrow effective FWHM, which in turn translates into a high FOM. The sensitivity is enhanced by engineering the shape and dielectric dispersion of the nanoparticle to make it sensitive to local refractive index changes.

Chapter 5: Active nanorheology
The second aim is to develop the chiral nanocolloids as nanorheological probes, by spectroscopically tracking the particle dynamics in a fluid. For this it is necessary to be able to exert a torque on the chiral plasmonic nanoparticles, so that they are capable of aligning with an external magnetic field. The chiroptical spectrum then corresponds to the particles' orientation to the incoming light. This allows a size-dependent measurement of the viscosity, which is an important consideration for bio-applications, which is not possible with conventional macro rheometers.

The results presented in this thesis have (in part) been published (or will be published in the near future). This thesis is a cumulative thesis and the chapters are taken from the publications listed below. In particular, figures and excerpts were taken from the following sources:

Chapter 2:

[59] Shape control in wafer-based aperiodic 3D nanostructures, **H.-H. Jeong**, A.G. Mark, J.G. Gibbs, T. Reindl, U. Waizmann, J. Weis, and P. Fischer, ***Nanotechnology*** 25, 235302 (2014) - Cover article

[49] Selectable nanopattern arrays for nanolithographic imprint and etch-mask applications, **H.-H. Jeong**, A.G. Mark, T.-C. Lee, K. Son, W. Chen, M. Alarcón-Correa, I. Kim, G. Schütz, and P. Fischer, ***Advanced Science*** 2, 1500016 (2015) - Cover article

Chapter 3:

[135] Corrosion-protected hybrid nanoparticles, **H.-H. Jeong**, M. Alarcón-Correa, A.G. Mark, K. Son, T.-C. Lee, and P. Fischer (s*ubmitted*)

Chapter 4:

[93] Dispersion and shape engineered plasmonic nanosensors, **H.-H. Jeong**, A.G. Mark, M. Alarcón-Correa, I. Kim, P. Oswald, T.-C. Lee, and P. Fischer, ***Nature Communications*** 7, 11331 (2016)

[109] Magnesium plasmonics for UV applications and chiral sensing, **H.-H. Jeong**, A.G. Mark, and P. Fischer, ***Chemical Communications*** 52, 12179 (2016)

Chapter 5:

[136] Active nanorheology with plasmonics, **H.-H. Jeong**, A.G. Mark, T.-C. Lee, M. Alarcón-Correa, S. Eslami, T. Qiu, J.G. Gibbs, and P. Fischer, ***Nano Letters*** 16, 4887 (2016)

Chapter 2 Nano glancing angle deposition

Controlled local fabrication of three-dimensional (3D) nanostructures is important to explore and enhance the function of single nanodevices, but is experimentally challenging. In this chapter, a scheme, nano glancing angle deposition (nanoGLAD) is presented based on e-beam lithography (EBL) written seeds, and GLAD grown structures to create nanoscale objects with defined shapes but in aperiodic arrangements. By using a continuous sacrificial "corral" surrounding the features of interest it is possible to grow isolated 3D nanostructures that have complex cross sections and sidewall morphology that are surrounded by a zone of clean substrate. Then, nanoGLAD scheme is used for the production of large-area nanopatterns, in conjunction with block-copolymer micelle nanolithography (BCML). It is discussed how the sizes of regular BCML patterns can be tuned via GLAD and how additional functional materials can be incorporated to generate new nanostructures. The combination with simple etching steps extends the utility of the method. In particular, arrays of nano-ring, -holes, -domes and multilayer nano-spheres are generated. All arrays and shapes can be readily obtained from a single common precursor that is subjected to different simple post-processing steps. The patterned nanoarrays are useful for plasmonic and nanoimprint applications.

This chapter is based on the published articles:

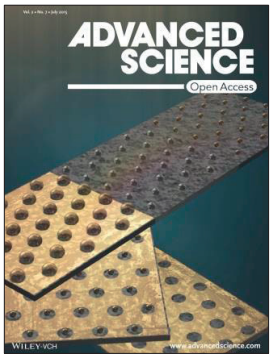

[59] Shape control in wafer-based aperiodic 3D nanostructures, **H.-H. Jeong**, A.G. Mark, J.G. Gibbs, T. Reindl, U. Waizmann, J. Weis, and P. Fischer, ***Nanotechnology*** 25, 235302 (2014) - Cover article

[49] Selectable nanopattern arrays for nanolithographic imprint and etch-mask applications, **H.-H. Jeong**, A.G. Mark, T.-C. Lee, K. Son, W. Chen, M. Alarcón-Correa, I. Kim, G. Schütz, and P. Fischer, ***Advanced Science*** 2, 1500016 (2015) - Cover article

Reprinted from Ref. 59 (Copyright 2014 Institute of Physics) and Ref. 49 (Copyright 2015 Wiley-VCH publisher)

Author Contributions:

For Ref. 59 P.F. proposed the idea. H.-H.J., A.G.M., and P.F. designed the experiments. H.-H.J. performed the GLAD and SEM. H.-H.J., T.R., U.W., and J.W. conducted the EBL. H.-H.J. and A.G.M. analysed the data. H.-H.J., A.G.M., and P.F. wrote the paper.

For Ref. 49 H.-H.J. proposed the idea. H.-H.J., A.G.M., T.-C.L., and P.F. designed the experiments. H.-H.J. performed the GLAD, SEM, chemical etching, and optical measurements. C.M. conducted the BCML. H.-H.J. and W.C. performed the RIE, H.-H.J. and I.K. conducted the Raman measurements, K.S. performed the NIL. T.-C.L. and M.A.-C. carried out the TEM imaging. H.-H.J., A.G.M., T.-C.L., and P.F. wrote the paper.

2.1 Shape control in nano glancing angle deposition

2.1.1 Introduction

Structural control of nanoscale devices is a key issue for enhancing their performance, which depends critically on the nanostructure's shape, size, and composition. For instance, the electrical properties of memristors,[137, 138] and photovoltaic devices,[139, 140] the optical properties of metal plasmonic nanoparticles,[78, 141] and the magnetic properties of nanomagnets for magnetic memory devices [142, 143], all depend on the geometry of the device. Therefore, in order to improve the performance of nanodevices, three-dimensional (3D) nanofabrication techniques are becoming more important to nanoscience and nanoengineering. 3D structures including rods, helices, etc. have been obtained via template-assisted growth,[139, 144] scanning probe lithography,[145] 3D assembly of nanoparticles,[146] DNA origami,[147-149] multi-photon lithography,[150, 151] colloidal lithography,[152] and chemical synthesis,[153] but these approaches are not well suited for locally fabricating 3D-shaped nanostructures on a wafer or planar surface. For instance, colloidal lithography is capable of rapidly patterning large areas, but only with periodic arrays, and only to give 2D patterns. On the other hand, scanning probe lithography can create arbitrary aperiodic structures (albeit at reduced write speeds). So there remains a pressing demand for techniques to generate 3D structures in arbitrary arrangements with rapid write times.

A promising technique to address this is glancing angle deposition (GLAD), a physical vapour deposition (PVD) technique where the vapour is deposited on the substrate at a high incidence angle and the substrate can be rotated during deposition.[154] GLAD has been used to fabricate various complex 3D structures including rods, helices, zigzags, etc. where the structural dimensions are directly controlled by the incident molecular flux angles, the molecular deposition rate, and the rotation rate of the substrate. It has the advantage of being a simple and fast fabrication process appropriate for a variety of materials including insulators, semiconductors, magnetic materials and conductors.[52, 155, 156] Seeding the substrate before the GLAD exposure has proven to be an effective technique to homogenise the resulting structures by restricting extinction, and controlling the symmetry of the array.[157] Recently, it has been shown a rapid and scalable approach to obtain 3D nanocolloids using GLAD on substrates seeded with ~10 nm gold nanodot arrays grown with block-copolymer micelle nanolithography (BCML).[56] To date, however, studies of GLAD seeding have focused on the role of highly symmetric, periodic, and quasi-infinite seed arrays.[158-160] Thus they are not appropriate for growing the isolated or aperiodic 3D nanostructures that are required for many technological applications.

In this chapter, electron-beam lithography (EBL) is used to write nanoscale seed layers having complex seed shapes, and isolated aperiodic arrangements. It is started by exploring the growth properties of nanostructures on periodic patterned seed arrays and demonstrated that the lattice spacing of the array influences and thus limits the dimensions of the nanostructure. To address this, a new geometry, the sacrificial corral, is introduced to protect the main structure and allow more precise control of the structural dimensions. Examples of GLAD grown nanostructures are provided; in all cases the structures grown within corrals exhibit better uniformity, and show superior fidelity for the underlying seed geometry and the growth program than isolated seeds or periodic seed arrays.

2.1.2 Theoretical concept

In the absence of diffusion, when adsorbate atoms hit and stick where they land, the morphology of GLAD grown structures is dominated by ballistic shadowing by adjacent structures. In the presence of seeds the diameters of the grown structures are dependent on the seed diameter d_s, and the gap between adjacent seeds g_s, figure 2:1e [28]. The maximum effective gap between seeds g_{max} is defined by the geometrical relation, $g_{max} = h_s \cdot \tan\alpha$, where h_s is the seed height, and α is the polar angle of the incoming flux. When the seed gaps are wider than the maximum effective gap distance ($g_s > g_{max}$), unseeded nanostructures grow between seeds due to the absence of the shadow effect in these regions. On the other hand, columnar competition, the complete shadowing and stochastic extinction of some structures by their neighbours decreases the uniformity of growth when the seed gaps are in the range of $d_s \leq g_s \ll g_{max}$. The centre-to-centre spacing of seeds in an array is simply $s = g_s + d_s$, and the maximum effective spacing is $s_{max} = g_{max} + d_s$.

2.1.3 Fabrication concept

The fabrication scheme for one of the designed nanostructures is depicted in figure 2:1. Nanopatterned seeds based on hydrogen silsesquioxane (HSQ) negative tone electron-beam resist were fabricated by electron-beam lithography (EBL, see Methods for details). Then, nanostructures were grown on such seeded substrates in a GLAD system based on electron-beam evaporation at room temperature with a base pressure of 5×10^{-7} mbar (see figure 1:5). The substrate manipulator provides independent control over the azimuthal direction φ, and molecular flux direction α during deposition. The flux angle α and the azimuthal rotation rates per unit thickness $d\varphi \cdot dw^{-1}$ were constantly updated with closed-loop feedback based on measurements of material deposition rates on a quartz crystal monitor (QCM) and controlled by a computer running code developed in the lab.

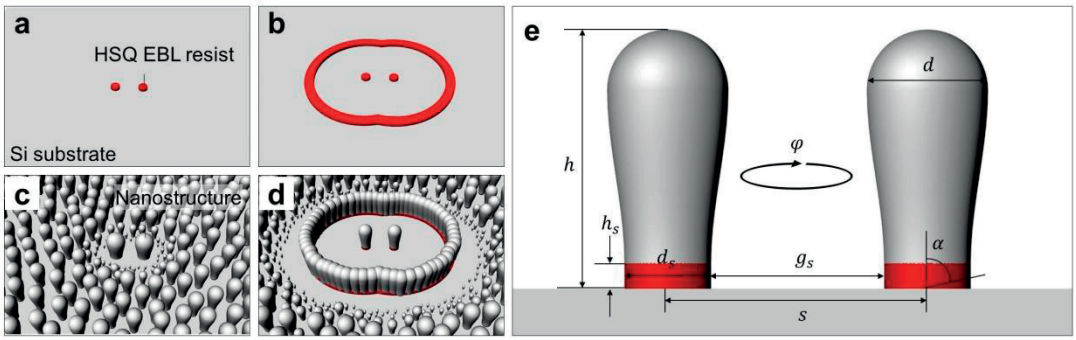

Figure 2:1 Illustration of controlled local fabrication of 3D nanostructures on nanopatterned seeds. Fabrication of HSQ nanopatterns (a) without and (b) with a sacrificial corral on Si substrate using EBL. Fabrication of 3D nanostructures on the nanopatterned seeds for (c) the isolated double dots and (d) the corralled double dots. (e) Side view of nanostructures showing dimensions of the seed particles (red) and the nanostructures that grows upon them. Reprinted from Ref. 59 (Copyright 2014 Institute of Physics)

In order to examine only the geometrical effect of the designed structures, other deposition parameters including the temperature, the material, the deposition rate, and the incident molecular flux were kept constant between different samples. In particular, the flux angle α was fixed to 85°, because it is the primary factor determining film density.[160] At α = 85° the polar angle is high enough for shadowing to produce high fidelity structures, but not so high that roughness in the mask layer plays an important role in shadowing. A typical growth process consisted of Ti deposited on top of the nanopatterned seeds as an adhesion

layer with a deposition rate ~ 0.1 nm·sec^{-1} at α = 10°, $d\varphi \cdot dw^{-1}$ = 210 °·nm^{-1}. This was followed by alumina (Al_2O_3) which made up the bulk of the nanostructure, deposited to give either nanorods by fast azimuthal rotation ($d\varphi \cdot dw^{-1}$ = 18±0.2 °·nm^{-1} at 0.1 nm·sec^{-1} deposition rate and α = 85°) or helices using slow rotation ($d\varphi \cdot dw^{-1}$ = 1.8±0.1 °·nm^{-1}).

2.1.4 Role of periodicity in nanoGLAD

The ability of EBL to write arbitrarily shaped seed layers of small sizes allows the effect of those seed layers on the resulting GLAD-grown nanostructures to be studied systematically. It is started by examining circular seeds arranged in periodic square lattices. This was followed by GLAD deposition of about 250 nm of Al_2O_3 at high substrate rotation rate to give columnar nanostructures as shown in figure 2:2. The seeds increase in diameter (d_s) from top to bottom, and increase in centre-to-centre spacing ($s = g_s + d_s$) from left to right. Each zone of seeds is 10 µm × 10 µm but the images show only the central 1.3 µm × 1.3 µm to avoid edge effects. The diameters of the resulting nanocolumns were measured by analysing the SEM images. Ideally, the diameter of the nanorod should be equal to that of the seed upon which it grows. However, figure 2:2b shows that for a given seed diameter, the diameter of the nanorod increases with spacing. When $d_s \leq g_s \ll g_{max}$, the uniformity of the nanorods decreased due to columnar competition. Conversely, when the seed gap exceeded that established by equation 1:3, (e.g. for d_s = 50 nm, h = 30 nm, s = 550 nm), unintended nanoislands were formed within the gaps of the patterns due to incomplete shadowing. Therefore, in periodic lattices, the nanorod diameter is a function of both the seed diameter and spacing at the given seed height incident flux angle. This poses a problem for aperiodic arrangements where a fixed column diameter is desired, but the spacing between columns, or their arrangement is not uniform. This is an important consideration in structure design that has received little attention, because GLAD has traditionally been applied to the growth of periodic, quasi-infinite films.

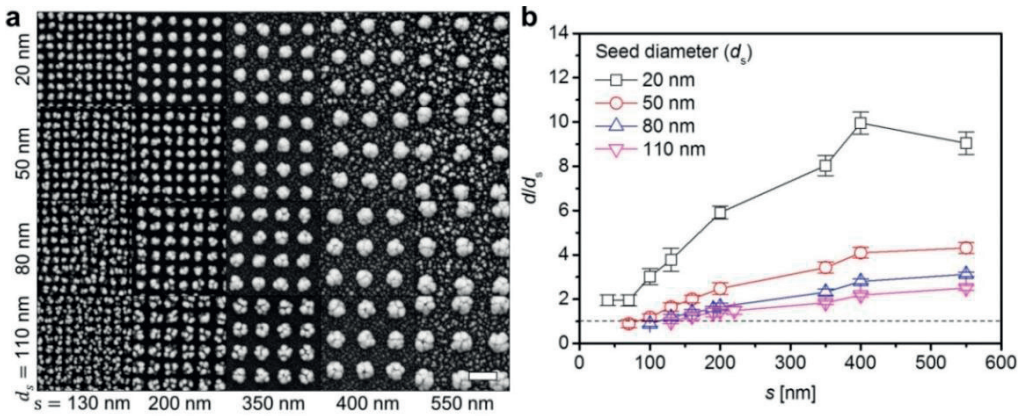

Figure 2:2 Fabrication of a variety of nanorods by varying seeds diameters (d_s) and spacings (s). (a) Top-view SEM images for the fabricated nanorods on various seeds arrays. The seeds diameters were increased from 20 nm (top) to 110 nm (bottom) with 30 nm intervals. The seeds spacing were increased from 130 nm (left) to 550 nm (right). Scale bar is 400 nm. (b) The measured diameters of various nanorods at different seed spacings (s). *Y*-axis is presented as the ratio of $d \cdot d_s^{-1}$. Reprinted from Ref. 59 (Copyright 2014 Institute of Physics)

2.1.5 Aperiodic 3D nanostructures

A new motif for the controlled growth of isolated structures is introduced that is the sacrificial corral, which manipulates the shadow effect locally and protects the target structures within. The model structure for testing the efficacy of corrals is a pair of circular seeds d_s = 50 nm in diameter and separated by 100 nm

(see figure 2:1b). These represent the electrodes of any simple two-terminal device. The corral is a continuous closed path drawn around these seeds at a constant minimum distance. EBL was used to draw 50 nm wide corrals at different distances (100, 250, 400, and 550 nm) from the central structure, as shown in figure 2:3a. These patterns are used as seed layers for growing Al_2O_3 by GLAD to yield the nanostructures in figures 2:3b and 2:3c. The top down SEM images (figure 2:3b) show that shadowing from the corral produces a denuded area on both its interior and exterior. The pair of nanocolumns grown in the centre of the corrals increase in diameter as the corral gap increases, similar to the effect seen with periodic arrays. For α = 85° the maximum effective gap is expected to be $g_{\max}$ = 342 nm. This is consistent with the appearance of unintended deposition near the nanodot pair for the corral with 550 nm gap. Thus, within the limits imposed by geometrical shadowing, the corral acts as a "resistless mask" that maintains a clear area in the vicinity of the double dots, without the need for additional mask steps. As a control system to confirm the role of the sacrificial corral, the nanorods were fabricated on double dots arrays (figure 2:3d) using lattice spacings between the dot pairs the same as the gaps used for the corrals in figure 2:3a. One additional layout was used with very large inter-pair spacing corresponding to isolated double dots. The nanorods' heights and lengths were measured and plotted in figure 2:3e for comparison against those of the corral structures. The measured values of the nanorods' heights were calibrated by geometrical relations between the projection viewed by SEM and nanorods' geometry (see Methods for details).

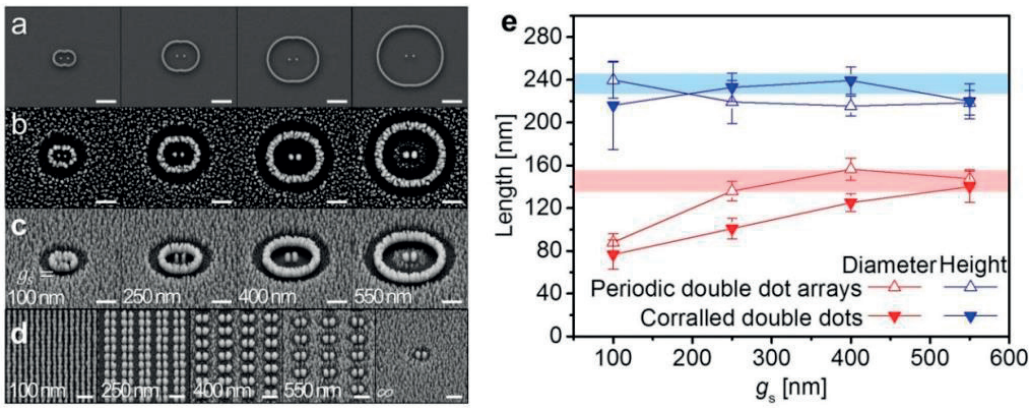

Figure 2:3 Nanorods in a corral or in aperiodic arrangement. (a) Top view of SEM images for nanopatterned seeds in various corrals. The diameters and the heights of double dot seeds were 50 nm and 30 nm, respectively. The gaps of sacrificial corrals were varied from 100 nm (left) to 550 nm (right) with 150 nm intervals. (b) Top view and (c) 45°-tilted view of SEM images for the nanorods on the nanopatterned seeds. (d) 45°-tilted view of SEM images for the nanorods on various periodic double dots arrays (each scale bar: 400 nm). (e) The measured heights (blue) and diameters (red) of the fabricated nanorods on the seeds of the corralled double dots (down-triangles) and the periodic double dot arrays (up-triangles). The blue and red zones indicate the height and diameter of the isolated dot doublet, respectively. Reprinted from Ref. 59 (Copyright 2014 Institute of Physics)

This shows a strong trend for larger diameter dots as the spacing is increased in both corrals and arrays. In the limit of large spacing they converge towards the measured values for the isolated double dots (blue and red bars), as expected. Corralled double dots consistently have substantially smaller diameters (by approximately 20%) than their array counterparts. This results in an enhanced aspect ratio for corralled double dots for spacings less than $s_{\max}$ (it was not possible to measure the height of corralled structures for g_s = 100 nm at 45° tilt because the corral itself obscures the base of the nanorod during imaging. Instead, these were measured at 20° tilt). At the lower end of the gap range (g_s = 100 nm) the aspect ratio for corralled structures is no better than that of the periodic ones. This arises because densely spaced seeds admit fewer

gaps between them, and so are shadowed for proportionally more of the azimuthal sweep. A simple single ray analysis, shows that the g_s = 100 nm structures are shadowed for twice as much of the deposition cycle as for 250 nm spacing (see Appendix A.1.1 The Effect of Seed Spacing on Column Broadening for details). The ratio of $d \cdot d_s^{-1}$ for corralled dots is a function of the gap size, but is insensitive to the spacing between corrals. Thus, the corral motif decouples the shape of the nanostructures from the distance between them. Adding an additional corral surrounding the first one creates a double corral (see Appendix figures A:1-2). Doing so has no effect on the dimensions of the target inside the first corral. The utility of including extra corrals is that they provide additional annular regions of clean substrate around the target structure.

The greatest strength of the GLAD technique is its ability to grow structures that have 3D shapes, and are sculpted perpendicularly to the substrate normal.[52, 56, 154] It is demonstrated that, in addition to controlling the aspect ratios of nanorods, the sacrificial corrals enhance the fidelity of nanostructures with 3D shapes. In this process, 500 nm thick Al_2O_3 was deposited by GLAD with slow substrate rotation corresponding to 200 nm per turn. This growth program should produce left-handed helices with 2.5 turns. Figure 2:4 shows the results when grown on an isolated dot doublet (a), a double dot array (b), and a double dot enclosed in a corral (c). Neither the structures grown on the isolated double dot, nor the double dot array have a helical shape. However, the nanostructures grown within the corral demonstrate clear helicity as expected from the growth program, with a total height of ~180 nm and pitch of ~65 nm. This can be attributed to the homogenising effect of the constant shadow cast by the corral, versus the irregular variations in shadow length experienced by the periodic seeds. A structure within a periodic array is shadowed only periodically whenever the azimuthal angle coincides with the direction of one of its neighbours. Between these angles the structure is not shadowed, and receives flux on its flanks, as well as its top surface. This introduces a shadowing modulation in addition to the deliberate modulation that comes from the substrate rotation.

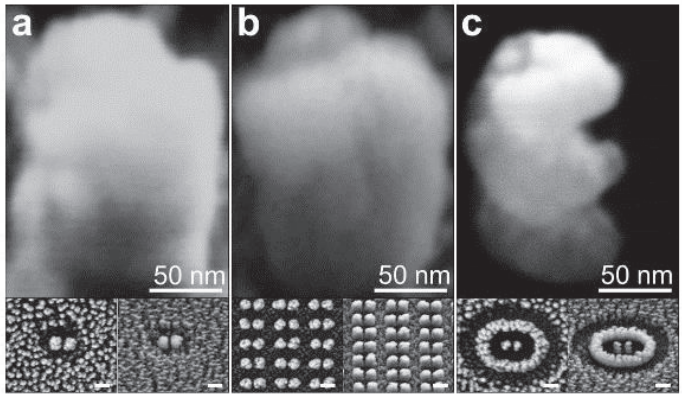

Figure 2:4 SEM images of the fabricated 3D-shaped nanostructures. 3D nanostructures on (a) an isolated dot doublet, (b) a double dot array, and (c) double dot enclosed in a corral (each scale bar: 200 nm, except for specified scale bars). Reprinted from Ref. 59 (Copyright 2014 Institute of Physics)

2.1.6 Single 3D nanoparticle on a complex seed

Ultimately, the goal is to construct 3D structures grown on seeds with complex shape. For this it is necessary to preserve the cross section of the seed shape as it is swept through the 3D profile grown by the GLAD process. Previous work on GLAD seeding has been restricted to spherical, hemispherical, and square shaped seeds.[55, 56, 157, 160-165] Figure 2:5 shows this for an 'A' shaped seed, using growth conditions

identical to those for figure 2:4. The growth was performed on a patterned substrate consisting of isolated 'A' seeds, an array of such seeds, and a corralled seed. The isolated 'A' yields grainy and overgrown structures with poor fidelity for the underlying seed and weak helicity. Similarly, the array structures suffer from unintended deposition throughout the spaces between the seeds, with particularly strong growth between the strokes of adjacent 'A's at their baseline. Conversely, the corralled structure shows close reproduction of the original seed, clean substrate within the corral, and good helicity. It remains afflicted by some graininess, but this can be mitigated by further optimising the growth processes such as the rotation speed, the incident flux angle, or the materials.[165]

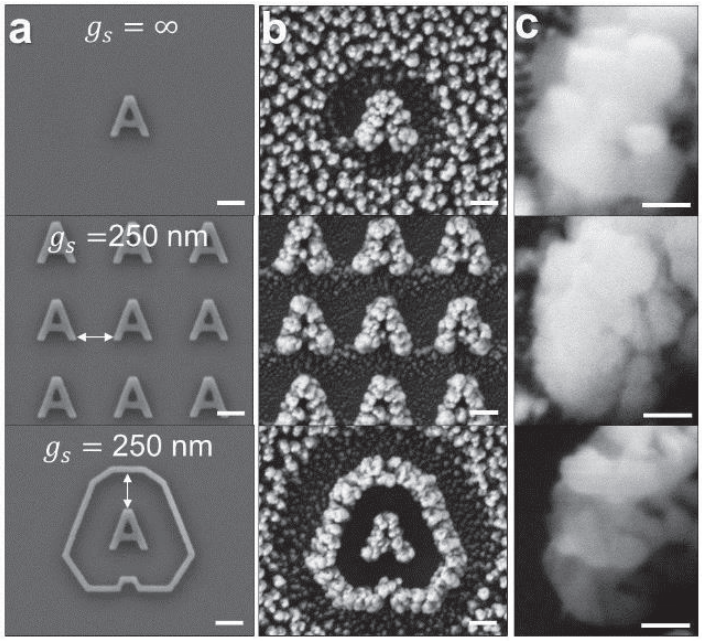

Figure 2:5 SEM images for 3D-shape 'A' structure. Top view of SEM images for (a) nanopatterned seeds and (b) 3D-shape 'A' structure on the nanopatterned seeds (scale bar: 200 nm). (c) Close up image of the central target structures for each configuration (scale bar: 50 nm). Reprinted from Ref. 59 (Copyright 2014 Institute of Physics)

2.2 Large-scale nanopatterning by nanoGLAD

2.2.1 Introduction

Micro- and nanotechnological processes depend critically on lithography and patterning techniques. The development of rapid and precise nanopatterning methods that are time- and cost- effective is a key to fundamental nanotechnology research as well as a number of industrial processes. For high-resolution nanopatterns a number of techniques are well developed, including electron-/ion-beam-based lithography [166-168] and tip-based lithography,[145, 152, 169-172] but they are often too slow for wafer-scale processes that demand fast processing times. On the other hand, for large-area nanopatterning, optical/plasmonic lithography,[81, 82, 84, 150, 151, 173] contact printing-based lithography,[174-177] and template-assisted lithography [178-181] are promising candidates, however, they require additional expensive and time-consuming pre-fabrication processes, such as the preparation of a master template. Colloidal lithography including nanosphere lithography (NSL),[182] nanoparticle lithography,[183, 184] and block copolymer micelle nanolithography (BCML) [57] are attractive large-scale parallel patterning methods that permit time- and cost-effective patterning at the wafer-scale. Nevertheless, they suffer from a number of

limitations regarding material compatibility, which is an important consideration when preparing etching masks, as well as limitations in the size and the shapes of the nanopatterns that can be fabricated by these methods.

As a second part of this chapter, GLAD scheme is now used for wafer-scale nanolithography that, in conjunction with BCML (instead of EBL used for studies in Chapter 2.1) permits to grow quasi-hexagonal nanopatterns of nanodots or other, more complex, nanopatterns on large scales with tunable feature sizes and a wider array of materials than is possible with either method alone. Firstly, this technique extends the sizes of "dots" that can be fabricated, to cover the range from BCML (< 10 nm) to NSL (> 100 nm). This is important for applications in plasmonics for which particle size is closely linked to optical response. It is rather straightforward by this method to also change the materials of the nanopatterns and to generate multilayer nanopatterns containing a number of different materials, such as spherical trilayer particles, which prove useful for certain additional processes (including etch masks). By employing wet chemical etching this nanolithography scheme can in addition be used to rapidly fabricate patterns that cannot be obtained with other colloidal lithography techniques, in particular hollow domes. [57, 182-185]. One important feature of this scheme is that a single multifunctional pattern can, through simple subsequent processing steps, generate a series of novel secondary nanopatterns with different features and 3D morphology. Finally, two demonstrations of the nanopatterns are presented in technological applications. They are effective enhancers for surface enhanced Raman spectroscopy (SERS), and used as a large area mask for nanoimprint lithography (NIL).

2.2.2 Fabrication concept

BCML is a parallel nanopatterning technique that is used to fabricate highly ordered arrays of spherical Au or Pt nanodots with controllable size and interparticle spacing across an entire wafer.[57, 186] The spatially separated (small) nanodots can serve as nanoscale seeds for the subsequent growth of complex hierarchical nanostructures. While it is possible to enlarge the nanoparticle seeds using electroless deposition,[187] there is still a limited choice of materials and range of sizes and shapes that can be achieved. To address this, GLAD has been selected to grow materials onto the nanoseed pattern, as it dramatically extends the range of sizes and materials that can be used as well as the shape of the resulting growth. GLAD is a vacuum deposition technique that can be used to selectively grow nanostructures onto patterns in a parallel manner by exploiting the shadow effect between the constituent seed particles to control the direction of the growth. [28, 56] A key point is that in ordinary (normal incidence) physical vapour deposition the entire wafer would be coated and the nanoseeds would therefore be electrically connected. This is avoided when using shadow growth methods, such as GLAD. The previous work combining BCML and GLAD, namely "nanoGLAD", has focused on generating nanoparticles with complex, often chiral, shapes.[56, 64] Using BCML-grown seeds improved the uniformity of the resulting structures, but the pattern itself has so far been of secondary importance. Shadow deposition has already been introduced in conjunction with regular patterns formed by e-beam lithography,[55] NSL,[188-190] and nanoimprint lithography (NIL).[191] However, these schemes do not readily permit simultaneous nanometre scale shape-control of the patterns and wafer-scale fabrication. The work here is concentrated on producing wafer-level uniform arrays of high symmetry nanodot-patterns at below 100 nm for subsequent use, for instance as a simple array of plasmonic structures or as a mask. The symmetry and spacing of the pattern is governed by the BCML step, while the GLAD and following processing steps determine the exact shape of the seed pattern, and hence the polarity (negative or positive) of the mask.

The approach is illustrated by (but not limited to) the 3 step fabrication process depicted in figure 2:6. First, a quasi-hexagonal array of Au nanodots with diameter 12.1±1.8 nm was patterned on a silicon wafer by BCML (figure 2:6a). Second, this nanoseed pattern was exposed to a vapour flux in a physical vapour deposition system at an incident angle of 87^{o} with a base pressure of 1×10^{-6} mbar to grow hybrid nanoparticles (NPs) upon the nanoseeds using GLAD (figure 2:6b). Based on the result in Chapter 2.1, the spacing between the nanoseeds is chosen to be large enough so that the nanostructures do not fuse during the growth process. The deposition process itself consists of three steps; first Au was grown on the Au nanoseed pattern to increase the size of the seed particles (if necessary). Next, Ag was deposited as a sacrificial layer. Third, a thin Au film was grown on the array of the Au-Ag hybrid NPs at normal incidence (0^{o}) to cover the entire nanopatterned substrate (figure 2:6c).

Figures 2:6d–f show SEM images of the array of the Au nanodots patterned by BCML (figure 2:6d) and the resultant nanopatterned substrate after the 3 step fabrication process. The hybrid NP array can be further processed to create a variety of final patterns, so it is named as a multifunctional pattern (see figure 2:6e for top view and figure 2:6f for tilted view). It can be grown in a very short time (total processing time less than an hour) and consists of an array of Au-Ag-Au hybrid NPs (37.1±4.0 nm in diameter) that covers the entire wafer. The main targets are the patterns formed by the noble metals Au and Ag since they can be used both as metal etch-stop layers in a number of different plasma environments [192] and since they can also function as plasmonically active materials.[193] However, the fabrication scheme is general and permits the use of a wide selection of materials and material combinations, including alloys.

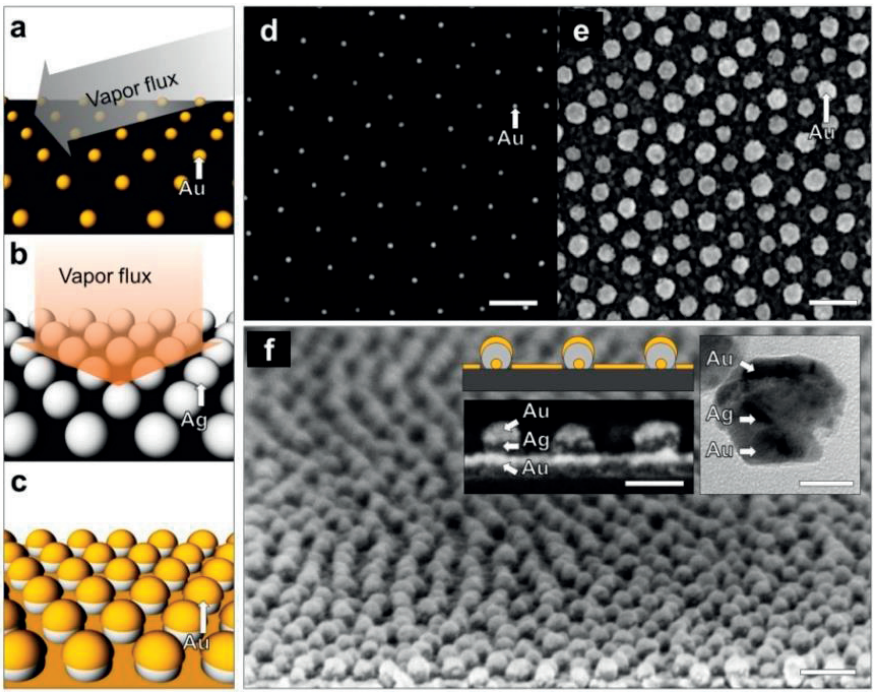

Figure 2:6 Fabrication of a large-area multifunctional nanopattern. (a) Fabrication of a hexagonal array of Au nanodots on a silicon (or glass) wafer by BCML. (b) Growth of Au and Ag on the array of Au nanodots using shadow PVD (GLAD). (c) Deposition of an Au thin film on the array of Au-Ag hybrid NPs. SEM images of (d) the array of Au nanodots and, (e) top view and (f) tilted view of the multifunctional nanopattern (scale bar: 100 nm). Inset shows the side view of the SEM image (scale bar: 50 nm) and the TEM image (scale bar: 20 nm) of the multifunctional nanopattern. Reprinted from Ref. 49 (Copyright 2015 Wiley-VCH publisher)

2.2.3 Selectable nanopattern arrays

A key feature of the scheme here is that a series of secondary nanopatterns can be obtained from the initial multifunctional pattern via simple additional processes. In particular, starting from the Au-Ag-Au NP layer, a variety of patterns including nanoholes, nanorings, and hollow nanodomes can be generated (figure 2:7). A nanohole pattern can be obtained by sonicating the multifunctional pattern in water for 1 h (figure 2:7c). During the sonication process the NPs (including the original Au seeds) are removed from the substrate, leaving behind a hexagonal array of circles in the Au film. The spacing of the holes is determined by the spacing of the original BCML array, and their diameter by the size of the Ag in the second growth step. Selective chemical etching of Ag increases the possible secondary nanopatterns that can be fabricated from the multifunctional nanopattern (figure 2:7b). Overnight immersion of the multifunctional pattern in a mixture of H_2O_2:NH_3 = 1:1(v:v) produces a pattern of hollow nanodomes surrounding Au NPs with a yield of over 90% (this yield might be enhanced by reducing the Ag etch rate to reduce the rate of bubble generation). The nanocaps (NCs) adhere to the substrate due to significant London-van der Waals attraction between the structures and the substrate with high Hamaker constant of gold of ~40×10^{-20} J in water (figure 2:7e).[194] The diameter of the NCs is again controlled by the Ag deposition step, and the cap thickness by the final Au coverage. Finally, through the sonication process on the hollow nanodome pattern, Au NCs can be readily lifted off from the substrate and this leaves behind the nanohole pattern containing at its centre the Au nanodots. This pattern is called as “nanoring” pattern. The nanodot diameter is controlled by the initial Au deposition that was used to enlarge the original BCML patterned Au nanodots. An important ancillary benefit is that after the sonication processes, the removed NPs are suspended in the supernatant. In the case of the nanohole pattern and the nanoring pattern, sonication yields colloidal Au-Ag-Au hybrid structures and hollow NCs respectively (see Appendix figure A:4). Thus, this scheme not only generates a patterned surface, but can also be useful in generating colloidal solutions of hybrid NPs. Figures 2:7f–h show SEM images of the three secondary patterns. The nanoholes have an inner diameter of 36.7±4.4 nm (figure 2:7f), and the nanorings have a gap width of 9.9±1.8 nm separating the central Au NP (21.1±1.5 nm) from the surrounding Au film (figure 2:7h). For the nanoring pattern the sonication time has been optimised to 10 min to yield the nanoring structures with a yield of over 70% of the multifunctional nanopatterned substrate. The structural dimensions of such fabricated nanopatterns were in the range of 10 nm to 100 nm which cannot be fabricated by comparable colloidal lithography methods[57, 182-185] in particular the tri-layer nanodot, the nanoring, and the 3D hollow nanodome were designed in more complex (but smaller) than conventional patterns including dots, rods, rings, triangles, etc. fabricated by GLAD schemes.[55, 188-191] Additionally, to further illustrate the flexibility of this technique in terms of materials composition, a multifunctional pattern was fabricated with a SiO_2 top film (instead of the final Au film in figure 2:6). Since the SiO_2 film is CMOS compatible it may be useful for the fabrications of MEMS and CMOS devices, especially 3D devices, based on those fabricated patterns.[195] The resulting nanoring pattern is shown in figure 2:8. Note that this scheme is capable of growing many different shapes, but of course only shapes that are linear and grow away from the substrate are possible. Shapes that branch, or curve downwards towards the substrate can in general not be fabricated, although there are exceptions.[196] For a more complete discussion of possible shapes refer to the nanoGLAD paper.[56] Further, the multifunctionality depends on the relative reactivity of the Ag vs. Au under attack by H_2O_2.[197] Using other materials requires consideration of their reactivities or the choice of solvent. Finally, interparticle spacing defines the size of PVD enlargement that is possible.

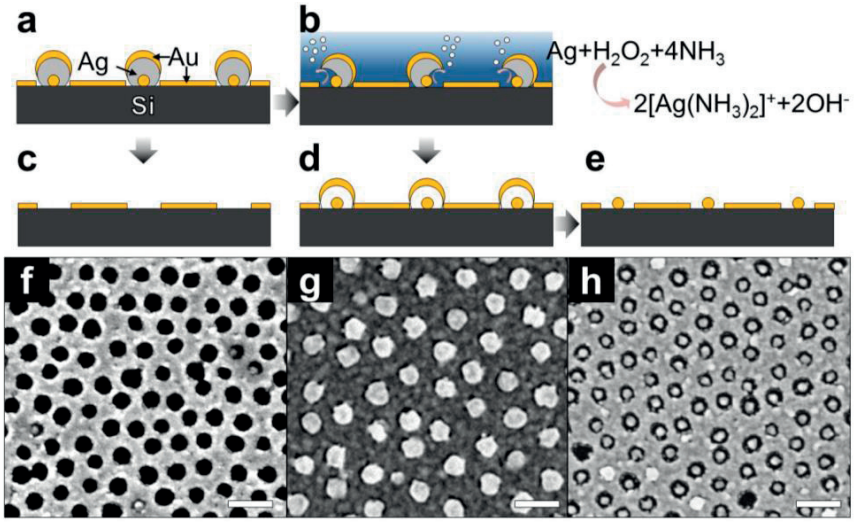

Figure 2:7 Fabrications of secondary nanopatterns from the multifunctional nanopattern in figure 2:6. Schematic views of (a) the multifunctional nanopattern as an initial patterned substrate and (b) subsequent Ag etching process with the multifunctional nanopattern in the mixture of H_2O_2:NH_3 (v:v=1:1). The schematic views of the resultant secondary nanopatterns including (c) nanohole, (d) hollow nanodome, and (e) nanoring patterns. The corresponding SEM images of (f) nanohole, (g) hollow nanodome, and (h) nanoring patterns (scale bar: 100 nm). Reprinted from Ref. 49 (Copyright 2015 Wiley-VCH publisher)

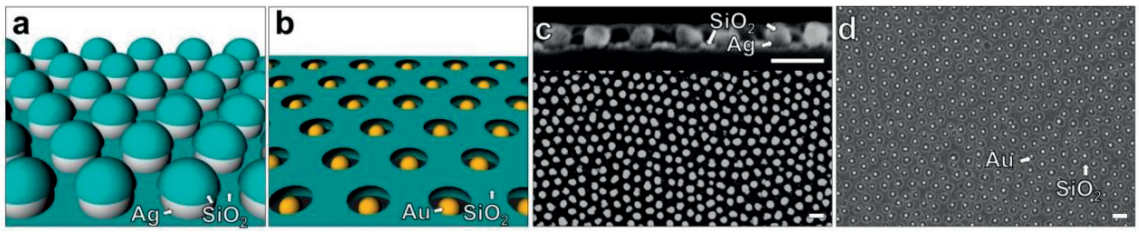

Figure 2:8 Fabrications of (a) multifunctional nanopattern and (b) nanoring patterns with a SiO_2 film. SEM images of (c) the multifunctional nanopattern (top: side view, bottom: top view) and (d) the nanoring pattern (scale bar: 100 nm). Reprinted from Ref. 49 (Copyright 2015 Wiley-VCH publisher)

2.2.4 Applications

2.2.4.1 Nanoimprint lithography (NIL)

This fabrication scheme has a number of potential uses in nanoscience and nanotechnology. Among them two applications are here provided: patterns for NIL and nanoplasmonic patterns. NIL is useful for large-scale repeat-patterning of entire wafers. Its drawback is the preparation of the initial mask that is expensive and time-consuming.[176] It is shown that this method lends itself to the fabrication of certain NIL master templates, figure 2:9. First, a nanohole pattern on silicon substrate was etched using reactive ion etching (RIE) under a SF_6:O_2 (3:1) plasma environment, where the etch rate of Si was ~1 nm·s^{-1} (See figures 2:9d-e). The Au acts as an etch-stop layer and restricts etching of the Si substrate to the exposed circles within the nanoholes. Next, the Au etch-stop layer was removed and the patterned Si substrate was covered with a fluoro-silane for easy detachment of the imprinted surface after the nanoimprint process (see figure 2:9c and Method for further details). Figure 2:9f shows a SEM image of the fabricated nanotemplate with ~ 120 nm depth.

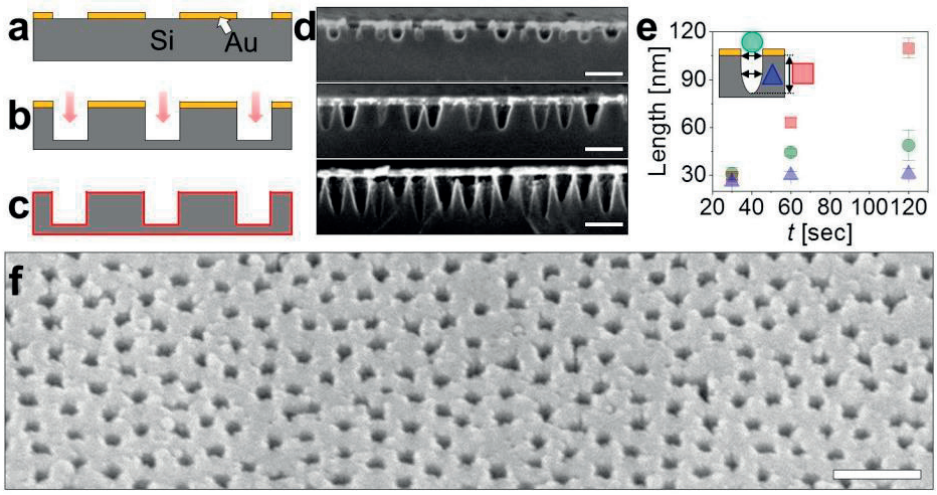

Figure 2:9 Fabrication of a nanotemplate from the nanohole pattern. Schematic views of (a) the nanohole pattern, (b) the patterned substrate after RIE etching under SF_6:O_2 plasma environment, and (c) the fabricated NIL template after wet-etching the Au film on the patterns functionalised with a fluoro-silane. (d) Side view of the SEM images of the etched silicon substrate after etching for 30 s, 60 s, and 120 s under SF_6:O_2 plasma environment (from top to bottom, scale bar: 100 nm). (e) The plot of the etched depth (red square), width (green circle), and full width at half maximum (blue triangle) of Si substrate as a function of time. Their etch rates were ~0.95 nm·s^{-1}, ~0.28 nm·s^{-1}, and ~0.06 nm·s^{-1}, respectively. Reprinted from Ref. 49 (Copyright 2015 Wiley-VCH publisher)

Then the templating ability of this master was tested under typical nanoimprint conditions with intermediate polymer stamps (IPS) film, figure 2:10. Figures 2:10c–d show SEM images of the large-area arrays of polymer nanowires (NWs) with different heights of ~30 nm and ~120 nm by using two different master templates that have different depths. From this, it has been confirmed that this patterning technique can be used to create master templates that work well with commercial NIL processes to imprint nanopatterns with soft organic materials. Creating new wafer-scale template patterns with different feature sizes and periodicity is a simple, parallel and fast process. It is anticipated that these polymer NWs could be potentially useful to produce nanostructured gecko tape [198, 199] or super-hydrophobic surfaces.[200]

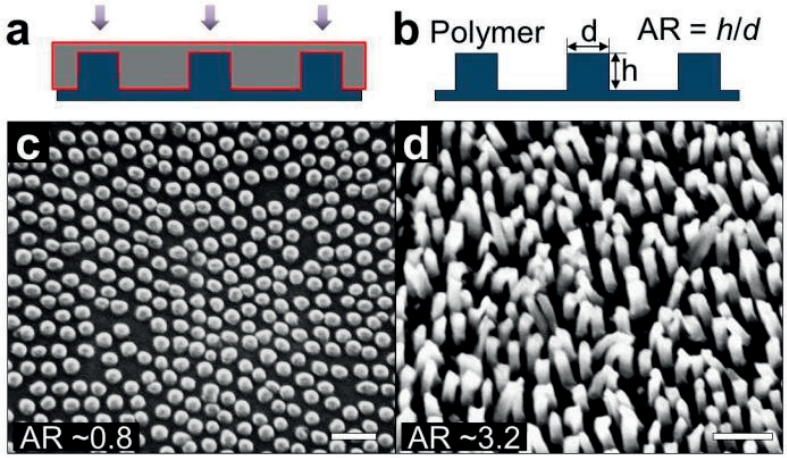

Figure 2:10 Fabrication of polymer NWs by nanoimprint. Schematic views of (a) NIL process and (b) the resultant polymer NWs. SEM images of the fabricated polymer NWs with (c) AR ~0.8 and (d) AR ~3.2, respectively (scale bar: 200 nm). Reprinted from Ref. 49 (Copyright 2015 Wiley-VCH publisher)

2.2.4.2 Plasmonic substrate

The suitability of the grown patterns for plasmonic applications was also investigated. Measuring the extinction spectra of patterned arrays on quartz glass substrates reveals plasmon resonances that represent the sizes and material composition of nanomaterials (figure 2:11). Normalised UV-Vis spectra of the nanoring and the hollow nanodome patterns can be seen in figure 2:11a. The extinction of the multifunctional nanopattern is stronger than that of the other patterns and shows a superposition of plasmonic resonances from the Au-Ag-Au NPs and the nanohole patterned substrate. However, in the case of the nanoring and the hollow nanodome patterns, the absence of Ag leads to a sharp dip in the extinction at ~470 nm which corresponds to the Ag contribution in the multifunctional pattern.[201] Resonance modes of Au near the wavelengths of ~610 nm are clearly seen. Moreover, comparison between the spectra from the nanoring and the hollow nanodome patterns shows a peak broadening and blue-shift, which was attributed to the contribution from the Au NCs. The ease with which different patterns with tunable spectral response can be obtained suggests their use for plasmonic-based sensing,[107, 202-204] imaging,[205] and lithography.[82]

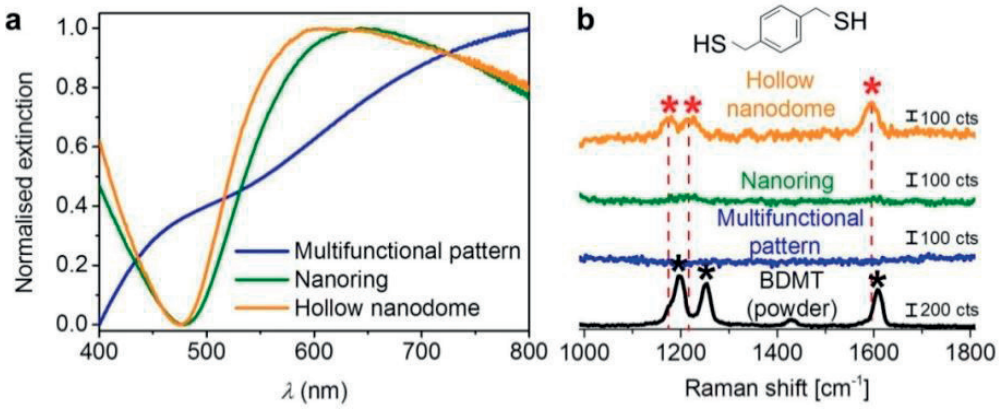

Figure 2:11 Plasmonic nanopatterns. (a) Extinction spectra of the multifunctional nanopattern (blue line), nanoring pattern (green line), and hollow nanodome pattern (orange line). (b) Raman spectrum of concentrated BDMT as a reference (black line) and associated SERS spectra from the chemisorbed BDMT on the multifunctional nanopattern (blue line), the nanoring pattern (green line), and the hollow nanodome pattern (orange). Reprinted from Ref. 49 (Copyright 2015 Wiley-VCH publisher)

Electric-field enhancement ('hot-spot' effect) are expected for some of the nanopatterns, for instance at the edge of the nanohole pattern.[206] Here, the interaction between the Au NCs and the nanohole pattern on the nanoring patterned substrate,[207] and the nanogaps between the Au NCs and the nanoring patterns on the hollow nanodome patterned substrate,[208] can be used to obtain defined structures on a large scale. This is in contrast to many nanoparticle structures that either require lengthy electron beam lithography or that are obtained by randomly drying nanoparticles on a substrate.[209, 210] To test the usefulness of those patterns for surface-enhanced Raman spectroscopy (SERS), a hollow nanodome pattern was prepared and used to detect the chemisorbed 1,4-benzenedimethanethiol (BDMT), a common Raman reporter (figure 2:11b). The SERS signal was measured with 20 s integration time and 0.6 mW power at λ = 633 nm using a He-Ne laser (see Methods for details). The largest SERS signals were detected on the hollow nanodome patterns at 659.3, 1171.5, 1225.8, and 1593.6 cm^{-1} corresponding, respectively, to the 667.9 cm^{-1} (vC–S), 1197.3 cm^{-1} (substituent-sensitive band of CH_2 wagging), 1254.3 cm^{-1} (CH_2 wagging) and the 1607 cm^{-1} (vcc – ring stretch) Raman modes of BDMT.[211] In contrast to the hollow nanodome patterns, no enhancement of the BDMT signal was found when the ring pattern was used, which suggests that the

enhancement in the case of the hollow nanodomes is indeed due to hotspots in the array structures. In the case of the nanoring pattern the similar SERS effect was observed, probably due to hotspots formed by the 2D gap between the Au seed and its circular hole; and in the case of the nanodomes the 3D gap between the Au seed and the NCs that covers it.[208, 212] It is anticipated that the SERS effect can be further increased by optimising the material composition and feature size of the patterns.

2.3 Methods

Electron beam lithography (EBL): EBL (Jeol, JBX-6300FS) was used for the preparation of various nanopattern based on hydrogen silsesquioxane (HSQ) negative tone electron-beam resist. HSQ resist was spin coated onto Si wafers at speeds of 6000 rpm for 1 min to yield a 30 nm thick resist layer. After spin coating, the samples were baked at 90^{o}C for 1 min. The custom seed patterns were written in a JBX-6300FS lithography system at 100 kV acceleration voltage and 1 nA beam current. The resist were developed by immersion in MF322 for 80 sec, and rinsed in deionised water for 30 sec.

Block copolymer micelle nanolithography (BCML): A hexagonal array of Au NPs was fabricated using BCML as a seed layer as previously reported.[27] Poly(styrene)-b-poly(2-vinylpyridine) (S units: 1056; VP units: 671) was dissolved in toluene at a concentration of 4 mg·mL^{-1} and stirred overnight. $HAuCl_4 \cdot 3(H_2O)$ was added to the polymer solution at a molar ratio of 0.5 per vinyl pyridine unit and stirred for at least 48 h. This generates self-assembled spherical micelles loaded at the centre with Au salt. To form quasi-hexagonally close-packed arrays of the micelles, the micelles are spin-coated on a two inch Si wafer at 8000 rpm for 1 min. After that, the micelles are removed under 10% H2 and 90% Ar plasma treatment (power: 350 W, pressure: 0.4 mbar, time: 45 min). In this process, Au is reduced and crystallised as 12.1±1.8 nm NPs with ~90 nm interparticle spacing.

Glancing angle deposition (GLAD): Nanostructures (including Ag NPs) and Au films are grown on the seed layer in a custom-built GLAD system with independent control over the substrate's azimuthal directionφ, and the molecular flux direction α. The typical base pressure during deposition was 1×10^{-6} mbar. To grow NPs, the flux angle α and the azimuthal rotation rates per unit thickness $d\varphi \cdot dw^{-1}$ were kept to 85^{o} and 12 ±0.2 ^{o}·nm^{-1}, respectively, with closed-loop feedback based on measurements of material deposition rates using a quartz crystal monitor (QCM). The Au nanoseeds with 12.1±1.8 nm diameter where then expanded by the Au deposition with the tooling factor of 44.5% to 21.1±1.5 nm. Similarly, Ag was grown on the Au nanoseeds with the tooling factor of 12.3% to yield Au-Ag hybrid NPs with a diameter of 37.1±4 nm. The growth of planar films was performed with a 0^{o} tilt of the substrate and without any azimuthal rotation. Figure 2:12 shows the SEM image of the grown multifunctional nanopatterns with thicknesses of the Au films of respectively 5 nm, 10 nm, and 15 nm. To increase adhesion between the Si substrate and the Au layer, a 5 nm Cr layer was grown before the Au growth.

Fabrication of the nanotemplate: The nanohole patterned substrate was etched under SF6:O_2 (3:1) plasma environment, where the etch rate of the depth of Si was ~1 nm s^{-1} (pressure: 8 mTorr, forward bias power: 20 W, ICP power: 100 W, temperature: 20 ^{o}C). Figure 2:9 shows the SEM images of the fabricated Si nanotrenches as a function of the etching time and their corresponding structural dimensions. After that, the Au etch-stop layer was removed by wet chemical etching in the mixture of KI:I_2 for 1 s and the Cr adhesion layer chemically wet etched in the commercial chromium etchant (Technic Inc.). Finally, the patterned substrate was modified with 1H,1H,2H,2H-perfluorodecyltrichlorosilane by gas phase silanization for 45 min and followed by incubating in oven at 85^{o}C for 1h.

Nanoimprint lithography: Using thermal and UV nanoimprint lithography (Eitre 3, Obducat), the array of polymer nanowires were fabricated by imprinting the IPS film onto the nanotemplate. The NIL process was performed at a pressure of 40 bar and at a temperature of 160 ^{o}C for 60 s. After cooling down to 70 ^{o}C, the IPS film was easily peeled off from the template.

Characterization by SEM and TEM: The fabricated nanopatterns were imaged by SEM under an accelerating voltage of 5-10 kV. The TEM images of the nanoparticles were recorded on a Philips CM200 TEM under an accelerating voltage of 200 kV. TEM samples were prepared by drop casting ~10 µL of the colloidal solution onto a Holey® carbon-coated TEM grid (Cu 400 mesh), followed by drying under a gentle flow of argon gas.

UV-Vis spectroscopy and Raman spectroscopy: Extinction spectra of the nanopatterns were measured in the range of 400 nm to 800 nm with a resolution of 1 nm on a Cary UV-vis 4000 spectrometer. For the SERS experiments, the nanopatterns were immersed in 1 mM BDMT dissolved in toluene for 3 h. The samples were then gently washed with toluene and deionised water, and dried. The SERS signals were measured using the 633 nm line of a He-Ne laser for 20 s, where the laser power at the sample was 0.6 mW. The Raman spectrum between 1000 to 1800 cm^{-1} was collected with a spectral resolution of $\sim$ 3 cm^{-1}.

Calibration method to determine the height of a nanorod with SEM view:

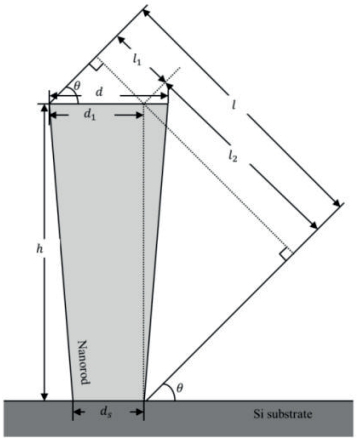

Using Trigonometric function, the height of nanorod is given by

$$h = \frac{l_2}{\cos\theta} = \frac{l - l_1}{\cos\theta}, \tag{2:1}$$

where $l = l_1 + l_2$ is the measured length of nanorod, h is the height of nanorod, and θ is the angle of the projection view of SEM. Herein, l_1 is defined as

$$l_1 = d_1 \cdot \sin\theta = \frac{d + d_s}{2} \cdot \sin\theta, \tag{2:2}$$

where d is the measured diameter of nanorod, d_s is the diameter of nanopatterned seed, and $d_1 = \frac{d+d_s}{2}$. Therefore, h is given as

$$h = \frac{2l - (d + d_s)\sin\theta}{2\cos\theta} \quad . \tag{2:3}$$

Chapter 3 Corrosion-protected hybrid nanoparticles

Nanoparticles composed of functional materials hold great promise for applications due to their unique electronic, optical, magnetic, and catalytic properties. However, a number of functional materials are not only difficult to fabricate at the nanoscale, but are also chemically unstable in solution. Hence, protecting nanoparticles from corrosion is a major challenge for those applications that require stability in aqueous solutions and biological fluids. Here, we present a generic and facile scheme to grow hybrid 3D nanoparticles that are completely encapsulated within a nm-thin protective shell. The method consists of vacuum-based growth and protection, and combines oblique physical vapour deposition with atomic layer deposition. It provides wide flexibility in the shape and composition of the nanoparticles, and the environments against which particles are protected. We demonstrate the approach with multifunctional nanoparticles possessing ferromagnetic, plasmonic, and chiral properties. The present scheme allows nanocolloids, which immediately corrode without protection, to remain functional, at least for a week, in acidic solutions.

This chapter is based on the manuscript:

[135] Corrosion-protected hybrid nanoparticles, **H.-H. Jeong**, M. Alarcón-Correa, A.G. Mark, K. Son, T.-C. Lee, and P. Fischer (*Submitted*)

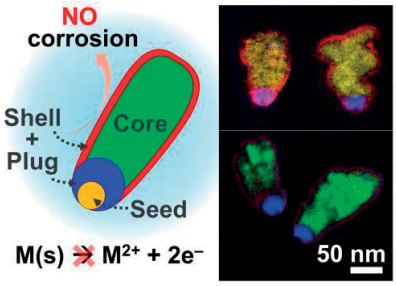

Author Contributions:

H.-H.J. and T.-C.L. proposed the idea. H.-H.J., T.-C.L., A.G.M., and P.F. designed the experiments. H.-H.J. performed all the experiments except for the BCML, EF-TEM, and EDX. M.A.-C. carried out the EF-TEM and EDX imaging. C.M. conducted the BCML. K.S. supported the SQUID experiments. H.-H.J. analysed the data, and H.-H.J., A.G.M., and P.F. wrote the paper.

3.1 Introduction

Corrosion is a ubiquitous characteristic of metallic solids in which a base metal is converted into its ionic state or oxide form by electrochemical surface reactions.[213] Nanoparticles are especially vulnerable because of their high surface-to-volume ratios.[214] In many cases, since the reaction products are soluble, corrosion leads to complete destruction of the original nanostructure. This means that in real world applications the dominant materials consideration has often been corrosion stability, and the functional property required by the application – e.g. optical response, mechanical strength, magnetic susceptibility – is secondary. With effective corrosion protection materials selection can be made on the basis of the functional property. This will permit better materials optimization and lead to nanoparticles that are less expensive or more effective at the targeted application.

A rational approach to prevent the corrosion of a nanoparticle is to isolate it from the environment within an inert conformal shell. This is challenging however, as the protection layer must be stable in various environments and compatible with the nanoparticle itself, while simultaneously preserving the intended function of the nanomaterial. For instance, in plasmonic sensing applications, the near field sensing volume of a metal nanoparticle decays exponentially into the environment, so thick shell layers (>5 nm) reduce the effective sensing volume and efficiency.[209] Moreover, for *in vivo* medical application, the magnetic particles should not corrode, and be small enough for extrusion.[22] Encapsulating nanoparticles by chemical means has been proposed for protection, but for solution based processes the core material often oxidizes and corrodes before the protective coating is complete.[215] It is also difficult to form a complete defect-free shell with well-defined thickness, since chemical coating methods typically require careful and laborious optimization whenever the core material is changed.[215, 216]

This chapter reports an approach for the design and fabrication of 3D core-shell nanoparticles and nanostructures with a nm-thick shell that encapsulates the entire nanoparticle. A key element of the scheme is an inert protective segment, directly incorporated into the core's growth process, which shields the particle's underside (see figure 3:1a). It is shown that particles protected in this way are stable for days in acidic solutions in which in their unprotected state they dissolve in minutes. This work paves the way for the use of reactive, toxic, and unstable magnetic and plasmonic nanoparticles in physiological fluids.

3.2 Fabrication concept

Here method is based on nanoGLAD, [28, 56, 59], described in chapter 2, which combines block copolymer micelle nanolithography (BCML)[57] with glancing angle deposition (GLAD).[54, 217] The method permits control over both the shape and material composition of 3D hybrid nanostructures. However, many of the materials that can be successfully grown with this technique are not chemically stable when exposed to air or water. This limits the scope of potential applications that require nanoparticles in a colloidal form.

Atomic layer deposition (ALD) is a promising general method for corrosion protection, since it is compatible with many materials and provides well-controlled surface coatings.[218, 219] In contrast to chemical processes, one advantage of ALD is that, because it is a vacuum and gas phase technique, corrosion during the application process can be minimized. However, in a typical ALD process, nanoparticles are deposited onto a substrate for the coating step. This means that the undersides of the nanoparticles, which face the substrate, are not exposed to the reacting species in the ALD process.[220, 221] Thus the nanoparticles are not fully coated and their protective shells have defects. Once the nanoparticles are transferred to solution,

corrosion will proceed via the defect which limits the lifetime of the nanomaterial. Thus, the practical challenge for the protection of nanoparticles *via* an ALD process is to ensure the complete encapsulation by a continuous shell layer without defects.[41]

To address this, the bottom-up parallel fabrication scheme is developed and depicted in figure 3:1. BCML is used to spin-coat an array of metallic nanoparticles with the desired particle diameter and spacing (here 10 nm and 100 nm respectively) on a substrate such as a wafer (figure 3:1b). The self-assembled nanoparticles serve as nanoseeds for the subsequent vapour deposition of an inert 'plug' segment. The plug is the crucial element that ensures that the bottom-facing surface of the nanoparticle is protected (figure 3:1c). The deposition of this small nanopatch is only possible with a shadow growth technique, as other methods would coat the entire surface and cannot deposit a material at defined positions.[49] It is important that the material of the plug is stable in solution, ideally under a wide range of chemical conditions. We find that metals which form tenacious metal oxides, particularly Ti, act as good plugs (Appendix figure A:5). Next, the functional, but reactive 'core' of the nanoparticle is grown on top of the plug by further nanoGLAD deposition (figure 3:1d).[28, 56] Many core shapes are readily obtained using this technique (see Chapter 2 for further details), but here focus is on protecting two representative shapes: nanorods and nanohelices. In a final step the core is encapsulated by ALD, which forms a thin and chemically inert oxide 'shell' over the exposed surface of the nanostructures (figure 3:1e).[222] Here HfO_2 and Al_2O_3 are used, but other inert and ALD-compatible materials including TiO_2, SiO_2, ZnO, Pt, etc. could be also used for protection.[223-225] The ALD layer covers the core nanomaterial and overlaps the plug; together the plug and shell ensure complete protection of the core from chemical attack at all points. Finally, depending on the application, the protected functional nanoparticles can be released into solution by sonication (figure 3:1f). The advantage of our scheme is that it is general and that it readily accommodates changes in the shape and material composition of the hybrid nanocolloids.

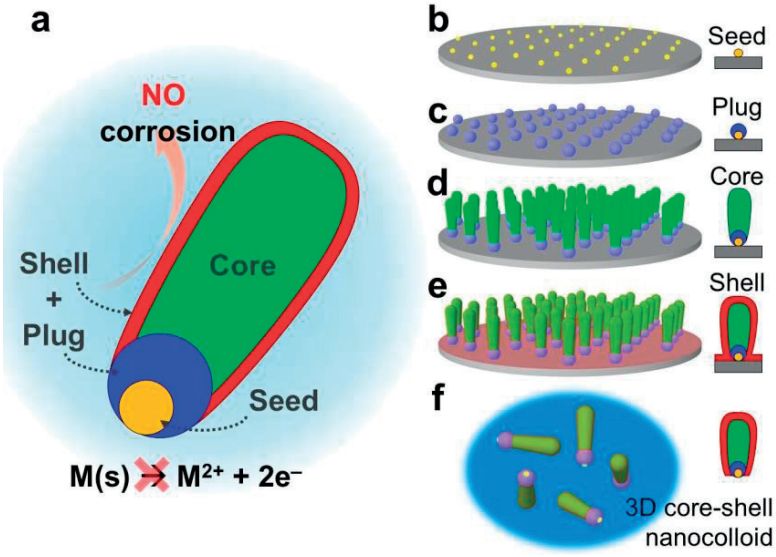

Figure 3:1 Fabrication of corrosion-resistant 3D core-shell nanocolloids. (a) Schematic view of no corrosion reaction with 3D core-shell nanoparticle. (b) Patterning a silicon wafer with self-assembled Au nanodots using BCML. (c) Growth of a protection patch, the 'plug', using GLAD. (d) Growth of the 'core'; the 3D functional nanostructures in need of protection. (e) Formation of the second protection component, the 'shell', using ALD. (f) A suspension of 3D core-shell nanoparticles in solution after detachment from the wafer by sonication.

3.3 Corrosion kinetics

Corrosion reaction of metal nanoparticles can be simplified as, [213]

$$M(\mathrm{s}) \rightarrow M^{2+} + 2e^{-}. \tag{3:1}$$

This reaction can be approximated as a first order reaction and the reaction decay in our measurements can be fitted by the exponential function, which is given by

$$A = A_o \cdot \mathrm{e}^{-kt}, \tag{3:2}$$

where A is functional property of nanoparticles (i.e. magnetization, optical extinction, and circular dichroism), k is first order reaction rate, and t is reaction time. As copper ions do not give rise to optical (plasmonic) signal, the decay rate of Cu nanoparticles (both rod and helix) can be readily estimated by equation 3:2. However, Co ions possess a weak magnetic property (~2 emu/g),[226] so that the equation 3:2 should be extended as

$$A = A_o \cdot \mathrm{e}^{-kt} + A_o{}'\left(1 - \mathrm{e}^{-kt}\right), \tag{3:3}$$

which reflects the evolution of magnetization of Co ions in the second term. So, according to equations 3:2 and 3:3, the decay rates and lifetime of all the particles can be calculated.

3.4 3D core-shell nanoparticles

Magnetic and metallic nanoparticles are of interest for medical applications ranging from sensing [22, 73, 107, 227, 228] to therapy,[18, 108] but often the optimal materials for a given application are cannot be used for reasons of physiological incompatibility. For instance, hard magnetic materials are often toxic and many metals such as copper or silver corrode easily. The following sections now show how Cu and Co nanocolloids grown using physical vapour deposition can be stabilised such that they remain functional in a variety of aggressive aqueous solutions for many days.

3.4.1 Magnetic nanoparticles

The protection scheme is here demonstrated with cobalt, a strong ferromagnetic material, but one that is not chemically stable in solution when grown in the form of nanoparticles using physical vapour deposition.[229] Figure 3:2a shows two Co nanorods protected with ~20 nm Ti plugs and a 4 nm thick HfO_2 shells. The materials-resolved energy filtered transmission electron microscope (EF-TEM) image, acquired after seven day's immersion in water, clearly shows that the Ti plug (blue) and HfO_2 shell (red) combine to cover the entire surface of the reactive Co core (green). Even after 30 days, corrosion of the nanoparticles was not observed (see figure 3:2d and Appendix figure A:6). Figure 3:2b shows the out-of-plane ferromagnetic character of Co nanorods measured on the wafer before exposure to water. In this geometry the long axis of the particles is parallel to the applied magnetic field direction and the sample exhibits a coercive field of ~1 kOe and a remanence of ~14 emu·g^{-1} (see Methods for details). The effectiveness of protection can be assessed by monitoring the saturation magnetization (B = 15 kOe) after immersion in water. Figure 3:2c shows the evolution of the saturation magnetization for three different samples: unprotected (red circles) and protected (blue triangles) particles on-wafer, immersed in water with rod axes normal to the applied magnetic field (see Appendix figure A:7 for details), and protected particles with isotropic orientations in an agarose gel stabilised colloidal suspension (green triangles). The gel matrix traps the particles and prevents

their aggregation and sedimentation over long times (at least several days) but is highly permeable to solvent and ions.[230, 231] Upon immersion, the magnitude of the signal for the unprotected particles is strongly attenuated, whereas both protected samples show no substantial change in signal over the course of the experiment (see also Appendix figure A:8 for details). The behaviour of the unprotected particles is well described by first order kinetics; fitting with a decaying exponential and accounting for the finite magnetization of the Co ion products yields an unprotected nanoparticle' half-life of 81 min. The asymptotic magnetization of ~ 1 emu·g^{-1} is consistent with complete conversion of metallic Co to Co^{2+} which is expected to have a magnetization of ~2 emu·g^{-1} at 15 kOe.[226] SEM images of the two on-wafer samples acquired after 30 days of immersion (figure 3:2d) show strong degradation of the unprotected structures (lower) but the protected structures appear essentially unaffected (upper).

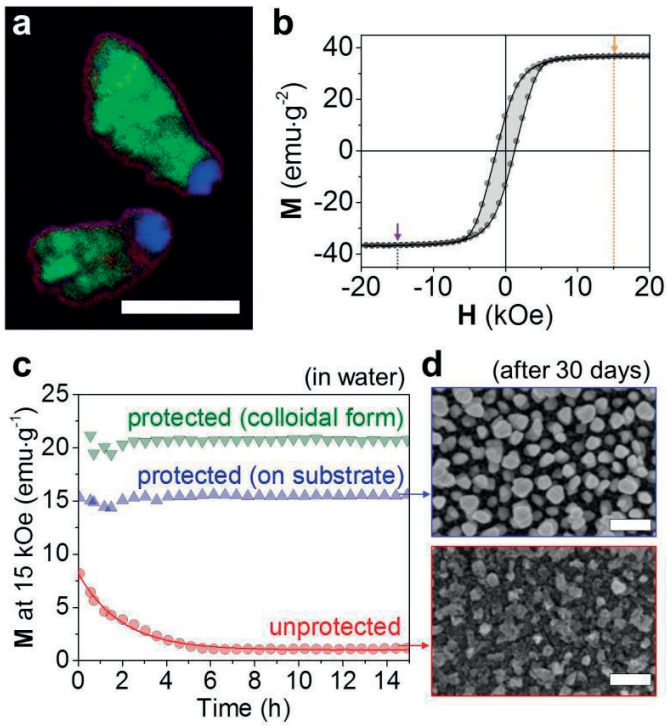

Figure 3:2 Protection of Co nanorods. (a) EF-TEM elemental map of the protected Co nanorods (green: Co, blue: Ti, red: O, scale bar: 100 nm). (b) Out-of-plane magnetization measurement of Co nanorods as-grown on the Si substrate, showing an open ferromagnetic hysteresis loop. The arrows indicate the saturation magnetization of Co nanorods (at ± 15 kOe), whose values were used to track the stability of the nanorods. (c) *In situ* trace in saturation magnetization of the Co nanorods: In-plane saturation magnetizations of the protected (blue, up triangle) and unprotected (red, circle) Co nanorods on-water at **H** = 15 kOe in water as a function of time. The unprotected particles had decayed substantially in the short amount of time between preparation and measurement. The solid red line was fitted by using first order reaction and the decay rate of k is 142×10^{-6} s^{-1}. Saturation magnetization of the protected Co nanorods suspended with the isotropic orientation in 2% agarose gel (green, down triangle) at **H** = 15 kOe in water as a function of time. (d) SEM images of the protected Co nanorods (top panel) and the unprotected Co nanorods (bottom panel) after 30 days in water.

For biomedical applications the nanoparticles also must be chemically stable in solutions with a variety of ion concentrations and pH values. Figure 3:3a shows the saturation magnetization of protected on-wafer Co particles after one week in 0.1M phosphate buffer solutions in the range of pH 3.7 to pH 9. Both the

SEM images (figure 3:4) and the SQUID measurements demonstrate that the protected hybrid nanocolloids are stable even in highly acidic solutions (see also Appendix figure A:9).

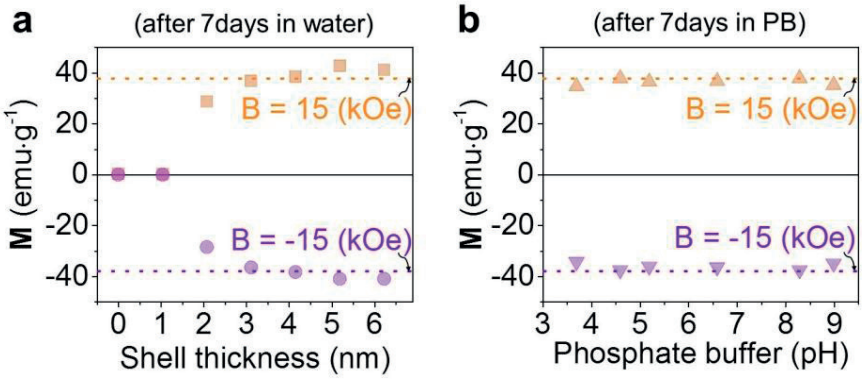

Figure 3:3 Out-of-plane saturation magnetization of Co nanorods protected with HfO_2 layer. (a) Protection with different thicknesses of HfO_2 layer at **H** = 15 kOe (orange) and -15 kOe (violet) after 7 days in water. (b) Protection with 4 nm thick HfO_2 and after 7 days in 0.1 M phosphate buffer solutions at 6 different pH conditions (pH 3.7 ~ pH 9). The dotted lines indicate the positive and negative saturation magnetizations of the particles as grown.

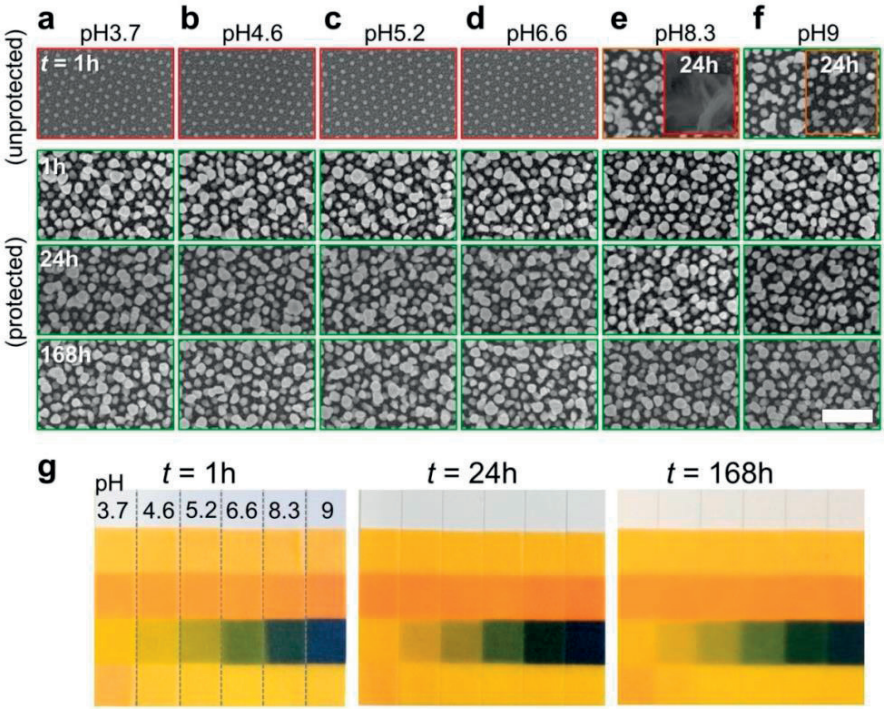

Figure 3:4 Stability of the protected Co nanorods in 0.1 M phosphate buffer solutions at (a) pH 3.7, (b) pH 4.6, (c) pH 5.2, (d) pH 6.6, (e) pH 8.3, and (f) pH 9. The first row shows the SEM images of the unprotected Co nanorods after 1h in the buffer solutions at different pH. The second to forth rows indicate the SEM images of the protected (encapsulated) Co nanorods with 4 nm HfO_2 layer after 1h, 24h, and 168h respectively in the buffer solutions at different pH (scale bar: 400 nm). (g) The pH measurements of each buffer solution after 1h, 24h, and 168h (left to right: pH 3.7, 4.6, 5.2, 6.6, 8.3, and pH 9). The different boundary colours of each image indicate the status of the particles stability (red: complete corrosion, orange: partial corrosion, green: stable).

The thickness of the HfO_2 shell is an important factor in the degree of protection, figure 3:5a. Figure 3:3b shows saturation magnetizations for on-wafer particles with shell thickness ranging from 0 nm (no shell protection) to 6.25 nm after one week in water (see also Appendix figure A:10). Oxide layer thickness less than ~3 nm offer poor protection but at shell thicknesses 3 nm and greater the magnetization is unchanged after seven days' immersion. These results are in excellent agreement with SEM analysis in figure 3:5b.

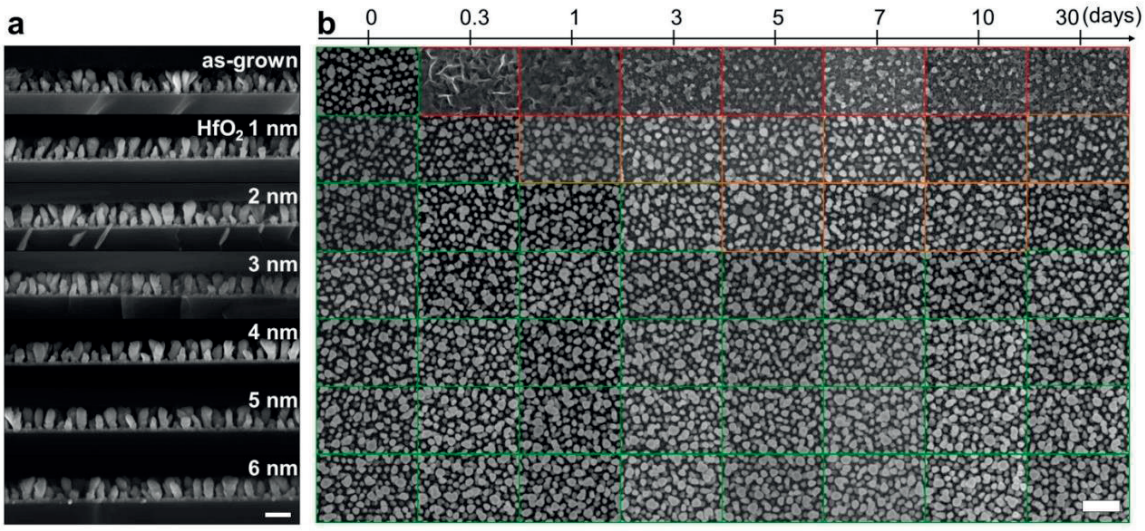

Figure 3:5 Stability of the protected Co nanorods in water. (a) SEM images (side view) of the Co nanorods protected with different thicknesses of the HfO_2 shell layer: 0 nm, 1 nm, 2 nm, 3 nm, 4 nm, 5 nm, and 6 nm (from top to bottom, scale bar: 200 nm). (b) Serial SEM images (top view) of the Co nanorods protected with HfO_2 shell layer in water over time (Scale bar: 400 nm). Each column indicates the different ALD conditions (0 to 6 nm thick HfO_2 layer from left to right). Each row indicates how long the particles kept in water before imaging. The different boundary colours of each image indicate the status of the particles stability (red: complete corrosion, orange: partial corrosion, green: stable).

3.4.2 Metal nanoparticles

Au is probably the most commonly used material in the nanoparticle field because of its exceptional stability and useful plasmonic properties.[89, 108, 232] However, other metallic materials (including Cu,[233-236] Al,[94, 237-239] and Mg[109, 240]) are often overlooked, despite favourable optical properties, due to their inherent instability in air and water. In particular, Cu is highly conductive, and could represent a cost-effective replacement for Au in plasmonic, photovoltaic, and catalytic applications,[74] but its use is limited as it oxidises quickly.[233] As a second demonstration, it is shown Cu nanorods protected with a ~20 nm Ti plug and 3 nm HfO_2 shell. Figures 3:6a and b shows an image of a single such nanorod after immersion in phosphate buffer solution (0.1 M, pH 3.7) for 2 days (see Appendix figure A:11 for a large number of particles). It can be clearly seen that the Cu core remains uncorroded thanks to the plug and shell protection.

Part of the appeal of Cu for nanoparticles is that it is a low-cost material that supports a local surface plasmon resonance (LSPR) observable in optical extinction spectroscopy (figure 3:6c, inset)[241]. Figure 3:6c shows the time evolution of the LSPR response of unprotected (red) and protected (blue) Cu nanorods dispersed with the isotropic order in a 2% agarose gel matrix. After ~1 h of immersion, phosphate buffer solution was added to the gel and allowed to mix by diffusion (see Methods for details). Again the signal from the unprotected particles shows a strong decay with a half-life of 125 min before PB addition and 22 min

after. Within 3 h the signal has reduced to <2%, indicating almost complete dissolution of the Cu core (see Appendix figure A:12 for the full extinction spectra). On the other hand, the protected particles show only a small (0.7%) decrease in intensity during the initial phase,[242] followed by a slow asymptotic decline after the PB is added to a steady state value of ~78%. It is speculated that the decay observed for the protected particles is due to a small fraction of colloids whose protective shell was damaged by sonication during the lift-off process. This is supported by the observation that protected Cu particles left on-wafer remained uncorroded after 2 days immersed in the same buffer solution.[135]

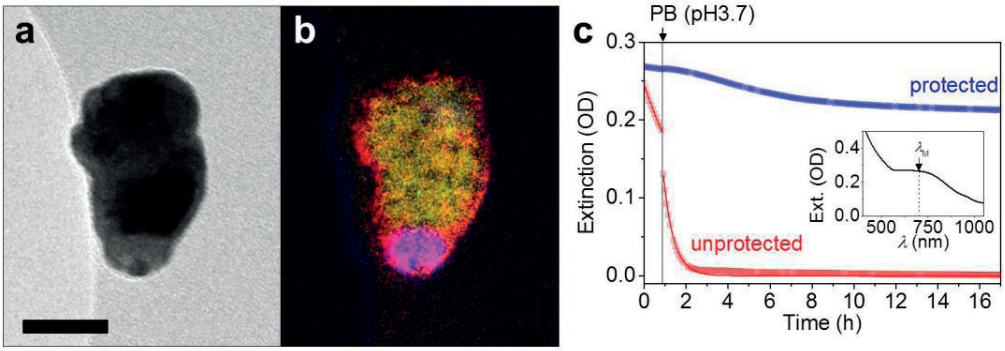

Figure 3:6 Protection of Cu nanorods. (a) TEM of the Cu nanorod protected with 3 nm HfO_2 layer and (b) its corresponding EF-TEM elemental map (yellow: Cu, blue: Ti, red: O, scale bar: 50 nm). (c) *In situ* extinction trace (at λ = 687 nm) of the protected Cu nanorods (blue) and the unprotected Cu nanorods (red) suspended in agarose matrix. Initially the liquid phase of the gel is water; the vertical line indicates the addition of acidic phosphate buffer which after mixing yields a concentration of 0.1 M at pH3.7. Each solid line was fitted by using first order reaction, which yields the decay rates of $k = 92\times10^{-6}$ s^{-1} (water) and $k = 563\times10^{-6}$ s^{-1} (PB). Inset shows the extinction spectrum of the protected Cu nanorods in 2% agarose gel.

3.4.3 Chiral nanoparticles

A particularly sensitive probe of the structure and symmetry of nanocolloids is circular dichroism (CD) spectroscopy. Chiral nanoparticles can be grown by simply changing the growth parameters in the nanoGLAD fabrication step.[93] Here Cu nanohelices were grown by nanoGLAD and they were encapsulated by a ~20 nm Ti plug and 3 nm HfO_2 shell, see figures 3:7a and b. The left panel of Figure 3:7c shows the corresponding normalised CD spectra for protected and unprotected particles immediately after immersion in water. The spectral peak of the protected particle is red-shifted relative to that of the unprotected one because the plasmon extinction spectrum is sensitive to the refractive index of the local environment, and the index of HfO_2 is larger than that of the water it displaces. Then, to test the particles' stability in acidic solution, the phosphate buffer was added in which yielded a concentration of 10 mM PB solution at pH 3.7 after mixing. In this case, as shown in the right panel of figures 3:7c, the signal of the unprotected particle has diminished in the short period of time between mixing the solution and making the measurement (< 4 min, see Appendix figure A:13). The strong attenuation of the peak is consistent with a population of fewer and smaller metallic Cu nanohelices. Corresponding dynamic light scattering (DLS) studies show that the protected Cu nanoparticles' size distribution is stable, whereas the unprotected colloids reveal no meaningful features (Appendix figure A:13). [243] After 20 min the signal from the unprotected sample is indistinguishable from baseline noise, whereas the protected sample, after 5 days, retains 50% of its original intensity. SEM (figure 3:8) and TEM images (Appendix figure A:14) show that the protected nanocolloids remain intact after at least 2 days immersion.

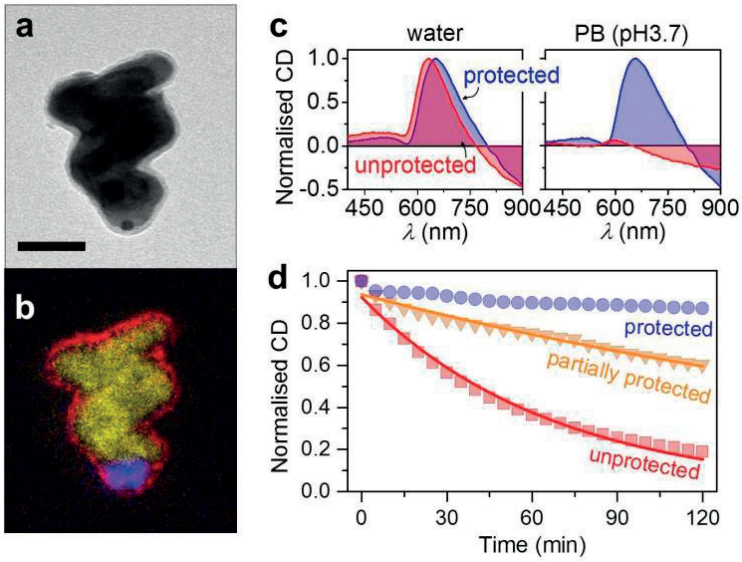

Figure 3:7 Protection of helix-shaped Cu nanoparticles. (a) TEM of the Cu nanohelix protected with 3 nm HfO_2 layer and (b) its corresponding EF-TEM elemental map (yellow: Cu, blue: Ti, red: O, scale bar: 50 nm). (c) The normalised CD spectra of the protected Cu nanohelices (blue) and the unprotected Cu nanohelices (red) in water (left panel) and 10 mM phosphate buffer at pH 3.7. For the PB results, the unprotected particles had decayed substantially in the short amount of time between preparation and measurement. (d) Comparison of the stabilities of the Cu nanohelices that are completely protected (blue), partially protected (orange), and unprotected (red) in 10 mM H_2O_2 by tracking their CD intensity with time. Each solid line was fitted by using first order reaction, which yields the decay rates of k = 63×10^{-6} s^{-1} (orange; partially protected) and k = 250×10^{-6} s^{-1}(red; unprotected).

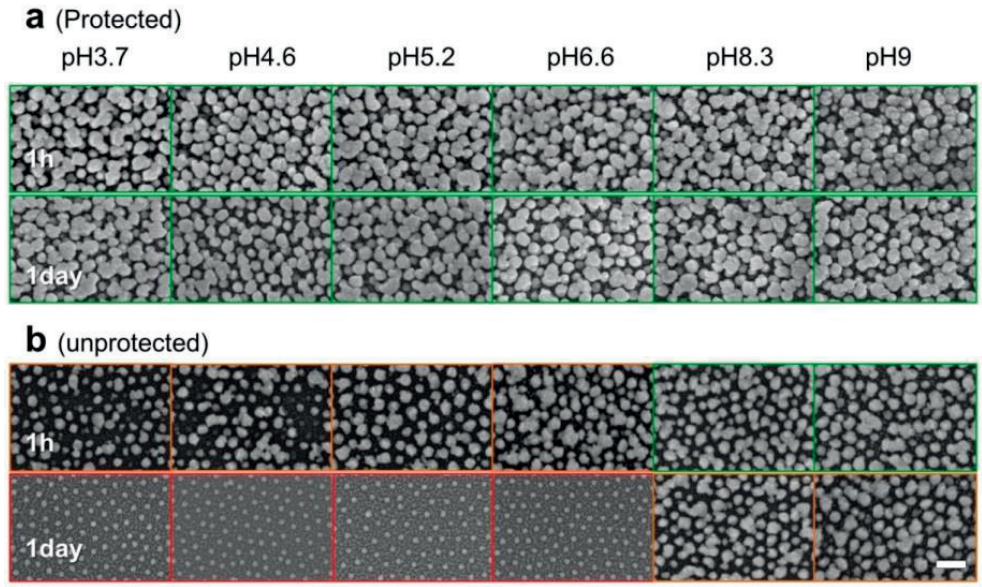

Figure 3:8 SEM images (top view) showing the stability of (a) protected and (b) unprotected Cu nanohelices in 0.1 M phosphate buffer solutions at pH 3.7, 4.6, 5.2, 6.6, 8.3, and 9 (scale bar: 200 nm). Each top panel is the resultant images after 1h in the buffer solution and each bottom panel is from the same sample after 1 day in solution. The different boundary colours of each image indicate the status of the particles stability (red: complete corrosion, orange: partial corrosion, green: stable).

The time evolution of protected (plug and shell, figure 3:7d, blue), partially protected (shell only, yellow), and unprotected (without plug and shell, red) Cu nanohelices are measured by monitoring their CD response. When immersed in a 10 mM H_2O_2 solution, the unprotected sample shows a ~81% drop in CD intensity over 120 min, while the signal from the protected sample decreases only ~13% in the same (see Appendix figure A:15 for complete CD spectra). The small decline seen by the protected particles is attributed to those that are mechanically damaged during release from the wafer. Interestingly, the partially protected sample, which lacks a protective plug, showed signal attenuation midway between the protected and unprotected samples (40% drop). This clearly illustrates that the ALD shell alone is not sufficient for particle protection, and that the underside plug is a crucial feature for long term nanoparticle protection in corrosive environments.

3.5 Methods

***Block copolymer micelle nanolithography (BCML)*:** The array of Au nanoseeds was prepared using block-copolymer micelle nanolithography as previously reported[57]. Briefly, the block-copolymer micelles are formed by self-assembly and then spin-coated onto a two-inch Si wafer where the micelles form a quasi-hexagonally ordered monolayer (spacing ~100 nm). Plasma treatment reduces the Au to form metallic nanoparticles with ~10 nm in diameter. These act as seeds for subsequent nanoGLAD growth.

***Nano glancing angle deposition (nanoGLAD)*:** nanoGLAD was used for two main steps, growing the plug and the nanoparticle core. In this process a substrate manipulator provides independent control over the azimuthal φ, and polar α angles of the vapour flux during growth, within a chamber with a base pressure of 1×10^{-6} mbar. To form well-isolated plugs, the flux angle α and the azimuthal rotation rate per unit thickness $d\varphi/d\theta$ were kept to respectively 85° and 36±0.1°/nm with closed-loop feedback based on measurement of the material deposition rate on a quartz crystal monitor. The core material was grown on the plugs, where $d\varphi/d\theta$ was maintained at a constant 18±0.1°/nm for Co (and Cu) nanorod and 1.8±0.1°/nm for Cu nanohelix, respectively, while keeping α = 87°.

***Atomic layer deposition (ALD)*:** a thin layer of alumina (Al_2O_3) or hafnium dioxide (HfO_2) was grown to cover the core's surface using Atomic Layer Deposition (Savanah 100, Cambridge Nanotech). The Al_2O_3 was grown at T = 100°C with a 0.1 nm/cycle growth rate by injecting trimethylaluminum (TMA) for 0.03 s and H_2O for 0.03 s repeatedly. The HfO_2 was grown at T = 150 °C with a 0.1 nm/cycle growth rate by injecting $Hf(NMe_2)_4$ for 0.15 s and H_2O for 0.015 s repeatedly.

***SEM, TEM, and EELS analysis*:** Structures were imaged with SEM (Gemini Ultra55, Zeiss), TEM (CM200, Philips), STEM (SESAM, Zeiss), EDX, and EELS. TEM samples were prepared by drop casting ~20 µL of the colloidal suspension onto a Holey carbon coated TEM grid (Cu or Ni 400 mesh), followed by drying under a gentle flow of Ar gas. Bright field and EF-TEM images were recorded on a Zeiss 912 Omega electron microscope under an accelerating voltage of 120 kV. For the EF-TEM images the in-column electron energy filter was used. The exposure time ranged from 5 to 30 seconds for the different samples and materials. Each elemental core-loss image was measured, modelled and subtracted by the "three-window technique" using the power law model in the Gatan Digital Micrograph program (http://www.gatan.com/software/)

***SQUID magnetometry*:** The magnetization of the Co nanorods was measured at 300K using a Quantum Design magnetic property measurement system (MPMS) magnetometer. For the analysis of the on-wafer nanorods' stability in water, a small piece (~10 mm^2) of the Si wafer on which the nanorods were grown

was immersed in water contained in a quartz NMR tube and sealed with a rubber cap (see Appendix). The *M-H* curves are corrected for the diamagnetism of the Si substrate by subtracting a linear background whose slope matches the high field diamagnetic response of the Si beyond the Co saturation magnetization.

***Colloids and buffer solution*:** The nanoparticles were detached from the wafer by sonicating a wafer piece in an aqueous solution of 0.1 $mg \cdot mL^{-1}$ polyvinylpyrrolidone (PVP) for ~2 min. The phosphate buffer was prepared using phosphate salts pairs, (Na_2HPO_4 - KH_2PO_4), as well as NaCl and KCl. The pH for each solution was adjusted when necessary with HCl. Buffers were prepared as stock solutions and stored at 4°C until further use.

Agarose Gels: For measurements on colloidal suspensions, agarose gel was used to prevent agglomeration of the particles during the long measurement.[230] 4% agarose gel was melted at 100°C then mixed at 1:1 with an aqueous colloidal suspension of the nanoparticles. The mixture, with 2% agarose concentration, was cooled in a fridge to form a gel. For the experiment described in figure 3:3c and 4c, concentrated PB was added above the gel in sufficient volume that after diffusive dilution with the water phase of the gel the PB concentration was 0.1 M at pH 3.7.

UV-VIS-NIR spectroscopy and CD spectroscopy: Extinction spectra of the nanocolloids were measured on a Cary UV-VIS-NIR 5000 spectrophotometer. Circular dichroism spectra were obtained with a Jasco J-810 circular dichroism spectrometer. Samples of nanoparticles trapped in agarose matrix were contained in quartz cuvettes with 10 mm path length. All the spectra were measured with a scan rate of 500 $nm \cdot min^{-1}$ in the wavelength range of 400 to 1000 nm at 0.1 nm intervals. Extinction results were baseline corrected by subtracting a spectrum acquired from a glass cuvette containing PB solution and agarose gel.

***DLS analysis*:** A colloidal solution (0.5 mL) of nanohelices was measured in a Malvern Zetasizer Nano ZS at 2 min intervals. For the analysis of the Cu nanoparticles the refractive index and extinction of Cu at λ = 632.8 nm (He-Ne laser) were taken from Ref. 92.

Chapter 4 Chiral plasmonic nanosensors

Biosensors based on the local surface plasmon resonance (LSPR) of individual metallic nanoparticles promise to deliver modular, low-cost sensing with high detection thresholds. However, they continue to suffer from relatively low sensitivity and figures of merit (FOMs). In this chapter the idea of sensitivity enhancement of LSPR sensors is introduced through (1) engineering of the material dispersion function and (2) strong dispersion of most substances in the UV region. Employing dispersion and shape engineering of chiral nanoparticles leads to remarkable refractive index sensitivities (1091 nm·RIU^{-1} @ λ = 921 nm) and FOMs (> 2800 RIU^{-1}). A key feature is that the polarization-dependent extinction of the nanoparticles is now characterised by rich spectral features, including bipolar peaks and nulls, suitable for tracking refractive index changes. This sensing modality offers strong optical contrast even in the presence of highly absorbing media, an important consideration for use in complex biological media with limited transmission. The technique is sensitive to surface-specific binding events that are demonstrated through biotin-avidin surface coupling.

This chapter is based on the published articles:

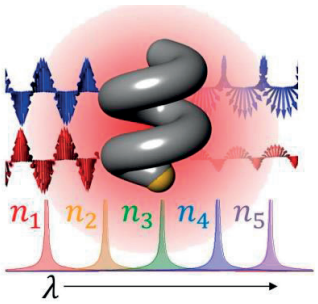

[93] Dispersion and shape engineered plasmonic nanosensors, **H.-H. Jeong**, A.G. Mark, M. Alarcón-Correa, I. Kim, P. Oswald, T.-C. Lee, and P. Fischer, ***Nature Communications*** 7, 11331 (2016)

[109] Magnesium plasmonics for UV applications and chiral sensing, **H.-H. Jeong**, A.G. Mark, and P. Fischer, ***Chemical Communications*** 52, 12179 (2016)

Author Contributions:

For Ref. 93 P.F. proposed the idea and H.-H.J., A.G.M., T.-C.L and P.F. designed the experiments. H.-H.J. performed the experiments except for BCML, TEM, ellipsometry, and ICP-OES. C.M. conducted the BCML. A.G.M. developed the analytical theory. M.A. carried out the TEM imaging. I.K. conducted thin film analysis theoretically and experimentally. P.O. designed bio-experiment. H.-H.J. and A.G.M. analysed the data, and H.-H.J., A.G.M., and P.F. wrote the paper.

For Ref. 109 P.F. proposed the idea. H.-H.J. designed and performed all the experiments except for BCML. C.M. conducted the BCML. H.-H.J. and A.G.M. analysed the data and H.-H.J., A.G.M., and P.F. wrote the paper.

4.1 Dispersion and shape engineered plasmonic nanosensors

4.1.1 Introduction

Devices based on surface plasmon resonance (SPR) phenomena detect shifts of the resonance wavelength in response to changes of the refractive index of the medium surrounding the plasmonic material.[244] This may, for instance, be due to biomolecules that bind to the sensor. SPR offers high sensitivities,[72] but requires extended smooth surfaces.[92, 245] In many situations, it would be desirable to have a local sensor for use *in situ* or *in vivo* (for instance within a cell) and here the local surface plasmon resonance (LSPR) supported by nanostructures offers substantial advantages.[71, 73, 246] The short penetration depth of plasmon oscillations into the surrounding fluid makes for small, spatially localised sensors which promise to be effective in a range of biomedical applications.[23, 107, 108, 247] However, compared to plasmonic biosensors that utilise extended SPR, which serve as the reference standard for optically addressed sensors, LSPR sensors generally have a reduced sensitivity (S_n < 1,000 nm·RIU^{-1}) and a lower figure of merit (FOM < 100 RIU^{-1}).[72, 73]

The typical strategy employed to enhance the sensitivity of LSPR nanosensors is to manipulate the aspect ratio of symmetrical nanoparticles, with more elongated particles yielding higher sensitivities.[89, 91] This approach has been demonstrated with nanorods and nanoprisms that show improved sensitivities.[118, 248, 249] On the other hand, the materials selected for such particles have, quite reasonably, been restricted to those with strong plasmonic properties: e.g. Ag,[250] Au,[108] Al.[94] This has been driven by the desire for a high FOM that comes from the low interband damping, and sharp resonance of pure metals. However, it means that the material dispersion function, a key factor in the sensitivity of LSPR nanosensors, has been limited to the dielectric functions inherent to those pure metals.

This chapter shows how dispersion-engineering introduces a new material based parameter for improving the sensitivity of LSPR sensors. When combined with shape-engineering this leads to extremely high LSPR sensitivities and FOMs. An analytical model of chiral plasmonic sensing is introduced that illustrates the roles of chirality and materials properties for the important sensing characteristics. Based on this understanding this chapter introduces colloidal nanostructures that are the most sensitive LSPR sensors reported to date.[95, 118] Furthermore, the utility of the engineered particles is introduced as surface sensitive probes for biotin-avidin binding. This scheme is particularly robust as it is immune to changes in the optical density of the background, and can thus be used in complex environments.

4.1.2 Theoretical concept

Plasmon-based LSPR sensors operate by tracking the shift in the resonance peak of the plasmon absorption in response to changes in n, the refractive index of the local medium.[73] The resonance condition is met when

$$\varepsilon_r^* = \varepsilon_r(\lambda^*) = -\bar{\chi} n^2, \tag{4:1}$$

where λ^* is the peak wavelength, ε_r is the real part of the dielectric function describing the plasmonic material, and the factor $\bar{\chi}$ describes the shape of the particle (for spheres$\bar{\chi} = 2$). Ideally, the dispersion of ε_r should be such that even very small changes in n cause appreciable changes in the resonance wavelengthλ^*, i.e. large resonance shifts. The sensitivity of the system is defined as,[91]

$$S_n = \frac{d\lambda^*}{dn} = \frac{\frac{d\varepsilon_r^*}{dn}}{\left(\frac{d\varepsilon_r}{d\lambda}\right)_{\lambda^*}} = \frac{-2\bar{\chi}n}{\left(\frac{d\varepsilon_r}{d\lambda}\right)_{\lambda^*}}, \tag{4:2}$$

so decreasing the wavelength dependence of the real part of the material's dielectric constant (the denominator) leads to an increase in sensitivity. The dielectric response of the nanoparticles is engineered by alloying a plasmonic material with a weakly dispersive one to yield a negative, but flatterε_r. This dramatically increases the sensitivity of any plasmonic sensor (of any shape).

In conjunction with the sensitivity it is also of interest to consider the accuracy with which a spectral feature can be resolved. For a spectral peak, the standard measure is its full width at half maximum (FWHM). Engineering the real part of the particle's dielectric function [251] in equation 4:2 through alloying, is generally accompanied by a concomitant increase in the plasmon damping and broadening of the extinction spectrum,[252] and thus suggests that the FOM (= S_n/FWHM) is also lowered. This can be addressed by noting that traditional plasmon based sensors are generally polarisation independent, because the particles themselves are highly symmetrical (see figure 1:7). Circular dichroism (CD) offers an alternative to extinction based sensing techniques,[15, 40] and CD spectra are typically more feature rich than extinction spectra,[46, 102] which increases the number of spectral signatures that can be tracked when the local environment changes, figure 4:1. Crucially, CD spectra are also bipolar, and the crossing-points where the signal changes sign are ideal features to track, because of the simplicity of identifying the null point. Earlier work on CD-based sensing made use of magneto-optical modulation of an achiral nanoantenna LSPR to induce ellipticity in the transmitted beam.[110] In this case the choice of material was dictated by the requirement to induce a magneto-optical response. However, performing CD-based measurements on chiral particles, that exhibit a natural circular dichroism, offers the possibility of tuning the material properties independently of the chirality (shape), and this approach is exploited to maximise the LSPR sensitivity (and FOM).

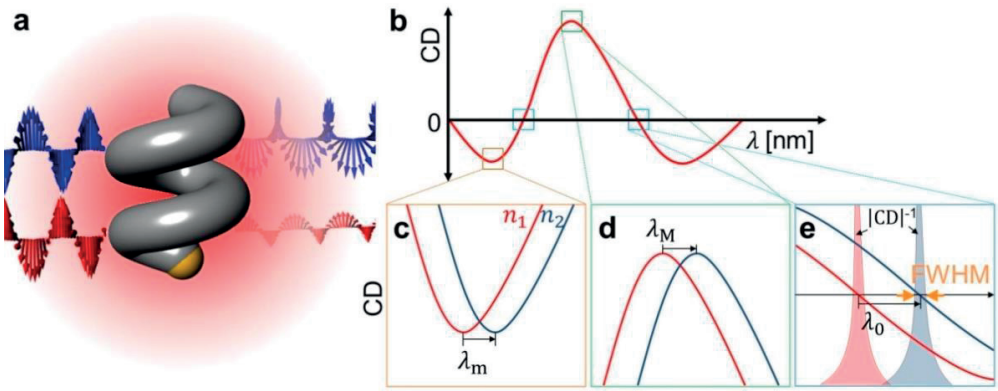

Figure 4:1 Schematic view of polarization dependent chiral plasmonic sensing. (a) The interaction of a left-handed nanohelix with circularly polarised light and (b) its corresponding CD spectrum as a function of λ. Three bottom panels indicate the resonance shifts at (c) λ_m, (c) λ_M, and (d) λ_0 where the refractive indices of the surrounding media are varied between n_1 and n_2. Reprinted from Ref. 93 (Copyright 2016 Nature Publishing Group)

The exact optical responses for such complex nanoparticles are only calculable using numerical methods.[56] However, the chiral form of nanoparticle plasmonic extinction is introduced that captures the key features of extinction in response to left (-) and right (+) circularly polarised light,[89, 91]

$$E_{\mathrm{L}/\mathrm{R}} \propto \frac{1}{\lambda}\left(\frac{\varepsilon_i}{(\varepsilon_r + (\bar{\chi} \pm \delta\chi)n^2)^2 + \varepsilon_i^2}\right). \tag{4:3}$$

The shape factor now includes an achiral term $\bar{\chi}$ plus a chiral term $\delta\chi_{\mathrm{R}} = -\delta\chi_{\mathrm{L}}$ specific to right (R) or left (L) handed enantiomers. The circular dichroism (CD) is the difference between the extinction for ± polarisations, $\mathrm{CD} = E_{\mathrm{L}} - E_{\mathrm{R}}$. The CD signal is bipolar, and the wavelength at which the extinctions are equal yields a zero-crossing in the spectrum, which serves as a natural point for tracking. Within this formulation the crossover wavelength coincides with the achiral resonance-condition $\varepsilon_r^* = -\bar{\chi}n^2$, in the limit of small, slowly-varying ε_i. So the sensitivity of nanohelix sensors follows that of achiral ones. Plotting the reciprocal of the absolute value of the CD (e.g. figure 4:2e) gives an intrinsically sharp representation of the crossover point, one whose FWHM is defined by the instrumental resolution σ [110] and $\left.\frac{\mathrm{dCD}}{\mathrm{d}\lambda}\right|_{\lambda^*}$, the slope of the CD spectrum at the crossing. This yields a FWHM (see Appendix A.3.1 Chiral plasmonic sensitivity, FWHM, and FOM for details), based on equation 4:3, of

$$\mathrm{FWHM} = \frac{4\sigma\varepsilon_i^2}{|\delta\chi|n^2\left|\frac{\mathrm{d}\varepsilon_r}{\mathrm{d}\lambda}\right|_{\lambda^*}}, \tag{4:4}$$

and a FOM of

$$\mathrm{FOM} = \frac{S_n}{\mathrm{FWHM}} = \frac{2\bar{\chi}|\delta\chi|n^3}{\varepsilon_i^2\sigma}. \tag{4:5}$$

Thus, higher figures of merit can be achieved by increasing the magnitude of the chiral shape factor $\delta\chi$.

4.1.3 Dielectric constants of Ag-Ti alloys

As a proof-of-concept experiment for the control of the dielectric constant over the whole wavelength range, 150 nm thick Ag-Ti bulk thin films have been grown on a 2 inch silicon wafer with different atomic ratios (Ti, $Ag_{0.26}Ti_{0.74}$, $Ag_{0.55}Ti_{0.45}$, $Ag_{0.82}Ti_{0.18}$, and Ag), where Ag_aTi_b is the material atomic ratios of Ag and Ti with a% and b% respectively, and analysed their dielectric constants by the ellipsometry in the wavelength range of 300 nm to 1100 nm. Each material composition was analysed by the inductively coupled plasma optical emission spectroscopy (ICP-OES), table 4:1, and their results were well-matched to the targeted conditions.

Sample	Atomic ratio of Ag : Ti [%]
Ti	0 : 100 (±0)
$Ag_{0.26}Ti_{0.74}$	25.7 :74.3 (±0.3)
$Ag_{0.55}Ti_{0.45}$	54.6 : 45.4 (±0.7)
$Ag_{0.82}Ti_{0.18}$	82.3 : 17.7 (±0)
Ag	100 : 0 (±0)

Table 4:1 ICP-OES measurements of the grown Ag-Ti thin films.

For the calculation of the dielectric constants of such alloys, the effective medium approximation, assuming both the host and inclusion dielectric responses are already known, was required and the Bruggeman model was used, which is employed as,[253]

$$n_{\mathrm{Ag}}\left(\frac{\varepsilon_{\mathrm{Ag}} - \varepsilon}{\varepsilon_{\mathrm{Ag}} + 2\varepsilon}\right) + n_{Ti}\left(\frac{\varepsilon_{\mathrm{Ti}} - \varepsilon}{\varepsilon_{\mathrm{Ti}} + 2\varepsilon}\right) = 0, \tag{4:6}$$

where n_{Ag} and n_{Ti} are the volume fractions of Ag and Ti, $\varepsilon_{\mathrm{Ag}}$ and $\varepsilon_{\mathrm{Ti}}$ are dielectric constants of Ag and Ti, and ε is effective dielectric constant of Ag-Ti alloy. Figure 4:2 shows the dielectric constants of the grown

Ag-Ti thin films having different atomic ratios and this clearly presents that the dielectric constants of materials can experimentally be tuned by mixing two (or more) materials as expected theoretically.

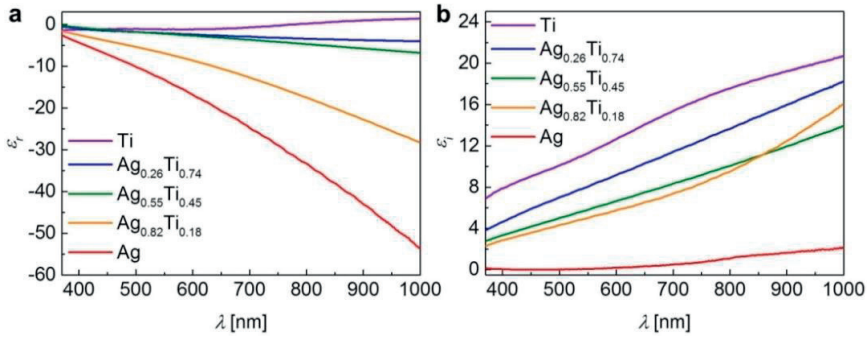

Figure 4:2 The experimental dielectric constants of 150 nm thick Ag-Ti alloyed thin films with different Ti contributions. (a) ε_r and (b) ε_i (Ag: red, $Ag_{0.82}Ti_{0.18}$: orange, $Ag_{0.55}Ti_{0.45}$: green, $Ag_{0.26}Ti_{0.74}$: blue, and Ti: violet). Reprinted from Ref. 93 (Copyright 2016 Nature Publishing Group)

4.1.4 Fabrication of shape and material engineered Ag-Ti nanohelices

A series of Ag-Ti nanohelices was fabricated using the nanoGLAD that allows precise control of the particles' alloy composition and shape $\delta\chi$.[56, 64] The former can be used to engineer the material dielectric function to maximise sensitivity, while the latter is used to adjust the achiral and chiral shape factors to affect sensitivity and introduce a chiroptical response. Table 4:2 presents all the information of the grown Ag-Ti nanohelices both that were programmed in the growth system and that were measured experimentally. Here, firstly the sizes of the nanohelices have been controlled with fixed material ratios of Ag:Ti = 97%:3%. Next, at the given length L_1, material composition ratios have been tuned by controlling each material growth rate with closed-loop feedback to uniformly form the material composition through the whole nanostructure. The material composition was analysed by the ICP-OES and the measured values were considerably close to the desired values. Figure 4:3 shows the SEM images of the grown Ag-Ti nanohelices.

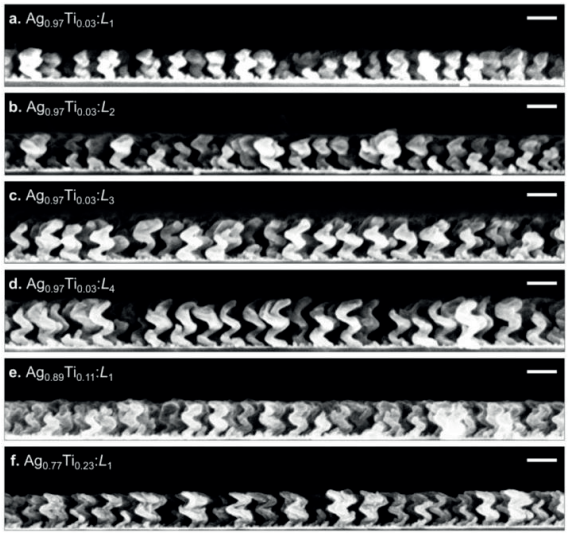

Figure 4:3 The side view of SEM images of the grown Ag-Ti nanohelices. (a) $Ag_{0.97}Ti_{0.03}$:L_1, (b) $Ag_{0.97}Ti_{0.03}$:L_2, (c) $Ag_{0.97}Ti_{0.03}$:L_3, (d) $Ag_{0.97}Ti_{0.03}$:L_4, (e) $Ag_{0.89}Ti_{0.11}$:L_1, and (f) $Ag_{0.77}Ti_{0.23}$:L_1. Reprinted from Ref. 93 (Copyright 2016 Nature Publishing Group)

Sample	Atomic ratio of Ag : Ti (%)		Height (nm)	
	QCM	ICP-OES	QCM	SEM
$Ag_{0.97}Ti_{0.03}$:L_1	95 : 5	96.7 : 3.3 (±0.7)	600	113
$Ag_{0.97}Ti_{0.03}$:L_2	95 : 5	97.2 : 2.8 (±0.4)	700	128
$Ag_{0.97}Ti_{0.03}$:L_3	95 : 5	97.1 : 2.9 (±0.4)	800	141
$Ag_{0.97}Ti_{0.03}$:L_4	95 : 5	95.8 : 4.2 (±1.7)	900	157
$Ag_{0.89}Ti_{0.11}$:L_1	85 : 15	89.5 : 10.5 (±0.6)	600	119
$Ag_{0.77}Ti_{0.23}$:L_1	75 : 25	77.3 : 22.7 (±0.6)	600	124

Table 4:2 Structural parameters of the grown Ag-Ti nanohelices.

4.1.5 Colloidal stability

Considering the colloidal stability of the plasmonic nanoparticles is crucial as 'hotspot effect' from the closely neighbouring particles leads changing the absorption signals of the nanocolloids.[88] Hence, to prevent such disturbances on a linear function of the plasmonic resonance shift caused by the line-width broadening and peak drift, the stability as well as the real n of the colloidal solutions of the Ag-Ti nanohelices have been analysed by using dynamic light scattering (DLS),[186] during the CD measurement of specimen at the same time. Figure 4:4 shows the corresponding measured relaxation times of the colloids in 5 different refractive index media under the given material (Ag-refractive index: 0.135 and extinction: 3.990) and environmental fitting parameter.[254] Such the overlapping responses over the 5 different dielectric media indicate that not only the prepared glycerol-water mixtures are well matched to the theoretical environmental conditions (e.g. viscosity, refractive index, etc.), but also the nanohelices have no significant aggregation in all the conditions.

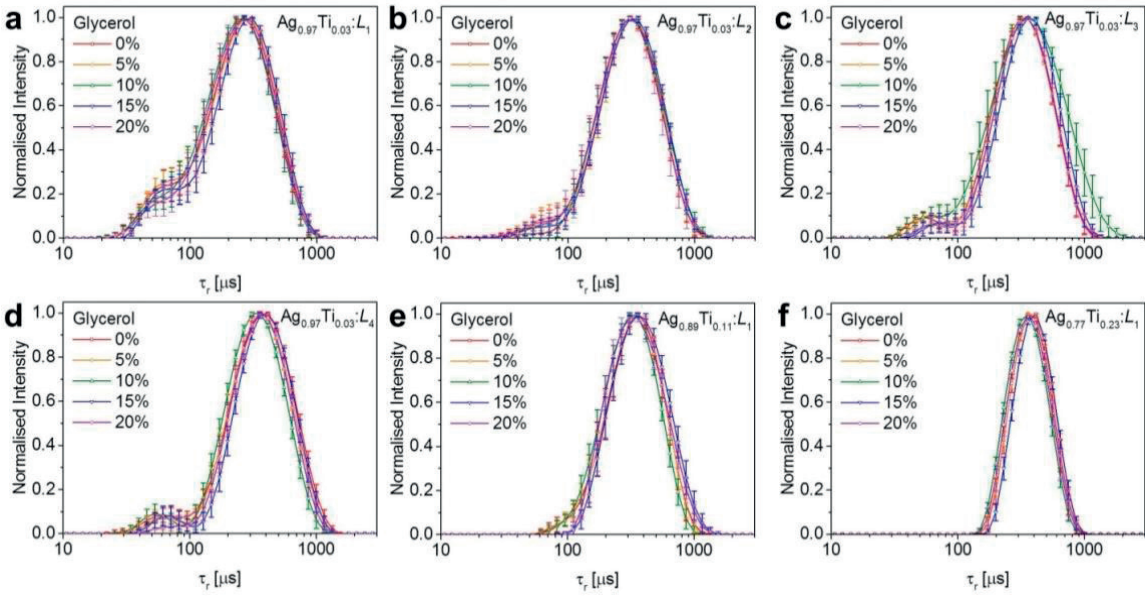

Figure 4:4 Relaxation times of the colloidal Ag-Ti nanohelices in media of five different refractive indices measured by the DLS. (red: 0%, orange: 5%, green: 10%, blue: 15%, and violet: 20% glycerol-water mixtures). (a) $Ag_{0.97}Ti_{0.03}$:L_1, (b) $Ag_{0.97}Ti_{0.03}$:L_2, (c) $Ag_{0.97}Ti_{0.03}$:L_3, (d) $Ag_{0.97}Ti_{0.03}$:L_4, (e) $Ag_{0.89}Ti_{0.11}$:L_1, and (f) $Ag_{0.77}Ti_{0.23}$:L_1. Reprinted from Ref. 93 (Copyright 2016 Nature Publishing Group)

4.1.6 Bulk refractive index sensing

A typical particle, a two-turn left-handed 128 nm tall helix composed of 97% Ag and 3% Ti, is shown in figure 4:5a. The small amount of Ti alloying agent improves the helix fidelity over pure Ag.[255] For the refractive index sensing the suspensions of those $Ag_{0.97}Ti_{0.03}$:L_2 nanohelices have been suspended in glycerol-water mixtures varying from 0 to 20% concentration (refractive indices between 1.333 and 1.357 [254]). Figure 4:5b shows their corresponding CD spectra as a function of λ. As expected, the CD spectra exhibit multiple features, shown in figures 4:5c-f: a maximum λ_{M}, a minimum λ_{m}, and two crossing points λ_{01} and λ_{02}, all of which can be tracked in response to changes in the refractive index of the medium. The wavelength shifts, relative to the pure water reference, are shown in figure 4:2g, and indicate sensitivities S_n of 275, 320, 379, and 571 nm·RIU^{-1} for λ_{m}, λ_{01}, λ_{M}, and λ_{02}, respectively.

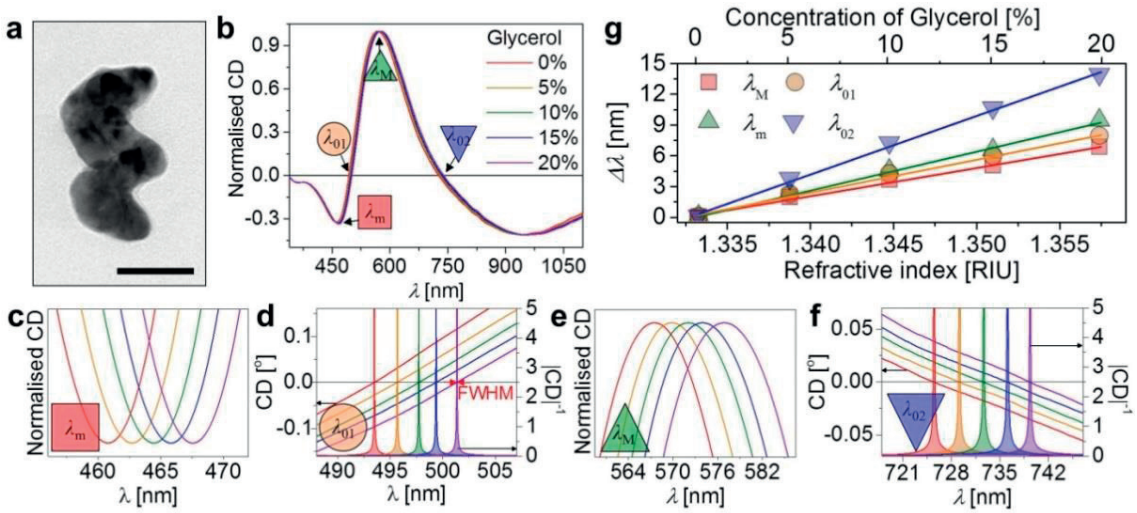

Figure 4:5 Bulk refractive index sensing. (a) TEM image of a single $Ag_{0.97}Ti_{0.03}$:L_2 nanohelix (Scale bar: 50 nm). (b) CD spectra of colloidal $Ag_{0.97}Ti_{0.03}$:L_2 nanohelices in media of five different refractive indices (red: 0%, orange: 5%, green: 10%, blue: 15%, and violet: 20% glycerol-water mixtures) over the full spectral range and detailed plots of the resonance shifts at (c) λ_{m} (red square), (d) λ_{01} (orange circle), (e) λ_{M} (green top triangle), and (f) λ_{02} (blue bottom triangle). For (d) and (f) the filled curves represent $|\mathrm{CD}|^{-1}$. (g) Wavelength shift, relative to water, of the four spectral features as functions of the glycerol-water concentration (top *x*-axis) and its corresponding n (bottom *x*-axis). Reprinted from Ref. 93 (Copyright 2016 Nature Publishing Group)

These results demonstrate that features, like λ_{M}, and λ_{02}, found at longer wavelengths exhibit greater sensitivity, consistent with equation 4:2. Since larger values of the achiral shape factor increase the wavelength of the resonance condition, it is possible to increase the sensitivity by growing particles that are more elongated (see figure 4:6a). This has been the approach most often pursued in the search for higher sensitivities from extinction based LSPR sensors.[89, 91, 95, 118] Here the same principle is applied to a chiral sensor, by growing a series of nanohelices with a range of heights, labelled L_1 (113 nm) through L_4 (157 nm). The results, shown in figure 4:3c, confirm that the peak and crossing features of longer structures are red-shifted relative to the smaller ones and that the sensitivity of each feature is directly proportional to its wavelength (figure 4:6d, red points). However, equation 4:2 also suggests that the sensitivity can be improved by reducing the wavelength dependence of ε_r, the real part of the material dielectric function. This is done by exercising control over the structures' Ag-Ti stoichiometry during their growth. Figure 4:6b shows the effective ε_r of Ag-Ti alloys of varying compositions (see also figure 4:2). As the alloy becomes more Ti-rich, the wavelength shift $\Delta\lambda$ increases for a given change in the medium's refractive index, due to

a progressive flattening of the material's dielectric function. The effect of dispersion engineering in practice is illustrated in figure 4:6c for nanohelices having fixed size, but composed of alloys containing 3%, 11% and 23% Ti. Higher Ti composition red-shifts the features, and as shown in figure 4:6d, and increases the sensitivity. Indeed, the sensitivity trends show a systematic enhancement for the 11% (green) and 23% (blue) alloy relative to the minimal Ti samples (red) (see Appendix figures A:16-21 for detailed plots).

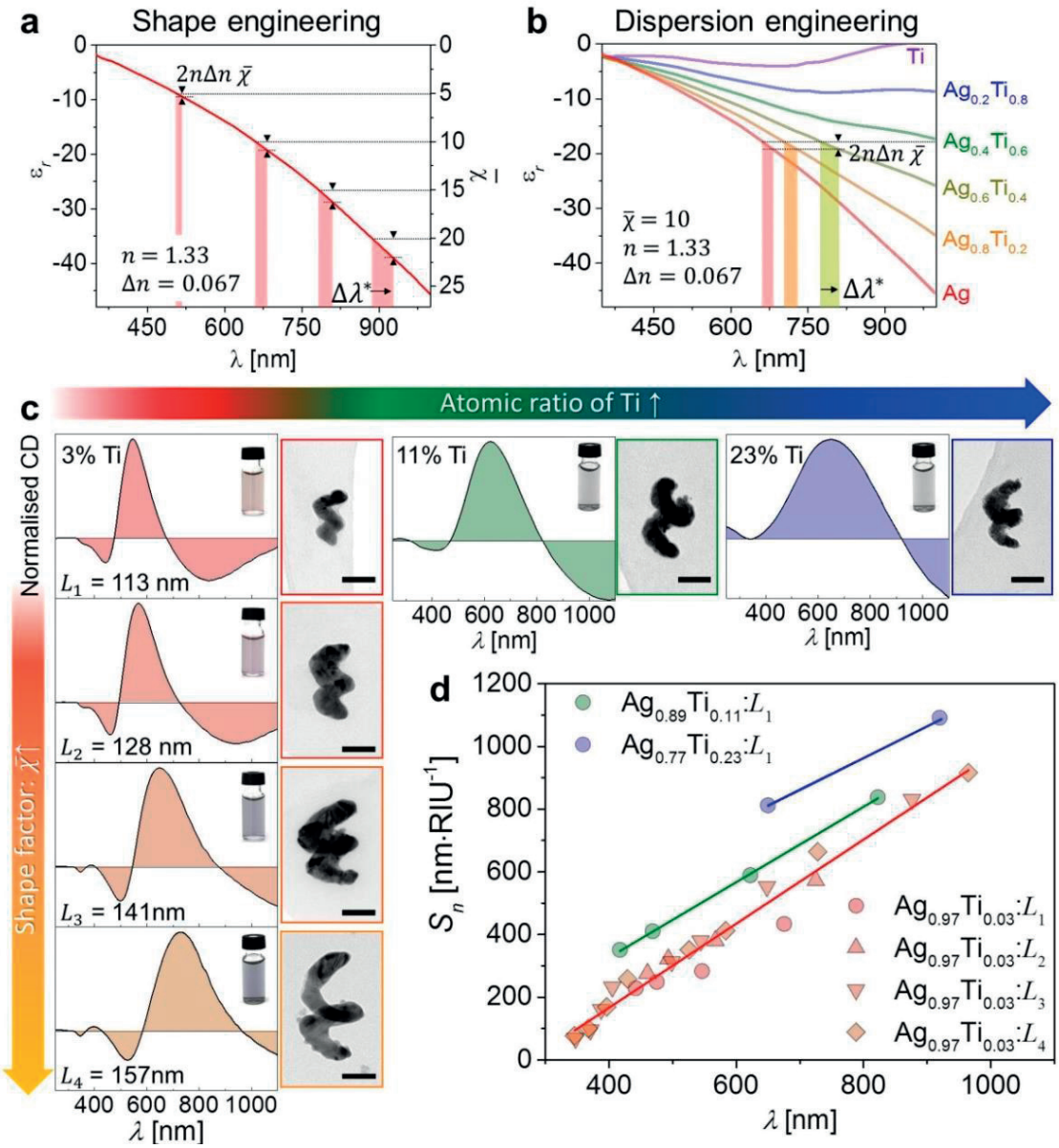

Figure 4:6 Shape and dispersion engineering of Ag-Ti nanohelices. (a) The effect of the achiral shape factor $\bar{\chi}$ on the wavelength shift $\Delta\lambda$ observed for a given change in refractive index Δn (= 0.067). (b) The effect of ε_r on the wavelength shift based on calculated dielectric constant of Ag-Ti alloys with varying Ti composition. As the proportion of Ti increases the real part of the dielectric function becomes flatter, and the resulting wavelength shift increases. (c) CD spectra (panel left), TEM images (panel right), and colloidal solutions (each inset) of the grown Ag-Ti nanohelices. The achiral shape factor $\bar{\chi}$ increases moving down the rows, and the atomic ratio of Ti increases moving to the right. (d) The measured S_n of the Ag-Ti nanohelices as a function of λ at 1.333 RIU (the symbols and colours are different for the $\bar{\chi}$ and the atomic ratio of Ti respectively). Reprinted from Ref. 93 (Copyright 2016 Nature Publishing Group)

In order to define the FWHMs of those particles a simple linear fit of the form CD $= m(\lambda - \lambda_0)$ is used to fit the bipolar CD signal near the zero crossing point λ_0. The standard error of the fit parameter, $\delta\lambda_0$ is indicative of the precision with which the crossing point can be localised[110]. Figure 4:7a shows an example of the data analysis with the CD spectrum of colloidal $Ag_{0.97}Ti_{0.03}$:L_1 nanohelices in water. In this case the resolution $\delta\lambda_0$ was 0.005 nm. Figure 4:7b shows $\delta\lambda_0$ as a function of n taken from the CD spectra of all the Ag-Ti nanohelices.

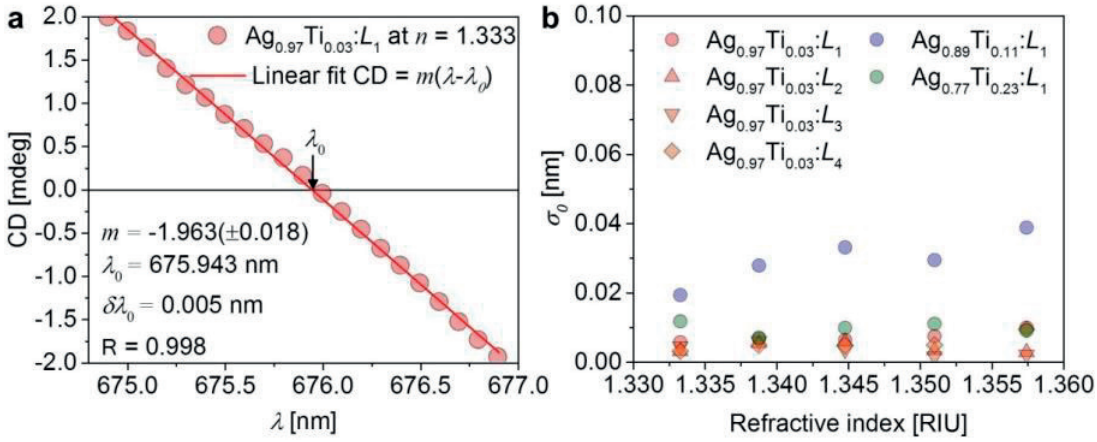

Figure 4:7 Spectroscopic resolution at zero-crossing. (a) A CD spectrum of colloidal $Ag_{0.97}Ti_{0.03}$:L_1 nanohelices in water and its corresponding linear fit. (b) $\delta\lambda_0$ at λ_0 of $Ag_{0.97}Ti_{0.03}$:L_1 (red circle), $Ag_{0.97}Ti_{0.03}$:L_2 (red top-triangle), $Ag_{0.97}Ti_{0.03}$:L_3 (red bottom-triangle), $Ag_{0.97}Ti_{0.03}$:L_4 (red diamond), $Ag_{0.89}Ti_{0.11}$:L_1 (blue circle), and $Ag_{0.77}Ti_{0.23}$:L_1 (green circle) as a function of n. Reprinted from Ref. 93 (Copyright 2016 Nature Publishing Group)

The results all together are summarised in figure 4:8. The left column in the plots shows the effect of increased nanohelix length on the crossing point wavelength, sensitivity, FWHM and FOM. The null wavelength and sensitivity both increase as the nanohelices lengthen. However, the FWHM remains unchanged, so that the FOM increases dramatically. The L_4 helix exhibits a FOM = 2859 RIU^{-1}, which is larger than what has been previously reported for LSPR based sensors [248, 249, 256] including those based on a magnetochiral response.[110] Relative to the latter, the improvement comes from a combination of improved sensitivity (~4×) and decreased FWHM (~5×) thanks to a steeper crossing of the CD signal at the null point. The right hand column of figure 4:8 illustrates the effect of engineering the dispersion function through the addition of Ti. In this case the increase in sensitivity that comes from flattening the material dispersion function also leads to an increase in the FWHM due to the ε_i contribution in equation 4:4. The net effect is a decrease in the FOM relative to the low alloy sample. Nevertheless, the flatter dispersion curve does have the effect of increasing the sensitivity beyond what is achievable in the pure metal or the low alloy sample. A sensitivity greater than 1000 nm·RIU^{-1} was achieved at a wavelength of 921 nm. For applications where sensitivity is the primary concern, dispersion engineering provides a powerful technique for reaching the highest possible refractive index sensitivities.

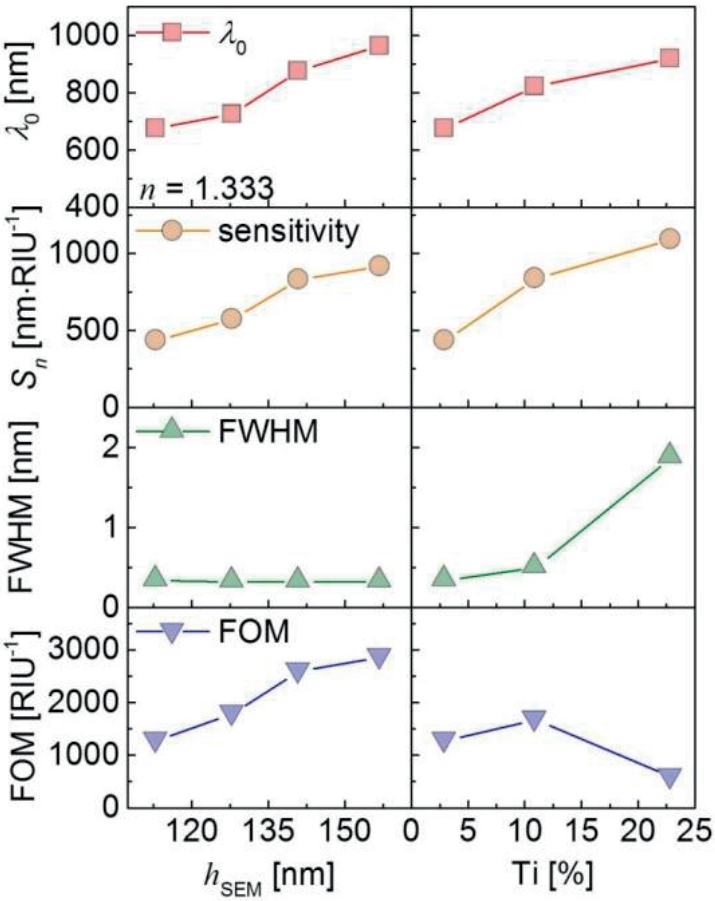

Figure 4:8 Summary of shape and dispersion engineering of nanohelices. Left panels show the effect of increasing nanohelix length and the right panels show the effect of increasing Ti composition (red square: zero-crossing wavelengths at n = 1.333, orange circle: refractive index sensitivities, green top triangles: FWHMs, and blue bottom triangles: FOMs). Reprinted from Ref. 93 (Copyright 2016 Nature Publishing Group)

4.1.7 Strong optical contrast in the presence of absorbers

One appealing characteristic of circular dichroism is that it is insensitive to achiral absorbers or scatterers.[257] So unlike traditional extinction measurements, high signal-to-noise CD measurements of a chiral analyte are possible even in the presence of strong achiral absorbers. Figure 4:9 illustrates such a measurement, where the spectra of colloidal $Ag_{0.97}Ti_{0.03}$:L_3 nanohelices were detected with the addition of absorbers in the form of blue and yellow filters in the optical path. In both cases the maximum absorbance exceeds an optical density of 2 (< 0.1% transmission, right panels of figure 4:9a). This introduces small distortions into the CD signal, however as it has been already seen, CD offers several spectral features for sensing, the majority of which are here unperturbed. Notably, since CD based sensing offers a clearly distinguishable signal, even in the presence of absorbance that would be strong enough to obscure optical extinction based sensing methodologies, figure 4:9b. The same experiment demonstrated with molecular absorbers rhodamine (left panel) and indigo (right panel) yield similar results, figure 4:9c.

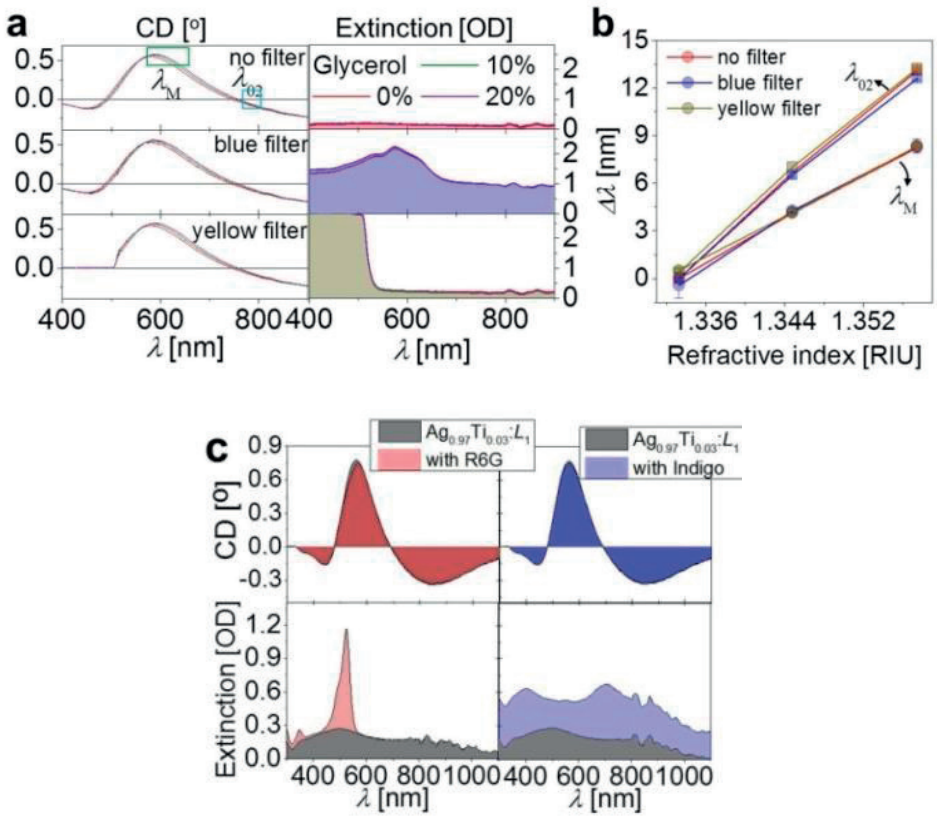

Figure 4:9 Optical contrasts of chiral plasmonic nanoparticles in the presence of achiral absorbers. CD spectra (left panels) and extinction spectra (right panels) of the colloidal $Ag_{0.97}Ti_{0.03}$:L_3 nanohelices in the presence of complex absorbing environments (top: no filter, middle: blue filter, bottom: yellow filter), (b) their corresponding wavelength shifts, relative to water, of the two spectral features (λ_M and λ_{02}) as functions of the n (error bar: standard deviation). (c) CD spectra (each upper panel) and extinction spectra (each lower panel) of the colloidal $Ag_{0.97}Ti_{0.03}$:L_1 nanohelices in the presence of molecular dyes (left panel: 10 μM rhodamine 6G, right panel: 100 μM indigo). Reprinted from Ref. 93 (Copyright 2016 Nature Publishing Group)

4.1.8 Surface sensitive sensing

Since the evanescent field of the excited plasmon decays rapidly into the medium, LSPR sensors are ideally suited to making surface sensitive measurements.[258] The plasmonic Ag-Ti nanohelices are used to sense the biotin-avidin binding events. Biotin-avidin affinity is a well-known common binding protocol and this is often used as a proof-of-concept experiment for plasmonic biosensors.[256] First, the surfaces of the nanohelices ($Ag_{0.97}Ti_{0.03}$:L_1 and $Ag_{0.89}Ti_{0.11}$:L_1) are functionalised with biotin (see Methods for details) which acts as a complementary and specific binding factor for avidin in solution (figure 4:10a). The wavelength of the λ_{02} crossing in the CD spectrum (figure 4:10b, lower), and the change in the CD amplitude at the initial crossing wavelength (figure 4:10b, upper) were measured at 1 min intervals. Prior to the addition of avidin both signals are stable, but they experience a prompt shift upon the addition of 1 μg·mL^{-1} avidin. For the $Ag_{0.97}Ti_{0.03}$:L_1 nanohelices the crossing point $\Delta\lambda_{02}$ redshifts by approximately 3 nm (blue), and the CD intensity at the initial crossing wavelength increases by 6 mdeg (green). The rise time is approximately 5 min. The $Ag_{0.89}Ti_{0.11}$:L_1 nanohelices show an even stronger response with shifts of 5 nm (red) and 10 mdeg (yellow) respectively, thanks to the increased sensitivity that comes from the reduced dispersion (figure 4:10c).

Control experiments (grey) where the nanohelices lack biotin functionalization show no distinct shift upon the addition of avidin confirming that the signal is truly surface sensitive and arises from specific binding. The two measurement modes suggest alternative sensing schemes for real time monitoring of binding events: one based on tracking the crossing point wavelength (figure 4:10b, blue and red), and another based on identifying the change in CD intensity at fixed wavelength (figure 4:10b, green and yellow). Both offer a highly sensitive and rapid measurement of the specific binding at surfaces. Figures 4:10 d–e show the sensing task in different avidin concentrations and, as expected, this shows the differential shifts as a function of the introduced avidin concentrations. Moreover, this binding was clearly monitored even under the complex absorbing medium, 10 µM R6G, Figure 4:10f.

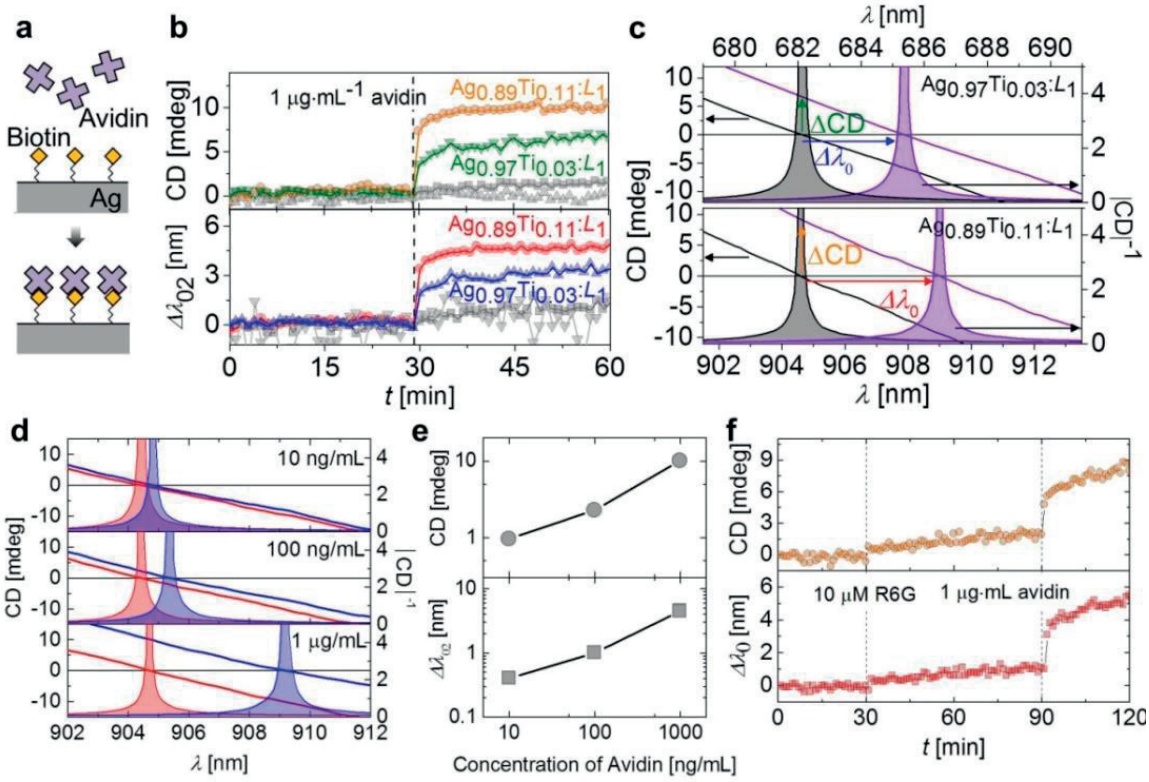

Figure 4:10 Sensing of specific binding events. (a) Schematic view of biotin-avidin interaction on the surface of a Ag-Ti nanohelix. (b) *In situ* measurements of the biotin-avidin interaction by monitoring the change of CD at the initial λ_{02} (upper plot) and the wavelength shift of $\Delta\lambda_{02}$ (lower plot) with 1 min intervals. The coloured plots indicate the response of specific binding of biotin-avidin ($Ag_{0.97}Ti_{0.03}$:L_1 blue, green; $Ag_{0.89}Ti_{0.11}$:L_1 red, yellow) and the grey plots indicate non-specific binding of avidin with Ag-Ti nanohelices (without biotin) in the control group. (c) Close-up view of the CD spectra for the two biotinylated nanoparticle systems showing the wavelength shift and CD amplitude increase after avidin introduction. (d) The resonance shift at λ_{02} of the colloidal $Ag_{0.89}Ti_{0.11}$:L_1 nanohelices for the different concentrations of avidin (10 ng·mL^{-1} to 1 µg·mL^{-1} with 1 order intervals, top to bottom). Each red signal and blue signal indicates the λ_{02} before and after avidin binding, respectively. (e) Change of CD at the initial λ_{02} (upper plot) and the wavelength shift $\Delta\lambda_{02}$ (lower plot) as a function of the injected concentrations of avidin. (f) *In-situ* measurements of the biotin-avidin interaction in the presence of complex absorbing medium (here, 10 µM R6G) by monitoring the change of CD at the initial λ_{02} (upper plot) and the wavelength shift $\Delta\lambda_{02}$ (lower plot) with 1 min intervals. Reprinted from Ref. 93 (Copyright 2016 Nature Publishing Group)

4.2 Ultraviolet plasmonics and chiral sensing

4.2.1 Introduction

Nanoparticles whose size is smaller than the wavelength of light can give rise to a light-induced collective electron oscillations, known as local surface plasmon resonance (LSPR).[67, 68] The resonance wavelength in LSPR is sensitive to the environment, which is the basis for a number of sensing applications.[68] Improvements in sensitivity have been achieved by engineering the particles' size, shape, and material composition,[95, 118] and the mode of detection.[93, 110] Work to date has primarily focussed on increasing the shift of the resonance for a given change in refractive index. However, in many applications the quantity of ultimate interest is not the medium's refractive index, but the concentration of some chemical species.[73, 107] One particularly promising route to improve the concentration sensitivity is to exploit the natural refractive index dispersion of the molecule (analyte) of interest. Most molecules show notably higher and more dispersive refractive indices at short wavelengths, because of electronic resonances (transitions) in the UV. Changes in the concentration of the analyte therefore yield larger changes in the refractive index at shorter wavelengths, and therefore larger shifts in the plasmon resonance. However, this also requires a plasmonic probe that shows a UV resonance.

Here, the first magnesium (Mg) nanoparticles are introduced for UV plasmonics and LSPR sensing. The Mg nanoparticles are grown with a helical shape. Their exceptionally strong chiroptical response in the near UV gives rise to a concomitant enhancement of the LSPR sensitivity.

4.2.2 Theoretical concept

In the former chapter,[93] a chiral plasmonic sensing approach is introduced that is based on a chiral nanoprobe (i.e. measures the differential extinction between left-handed (LH) and right-handed (RH) circularly polarised light with CD spectroscopy, i.e. CD $\propto E_L - E_R$. The change in response to the change of refractive index of the medium surrounding the nanoparticles is tracked, as schematically shown in figure 4:1. CD-based sensing with chiral nanoparticles offers two distinct advantages over traditional polarisation independent measurements: firstly, the CD signal of a chiral absorber naturally comprises multiple spectral features compared to an extinction peak, and each feature can be tracked. This provides high sensing flexibility and fidelity. In particular, the zero crossings (CD = 0^{o}) where the LH and RH extinctions are equal are ideal for tracking, because they are intrinsically narrow and possess high figures of merit.[93] Secondly, the chiral particles provide a strong optical contrast, even in the presence of optically dense fluids, as any achiral background signals are cancelled. Hence, chiral nanoparticles can even be "seen" in strongly absorbing physiological fluids (e.g. blood).[136]

The chiral LSPR sensor operates by tracking the shift in the zero crossing of the CD signal in response to changes in n, the refractive index of the local medium, which surrounds the particles. The resonance condition is $\varepsilon_r(\lambda^*) = -\overline{\chi}n^2$ (equation 4:1), where λ^* is the resonance wavelength at zero crossing, ε_r is the real part of the dielectric function of the plasmonic nanoparticle, and $\overline{\chi}$ is a shape-dependent factor).[93] For sensing tasks undertaken in the visible to NIR regime typical of conventional plasmonics equation 4:1 is reasonable (e.g. figure 4:11b).[73, 91] However, for measurements in the UV the dispersion of the medium (solvent and analyte) $n(\lambda)$ needs to be considered, such that $\varepsilon_r(\lambda^*) = -\overline{\chi}[n(\lambda^*)]^2$. In LSPR sensing it is customary to define a refractive index sensitivity, which describes the change in the resonance position (wavelength) as a function of refractive index (see equation 4:2).[93] However, another important factor in

assessing sensitivity is to determine by how much the tracking wavelength λ^* changes in response to the volume concentration c of the species of interest

$$\frac{d\lambda^*}{dc} = \frac{d\lambda^*}{dn}\frac{dn}{dc} = S_n\frac{dn}{dc}. \tag{4:7}$$

The refractive index of a mixture of a solute in a solvent with indices n_1 and n_2 can be approximated, using the rule of Arago and Biot, as[259]

$$n = n_2 c + n_1 \cdot (1 - c), \tag{4:8}$$

So

$$\frac{dn}{dc} = n_2 - n_1., \tag{4:9}$$

Consider dimethyl sulfoxide (DMSO) in water (figure 4:11).[260, 261] Within the visible region the refractive index of DMSO is everywhere higher than that of water, so the sign of equation 4:9 is always positive. But $\mathrm{d}n \cdot \mathrm{d}c^{-1}$ at λ = 600 nm is only 0.144 RIU, whereas at λ = 250 nm it is 0.229 RIU, almost 60% higher. Thus, enhanced sensitivity to changes in solute concentration (equation 4:7) can be achieved at shorter wavelengths, and in particular through measurements in the UV.

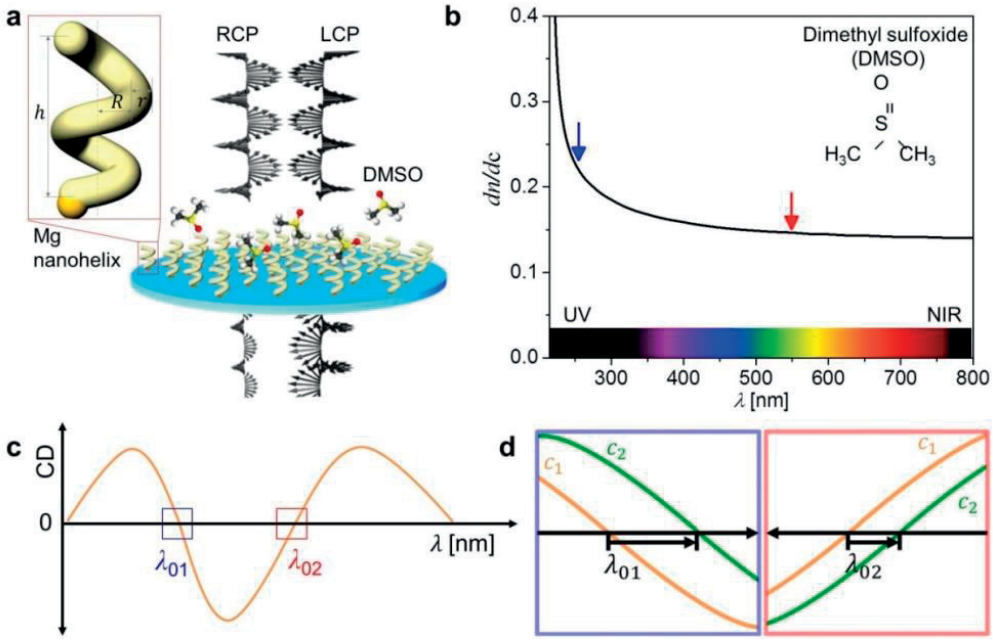

Figure 4:11 Sensing using UV chiral plasmonics. (a) Schematic that illustrates the interaction of left-handed (LH) nanohelices with left- and right-handed circularly polarised light (LCP, RCP) in the presence of dimethyl sulfoxide (DMSO). Inset shows the schematic view of 2-turn left-handed Mg nanohelix showing dimensions of the seed particle and the nanostructure that grows upon it (h: height, R: major radius, r: minor radius). (b) Change in the refractive index of DMSO solution in response to a change in its concentration ($\mathrm{d}n \cdot \mathrm{d}c^{-1}$) as a function of λ,[260, 261] which is larger in the UV (blue arrow) compared to the visible (red arrow). (c) A CD spectrum of LH nanohelices as a function of λ. Two boxes indicate zero crossing points, λ_{01} (blue: in UV) and λ_{02} (red: in visible). (d) Each panel indicates the resonance shifts at λ_{01} (left panel) and λ_{02} (right panel) where the concentrations of the molecules are varied between c_1 and c_1 ($c_1 < c_2$). Reprinted from Ref. 109 (Copyright 2016 Royal Society of Chemistry)

4.2.3 Ultraviolet plasmonics

Aluminium (Al) nanoparticles have thus far been favoured for UV plasmonics applications,[94, 239] even though theory predicts that Mg provides substantially higher far-field absorption efficiency and higher near-field electric field enhancements.[262] Further, Mg is abundant, biocompatible, and lightweight (two-thirds lighter than Al).[263] However, there is no report of Mg nanoparticles for UV plasmonics.[264] Here it is shown how large numbers of chiral Mg nanoparticles can be grown using the nanoGLAD, which allows precise controls of size, shape, and material composition of the nanoparticles at the wafer-level.[28, 56, 64] Briefly, an array of gold nanoseeds is first patterned on a 1 cm^2 quartz glass using block-copolymer micelle nanolithography (BCML).[57] Then, in a second step, Mg is evaporated onto the Au nanoseeds at an angle of, $\alpha = 87^o$ and T = ~100K in a vacuum chamber with a base pressure P = $1x10^{-6}$ mbar.[49, 54, 265-268] The substrate is continuously rotated during deposition, which, because of the high angle, leads to the growth of a nanohelix on each Au nanoseed by a self-shadowing effect.[56, 59, 269] Due to the fast diffusion of the Mg adatoms, it was not able to shape nanohelices with pure Mg, so Mg was co-deposited with 8% of titanium (Ti).[240] Doping Ti into the Mg matrix does not significantly change the optical properties, but it improves the structural quality of the nanostructures.[255] Moreover, as the nanoparticle becomes more Ti rich, the LSPR sensitivity is enhanced since Ti flattens the real part of the dielectric function of the composite.[93] The increase in damping also somewhat broadens the lines, but this effect does not diminish the overall improvement.[270] Finally, the nanohelices are coated with a thin layer of HfO_2 by atomic layer deposition (ALD, Savanah 100, Cambridge nanotech).[218] The 4 nm thin oxide layer improves the chemical resistance of the particles.[94] Figure 4:12a shows scanning electron microscope (SEM) images of arrays of two different chiralities of 8% Ti-doped Mg nanohelices (here samples are prepared on Si wafers for imaging). Helices with opposite chiralities are grown on different patterned glass substrates (as well as wafers) and during different depositions, but display very similar structural dimensions. The helices' height, major radius, and minor radius are 142 nm, 26 nm, and 18 nm respectively.

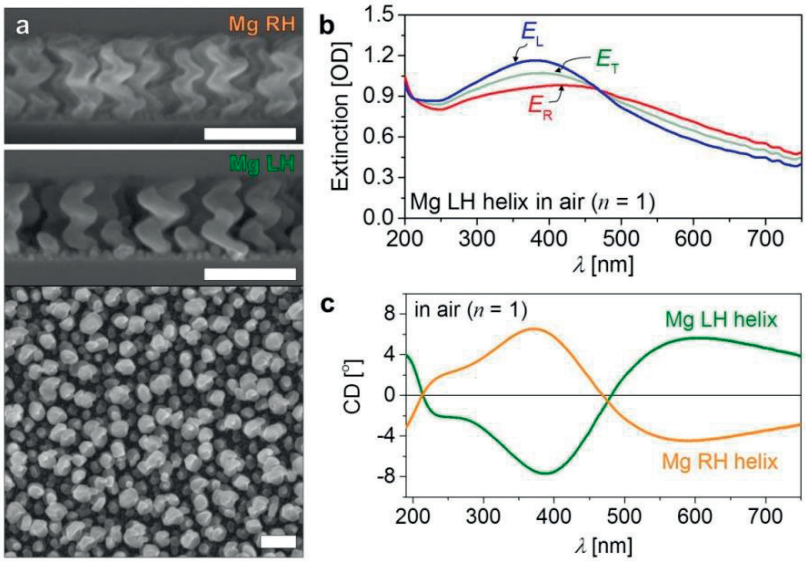

Figure 4:12 Mg nanohelices. (a) SEM images of Mg LH (left-top panel) and RH (left-bottom panel) nanohelices. The right panel shows the top view of the array of the Mg LH nanohelices (Scale bar: 200 nm). (b) Extinction spectra of the Mg LH nanohelices in air in response to the unpolarised light (E_T, green) and the circularly polarised light (LCP: E_L, blue and RCP: E_R, red). (c) CD spectra of the 178 nm thick film containing LH (green) and RH (orange) Mg nanohelices in air. Reprinted from Ref. 109 (Copyright 2016 Royal Society of Chemistry)

Figure 4:12b shows the extinction (upper panel) and CD (lower panel) spectra of Mg LH and RH nanohelices obtained with a Jasco J-810 CD spectrometer. The helices exhibit chiroptical responses that saturate the spectrometer even in its largest amplitude detection range, so the responses were measured with an external lock-in-amplifier (UHFL, Zurich instruments) referenced to the photoelastic modulator (PEM) and synchronised with the monochrometer. In accordance with theoretical predictions,[262] It has been observed that Mg nanohelices possess an extraordinary large short-wavelength extinction (~1 OD at λ = ~385 nm) and optical activity (CD = ~8° at λ = ~380 nm). The spectral features of both chiralites are well matched across the entire spectrum (max, min, and two zero crossings).

4.2.4 LSPR sensing

UV-enhanced LSPR refractive index sensing is demonstrated with a water-DMSO system. In neat DMSO the LH Mg nanohelices' CD spectra (figure 4:13) are shifted relative to the Mg spectra in air (figure 4:12b), because of the relative increase of the refractive index (see figure 4:11b). Figure 4:13 shows CD spectra of the Mg LH nanohelices in DMSO-water mixtures varying from 0 to 30%. DMSO shows strong electronic absorption < 230 nm. The CD resonances are tracked at the two zero crossings λ_{01} and λ_{02}. The crossings' wavelengths shifts in response to increasing the DMSO concentration are shown in figure 4:13c. Both depend linearly on the concentration of DMSO, but crucially, the shift of $\Delta\lambda_{01}$ in the UV is larger than the shift at the longer wavelength $\Delta\lambda_{02}$. This is in agreement with the 1.6 times larger $\mathrm{d}n \cdot \mathrm{d}c^{-1}$ in the UV compared to the visible, which in turn induces a larger plasmonic shift (see figure 4:11b). These results clearly show that UV plasmonics is promising for high sensitivity LSPR due to the medium's dispersion.

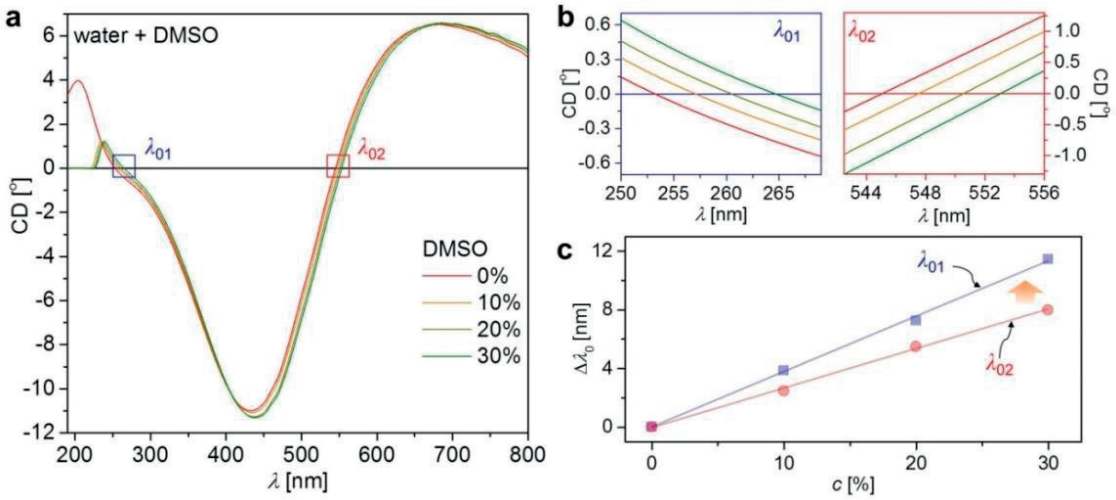

Figure 4:13 Molecular LSPR sensing. (a) CD spectra of Mg LH nanohelices in media with four different refractive indices (red: 0%, orange: 10%, yellow: 20%, and green: 30% DMSO-water mixtures) over the full spectral range and (b) detailed plots of the resonance shifts at λ_{01} (left panel) and λ_{01} (right panel). (c) Wavelength shift, relative to water, of the two spectral features as a function of the DMSO-water concentration. Reprinted from Ref. 109 (Copyright 2016 Royal Society of Chemistry)

4.3 Methods

Nano glancing angle deposition (nanoGLAD): The shadow growth technique [217] was used to grow the 3D nanocolloids in the manner previously reported.[56] Firstly, a hexagonal array of 12 nm Au nanoparticles was prepared by block-copolymer micelle nanolithography[57]. Next, Ag-Ti nanohelices were grown on

the array of the Au nanoparticles in a GLAD system based on co-deposition from dual electron-beam evaporators at T = 90K with a base pressure of 1×10^{-6} mbar. Their alloy stoichiometry was controlled by the deposition rates measured by QCM for each evaporator independently. Particles were grown with lengths (measured by SEM) of L_1=113 nm, L_2=128 nm, L_3=141 nm, L_4=157 nm, and Ti contents of 3%, 11%, and 23%. Finally, the grown Ag-Ti nanohelices were lifted off from the wafer by sonicating a piece of sample wafer (0.5~1 cm^2) in an aqueous solution of 0.15 µM polyvinylpyrrolidone (PVP) for ~2 min to prepare a stock solution. To minimise the effect of possible variations in structure and concentration, samples for each set of tests were always drawn from the same stock solution.

SEM and TEM analysis: The Ag-Ti helices were imaged in SEM (Gemini, Zeiss) and TEM (CM200, Philips) under the accelerating voltages of 10 kV and 200 kV respectively.

Circular dichroism (CD) analysis: Circular dichroism spectra were obtained with a Jasco J-810 circular dichroism spectrometer. All the spectra were measured with 500 $nm\cdot min^{-1}$ scan rate in the wavelength range of 300 to 1100 nm with 0.1 nm intervals. For selected regions of interest smaller 0.025 nm intervals were used.

DLS analysis: 200 µL of colloidal solution of nanohelices was measured using a zeta potential analyser (Zetasizer Nano ZS, Malvern) repeated ~ 10 times for 20 min with 2 min intervals. The material property of Ag-Ti nanohelices was fixed to Ag (RI: 0.135 and extinction: 3.990) and the environmental parameter was matched to literature values for the viscosity, and refractive index of the solution based on the temperature and concentration.[254]

ICP-OES analysis: ~ 1 cm^2 as-grown nanohelices supported on a Si substrate was dissolved into HNO_3:HF etchant and this solution was analysed by the ICP-OES (Ciros CCD, Spectro). The material composition of the nanohelices was evaluated by repeating the analysis three times with samples cleaved from different areas of the growth wafer.

Absorbers: Low pass and narrow band pass filters were separately inserted into the optical patch either before or after the sample cuvette. Similarly, 10 µM rhodamine 6G and 100 µM indigo were added to separate samples after acquiring baseline measurements.

Biotin-avidin binding procedure: The mixture of biotin-PEG-SH (25 mg·mL-1 in MOPS-DNA buffer of pH7.5) and CH_3O-PEG-SH (250 $mg\cdot mL^{-1}$ in MOPS-DNA buffer of pH7.5) in the ratio of 1:1 ($v\cdot v^{-1}$) was drop-cast onto ~ 0.5 cm^2 of as-grown nanohelix substrate and kept under humid condition overnight. For the control group, the nanohelices were exposed to only CH_3O-PEG-SH. Next, each substrate was immersed in 1 mL of 0.15 mM PVP solution and sonicated to remove the particles from the wafer and suspend them in solution. Finally, for the biotin-avidin interaction, 1 $\mu g\cdot mL^{-1}$ of avidin was injected to the colloidal solution and mixed by pipetting.

Chapter 5 Active nanorheology

Nanoplasmonic systems are valued for their strong optical response and their small size. Most plasmonic sensors and systems to date have been rigid and passive. However, rendering these structures dynamic opens new possibilities for applications. In this chapter it is shown that dynamic plasmonic nanoparticles can be used as mechanical sensors to selectively probe the rheological properties of a fluid *in situ* at the nanoscale and in microscopic volumes. Chiral magneto-plasmonic nanocolloids are fabricated that can be actuated by an external magnetic field, which in turn allows for the direct and fast modulation of their distinct optical response. The method is robust and allows nanorheological measurements with a mechanical sensitivity of ~0.1 cP, even in strongly absorbing fluids with an optical density of up to OD ~3 (~0.1% light transmittance) and in the presence of scatterers (e.g. 50% v/v red blood cells).

This chapter is based on the published article of

[136] Active nanorheology with plasmonics, **H.-H. Jeong**, A.G. Mark, T.-C. Lee, M. Alarcón-Correa, S. Eslami, T. Qiu, J.G. Gibbs, and P. Fischer, ***Nano Letters*** 16, 4887 (2016)

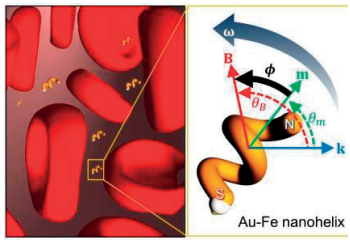

Author Contributions:
H.-H.J., A.G.M., T.-C.L, J.G.G and P.F. designed the experiments. H.-H.J. and J.G.G. performed the CD and dark-field experiments. T.-C.L. and M.A.-C. carried out the TEM imaging. S.E. and A.G.M. conducted the CD calculation. H.-H.J. and A.G.M. developed the experimental setup and measured and analysed the data. H.-H.J. and T.Q. performed the blood macrorheological measurements, and H.-H.J., A.G.M., T.-C.L. and P.F. wrote the paper.

5.1 Introduction

The resonant optical field enhancement in plasmonic nanostructures is of interest in research disciplines ranging from sensing to energy conversion, and is the basis for modern advances in metamaterials and the associated capabilities in shaping electromagnetic fields.[73-75] The scope of potential applications of nanoplasmonic structures is greatly extended by tailoring the nanostructure, for instance to shift the resonance frequency while keeping the overall size of the nanoparticle small,[93, 103-105] or by incorporating diverse functionalities, such as magnetic,[106] chiral,[102] and electrical.[76] Recent fabrication advances have also allowed the programmatic growth of nanoparticles that lack mirror symmetry.[35, 56, 98-100] Such chiral nanoparticles mimic their molecular counterparts by exhibiting optical activity, but with chiroptical effects many orders of magnitude stronger than what is observed in molecules.[64, 101, 102] These multifunctional nanoparticles promise new capabilities in sensing.[15, 32]

One particularly challenging application is the measurement of rheological properties in complex fluids. Such systems contain a mixture of multiple phases; for instance, many biological fluids contain solids consisting of isolated microparticles or a network of macromolecules suspended in a fluid phase.[271] Because of the solid phase, macroscopic rheological measurements will generally show non-Newtonian viscoelastic behaviour even if the liquid phase is a simple Newtonian fluid.[272] For instance, the viscosity of blood plasma is a crucial indicator for clinical diagnoses,[273, 274] but cannot be determined in whole blood due to the presence of leukocytes (10-15 µm) and erythrocytes (6-8 µm).[275, 276] Furthermore, the solid phase in complex fluids, such as blood cells, contributes to absorption and scattering which complicate optical measurements.

By combining multiple materials and shape control, this chapter introduces the first chiral magnetoplasmonic structures that can be actuated in solution. These colloids were used to measure the viscosity at the nanoscale of blood plasma in the presence of blood cells. This viscosity is a very important indicator for the disease diagnosis, but typically complicated to analyse using commercial rheometers as it needs a step in which the blood cells are separated.[273]

5.2 Theoretical concept

Since the chiroptical spectrum depends on the alignment of the chiral structure (figure 5:1a), chiroptical switching can be achieved and exploited for nanorheological measurements using picomolar probe concentrations. The scheme works by using the modulated chiroptical signal to measure the phase lag between the applied field and the particle's orientation and thereby determine the torque applied to the particles (figure 5:1c). The chiral shape permits background-free differential absorption measurements even in whole blood, where conventional plasmonic absorption measurements would be impossible due to the large background optical extinction (optical density ~3). Because the active plasmonic nanostructures are much smaller than the suspended microparticles (cells), they probe only the fluid phase – in the case of blood, the blood plasma (figure 5:1b) – and unlike macroscale instruments are insensitive to the solid phase even at very high volume fractions. Such *in situ* observations of the fluid viscosity would not be possible with a conventional rheometer or viscometer, which typically requires much larger volumes of the target fluid (> 10 mL).

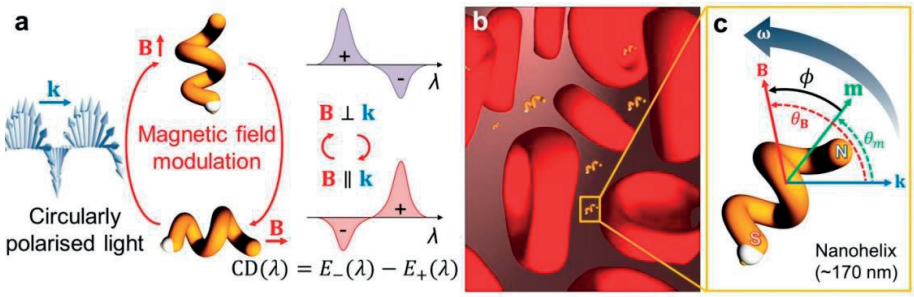

Figure 5:1 *In situ* active nanorheology with magneto-plasmonic enantiomorphs. (a) Principle of the magnetically driven chiroptical switching. Under the application of an external magnetic field $\mathbf{B}$ the ferromagnetic nanostructures align, and the CD response of a solution of chiral nanocolloids is modulated. (b) Schematic depicting a rotating magneto-plasmonic nanoprobe in a complex and optically dense medium (here blood plasma surrounded by erythrocytes). (c) Definition of the angles and parameters used in the nanorheological experiments ($\mathbf{B}$: applied magnetic field, $\mathbf{m}$: magnetic moment along the long axis of the nanohelix, $\mathbf{k}$: wave vector of the incident light, ϕ: phase lag between $\mathbf{B}$ and $\mathbf{k}$, $\theta_{\mathbf{B}}$: angle between $\mathbf{B}$ and $\mathbf{k}$, $\theta_{\mathbf{m}}$: angle between $\mathbf{m}$ and $\mathbf{k}$, $\boldsymbol{\omega}$: angular velocity of the nanohelix). Reprinted with permission from Ref. 136 (Copyright 2016 American Chemical Society)

In order to derive an equation that describes the nanorheology of the chiral magneto-plasmonic nanoparticle system, the theory for the hydrodynamic response of magnetic nanorods has been applied and adapted.[277] At steady state, the torque due to hydrodynamic drag will be balanced by the applied magnetic torque:

$$\boldsymbol{\tau_D}(=\chi\eta\boldsymbol{\omega}) = \boldsymbol{\tau}_{\mathbf{B}}(=\mathbf{m}\times\mathbf{B}), \tag{5:1}$$

where χ is the hydrodynamic shape constant (for a sphere $\chi = 8\,\pi R^3$),[278] η is the dynamic viscosity of the medium, $\mathbf{B}$ is the vector of the applied magnetic field, and $\mathbf{m}$ is the vector of the magnetic moment along the long axis of the nanohelix. $\boldsymbol{\omega}$ is the angular velocity of the nanohelix which is given as,

$$\boldsymbol{\omega} = \frac{d\theta_{\mathbf{m}}}{dt}, \tag{5:2}$$

where θ_m is the angle between $\mathbf{m}$ and the wave vector $\mathbf{k}$ of the incident light. By considering the angular function $\theta_{\mathbf{B}} = 2\pi f_{\mathbf{B}} t$ and $\phi = \theta_{\mathbf{B}} - \theta_{\mathbf{m}}$ where $\theta_{\mathbf{B}}$ is the angle between $\mathbf{B}$ and $\mathbf{k}$, $f_{\mathbf{B}}$ is the frequency of the applied rotating magnetic field, equation 5:2 can be written as

$$\frac{d\theta_{\mathbf{m}}}{dt} = 2\pi f_{\mathbf{B}} - \frac{d\phi}{dt}. \tag{5:3}$$

For a steady rotational of the nanohelix (i.e., below the step-out frequency) $d\phi \cdot dt^{-1}$ is zero and equation 5:1 can be rewritten as

$$\sin\phi = \frac{2\pi\chi\eta}{m_r \mathbf{B}}\, f_{\mathbf{B}}. \tag{5:4}$$

For a given magnetic field strength and a frequency below the step-out, the 1st derivative $dsin\,\phi \cdot df_{\mathbf{B}}{}^{-1}$ is a function of the viscosity,

$$\frac{d\sin\phi}{df_{\mathbf{B}}} = \frac{2\pi\chi}{m_r\mathbf{B}}\eta. \tag{5:5}$$

Therefore, by measuring the phase lag of the magnetic nanoparticle under the given magnetic field, it is possible to analyse the local viscosity of the fluid.

5.3 Magneto-plasmonic nanoparticle enantiomorph

Active plasmonic systems have recently been developed by controlling either the electromagnetic radiation applied to the metallic nanostructure [46, 127-129] or the dynamics of the nanostructures.[130-134] However, there are no plasmonic systems that can be switched repeatedly at high frequency and that satisfy the minimum requirements for *in situ* active nanorheology in a complex fluid: (1) a distinguishable optical contrast despite strong extinction (and no bleaching), (2) small size relative to the suspended microparticles (e.g. erythrocytes),[279, 280] and (3) high nanoparticle monodispersity for a precise hydrodynamic response.[281] These criteria are satisfied by the ~170 nm magneto-plasmonic nanohelices shown in figure 5:2. Briefly, their fabrication is based on the nanoGLAD.[56]. BCML is used to form a quasi-hexagonal array of Au nanoparticles with diameter 12±2 nm and an interparticle distance ~100 nm on a silicon wafer. Vapours of elemental Au and Fe were then co-deposited in a 1:1.5 ratio onto the nano-patterned substrate using a dual e-beam system to generate an array of Au-Fe nanohelices, figure 5:2a. Sonication in a fluid readily detaches the helices from the wafer to yield the nanocolloidal suspension used in the experiments, figures 5:2b-d. The structural dimensions of left-handed Au-Fe nanohelices are deduced from transmission electron microscopy (TEM) images of 100 individual nanohelices. (See table 5:1).

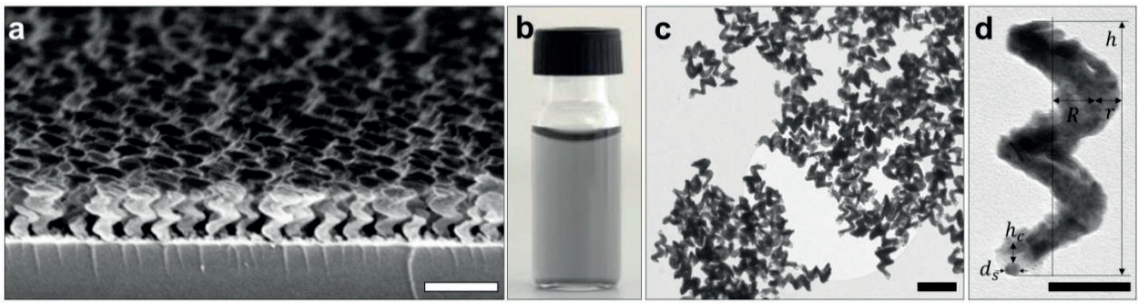

Figure 5:2 Fabrication of Au-Fe nanohelices. (a) The tilted view of the SEM image of 2-turn Au-Fe nanohelices on an array of Au-SiO_2 nanoparticles (scale bar: 200 nm). (b) A colloidal suspension of Au-Fe nanohelices after sonication. (c) Large-area TEM image of Au-Fe 2-trun left-handed nanohelices (scale bar: 200 nm). (b) A TEM image of a single Au-Fe nanohelix showing dimensions of the seed particle and the nanostructure that grows upon it (scale bar: 50 nm). Reprinted with permission from Ref. 136 (Copyright 2016 American Chemical Society)

2 turn left hand helices	d_s	h_c	h	r	$2R$
Mean [nm]	12.1	9.2	168.8	14.2	54.5
Standard deviation [nm]	1.8	2.9	8.4	2.1	4.65
Percentage Standard deviation [%]	14.9	31.5	5.0	14.5	11.2

Table 5:1 : Statistical analysis of 100 individual Au-Fe 2-turn left-handed nanohelices.

The compositional analysis of the Au-Fe nanohelices was performed using scanning TEM (STEM) imaging with energy-dispersive X-ray spectroscopy (EDX) measurements, ICP-OES, and Auger depth profiling. Figure 5:3a shows the STEM image of a single two-turn left-handed Au-Fe nanohelix and corresponding images of EDX false-colour elemental maps of Au, Fe, and O, respectively, which reveal nanoscale mixing between Au and Fe. The atomic ratio of Au to Fe was approximately 46.7:53.3 (±1.8%) based on integrated EDX intensity. This is consistent with measurements from the ICP-OES which indicates a ratio of 40.8:59.2 (±6.1%). Figure 5:3b shows the Auger depth profile of the Au-Fe nanohelices on Si wafer as a function of the etching time (i.e. depth) by Ar plasma. The low oxygen signal during the middle phase relative to the initial phase suggests that the oxygen is confined to the nanoparticles' surface.

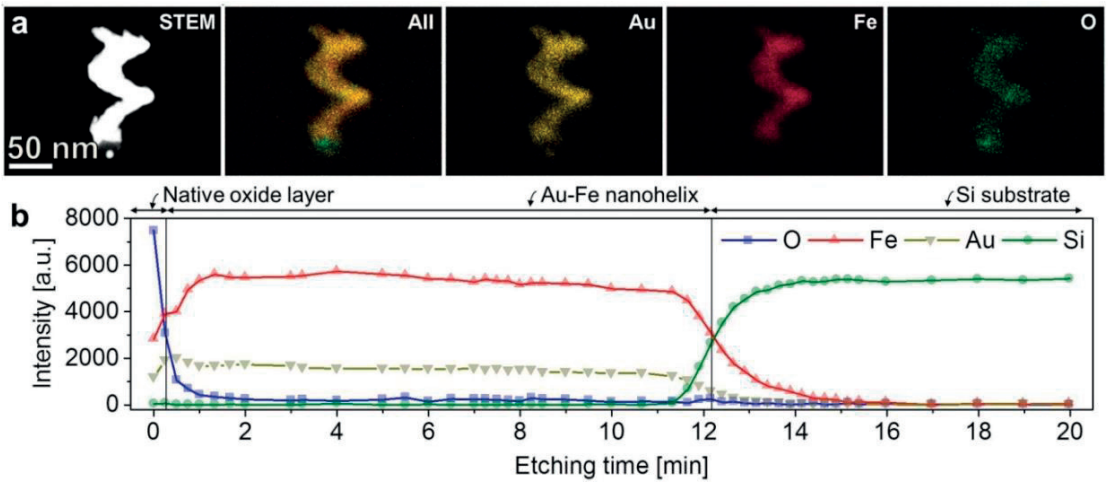

Figure 5:3 Material composition of Au-Fe nanohelix. (a) An STEM image and serial energy dispersive *x*-ray spectroscopy (EDX) false-colour elemental map of the 2-turn Au-Fe nanohelix ~170 nm in height. (b) Auger depth profiling of the Au-Fe nanohelix as a function of the etching time by Ar plasma. Auger electron scattering intensities of O (blue square), Fe (red top triangle), Au (yellow bottom triangle), and Si (green circle) according to 3 regions: a native oxide layer on top of the helix, a body of the Au-Fe helix, and a Si substrate (from left to right). Reprinted with permission from Ref. 136 (Copyright 2016 American Chemical Society)

Magnetic actuation of the nanoparticles is possible due to the presence of Fe (figure 5:3). Superconducting quantum interference device (SQUID) magnetometry was carried out on the array of Au-Fe nanohelices when they were still attached to the wafer. As expected, the helices display ferromagnetic behaviour, having a coercive field of 29.5 mT and a remanence of 1.2×10^{-14} emu per single helix, as seen in figure 5:4a.

In dilute suspensions, where the inter-particle separations are large, the nanoparticles will independently undergo Brownian motion and thus maintain random orientations in space. In this isotropic state, the optical response is simply given by the average response across all possible nanoparticle orientations. The optical properties of a suspension containing the nanohelices in the unaligned, isotropic state are summarised in figure 5:4b. The extinction spectrum, measured by UV-VIS-NIR spectrometry, shows a wide featureless spectrum typical of mixing a lossy material (Fe) with the plasmonic metal Au.[270, 282] However, the power of circular dichroism (CD) spectroscopy is apparent in the strong, sharp chiroptical response of the Au-Fe nanohelix metafluid. At a peak wavelength of 690 nm, it exhibits a molar CD = ~14×10^{9} $^{o}\cdot M^{-1}\cdot cm^{-1}$, stronger than that observed for other chiral assembled plasmonic systems.[35-37, 283] Complex fluids, such as blood, generally show no measurable chiroptical response of their own in this spectral region.[257] Thus

the chiroptical spectrum of chiral nanoparticles dispersed in such media is not affected by the background extinction from the fluid and can be 'seen', even in the presence of absorbers and strong scatterers.

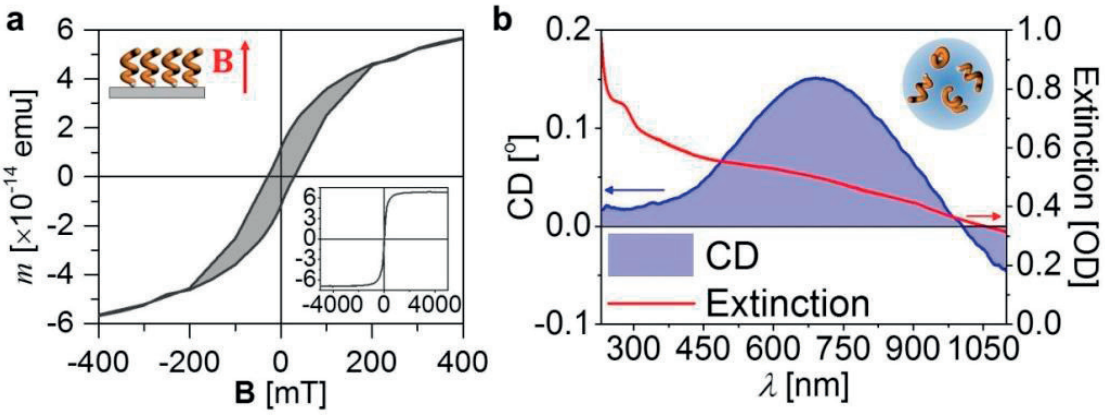

Figure 5:4 Characterisation of magneto-plasmonic enantiomorphs., (a) A magnetic hysteresis curve of an array of the Au-Fe nanohelices measured on a Si substrate with a static magnetic field along the long axis of the nanohelices, ranging from -400 mT to 400 mT (coercive field: ~29.5 mT). The inset shows the full hysteresis curve ranging from -5 T to 5 T. (b) CD spectrum (blue line and left y-axis) and UV-Vis-NIR spectrum (red line and right *y*-axis) of the colloidal Au-Fe nanohelices at **B** = 0 (isotropic state). Reprinted with permission from Ref. 136 (Copyright 2016 American Chemical Society)

5.4 Brownian motion of magneto-plasmonic nanohelix

By comparing the theoretical and experimental translational diffusion coefficients D_t of the nanohelix, it can be evaluated whether a single nanohelix is observed through the dark-field optical microscope. The centroid positions of 10 nanohelices were tracked in fluids with two different viscosities for 10 sec at 20 frames·sec^{-1} and their translational Brownian diffusion coefficient D_t (= MSD/4t) were calculated, where MSD is the mean squared displacement of the nanoparticles, figure 5:5.[186, 279] This gave D_t = 2.38 ± 0.05 μm^2·sec^{-1} in pure water and D_t = 0.37 ± 0.01 μm^2·sec^{-1} in a 50% glycerol-water mixture, which were analytically calculated using a MATALB code developed by the group,[186] figure 5:5e. By considering the geometry of the nanohelix as an ellipsoid with an aspect ratio (AR) of 2 ($h/2R$), the theoretical D_t of the nanohelix can be estimated from the Einstein-Smoluchowski relation as[284]

$$D_t = \frac{(D_a + D_b)}{2}, \tag{5:6}$$

where D_a is the diffusional coefficient at the long axis of the ellipsoid a and D_b is the diffusional coefficient at the short axis of the ellipsoid b. When AR $(a/b) \gg 1$, where $D_a$and D_b are given as[285]

$$D_a = \frac{k_B T \ \ln AR}{2\pi\eta a}, D_b = \frac{k_B T \ \ln AR}{4\pi\eta a}. \tag{5:7}$$

where the viscosity of the solution, η is 1.0049 cP for water and 8.3968 cP for the 50% glycerol-water mixture.[254] Thereby, D_t is 3.5 μm^2·sec^{-1} in water and 0.38 μm^2·sec^{-1} for 50% glycerol in water, in good agreement with the measured values. This indicates that the tracked nanohelices act as discrete particles undergoing Brownian motion.

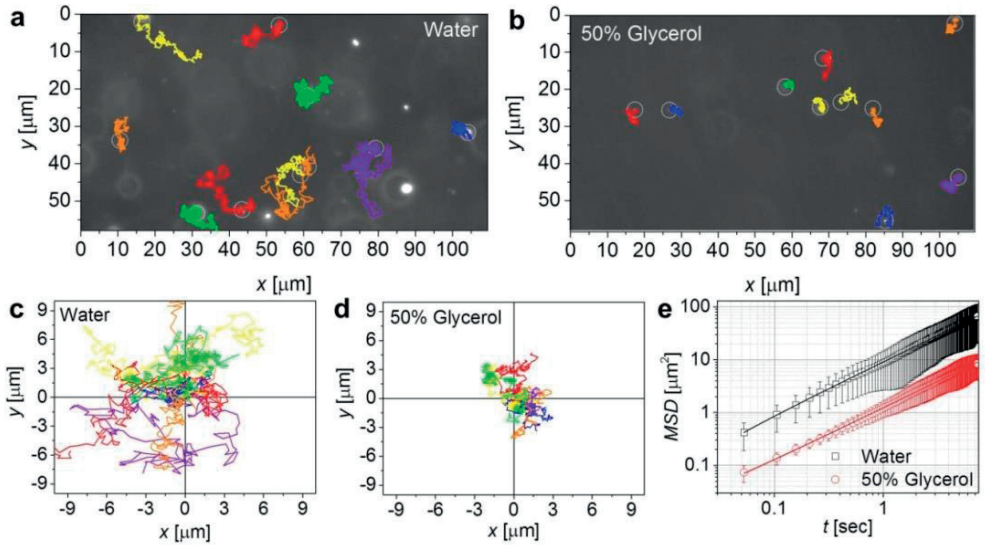

Figure 5:5 Brownian motion of the Au-Fe left-handed nanohelices. (a) in water and (b) 50% glycerol in water as observed by single particle tracking using dark-field optical microscopy. Each image shows 10 nanoparticle trajectories, where each trajectory's start position is set to (x = 0, y = 0) in (c) water and (d) 50% glycerol in water. (e) Corresponding MSDs of Au-Fe nanohelices plotted as a function of time (black square: water, red circle: 50% glycerol). Reprinted with permission from Ref. 136 (Copyright 2016 American Chemical Society)

5.5 Dynamic switching of the magneto-plasmonic nanohelices

Application of an external field causes alignment of the magnetic particles due to the natural magnetic anisotropy along the long axis of the helix.[286] In the static regime, a weakly ferromagnetic Au-Fe nanohelix will orient so that its magnetic moment, $\mathbf{m}$ and hence its body, lies parallel to the magnetic field, $\mathbf{B}$. However it retains rotational freedom to spin about its body-axes. The optical response of an asymmetric particle depends on its orientation relative to the wave vector $\mathbf{k}$ of the incoming beam. For linearly polarised light the optical response will be a function of two angles: $\theta_{\mathbf{B}}$ between $\mathbf{B}$ and $\mathbf{k}$ (assuming that $\mathbf{B}||\mathbf{m}$) and the angle between $\mathbf{B}$ and the plane of polarization. However, since circularly polarised light possesses no plane of polarization, the chiroptical response measured by CD spectroscopy will be a function of only the single parameter $\theta_{\mathbf{B}}$. Thus, in the chiral metafluid, the magnetic modulation effectively switches the isotropic medium into a uniaxial one, where the principal axis is defined by the magnetic field direction.

In experiments, the orientation of the Au-Fe nanohelices in solution was modulated by an external magnetic field generated by a gradient-free 3D Helmholtz coil.[156] To completely align a nanohelix with the external magnetic field $\mathbf{B}$, the magnitude of the magnetic field strength can be estimated by considering $m_r\mathbf{B} > k_{\mathrm{B}}\mathrm{T}$, where m_r is the remanence of a single Au-Fe nanohelix in figure 5:4a (1.174×10^{-14} emu), $\mathbf{B}$ is the magnetic field strength, k_{B} is the Boltzmann constant (1.38×10^{-23} J·K^{-1}), and T is the temperature (here 300K). Therefore, the minimum external magnetic field $\mathbf{B}_{\mathrm{m}}$ strength is given by

$$\mathbf{B}_{\mathrm{m}} = \frac{k_{\mathrm{B}}T}{m_r} = \sim 0.4\ \mathrm{mT}. \tag{5:8}$$

This suggests that the Au-Fe nanohelices can be aligned to the external magnetic field of $\mathbf{B}$ > 0.4 mT (40 G). Thus, the experiments were conducted with magnetic fields $|\mathbf{B}|$ > 0.4 mT (approx. 10 times Earth's magnetic field) to ensure alignment of the nanocolloids. Higher fields can exert stronger torques. Since a gradient-

free field was used, the translational diffusion of the particles was unaffected, even as the rotational diffusion was suppressed. Real-time direct observation of the colloidal nanohelices was performed with dark-field optical microscopy. The image panels in figure 5:6 show consecutive dark-field images of a single Au-Fe nanohelix captured during continuous in-plane rotation driven by the applied magnetic field ($\mathbf{B}$ = 5 mT with $f_{\mathbf{B}}$ = 1 Hz, in a 50% glycerol-water mixture). The features of the helix are too small to be resolved so it appears as an elongated ellipse; crucially, the ellipse axis, which corresponds to the helix axis, rotates in alignment with the magnetic field direction. Thus, the magnetic moment of the nanohelix allows an external magnetic field of this strength to control its orientation.

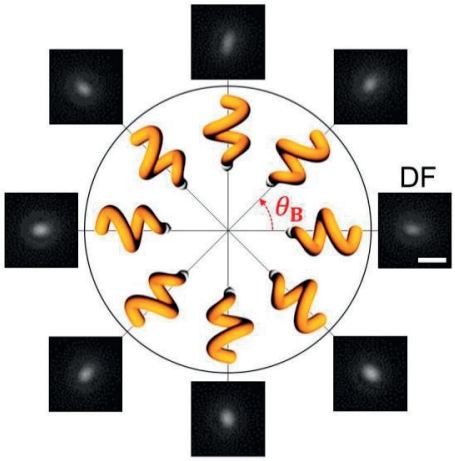

Figure 5:6 The dark-field images of a single Au-Fe nanohelix captured during continuous in-plane rotation driven by the applied magnetic field ($\mathbf{B}$ = 5 mT with $f_{\mathbf{B}}$ = 1 Hz) in a 50% glycerol-water mixture (scale bar: 1 μm). Reprinted with permission from Ref. 136 (Copyright 2016 American Chemical Society)

The effect of the nanocolloids' orientation on the chiroptical response was also evaluated through CD spectra acquired at various magnetic field intensities and orientations, figure 5:7. Firstly the chiroptical responses of the colloidal Au-Fe nanohelices were measured under the static magnetic field (red: $\mathbf{B} \parallel \mathbf{k}$, violet: $\mathbf{B} \perp \mathbf{k}$) with different intensities ranging from 0.5 to 7 mT. Figure 5:7b shows the chiroptical responses at λ = 880 nm of the colloidal Au-Fe nanohelices as a function of the magnetic field strength. Again, most of the nanohelices can be aligned with a magnetic field of at least $\mathbf{B}$ ~ 1 mT.

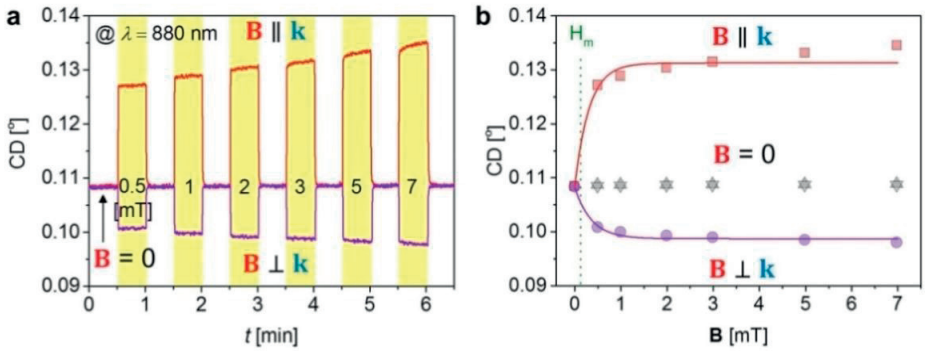

Figure 5:7 Chiroptical responses of the colloidal Au-Fe nanohelices at λ = 880 nm in the presence of a static magnetic fields along $\theta_{\mathbf{B}}$ = 0° (red line) and $\theta_{\mathbf{B}}$ = 90° (violet line). The strength of the magnetic field ranges from 0.5 to 7 mT. (b) The corresponding chiroptical responses re-plotted as a function of the magnetic field intensity. Reprinted with permission from Ref. 136 (Copyright 2016 American Chemical Society)

Such switching effect is now characterised in detail through the differential circular dichroism ΔCD = CD($\theta_{\mathbf{B}}$) – <CD> to emphasise differences between CD($\theta_{\mathbf{B}}$), the signal with the magnetic field oriented at $\theta_{\mathbf{B}}$, and <CD> the isotropic case with $\mathbf{B}$ = 0. The spectra in figure 5:8a show the experimental ΔCD spectra in response to applied magnetic fields at different orientations. They show a clear modulation of the signal, with symmetry that reflects the underlying symmetries of the particles and the imposed constraints. First, the spectra are invariant under π-rotation of $\theta_{\mathbf{B}}$ due to the C_2 symmetry of the helix. Second, the helices' unconstrained degree of freedom about their axis means that CD($\theta_{\mathbf{B}}$) = CD($-\theta_{\mathbf{B}}$). Figure 5:8b shows the differential CD spectra displayed as 2D maps in terms of λ and $\theta_{\mathbf{B}}$. These results are in excellent agreement with numerical simulations using the discrete dipole approximation (see figure 5:8c, and Methods for details of numerical calculation). Figure 5:8d shows ΔCD profiles at wavelengths λ = 360 nm and 1000 nm, where the ΔCD responses were minimal and maximal at $\theta_{\mathbf{B}}$ = 0° respectively, acquired with static magnetic fields at specified angles. For the long wavelength spectral curve at $\theta_{\mathbf{B}}$ = 0°, the CD is over 200 mdeg higher than in the isotropic state. With increasing $\theta_{\mathbf{B}}$ the differential CD diminishes until it reaches a minimum at $\theta_{\mathbf{B}}$ = 90°. The λ = 360 nm curve follows the opposite trend. The two curves cross each other, and the ΔCD = 0° axis at an angle of ~50°. The lower panel of figure 5:8d shows the corresponding results from numerical simulations.

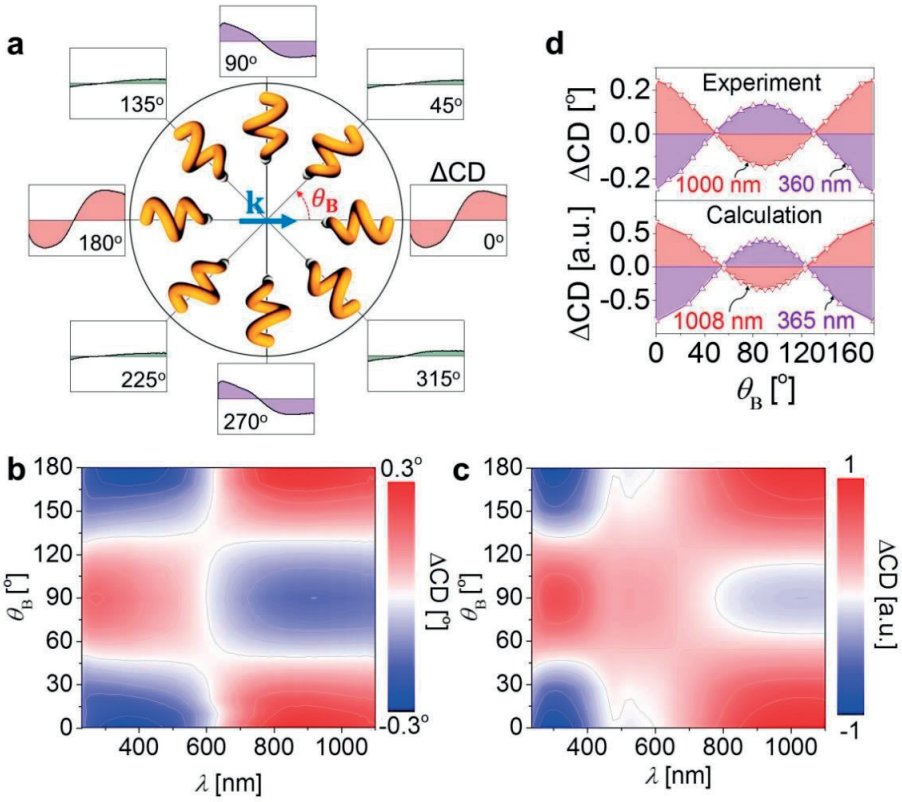

Figure 5:8 Magnetically driven chiroptical switching of the colloidal Au-Fe nanohelices. (a) ΔCD responses of the Au-Fe nanohelices as a function of λ under a static magnetic field ($\mathbf{B}$ = 1 mT) at 45° angular intervals. The spectra show a wavelength range of 230 – 1100 nm on the *x*-axis, and ΔCD from -0.3° to 0.3° on the *y*-axis. 2D maps of (b) experimental and (c) theoretical ΔCD responses of the Au-Fe nanohelices as functions of λ (*x*-axis) and $\theta_{\mathbf{B}}$ (*y*-axis). (d) ΔCD response of the colloidal Au-Fe nanohelices as a function of $\theta_{\mathbf{B}}$ (upper plots: experimental results at two wavelengths λ = 360 nm (violet) and λ =1000 nm (red), lower plots: theoretical results at λ = 365 nm (violet) and λ = 1008 nm (red)). Reprinted with permission from Ref. 136 (Copyright 2016 American Chemical Society)

High frequency modulation of the magnetic field leads to rapid, synchronous and reversible modulation of the differential CD. Figure 5:9 shows the differential CD at 360 and 1000 nm in response to a magnetic field rotating at various different $f_{\mathbf{B}}$ in the plane of incidence. The dominant frequency component of the resulting optical modulation is at twice the drive frequency $2f_{\mathbf{B}}$ because of the two-fold rotational symmetry observed in figure 5:8a. Particles that lack C_2 symmetry, or have their axis of rotation misaligned with respect to the rotation axis of the magnetic field would contribute to intensity at $f_{\mathbf{B}}$ in the discrete Fourier transform of the CD. The small component at $f_{\mathbf{B}}$, having a strength less than 30 dB below the dominant harmonic, attests to the uniformity of the nanohelices, and their high degree of magnetic alignment, figures 5:9h and i.

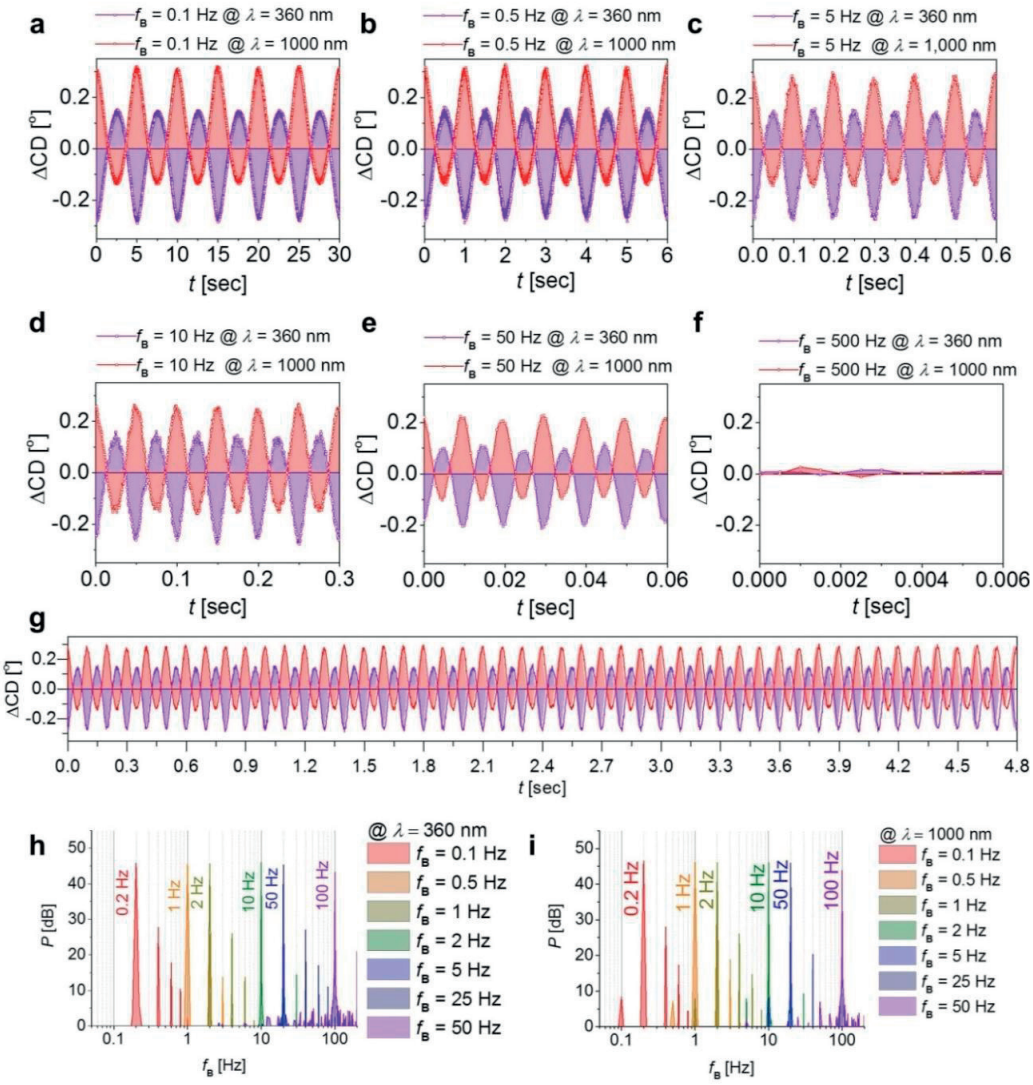

Figure 5:9 ΔCDs of the colloidal Au-Fe left-handed nanohelices at λ = 360 nm (violet line) and 1,000 nm (red line) for $\mathbf{B}$ = 1 mT at $f_{\mathbf{B}}$ = (a) 0.1 Hz, (b) 0.5 Hz, (c) 5 Hz, (d) 10 Hz, (e) 50 Hz, and (f) 500 Hz. (g) A continuous modulation of the ΔCDs at $f_{\mathbf{B}}$ = 0.5 Hz. The FFT analysis on the corresponding chiroptical response at (h) λ = 360 nm and (i) 1,000 nm. Each label indicates the frequency f_{CD} that is coincident with $2f_{\mathbf{B}}$. Reprinted with permission from Ref. 136 (Copyright 2016 American Chemical Society)

5.6 *In situ* active nanorheology

Switching the magneto-plasmonic nanohelices is the basis for their use as nanorheological probes that can operate even in complex fluid environments with strong absorption and a large volume fraction of scattering microparticles. The magnetic helices are subjected to a rapidly rotating magnetic field and, at the same time, the phase and amplitude of the resulting CD signal are measured. Figure 5:1c shows a helix rotating at an angular frequency $\boldsymbol{\omega}$ in response to a magnetic field rotating at frequency $f_{\mathbf{B}}$. Viscous drag causes a phase lag ϕ between the rotating magnetic field and the particle's magnetic moment $\mathbf{m}$, which is fixed to its orientation.[287] In the steady state, $\boldsymbol{\omega} = 2\pi f_{\mathbf{B}}$, the balance of torques means that the phase angle is related to the drive frequency according to equation 5:4.[159] The key insight is that the modulated chiroptical signal reflects the particle's alignment $\mathbf{m}$ and can therefore be used to extract the otherwise unknown phase angle ϕ. Figure 5:10 shows the schematic view of the designed phase sensitive detection system with the integrations of two lock-in amplifiers. The first lock-in-amplifier (LIA 1) reduces the noise level of the chiroptical response containing f_{CD} component by referencing the signal from the photomultiplier (PMT) to the photoelastic modulator (PEM) which modulates the light from left- to right-circularly polarised. The second lock-in LIA2 references this signal to the $f_{\mathbf{B}}$ from the coil system. LIA2 thus provides the phase difference between the optical response and the applied magnetic field.

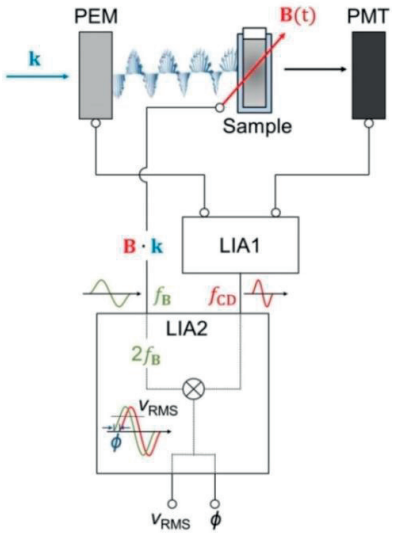

Figure 5:10 Schematic diagram of the phase sensitive chiroptical measurement system. Reprinted with permission from Ref. 136 (Copyright 2016 American Chemical Society)

Since the measured phase angle ϕ' also contains a phase lag due to the inductance phase lag of the coil system ϕ_L, and the initial chiroptical phase lag ϕ_0', one obtains the resultant geometrical phase lag ϕ:

$$\phi = \frac{1}{2}\phi' - \phi_0' - \phi_L. \tag{5:9}$$

For this experimental measurement only one operating wavelength is necessary so that the wavelength at λ = 880 nm is selected, where the optical density is maximal among the target systems used for nanorheology in this chapter (e.g. figure 5:13a). At higher frequencies (> 50Hz) the viscous drag exceeds the magnetic torque and the nanohelices no longer rotate synchronously, but in the synchronous regime $\sin\phi$ is proportional to the frequency. As shown in figure 5:11a, the slope $d\sin\phi \cdot df_{\mathbf{B}}^{-1}$ is itself linearly dependent on

the dynamic viscosity of the medium. The calibrated phase lag ϕ, which is small and expressed in radians, can be fitted by a 2nd order polynomial function. For example, in the case of water (η = 1.0049 cP at T = 20°C), the phase is approximately given as

$$sin\,\phi \sim \phi \sim 0.0085 + 0.0304 f_{\mathbf{B}}. \tag{5:10}$$

Based on equation 5:10, the 1st derivative ($dsin\,\phi \cdot df_{\mathbf{B}}{}^{-1}$) can be obtained as,

$$\frac{dsin\,\phi}{df_{\mathbf{B}}} = 0.0304. \tag{5:11}$$

Calibration measurements for glycerol-water mixtures of differing viscosities (see figure 5:11b) are used to obtain a reference curve for the absolute dynamic viscosity,

$$\frac{dsin\,\phi}{df_{\mathbf{B}}} = 0.00241\eta + 0.02787 \tag{5:12}$$

Figure 5:11b shows the experimental values of $dsin\,\phi \cdot df_{\mathbf{B}}{}^{-1}$ as a function of the theoretical viscosity, η of the glycerol-water mixture (see also Appendix A.4.1 Nanorheology in water-glycerol mixture). So by calibrating the response in a series of glycerol-water mixtures with known viscosities the value for the sole free parameter can be recovered, the shape constant, χ

$$\chi = 0.00241\frac{m_r \mathbf{B}}{2\pi} = 1.35 \times 10^7\ \mathrm{nm}^3. \tag{5:13}$$

An order of magnitude estimate of this quantity can be calculated by modelling the Au-Fe nanohelix as a cylinder. In this case the shape constant is given by,[288]

$$\chi = \frac{\pi l^3}{3\,\mathrm{g}\left(\frac{l}{d}\right)} \tag{5:14}$$

where $\mathrm{g}\left(\frac{l}{d}\right) = \ln\left(\frac{l}{d}\right) - 0.662 + 0.917\frac{l}{d} - 0.050\left(\frac{l}{d}\right)^2$.[287] With a length l = 168.8 nm and diameter d = 82.9 nm this predicts a shape constant of χ = 2.95×10^6 nm^3. This process allows the nanohelices to be used as calibrated probes of their local rheological environment.

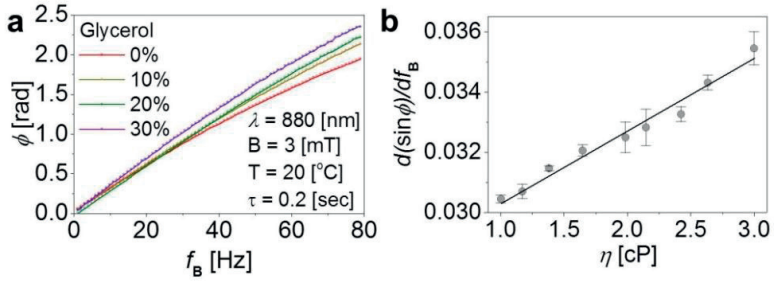

Figure 5:11 *In situ* active nanorheology in water-glycerol mixture. (a) Phase angle, ϕ of the colloidal Au-Fe nanohelices in the presence of different concentrations of a glycerol-water mixture as a function of $f_{\mathbf{B}}$ (at $\mathbf{B}$ = 3 mT, λ = 880 nm at T = 20°C). (b) The corresponding slopes, $dsin\,\phi \cdot df_{\mathbf{B}}{}^{-1}$, as a function of the dynamic viscosity of the medium, η. Reprinted with permission from Ref. 136 (Copyright 2016 American Chemical Society)

Using the same experimental procedure, the viscosities of complex fluids are measured that is composed of different volume fractions of 8 µm polystyrene microspheres with a fluid phase of water or 20% glycerol-water. Adding the microspheres produces a slurry and leads to a dramatic increase in the sample's optical density, as seen in the left panel in figure 5:12a, which rises from below OD 0.5 to OD ~2.5 (< 1% light transmittance). Sample opacities this high normally make optical measurements challenging. Nevertheless, the CD response from the magneto-plasmonic nanohelices is still apparent (see right panel in figure 5:12b and Appendix A.4.2 Nanorheology in slurry).

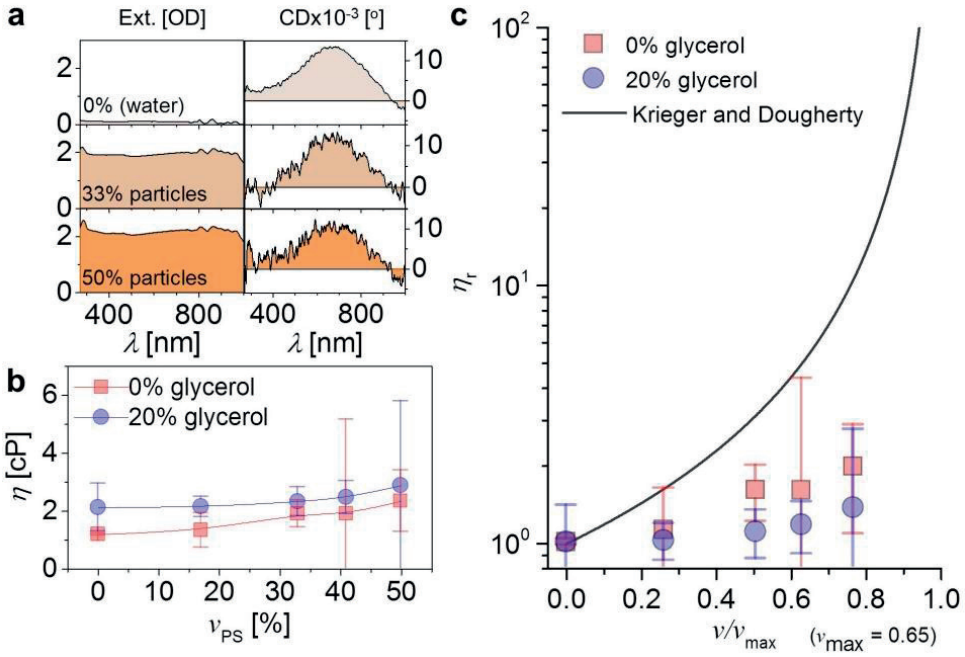

Figure 5:12 *In situ* active nanorheology in slurry. (a) Extinction (left panel) and CD (right panel) spectra of the colloidal Au-Fe nanohelices in water in the presence of polystyrene particles (8 µm in diameter) with different volume fractions (top: 0%, middle: 33%, bottom: 50%). The extinction spectra are featureless, whereas a clear CD peak is discernible even at high particle fraction. (b) Dynamic viscosity as a function of the volume fraction of the polystyrene microspheres in water (red squares) and 20% glycerol (blue circles). (c) The corresponding relative dynamic viscosities, η_r at the nanoscale (red squares and blue circles) and at the macro scale (solid line).[272, 289] Reprinted with permission from Ref. 136 (Copyright 2016 American Chemical Society)

The measured nanoscale viscosity (figure 5:12c) shows no substantial change in response to the increase in the microsphere volume fraction v_{ps} but clearly distinguishes the differences in fluid phase viscosity between the water (red) and 20% glycerol (blue) samples. Figure 5:12d shows that the measured relative dynamic viscosity $\eta_r = \eta/\eta_0$, where η_0 is the viscosity of the fluid phase, is essentially independent of the volume fraction of microspheres. On the other hand, the macroscale viscosity, characterised by the Krieger-Dougherty model, is over 10 times higher at a volume fraction of 50%.[272] The difference arises because macroscopic rheometry measures the complex viscoelastic contributions of the microspheres, whereas the nanohelices only measure the unchanging nanoscale viscosity of the interstitial fluid. Thus, nanohelices are able to measure the nanoscale mechanical properties of a matrix phase even in the presence of aggregates that strongly affect the optical extinction and macroscale rheology.

This sensing scheme can be extended to biological fluids. Blood is a particularly challenging test case as it strongly absorbs light.[23] However, experiments are conducted on isolated blood plasma, and blood plas-

ma reconstituted with four different haematocrit concentrations (blood cell volume fractions). Again, adding red blood cells (erythrocytes) leads to a significant increase in the sample's optical density (up to OD ~3, see left panel in Figure 5:13a), but the CD response from the helices is still measureable through whole blood in the spectral range from ~600 nm to ~1100 nm (right panel in figure 5:13a). One important consideration when using nanoparticles in real bio-fluids is the formation of protein coronas. These diffuse shells of proteins aggregated around the nanoparticle can affect its dynamics.[290, 291] To minimise differences between samples of different haematocrit levels, a standardised procedure was adapted whereby the nanoparticles were mixed in pure blood plasma to develop the corona, before introducing the erythrocytes and then quickly performing the nanorheological measurement. Control tests in phosphate buffer saline indicate that the colloids are stable over timescales longer than the 5 min it takes to make a rheological measurement (see Appendix A.4.3 Nanorheology in blood). Figure 5:13b shows the observed blood viscosities as a function of haematocrit concentration. Clear differences are apparent between the macrorheological measurements (blue and green), which rise with haematocrit percentage, and the nanorheological measurements (red), which show a low and constant viscosity (e.g. $p < 0.001$ at 50% haematocrit). Such measurements therefore represent an novel means for observing blood plasma viscosity, an important indicator in the diagnosis of chronic disorders, malignancy, vascular diseases, haematological cancers, and cardiovascular diseases,[273, 274] without the need to first separate blood cells from whole blood.

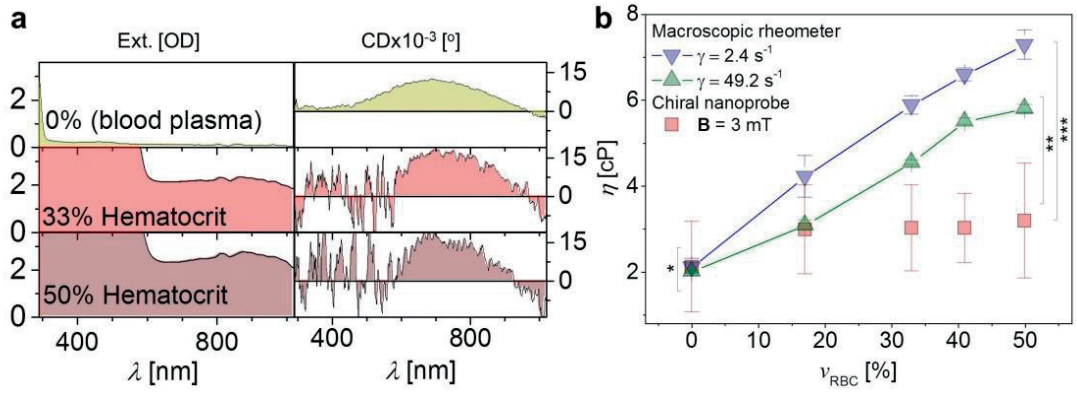

Figure 5:13 *In situ* active nanorheology in blood. (a) Extinction and CD spectra of the colloidal Au-Fe nanohelices as a function of λ in bovine blood plasma surrounded by the erythrocytes at different volume fractions (top: 0%, middle: 33%, bottom: 50%). (b) The measured dynamic viscosity, η of the bovine blood plasma in the presence of red blood cells with different hematocrit level. The macroscopic measurements were made at different shear rates (green top triangles: 2.4 s^{-1} and blue bottom triangle: 49.2 s^{-1}). The star symbols (*) represent the statistical analysis of the measured viscosities at 0% and 50% haematocrit (rheometer: 3 times, nanoprobe: 4 times). *$p > 0.1$, **$p < 0.01$, and **$p < 0.001$ (one-way ANOVA). Reprinted with permission from Ref. 136 (Copyright 2016 American Chemical Society)

5.7 Methods

Block copolymer micelle nanolithography (BCML): The hexagonal array of Au nanoparticles was prepared using block-copolymer micelle nanolithography as previously reported.[57] Poly (styrene)-b-poly (2-vinylpyridine) (S units: 1056; VP units: 671) was dissolved in toluene at a concentration of 4 mg·mL^{-1} and stirred overnight. $HAuCl_4 \cdot 3(H_2O)$ was added to the polymer solution at a molar ratio of 0.5 per vinyl pyridine unit and stirred for at least 48 hrs. Spherical micelles, loaded with Au salts in the core, form by self-assembly. The micelles are spin-coated onto a two-inch Si wafer at 8000 rpm for 1 min where they form a

quasi-hexagonally close-packed monolayer. Subsequent plasma treatment under 10% H_2 and 90% Ar plasma (power: 350 W, pressure: 0.4 mbar, time: 45 min) reduces the Au to form nanoparticles with ~12 nm in diameter and spaced ~100 nm apart (as measured by scanning electron microscopy (SEM)).

Nano Glancing angle deposition (nanoGLAD): Au-Fe nanohelices were grown on the array of the Au nanoparticles in a custom-built GLAD system at T = 90K, based on co-deposition from two electron-beam evaporators with a base pressure of 1×10^{-6} mbar. The substrate manipulator provides independent control over the azimuthal direction φ, and molecular flux direction α during deposition. To grow nanohelices, the flux angle α and the azimuthal rotation rate per unit thickness $d\varphi \cdot dw^{-1}$ were kept to respectively 87° and 1.8±0.1 °·nm^{-1} with closed-loop feedback based on measurements of material deposition rates on a quartz crystal monitor. The alloy stoichiometry was controlled by measuring and controlling the deposition rates from each evaporator independently to maintain the desired ratio.

Preparation of colloidal solution: The grown nanohelices were removed from the wafer by bath sonication of a wafer piece in an aqueous solution of 1 mM sodium citrate for ~2 min.

SEM, TEM, and STEM-EDX analysis: Structures were imaged with SEM (Gemini ultra 55, Zeiss), TEM (CM200, Philips), and STEM (SESAM, Zeiss). TEM samples were prepared by drop casting ~10 µL of the colloidal solution onto a Holey® carbon coated TEM grid (Cu 400 mesh), followed by drying under a gentle flow of Ar gas. Bright-field TEM images were recorded under an accelerating voltage of 200 kV.

UV-VIS-NIR spectroscopy and CD spectroscopy: Extinction spectra of the nanocolloids were measured on a Cary UV-VIS-NIR 5000 spectrophotometer. Circular dichroism spectra were obtained with a Jasco J-810 circular dichroism spectrometer. All the spectra were measured with a scan rate of 500 nm·min^{-1} in the wavelength range of ~300 to 1050 nm with 0.1 nm intervals.

Dark-field optical microscopy: Dark field microscopy videos were taken on a Zeiss Axio Observer Z1 inverted microscope with an attached Basler acA2000-340kc camera. Videos were taken at a frame rate of 20 f·sec^{-1}. A square, double-sided piece of tape with the centre removed was adhered on a clean glass cover slip to create a fluid chamber (~ 20 µL) and the colloidal solution was sandwiched between two cover slips. A 100× objective lens (NA = 1.25, oil immersion) and a dark filed condenser (NA = 1.2/1.4) were used to collect the light scattered from the Au-Fe nanohelices.

SQUID magnetometer: SQUID measurements were taken of the array of Au-Fe nanohelices on a piece of Si wafer (~ 0.5 cm^2) out of plane (OOP) at 300 K using a Quantum Design magnetic property measurement system (MPMS) magnetometer.

Numerical simulations: For the numerical calculation of the Au-Fe nanohelices CD spectrum, firstly the dielectric function of Au-Fe was calculated as a function of wavelength based on the optical constants provided by Paik.[292] An atomic ratio of 1:1.5 of Auer was assumed which is based on the ICP-OES results. The chiroptical response of the Au-Fe nanohelix alloy was computed using the DDASCAT 7.2.[293] The scattering and absorption of 2-turn left-handed helices were calculated for a geometry that is based on the statistical analysis of the TEM images of the 100 individual nanohelices. The helix is modelled as an array of polarizable point dipoles spaced 2.161 nm apart, and their interactions were calculated using the code developed by the group.[56, 64]. The optical response was computed by DDSCAT by averaging 342 orientations ($18\theta \times 19\beta$) of the Au-Fe nanohelix across the wavelength range from 200 nm to 1100 nm. θ and β are the rotational angles of the long-axis and short-axis of the helix respectively. The application of the external

magnetic field in the experiment constrains the helix's θ rotation, but not its rotation about β. Thereby, for the comparison between the calculation and experiment, the theoretical CD spectra have been recalculated as $CD_{exp}(\theta_{\mathbf{B}}) =< CD_{cal}(\theta) >_{\beta}$.

Fluid and blood sample preparation: Glycerol-water mixtures were prepared at concentrations of 0-50%. The viscosities were based on values found in 254. Polystyrene beads of 8 µm diameter suspended in water (PPS-8.0, Kiskerbiotech GmbH, Germany) were used for the particle rheology. The volume fraction of the beads was controlled with 2:10 (17%), 5:10 (33%), 7:10 (41%), 10:10 (50%) volume ratios in water. Blood plasma was separated from whole bovine blood stabilised in the anticoagulant citrate dextrose (ACD) solution (Fiebig-Nährstofftechnik, Germany) by centrifuging at 2000 g for 15 min. For the nanorheology measurements, the Au-Fe nanohelices were removed from the wafer by sonicating a piece of sample wafer (~ 0.3 cm^2) in 1 mL of blood plasma for ~2 min. Samples were also prepared with haematocrit by mixing blood plasma with packed erythrocytes at 2:10 (17%), 5:10 (33%), 7:10 (41%), 10:10 (50%) volume ratios. A rotational rheometer (HAAKE RheoStress 1, Thermo Scientific) with a parallel plate geometry was used to measure the viscosity, and ~40 mL of blood sample was measured at shear rates ranging from 2 to 100 s^{-1} (at a solution temperature of 20°C).

Nanorheological viscosity measurements: Suspended magnetic nanohelices were subjected to rotating magnetic fields over a range of frequencies $f_{\mathbf{B}}$ = 1 to 80 Hz at $\mathbf{B}$ = 3 mT at *T* = 20 °C. The amplitude and the phase angle of the CD response at λ = 880 nm were measured using a lock-in amplifier referenced to the magnetic field modulation. The phase was carefully corrected for phase lags introduced by the frequency dependent inductance of the magnetic coils, and the mechanical phase angle was recovered from the optical phase. Small volume cuvettes (~ 300 µL) with 1 mm path lengths were used.

Molar circular dichroism: For the evaluation of the molar CD of the Au-Fe nanocolloids, the molar concentration of colloidal nanohelices in 1 mL solution was calculated as 20.3 pM. The molar CD of the colloidal nanohelices is given as,[100] $\mathrm{Molar\ CD} = \mathrm{CD}/\mathrm{c} \cdot l$ [o · M^{-1} · cm^{-1}], where c is the molar concentration of the colloidal nanohelices, l is the optical path length of the cuvette (l = 0.5 cm).

Chapter 6 Conclusion

Chiral plasmonics concerns the optical behaviours of metal nanoparticles that are plasmonically active and chiral (or linked to chiral molecules).[102] As the fabrication of chiral nanoparticle is still challenging, many promising applications have not yet been fully realised. While some sensing applications have been demonstrated, the study of their underlying mechanisms, reaction yields, and the colloidal stability of the sensors are still under investigation.[15, 40, 125] In particular any corrosion of nanoparticles limits the possibility to apply nanoparticles in chemically demanding or biological environments.[18, 41, 294] Therefore, the primary focus of this thesis is novel chiral nanoparticles, with the aim to demonstrate how they can be efficiently grown, protected against corrosion in biological fluids, and then used for sensing application.

A robust fabrication method has been advanced so that unconventional nanopatterns, which cannot be fabricated by other existing techniques, including arrays consisting of tri-layer nanoparticle, nanohole, hollow nanodome, and nanoring patterns have been achieved.[49] These new functional nanopatterns have been used for two applications, nanolithography and plasmonics. Notably, in conjunction with atomic layer deposition (ALD) this scheme was extended to grow and protect chiral nanoparticles reproducibly on the wafer scale such that they were protected against corrosion.[135] The resultant nanocolloids, which corroded within hours without protection, remained functional for weeks (in some cases even months) in aqueous solutions. This has allowed the growth and application of the first Mg nanoparticles for UV plasmonics in aqueous solutions.[109]

Then, the flexibility of the growth method has been used to tailor the composition of the nanoparticles so that the dispersion of the dielectric function is changed and engineered to be favourable for local surface plasmon sensing (LSPR).[93] These designer colloids have been used to achieve a record LSPR sensitivity, even in the presence of optically complex fluids.

Unique nanoparticles grown using the nanoGLAD method, which combined a chiral shape with a plasmonic metal and a ferromagnetic material, permitted the observation and actuation of the colloids. These ‘chiral + magnetic + plasmonic’ nanoparticles serve as an “active” plasmonic system that can be efficiently and repeatedly switched. These multifunctional nanoparticles can be actuated in fluid, and used as nanorheological probes to measure the viscosity of blood plasma in the presence of whole blood, which is extremely challenging due to a strong optical absorption (~3 optical density) and large volume fraction (~50%) of the blood cells. This is the first *in situ* active nanorheology with plasmonics. [136]

A more detailed summary and future outlook of the topics regarding nano glancing angle deposition (nanoGLAD), corrosion protection of complex 3D nanoparticles, and chiral plasmonics for sensing and nanorheology are discussed in turn in the following subsections.

6.1 Nano glancing angle deposition [49, 59]

The growth method that is used in this thesis relies on physical vapour deposition onto seed patterns. The first results of the thesis concern how the pattern shape and spacing affects the growth patterns. Growth parameters are given. The work in this thesis shows that it is possible to grow complex shapes by surrounding the growth area for the particle by a boundary. The boundaries, here called corrals, serve three important roles: a) they permit the growth of aperiodic structures so that the dimensions of the structure do not depend on the spacing to adjacent structures; b) they improve the structural quality of the features they contain, with higher aspect ratios for nanorods, and better felicity for nanohelices; c) and they create a clean area around the structure and thus act as a type of "resistless mask". The corrals offer new possibilities in GLAD based growth of 3D nanostructures in particular since the dimensional control offered by corrals creates the opportunity to place nanoscale features in arbitrary arrangements with the knowledge that a feature's structural dimensions are not influenced by the spacing to its neighbours. Furthermore, the clear area within the corral that surrounds the features at the centre will be particularly useful for nanoelectronic applications involving metals where any (unintended) deposition on the substrate would lead to short circuits in the structures.[295-297] Another application area is the field of single molecule surface enhanced Raman scattering where the geometry is important to make for effective antennas. For instance two closely spaced posts make for a very effective optical antenna allowing single molecule detection.[207] Fabricating such devices with the techniques reported here would be not only simpler, requiring substantially fewer fabrication steps, but also offers the opportunity for shape control of the post structures. In particular, GLAD grown posts could be chiral which provides the opportunity for enantiospecific sensing.

While such single point lithography is useful, the focus of this thesis is the fabrication of large numbers of nanoparticles in a short time. So the second section of chapter 2 describes how the combination of block-copolymer micelle nanolithography (BCML) with GLAD permits to turn a pattern of more than a hundred billion well-spaced nanoseed structures per square centimetre into ones that are plasmonically active with a spectral response that can be shape-tuned. The method encompasses large-areas (entire wafers) that are quickly patterned with regular arrays of nanoparticles as well as tailored 3D structures whose size, material composition, and exact shape can be flexibly tuned. It was shown the size-tuning of hexagonal close packed arrays, as well as the fabrication of wafers with nanoring, nanodome, and nanohole arrays. The flexibility in the use of materials permits their use for plasmonic or nanoimprint applications. A large choice of materials is useful when designing etch masks or for secondary processing to obtain complex nanoparticles. This approach can readily be extended to fabricate more complex nanopatterns which might be useful for optically, catalytically, electronically, and magnetically-active nano-patterned substrates and devices.

6.2 Corrosion-protected hybrid nanoparticles [135]

In chapter 3 of this thesis it was shown that nanoparticles can be effectively protected against corrosion by combining a physical vapour shadow grown plug with an atomic layer deposited shell. The method permits the complete encapsulation of the nanoparticle and nanoparticle stabilities lasting from a week to over a month have been achieved without loss of magnetic or plasmonic functionality. The stability could be shown even when the nanoparticles are immersed in physiological buffers, acidic environments and reactive solutions. Further work is required to refine the lift-off process so that colloids in suspension retain the full protection exhibited by particles on-wafer. One approach would be to include an additional sacrificial layer under the seed particles that facilitates release without the need for sonication. The work has shown protection of both nanorods and nanohelices of Co and Cu, and expect that the scheme can be extended to

produce corrosion resistant nanoparticles with the full range of core shapes[93, 186] and compositions [56, 93, 136] that nanoGLAD is capable of. This opens up a number of potential applications for nanoparticles composed of materials that are, at present, considered too reactive or toxic for practical use. These include unstable magnetic and plasmonic materials as nanoparticles for sensing,[73, 109] imaging,[227, 228, 298] as catalysts,[26, 215, 299-302] and for biomedical applications .[22, 71, 136, 303, 304]

6.3 Chiral plasmonic nanosensors [93, 109]

In chapter 4 it was shown that flattening the dielectric function of plasmonic nanomaterials by alloying results in large LSPR shifts in response to changes in their local environment. If these nanostructures are also chiral, then their polarisation dependent spectra offer additional and sharper spectral features relative to optical extinction based measurement of achiral particles. These characteristics make chiral plasmonic nanohelices especially suited for sensing applications. Furthermore, the bipolar nature of circular dichroism spectra of chiral structures leads to points of zero-crossing which have very small effective line-widths and thus result in high figures of merit. Both bulk refractive index changes as well as surface specific binding events can be observed and tracked with the engineered nanocolloidal LSPR sensors. A sensitivity of ~1100 $nm \cdot RIU^{-1}$ and a FOM of ~2900 RIU^{-1} was achieved and these are higher than those previously reported for plasmonic sensors.

Aside from extremely high detection sensitivities, these chiral sensors offer unique advantages over existing plasmonic devices. Since they are freely suspended colloids they naturally suggest themselves as sensors for *in situ* or *in vivo* biological applications, particularly, because of their small size. Since the CD signal is robust against background interference, especially in absorbing media, the sensing scheme reported herein is particularly suitable for real biological media, which are typically opaque. For instance, in the presence of whole blood, this scheme has the potential for a real-time measurement of protein corona formation, a vitally important factor for the function of nanoparticles in biological media, but one that remains poorly understood.

Additionally, the second part of chapter 4 also reports the first Mg nanoparticles that have been used for plasmonics in water. Mg nanohelices were fabricated using advanced nanoGLAD (demonstrated in chapter 3) and their chiroptical response is exceptionally strong in the UV. This feature is crucial for the detection of molecules as in the UV the dispersion of the medium surrounding the plasmonic particle gives rise to larger refractive index changes. UV sensing may thus enable single molecule detection with a plasmonic nanosensor.[305] It should be possible to increase the LSPR sensitivity further through engineering the dielectric function of Mg nanoparticles.[93] Apart from UV sensing, Mg nanoparticles are promising for resonance coupling effects for chiral sensing,[15, 40, 238, 306] and plasmon resonance energy transfer (PRET) applications,[74, 307, 308] since the plasmonic resonance of Mg in the UV approaches molecular resonances.

6.4 Active nanorheology [136]

In chapter 5 it was shown that the chiral magneto-plasmonic nanoparticles can be used for nanorheological measurements. The combination of a magnetic and a plasmonic material in a chiral shape gives rise to distinct optical spectra that are a function of the nanocolloids' orientation in solution. A rotating magnetic field was used to actuate the nanocolloids and produce a modulated optical response. Such dynamically controllable chiroptical nanostructures have potential in their own right as nanoscale sensors, switches,[15, 32, 37, 309] and probes of higher order quadrupolar interaction terms that would normally be undetecta-

ble because of orientational averaging.[310] In chapter 5 it has been demonstrated that the chiral nanohelices function as wireless mechanical nanosensors capable of selectively measuring a fluid's viscosity even in the presence of scatterers and strong absorption, e.g. blood cells (50% volume fraction and OD~3). The presence of microparticles and cells can dominate any macroscopic rheological measurement, but they do not directly affect a nanorheological probe. Optical (plasmonic) sensing methods could be appealing for medical applications, as they allow for non-invasive measurements. *In situ* active nanorheology is seen as a promising candidate for the measurement of viscosity in complex biological fluids, such as blood plasma[311] in whole blood, with only microscopic sample volumes required. This scheme can also be applied to fluids with non-Newtonian properties[47], and would expand its breadth to include measurement of the nanoscale mechanics of biomaterials such as the intracellular matrix.

Appendices

A.1 Chapter 2: Nano glancing angle deposition

The results presented in this section were taken from the following sources:

[59] Shape control in wafer-based aperiodic 3D nanostructures, **H.-H. Jeong**, A.G. Mark, J.G. Gibbs, T. Reindl, U. Waizmann, J. Weis, and P. Fischer, ***Nanotechnology*** 25, 235302 (2014) - Cover article

[49] Selectable nanopattern arrays for nanolithographic imprint and etch-mask applications, **H.-H. Jeong**, A.G. Mark, T.-C. Lee, K. Son, W. Chen, M. Alarcón-Correa, I. Kim, G. Schütz, and P. Fischer, ***Advanced Science*** 2, 1500016 (2015) - Cover article

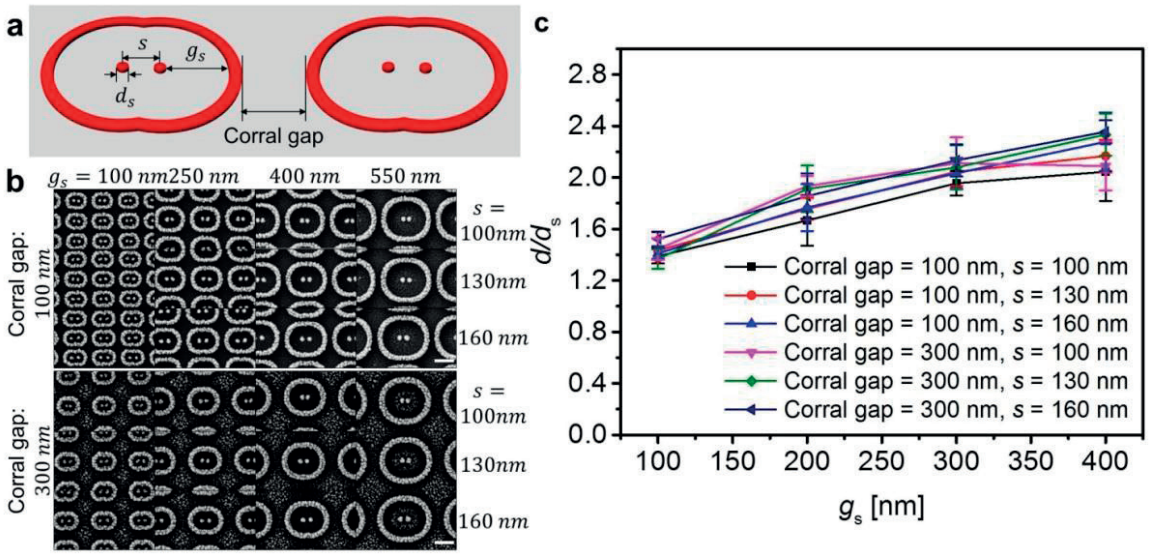

Figure A:1 The effect of corral spacing on nanodot shape. (a) Schematic of the relevant seed dimensions showing two closely spaced corrals separated by a gap. (b) SEM images of corrals with varying dot spacing (columns), dot-corral distance (rows), and corral gap (upper vs lower block). Each scale bar is 400 nm. (c) The ratio of nanocolum diametre to seed diametre. The trend in d/d_s is dominated by gs, the dot-corral distance, with no discernable dependence on the dot-dot spacing, or the gap between corrals. Reprinted from Ref. 59 (Copyright 2014 Institute of Physics)

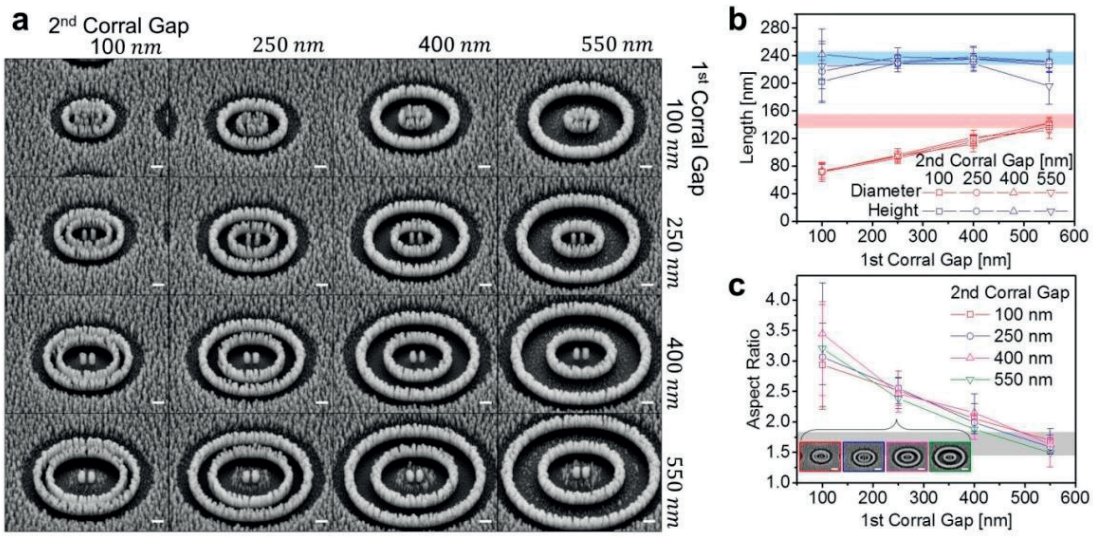

Figure A:2 Fabrication of nanorods on double dots in double sacrificial corrals. (a) 45°-tilted view of SEM images for the fabricated nanorods with a variety of conditions of double sacrificial corrals. The gaps of 1st and 2nd sacrificial corrals were increased from 100 nm to 550 nm with 150 nm intervals which were correspond to from top to bottom and from left to right. Each scale bar is 200 nm. (b) The heights, the diametres, and (c) the aspect ratios of nanorods with various sizes of double sacrificial corrals. Each scale bar of inset SEM images is 400 nm. Reprinted from Ref. 59 (Copyright 2014 Institute of Physics)

A.1.1 The Effect of Seed Spacing on Column Broadening

As described in chapter 2, columns in GLAD are grown by rapidly rotating the substrate. Ideally, shadowing from the adjacent structures limits deposition and growth to take place on the top of the structure. However, for a periodic structure there are necessarily gaps in the shadows because of the spaces between the seeds. Through those gaps the incident flux impinges upon the structures' sidewalls leading to broadening. The proportion of the 2π azimuthal sweep for which shadowing is takes place can be approximated by considering the projected angle subtended by each of a structure's nearest neighbours δ_N, and next-nearest neighbours δ_{NN}.

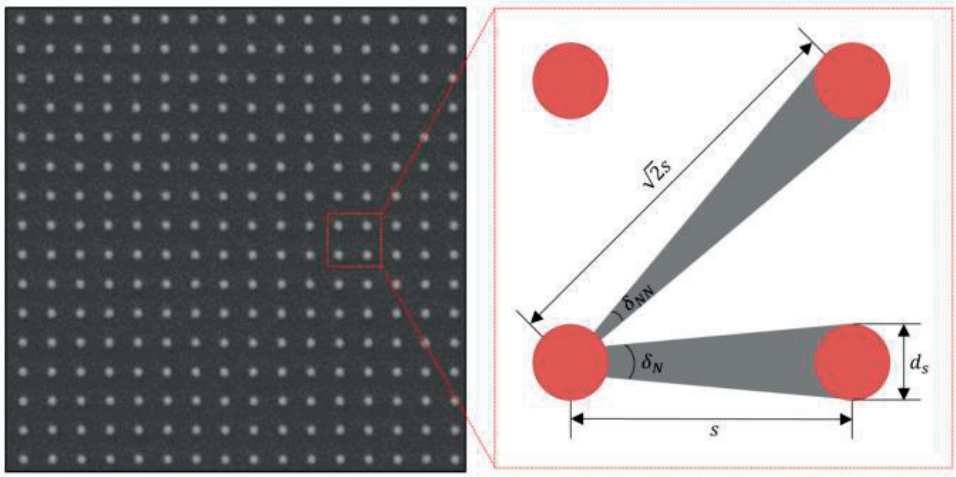

Figure A:3 Simplified schematic of shadowing on the bottom left seed from its nearest and next-nearest neighbours. Reprinted from Ref. 59 (Copyright 2014 Institute of Physics)

When the incident flux arrives from azimuthal angles within the grey regions, these are given by

$$\delta_N = 2\tan^{-1}\left(\frac{d_s}{2s}\right) \tag{A:1}$$

$$\delta_{NN} = 2\tan^{-1}\left(\frac{d_s}{2\sqrt{2}s}\right) \tag{A:2}$$

Therefore proportion of the rotation spent in shadow is

$$S = \frac{4(\delta_N + \delta_{NN})}{2\pi} \tag{A:3}$$

This fraction is tabulated below for the structures shown in figure 2:3:

g_s (nm)	100	250	400	550
S (%)	56	28	19	14

Thus, the 100 nm gap structures are shadowed for substantially longer than their 250 nm counterparts, and as a result will suffer less broadening.

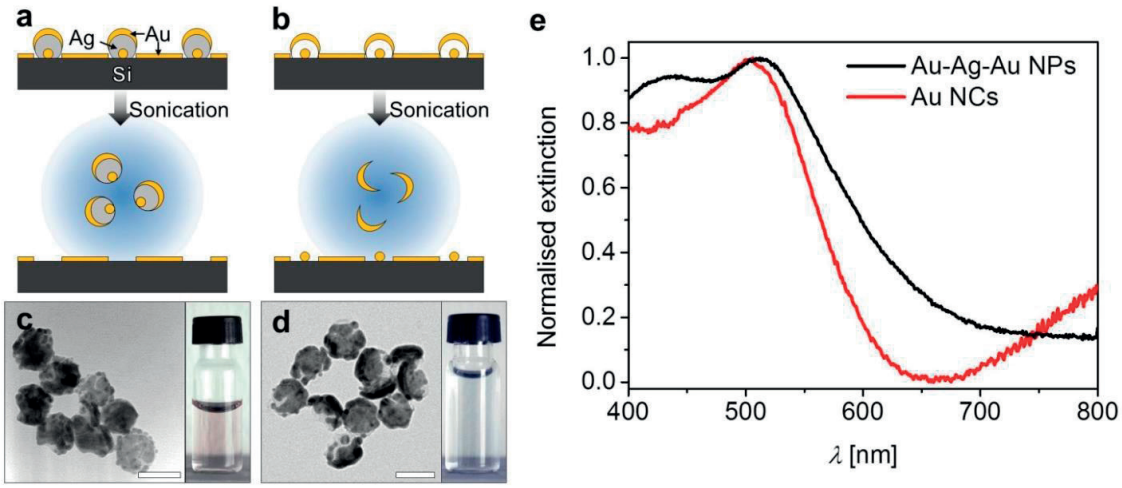

Figure A:4 Hybrid nanocolloids. Schematic views of the fabrication of (a) colloidal Au-Ag-Au hybrid NPs from the multi-functional nanopattern and (b) colloidal Au NCs from the hollow nanodome pattern. TEM images of (c) Au-Ag-Au hybrid NPs and d) Au NCs (scale bar: 50 nm). The photos of the 2 mL glass vials show the corresponding colloidal solution of the Au-Ag-Au hybrid NPs and the Au NCs. (e) Extinction spectra of colloidal Au-Ag-Au hybrid NPs (black line) and colloidal Au NCs (red line). Reprinted from Ref. 49 (Copyright 2015 Wiley-VCH publisher)

A.2 Chapter 3: Corrosion-protected hybrid nanoparticles

The results presented in this section were taken from the following source:

[135] Corrosion-protected hybrid nanoparticles, **H.-H. Jeong**, M. Alarcón-Correa, A.G. Mark, K. Son, T.-C. Lee, and P. Fischer (*submitted*)

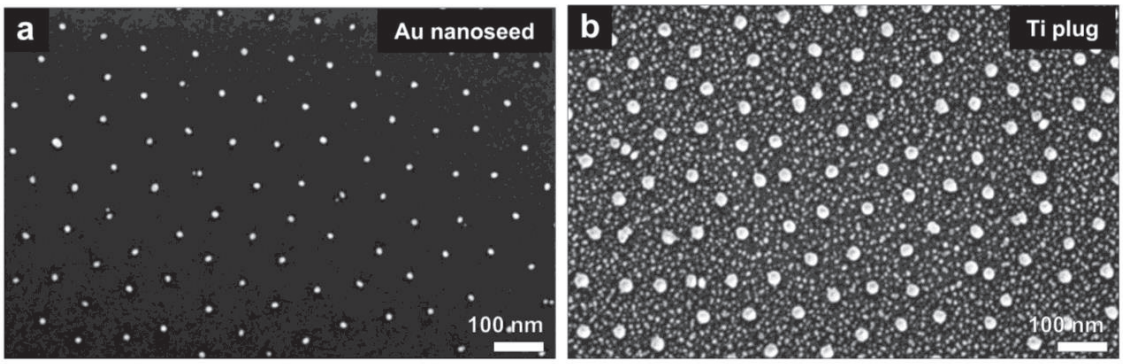

Figure A:5 (a) SEM image (top view) of an array of ~10 nm gold nanoparticles prepared by BCML. (b) SEM image of the well-isolated plugs (Ti) on top of the Au seeds grown by GLAD.

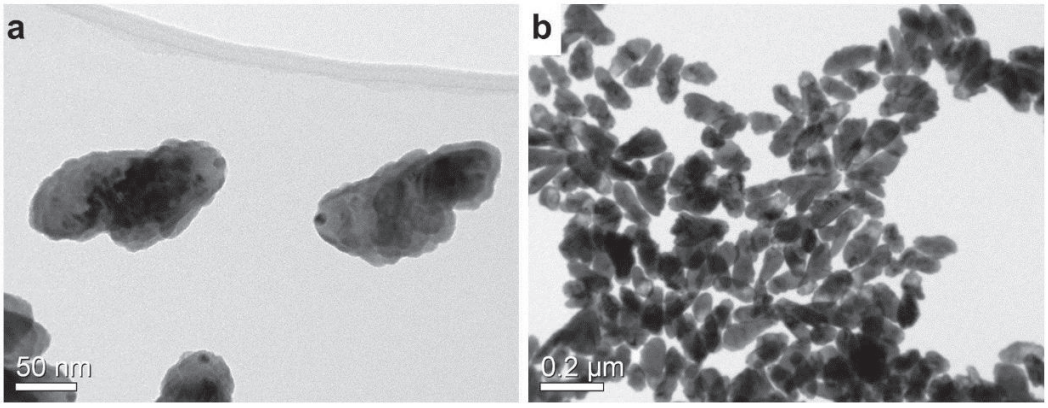

Figure A:6 TEM images of the Co nanorods protected with 4 nm thick HfO_2 layer after 7 days in water.

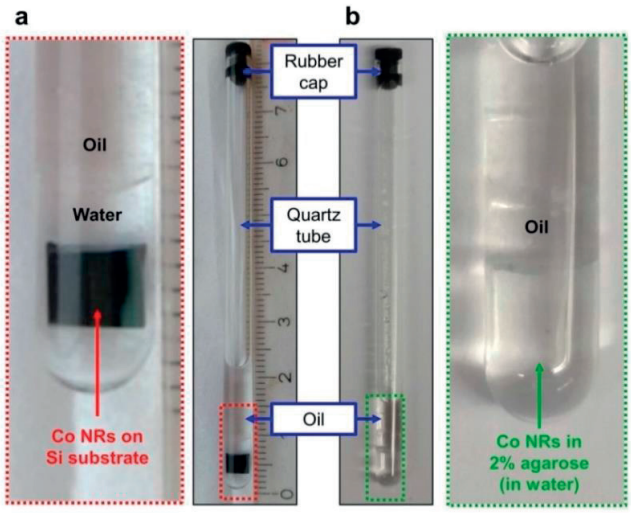

Figure A:7 Sample preparations for *in situ* observations of ferromagnetic properties of Co NRs in water. (a) A piece of Si wafer with the array of Co NRs was immersed in water in a quartz tube. To prevent water evapouration into the SQUID chamber, it was blocked by oil (left panel) and a 3D-printed rubber cap (right panel). (b) At high temp., the colloidal solution of nanoparticles was mixed with 4% agarose and it was quenched in a fridge. Then, it was blocked by oil (right panel) and a 3D-printed rubber cap (left panel).

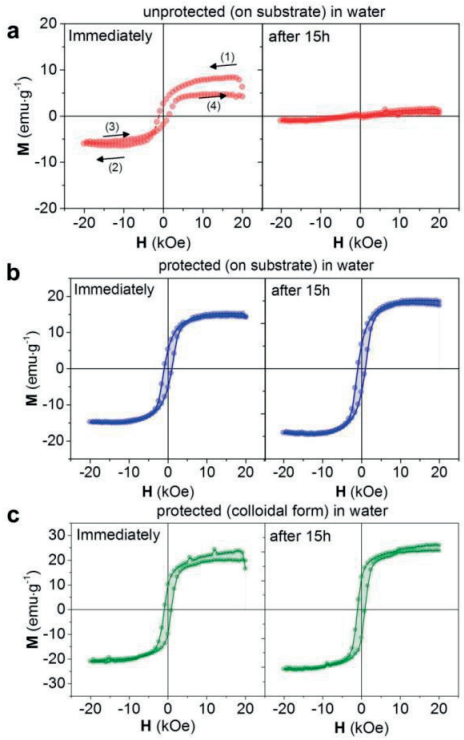

Figure A:8 *In situ* observation of the ferromagnetic properties of the Co nanorods in water: In-plane magnetic properties of (a) the unprotected Co nanorods and (b) protected Co nanorods with 4 nm HfO_2 layer on the Si substrate in water (the numbers indicate the order of the measurements with the arrows showing the magnetic field sweep direction). (c) Magnetic property of the protected Co nanorods with 4 nm HfO_2 layer suspended with the isotropic orientation in 2% agarose gel. Each panel on the left shows the measurement immediately after sample preparation and the right panels show measurements after the sample has been exposed to water for 15h.

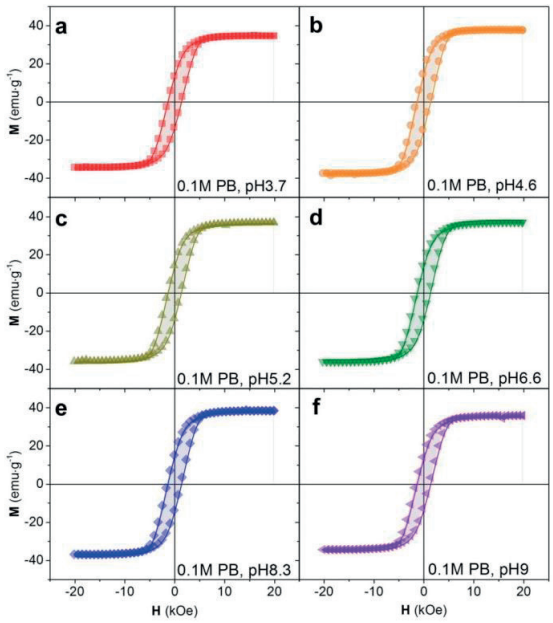

Figure A:9 Out-of-plane ferromagnetic properties of the protected Co nanorods on the Si wafer after 7 days in 0.1 M phosphate buffer solutions at (a) pH 3.7, (b) pH 4.6, (c) pH 5.2, (d) pH 6.6, (e) pH 8.3, and (f) pH 9.

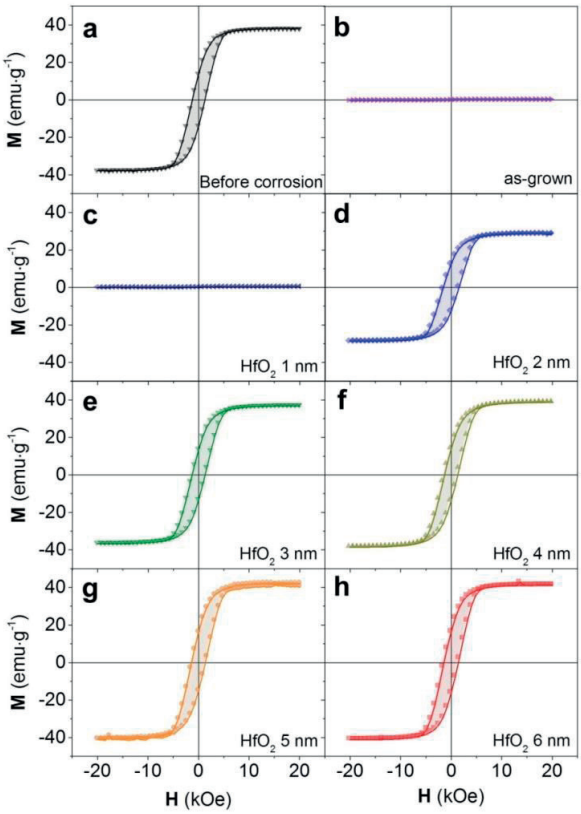

Figure A:10 Our-of-plane ferromagnetic properties of the Co nanorods protected with different thicknesses of the HfO_2 layer on the silicon wafer: 0 nm (a) before and (b) after exposure to water (corrosion) for 7 days, and (c) 1 nm, (d) 2 nm, (e) 3 nm, (f) 4 nm, (g) 5 nm, and (h) 6 nm after exposure to water for 7 days.

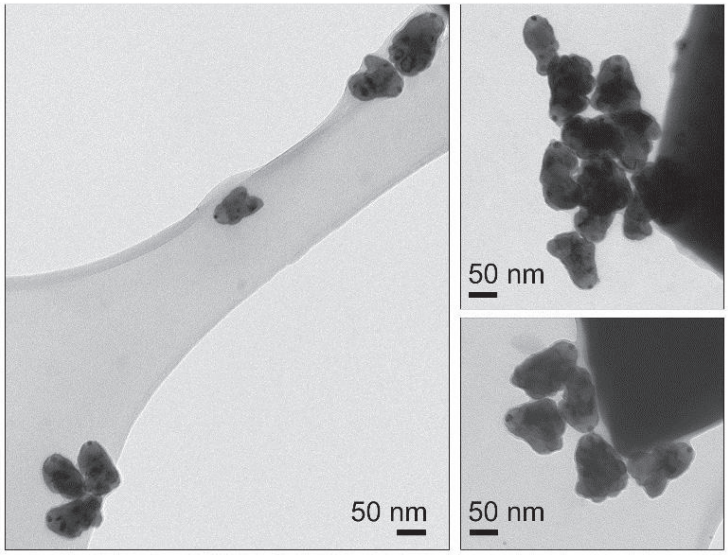

Figure A:11 TEM images of the Cu nanorods protected with 3 nm thick HfO_2 layer after 2 days in 0.1 M phosphate buffer solution at pH 3.7.

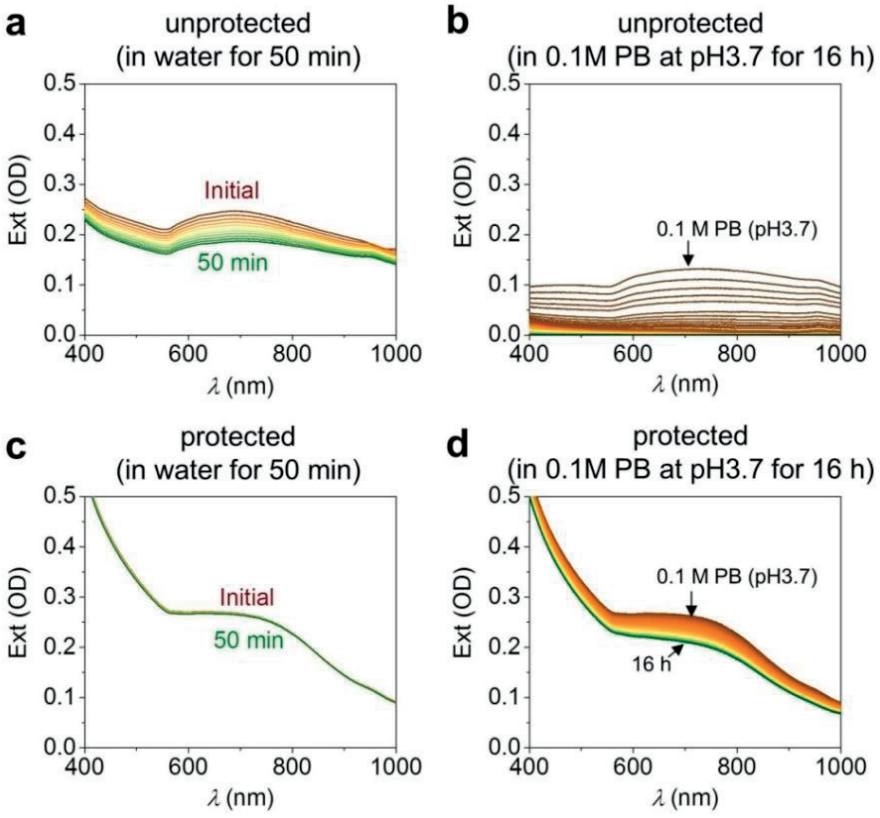

Figure A:12 *In situ* observation of the stability of colloidal Cu nanorods in 0.1M phosphate buffer solution at pH 3.7. The extinction spectra of the unprotected Cu nanocolloids in (a) 2% agarose gel for 50 min and (b) after adding 0.1M phosphate buffer solution for 16 h with 5 min intervals. The extinction spectra of the protected Cu nanocolloids with a 4 nm HfO_2 layer in (c) 2% agarose gel for 50 min and (d) after adding 0.1M phosphate buffer solution for 16 h measured in 5 min intervals.

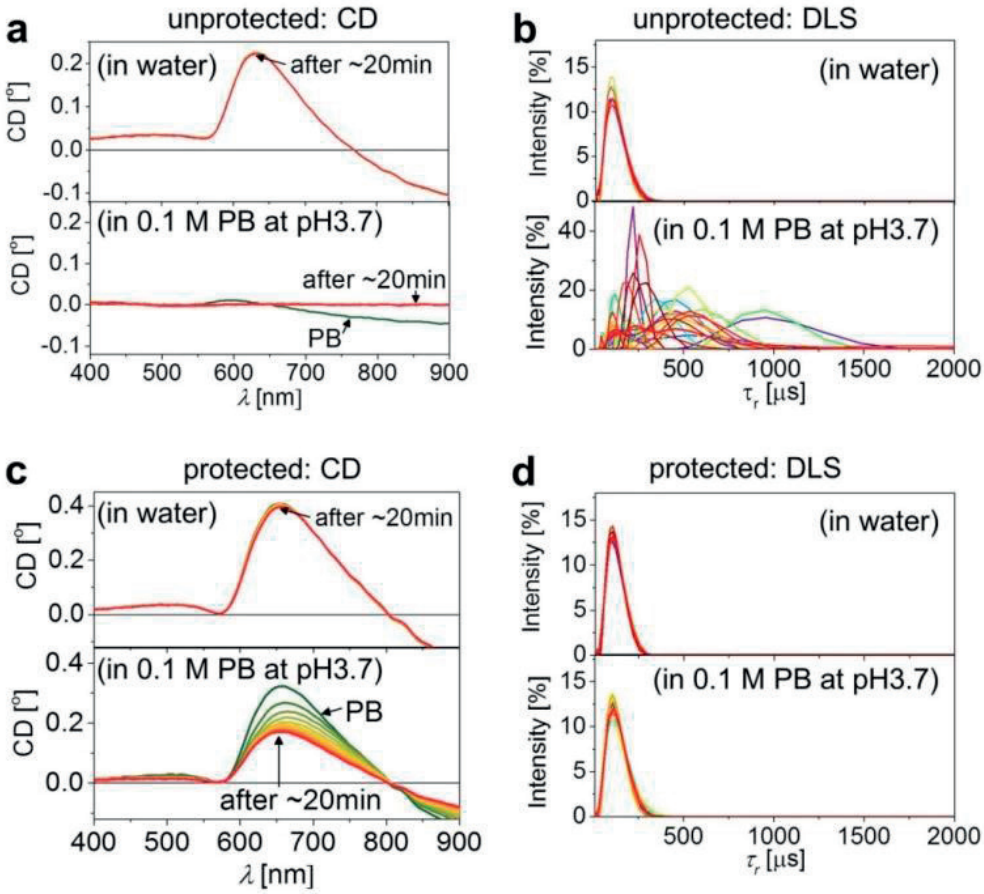

Figure A:13 Stabilities of the unprotected and protected Cu nanohelices in 0.1 M phosphate buffer solutions at pH 3.7. (a) The chiroptical spectra and (b) DLS spectra of the colloidal unprotected Cu nanohelices in water (top panel) and buffer (bottom panel) for 20 min with 2 min intervals. (c) The chiroptical spectra and (d) DLS spectra of the colloidal protected Cu nanohelices in water (top panel) and buffer (bottom panel) for 20 min with 2 min intervals.

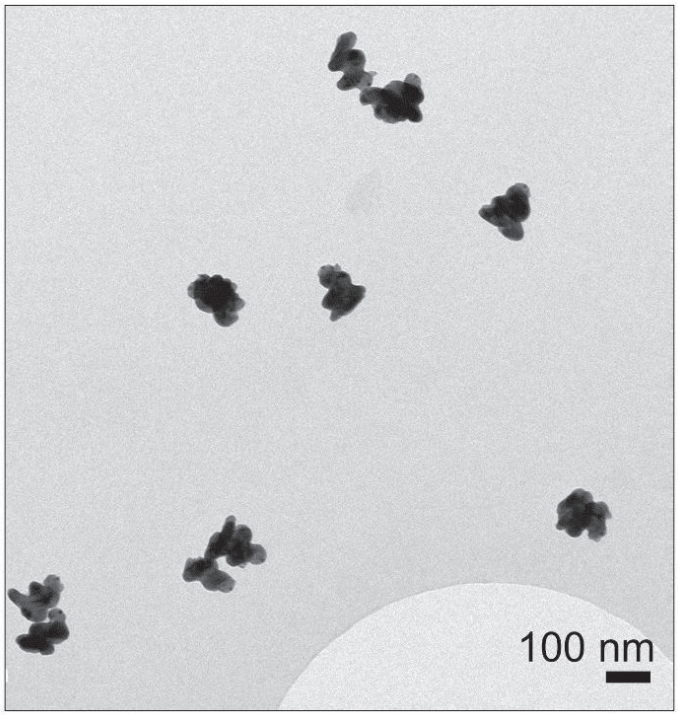

Figure A:14 TEM image of the Cu nanohelices protected with 3 nm thick HfO_2 layer after 2 days in 0.1 M phosphate buffer solution at pH 3.7.

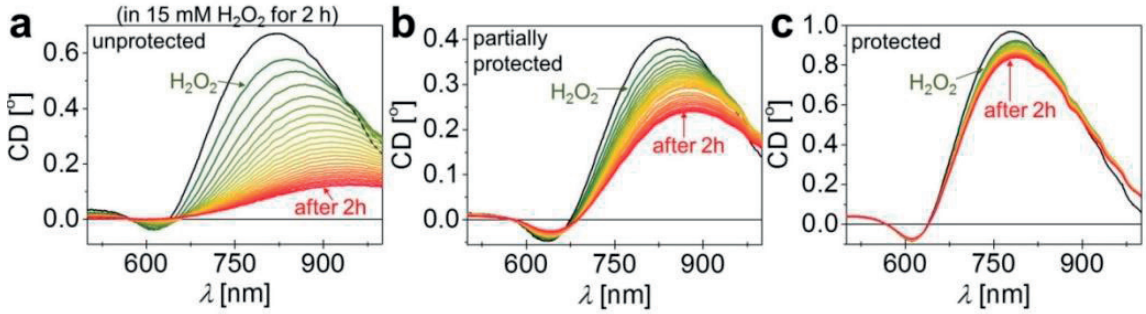

Figure A:15 *In situ* observation of the chiroptical spectra of colloidal Cu nanohelices in 15 mM (0.035%) H_2O_2. (a) unprotected (without plug and shell), (b) partially protected (without shell), and (c) completely protected (with plug and shell).

A.3 Chapter 4: Chiral plasmonic nanosensors

The results presented in this section were taken from the following sources:

[93] Dispersion and shape engineered plasmonic nanosensors, **H.-H. Jeong**, A.G. Mark, M. Alarcón-Correa, I. Kim, P. Oswald, T.-C. Lee, and P. Fischer, ***Nature Communications*** 7, 11331 (2016)

[109] Magnesium plasmonics for UV applications and chiral sensing, **H.-H. Jeong**, A.G. Mark, and P. Fischer, ***Chemical Communications*** 52, 12179 (2016)

A.3.1 Chiral plasmonic sensitivity, FWHM, and FOM

(This part is mainly invented and contributed by Dr. Andrew G. Mark)

In order to evaluate the refractive index sensitivity (S_n), full width half maximum (FWHM), and figure of merit (FOM) of the chiral plasmonic sensing, we start by defining a chiral version of the plasmonic extinction formula

$$E_{\pm} \propto \frac{1}{\lambda}\left(\frac{\varepsilon_i}{(\varepsilon_r + (\overline{\chi} \pm \delta\chi)n^2)^2 + \varepsilon_i^2}\right). \tag{A:4}$$

Here, the shape factor has been split into an achiral component $\overline{\chi}$, and a part $\delta\chi$ which depends on the chirality of the particle. If the particle is achiral then $\delta\chi$ = 0 and the equation above reduces to the usual one which peaks when $\varepsilon_r = -\overline{\chi}n^2$.[89, 91]

The circular dichroism is the difference between the extinctions for left and right handed polarised light

$$\mathrm{CD} \propto E_- - E_+. \tag{A:5}$$

Nulls in the CD occur when

$$0 = E_- - E_+ \tag{A:6}$$

$$\propto [\varepsilon_r + (\overline{\chi} - \delta\chi)n^2]^2 - [\varepsilon_r + (\overline{\chi} + \delta\chi)n^2]^2 \tag{A:7}$$

$$= \delta\chi\varepsilon_r n^2 + \overline{\chi}\delta\chi n^4 \tag{A:8}$$

$$\varepsilon_r^* = -\overline{\chi}n^2. \tag{A:9}$$

So the CD crossing point corresponds to the peak position in the extinction of an achiral particle with the same $\overline{\chi}$. The wavelength of the resonance condition shifts with refractive index according to

$$S_n = \frac{d\lambda^*}{dn} = \frac{\frac{d\varepsilon_r^*}{dn}}{\frac{d\varepsilon_r}{d\lambda}\Big|_{\lambda^*}} = \frac{-2\overline{\chi}n}{\frac{d\varepsilon_r}{d\lambda}\Big|_{\lambda^*}}. \tag{A:10}$$

Near the crossing point the CD can be linearised to have a form something like $\mathrm{CD} = m(\lambda - \lambda^*)$. The reciprocal of the absolute value of this, $|\mathrm{CD}|^{-1}$ is our "peak". Since it is divergent it has no well-defined maxi-

mum, so we follow the practice in Ref. 120, and define the maximum as the smallest CD we can reasonably measure: the instrumental resolution σ. This sets our peak maximum at σ^{-1}, which means we're looking for the width at $\frac{1}{2}\sigma^{-1}$. This gives a half width at half max of $\lambda - \lambda^* = \frac{2\sigma}{|m|}$. So the full width is

$$\mathrm{FWHM} = \frac{4\sigma}{|m|} = \frac{4\sigma}{\left|\frac{d\mathrm{CD}}{d\lambda}\right|_{\lambda^*}}. \tag{A:11}$$

What remains is to determine the slope. Let's start by looking at how the extinction for the (+) polarization changes with wavelength near λ^*.

$$\frac{dE_+}{d\lambda} = \frac{-E_+}{\lambda}\left(1 + \frac{2\lambda[\varepsilon_r + (\overline{\chi} + \delta\chi)n^2]}{[\varepsilon_r + (\overline{\chi} + \delta\chi)n^2]^2 + \varepsilon_i^2}\frac{d\varepsilon_r}{d\lambda}\right). \tag{A:12}$$

The slope of the CD signal is the difference between the slopes for positive and negative polarizations.

$$\frac{d\mathrm{CD}}{d\lambda} \propto \frac{dE_-}{d\lambda} - \frac{dE_+}{d\lambda} \tag{A:13}$$

$$= \frac{1}{\lambda}\left\{(E_- - E_+) + 2\lambda\left(\frac{\varepsilon_r + (\overline{\chi} - \delta\chi)n^2}{[\varepsilon_r + (\overline{\chi} - \delta\chi)n^2]^2 + \varepsilon_i^2} - \frac{\varepsilon_r + (\overline{\chi} + \delta\chi)n^2}{[\varepsilon_r + (\overline{\chi} + \delta\chi)n^2]^2 + \varepsilon_i^2}\right)\frac{d\varepsilon_r}{d\lambda}\right\}. \tag{A:14}$$

At the crossing point, the first term (i.e. the CD) is, by definition, zero. Also, since at the crossing point the resonance condition is fulfilled, $\varepsilon_r + \overline{\chi}n^2 = 0$, and this reduces to

$$\left.\frac{d\mathrm{CD}}{d\lambda}\right|_{\lambda^*} = \left(\frac{4\delta\chi n^2}{(\delta\chi n^2)^2 + \varepsilon_i^2}\right)\left.\frac{d\varepsilon_r}{d\lambda}\right|_{\lambda^*} \tag{A:15}$$

$$= \left(\frac{4\delta\chi n^2}{\varepsilon_i^2}\right)\left.\frac{d\varepsilon_r}{d\lambda}\right|_{\lambda^*}. \tag{A:16}$$

Combining this with the above FWHM eqnuation gives

$$\mathrm{FWHM} = \frac{4\sigma\varepsilon_i^2}{|\delta\chi|n^2\left|\frac{d\varepsilon_r}{d\lambda}\right|_{\lambda^*}}, \tag{A:17}$$

and a figure of merit of

$$\mathrm{FOM} = \frac{S_n}{\mathrm{FWHM}} = \frac{|\delta\chi|n^2}{\sigma\varepsilon_i^2}\frac{d\varepsilon_r^*}{d\lambda} = \frac{2\overline{\chi}|\delta\chi|n^3}{\sigma\varepsilon_i^2}. \tag{A:18}$$

A.3.2 Bulk refractive index sensing

To clarify the peak positions at λ_M and λ_m from the small signal fluctuation caused by the mechanical damping of the gratings, the measured CD spectrum has been smoothed in the Origin software. Figure A:16 shows, as an example, the comparison of CD spectrum of colloidal $Ag_{0.97}Ti_{0.03}$:L_4 nanohelices before and after signal smoothing process and this presents that the smoothed signal helps to recognise the peaks, but does not distort the signal information. The following figures A:17–21 show the bulk refractive index sensing using different colloidal solutions of the grown Ag-Ti nanohelices, $Ag_{0.97}Ti_{0.03}$:L_1, $Ag_{0.97}Ti_{0.03}$:L_3, $Ag_{0.97}Ti_{0.03}$:L_4, $Ag_{0.89}Ti_{0.11}$:L_1, and $Ag_{0.77}Ti_{0.23}$:L_1 respectively.

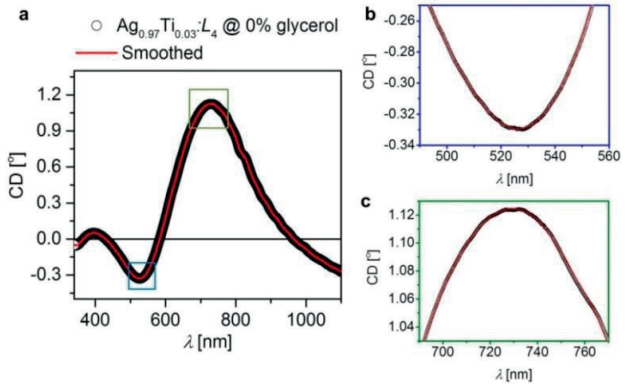

Figure A:16 Signal smoothing. (a) Comparison of the CD spectrum of colloidal $Ag_{0.97}Ti_{0.03}$:L_4 nanohelices at n = 1.333 RIU (water) before and after the signal smoothing process. (open black circle: measured data and red line: smoothed data). Its detailed plots of the resonance peaks at (b) λ_m and (c) λ_M. Reprinted from Ref. 93 (Copyright 2016 Nature Publishing Group)

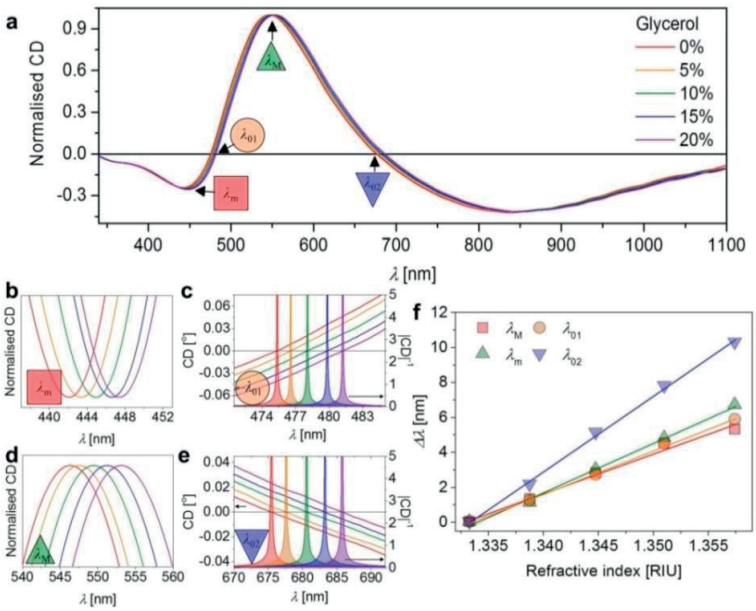

Figure A:17 (a) CD spectra of colloidal $Ag_{0.97}Ti_{0.03}$:L_1 nanohelices in media of five different refractive indices (red: 0%, orange: 5%, green: 10%, blue: 15%, and violet: 20% glycerol/water mixtures) over the full spectral range and detailed plots of the resonance shifts at (b) λ_m (red square), (c) λ_{01} (orange circle), (d) λ_M (green top triangle), and (e) λ_{02} (blue bottom triangle). (f) Wavelength shift, relative to water, of the four spectral features as a function of n. Reprinted from Ref. 93 (Copyright 2016 Nature Publishing Group)

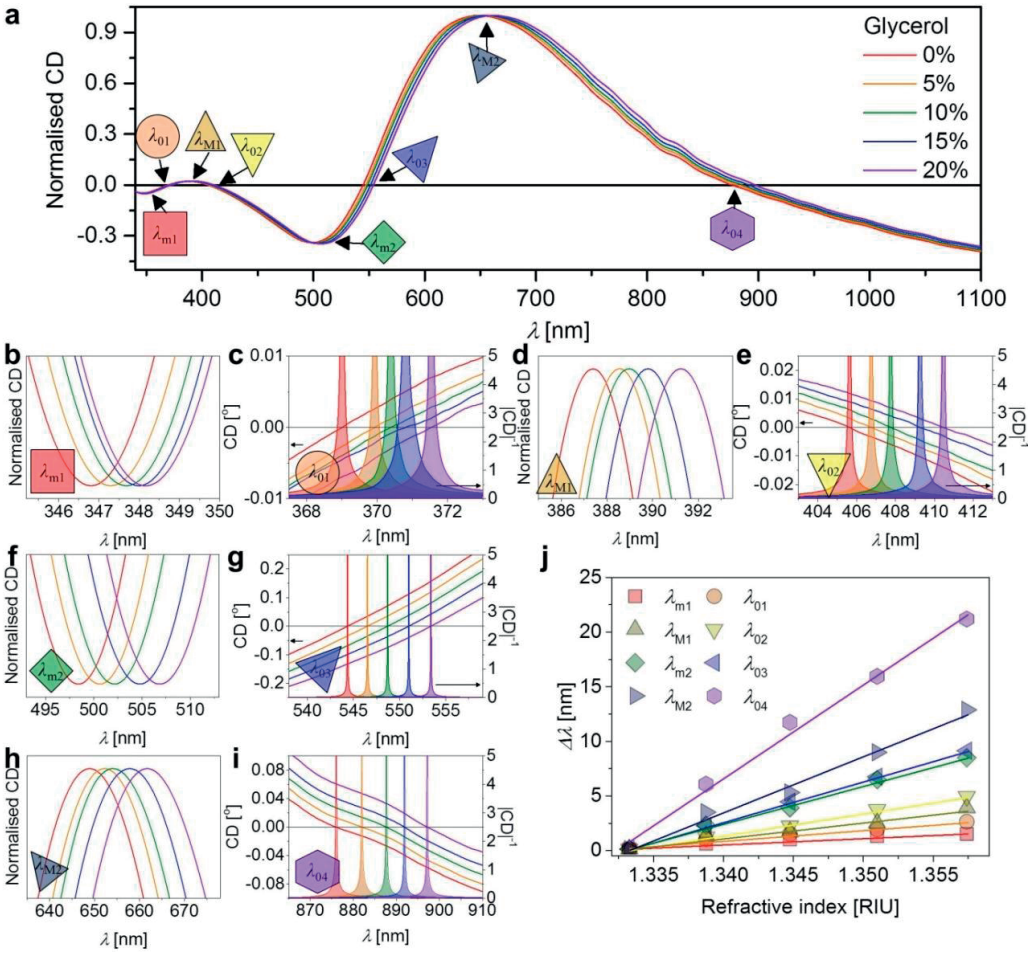

Figure A:18 (a) CD spectra of colloidal $Ag_{0.97}Ti_{0.03}$:L_3 nanohelices in media of five different refractive indices (red: 0%, orange: 5%, green: 10%, blue: 15%, and violet: 20% glycerol/water mixtures) over the full spectral range and detailed plots of the resonance shifts at (b) λ_{m1} (red square), (c) λ_{01} (orange circle), (d) λ_{M1} (dark yellow top triangle), (e) λ_{02} (yellow down triangle), (f) λ_{m2} (green diamond), (g) λ_{03} (blue left triangle), (h) λ_{M2} (navy right triangle), and (i) λ_{04} (violet hexagon). (j) Wavelength shift, relative to water, of the eight spectral features as a function of n. Reprinted from Ref. 93 (Copyright 2016 Nature Publishing Group)

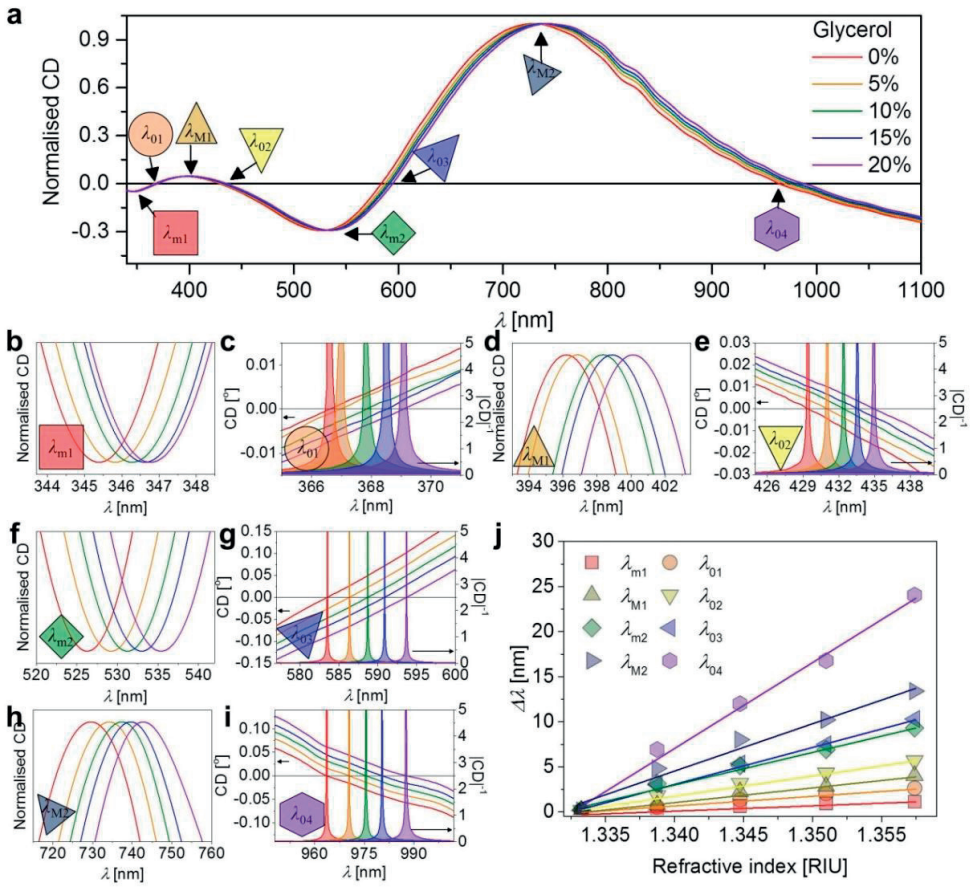

Figure A:19 (a) CD spectra of colloidal $Ag_{0.97}Ti_{0.03}$:L_4 nanohelices in media of five different refractive indices (red: 0%, orange: 5%, green: 10%, blue: 15%, and violet: 20% glycerol/water mixtures) over the full spectral range and detailed plots of the resonance shifts at (b) λ_{m1} (red square), (c) λ_{01} (orange circle), (d) λ_{M1} (dark yellow top triangle), (e) λ_{02} (yellow down triangle), (f) λ_{m2} (green diamond), (g) λ_{03} (blue left triangle), (h) λ_{M2} (navy right triangle), and (i) λ_{04} (violet hexagon). (j) Wavelength shift, relative to water, of the eight spectral features as a function of n. Reprinted from Ref. 93 (Copyright 2016 Nature Publishing Group)

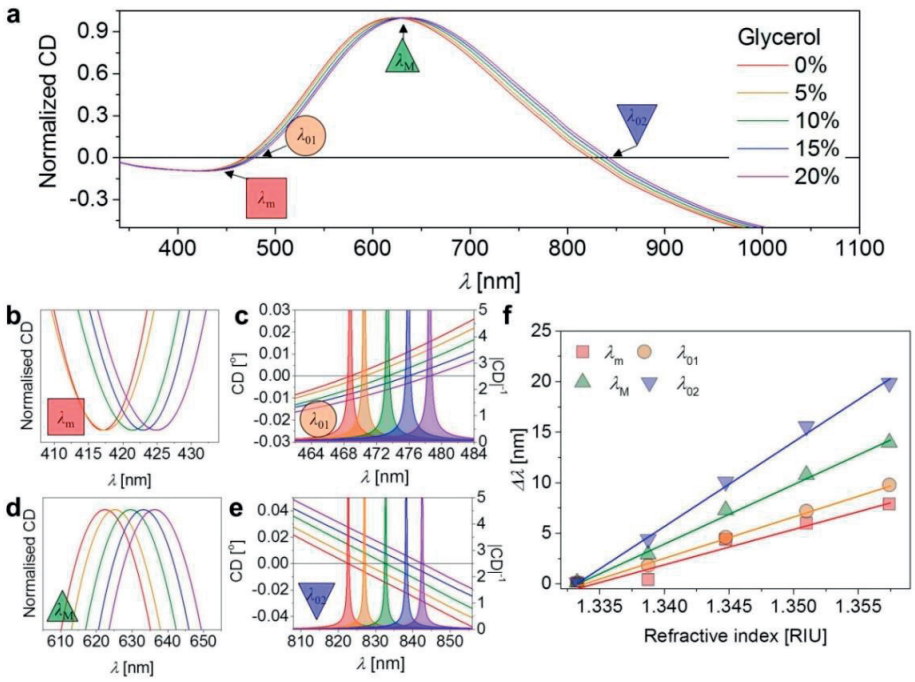

Figure A:20 (a) CD spectra of colloidal $Ag_{0.89}Ti_{0.11}$:L_1 nanohelices in media of five different refractive indices (red: 0%, orange: 5%, green: 10%, blue: 15%, and violet: 20% glycerol/water mixtures) over the full spectral range and detailed plots of the resonance shifts at (b) λ_{m} (red square), (c) λ_{01} (orange circle), (d) λ_{M} (green top triangle), and (e) λ_{02} (blue bottom triangle). (f) Wavelength shift, relative to water, of the four spectral features as a function of n. Reprinted from Ref. 93 (Copyright 2016 Nature Publishing Group)

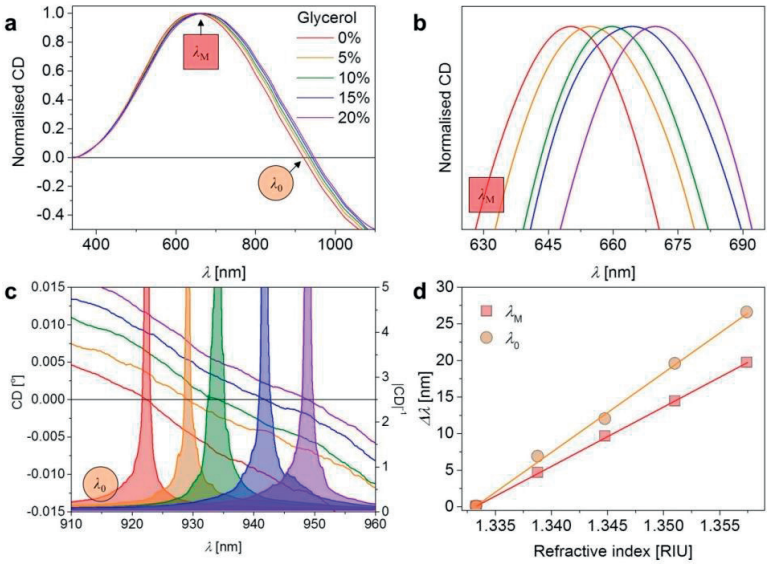

Figure A:21 (a) CD spectra of colloidal $Ag_{0.77}Ti_{0.23}$:L_1 nanohelices in media of five different refractive indices (red: 0%, orange: 5%, green: 10%, blue: 15%, and violet: 20% glycerol/water mixtures) over the full spectral range and detailed plots of the resonance shifts at (b) λ_{M} (red square) and (c) λ_0 (orange circle). (d) Wavelength shift, relative to water, of the two spectral features as a function of n. Reprinted from Ref. 93 (Copyright 2016 Nature Publishing Group)

A.4 Chapter 5: Active nanorheology

The results presented in this section were taken from the following source:

[136] Active nanorheology with plasmonics, **H.-H. Jeong**, A.G. Mark, T.-C. Lee, M. Alarcón-Correa, S. Eslami, T. Qiu, J.G. Gibbs, and P. Fischer, ***Nano Letters*** 16, 4887 (2016)

A.4.1 Nanorheology in water-glycerol mixture

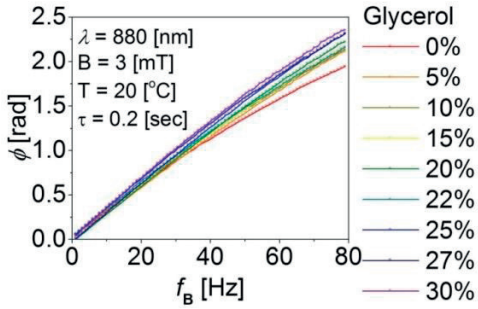

Figure A:22 Phase angle, ϕ of the colloidal Au-Fe nanohelices for glycerol-water mixtures of differing concentrations and hence viscosities, as a function of $f_{\mathbf{B}}$ at $\mathbf{B}$ = 3 mT, λ = 880 nm and T = 20°C. Reprinted with permission from Ref. 136 (Copyright 2016 American Chemical Society)

A.4.2 Nanorheology in slurry

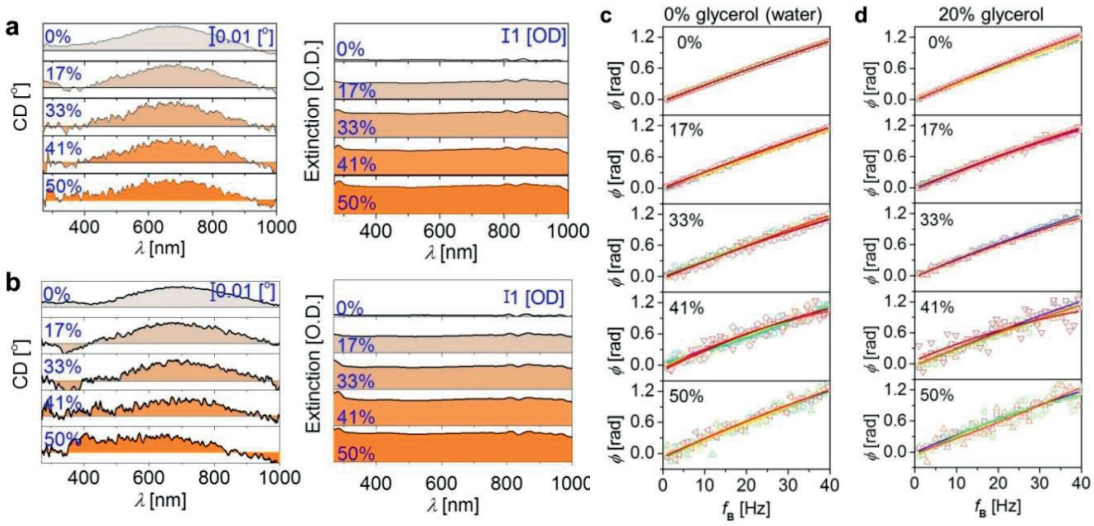

Figure A:23 *In situ* nanorheology measurements with colloidal Au-Fe nanohelices in glycerol-water mixtures in the presence of different concentrations of polystyrene microspheres. CD (left panel) and extinction (right panel) spectra of the colloidal Au-Fe nanohelices in (a) water and (b) 20% glycerol-water mixture surrounded by the polystyrene microspheres. The ϕ measurments as a function of $f_{\mathbf{B}}$ at λ = 880 nm, $\mathbf{B}$ = 3 mT and T = 20°C in the presences of (c) water and (d) 20% glycerol-water mixture. Reprinted with permission from Ref. 136 (Copyright 2016 American Chemical Society)

A.4.3 Nanorheology in blood

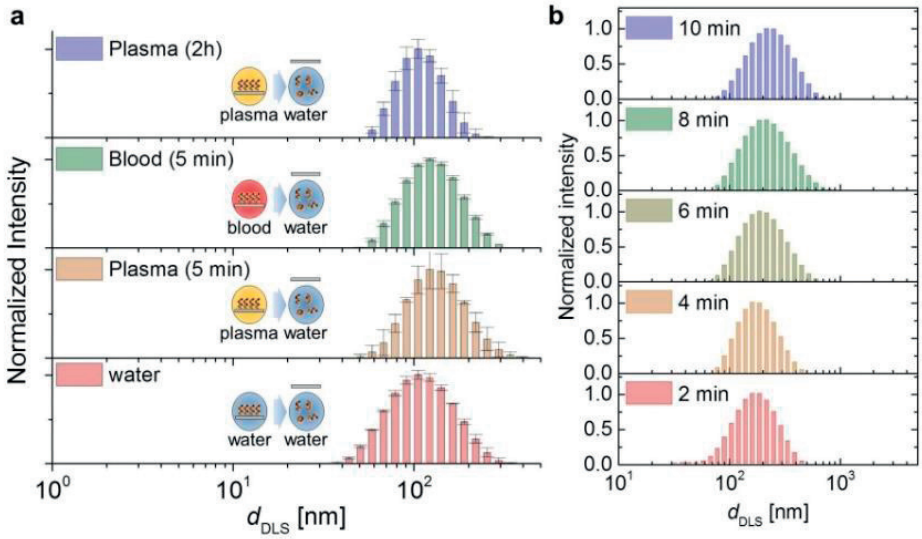

Figure A:24 (a) DLS measurements of the colloidal Au-Fe nanohelices in the presence of water after different pre-treatments in water (red), blood plasma (orange, for 5 min and blue, for 2h), and whole blood (green). (b) DLS measurements of the colloidal Au-Fe nanohelices in 1× phosphate buffer saline (PBS) solution at the specified times (red: 2 min, orange: 4 min, yellow: 6 min, green: 8 min, and blue: 10 min) after sonication. Reprinted with permission from Ref. 136 (Copyright 2016 American Chemical Society)

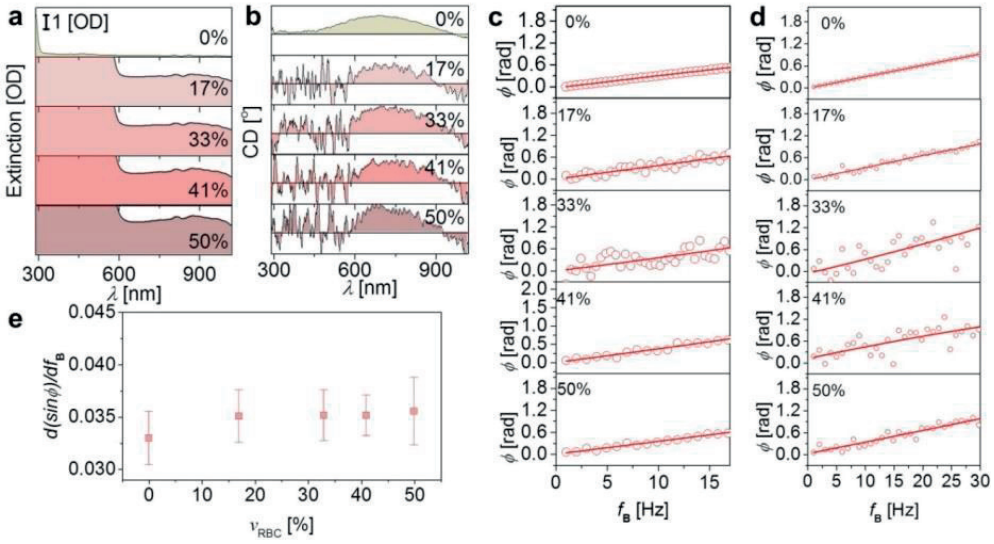

Figure A:25 (a) Extinction and (b) CD spectra of the colloidal Au-Fe nanohelices in the presence of different hematocrit levels. *In situ* nanorheology of bovine blood plasma in the presence of different concentrations of the erythrocytes. Measurements using colloidal Au-Fe nanohelices ((c) cattle A and (d) cattle B). (e) Their corresponding averaged $d\sin\phi/df_B$ as a function of the haematocrit volume fraction. Reprinted with permission from Ref. 136 (Copyright 2016 American Chemical Society)

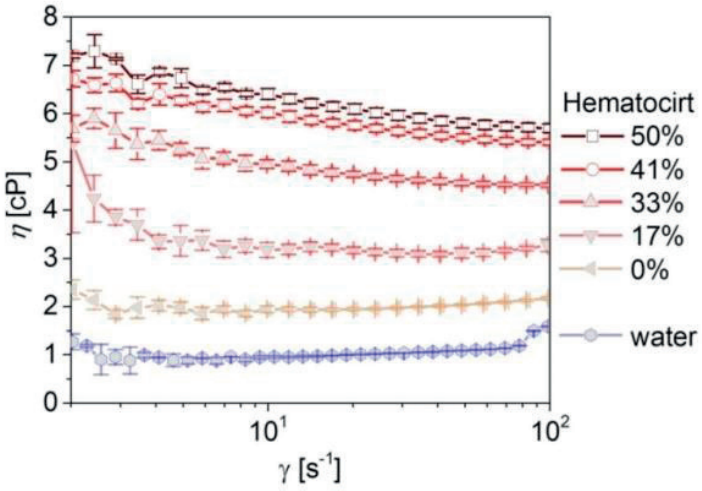

Figure A:26 Macro rheology of bovine whole blood with different concentrations of erythrocytes using a commercial viscometer at shear rates ranging from 2 to 100 s^{-1} at T = 20°C. Reprinted with permission from Ref. 136 (Copyright 2016 American Chemical Society)

Bibliography

[1] Kelvin W.T.B., The Molecular Tactics of a Crystal: Clarendon Press (1894).

[2] Tang Y. and Cohen A.E., Enhanced Enantioselectivity in Excitation of Chiral Molecules by Superchiral Light. *Science* **332** (2011), 333-6.

[3] Barron L.D., Molecular Light Scattering and Optical Activity: Cambridge University Press (2004).

[4] Grande C. and Patel N.H., Nodal signalling is involved in left-right asymmetry in snails. *Nature* **457** (2009), 1007-11.

[5] Mou Y., Yu J.-Y., Wannier T.M., Guo C.-L. and Mayo S.L., Computational design of co-assembling protein-DNA nanowires. *Nature* **525** (2015), 230-3.

[6] Balasubramanian K. and Burghard M., Chemically Functionalized Carbon Nanotubes. *Small* **1** (2005), 180-92.

[7] Hall D.M., Bruss I.R., Barone J.R. and Grason G.M., Morphology selection via geometric frustration in chiral filament bundles. *Nature Materials* **15** (2016), 727-32.

[8] Fasman G.D., Circular Dichroism and the Conformational Analysis of Biomolecules: Springer US (1996).

[9] Berova N., Nakanishi K. and Woody R., Circular Dichroism: Principles and Applications: Wiley (2000).

[10] Nakanishi K., Berova N. and Woody R., Circular Dichroism: Principles and Applications: VCH (1994).

[11] Fischer P. and Hache F., Nonlinear optical spectroscopy of chiral molecules. *Chirality* **17** (2005), 421-37.

[12] Sanchez-Castillo A., Eslami S., Giesselmann F. and Fischer P., Circular polarization interferometry: circularly polarized modes of cholesteric liquid crystals. *Optics Express* **22** (2014), 31227-36.

[13] Pfeifer M. and Fischer P., Weak value amplified optical activity measurements. *Optics Express* **19** (2011), 16508-17.

[14] Ghosh A. and Fischer P., Chiral Molecules Split Light: Reflection and Refraction in a Chiral Liquid. *Physical Review Letters* **97** (2006), 173002.

[15] Hendrye, Carpyt, Johnstonj, Poplandm, Mikhaylovskiy R.V., Lapthorn A.J., Kelly S.M., Barron L.D., Gadegaardn and Kadodwalam, Ultrasensitive detection and characterization of biomolecules using superchiral fields. *Nature Nanotechnology* **5** (2010), 783-7.

[16] Chen G., Roy I., Yang C. and Prasad P.N., Nanochemistry and Nanomedicine for Nanoparticle-based Diagnostics and Therapy. *Chemical Reviews* **116** (2016), 2826-85.

[17] Pietryga J.M., Park Y.-S., Lim J., Fidler A.F., Bae W.K., Brovelli S. and Klimov V.I., Spectroscopic and Device Aspects of Nanocrystal Quantum Dots. *Chemical Reviews* **116** (2016), 10513-622.

[18] Lu A.-H., Salabas E.L. and Schüth F., Magnetic Nanoparticles: Synthesis, Protection, Functionalization, and Application. *Angewandte Chemie International Edition* **46** (2007), 1222-44.
[19] Chen G., Qiu H., Prasad P.N. and Chen X., Upconversion Nanoparticles: Design, Nanochemistry, and Applications in Theranostics. *Chemical Reviews* **114** (2014), 5161-214.
[20] Comin A. and Manna L., New materials for tunable plasmonic colloidal nanocrystals. *Chemical Society Reviews* **43** (2014), 3957-75.
[21] Neuberger T., Schöpf B., Hofmann H., Hofmann M. and Von Rechenberg B., Superparamagnetic nanoparticles for biomedical applications: Possibilities and limitations of a new drug delivery system. *Journal of Magnetism and Magnetic Materials* **293** (2005), 483-96.
[22] Weissleder R., Nahrendorf M. and Pittet M.J., Imaging macrophages with nanoparticles. *Nature Materials* **13** (2014), 125-38.
[23] D. Howes P., Rana S. and M. Stevens M., Plasmonic nanomaterials for biodiagnostics. *Chemical Society Reviews* **43** (2014), 3835-53.
[24] Alarcón-Correa M., Walker D., Qiu T. and Fischer P., Nanomotors. *The European Physical Journal Special Topics* **225** (2016), 2241-54.
[25] Escudero-Escribano M., Malacrida P., Hansen M.H., Vej-Hansen U.G., Velázquez-Palenzuela A., Tripkovic V., Schiøtz J., Rossmeisl J., Stephens I.E.L. and Chorkendorff I., Tuning the activity of Pt alloy electrocatalysts by means of the lanthanide contraction. *Science* **352** (2016), 73-6.
[26] Huang X., Zhao Z., Cao L., Chen Y., Zhu E., Lin Z., Li M., Yan A., Zettl A., Wang Y.M., Duan X., Mueller T. and Huang Y., High-performance transition metal–doped Pt_3Ni octahedra for oxygen reduction reaction. *Science* **348** (2015), 1230-4.
[27] Soukoulis C.M. and Wegener M., Past achievements and future challenges in the development of three-dimensional photonic metamaterials. *Nature Photonics* **5** (2011), 523-30.
[28] Gibbs J.G., Mark A.G., Lee T.-C., Eslami S., Schamel D. and Fischer P., Nanohelices by shadow growth. *Nanoscale* **6** (2014), 9457-66.
[29] Shelby R.A., Smith D.R. and Schultz S., Experimental Verification of a Negative Index of Refraction. *Science* **292** (2001), 77-9.
[30] Zheng X., Smith W., Jackson J., Moran B., Cui H., Chen D., Ye J., Fang N., Rodriguez N., Weisgraber T. and Spadaccini C.M., Multiscale metallic metamaterials. *Nat Mater* **15** (2016), 1100-6.
[31] Schurig D., Mock J.J., Justice B.J., Cummer S.A., Pendry J.B., Starr A.F. and Smith D.R., Metamaterial Electromagnetic Cloak at Microwave Frequencies. *Science* **314** (2006), 977-80.
[32] Zhao Y., Xu L., Ma W., Wang L., Kuang H., Xu C. and Kotov N.A., Shell-Engineered Chiroplasmonic Assemblies of Nanoparticles for Zeptomolar DNA Detection. *Nano Letters* **14** (2014), 3908-13.
[33] Xia Y., Xiong Y., Lim B. and Skrabalak S.E., Shape-Controlled Synthesis of Metal Nanocrystals: Simple Chemistry Meets Complex Physics? *Angewandte Chemie International Edition* **48** (2009), 60-103.
[34] Glotzer S.C. and Solomon M.J., Anisotropy of building blocks and their assembly into complex structures. *Nat Mater* **6** (2007), 557-62.
[35] Kuzyk A., Schreiber R., Fan Z., Pardatscher G., Roller E.-M., Hogele A., Simmel F.C., Govorov A.O. and Liedl T., DNA-based self-assembly of chiral plasmonic nanostructures with tailored optical response. *Nature* **483** (2012), 311-4.
[36] Schreiber R., Luong N., Fan Z., Kuzyk A., Nickels P.C., Zhang T., Smith D.M., Yurke B., Kuang W., Govorov A.O. and Liedl T., Chiral plasmonic DNA nanostructures with switchable circular dichroism. *Nature Communications* **4** (2013), 2948.
[37] Kuzyk A., Schreiber R., Zhang H., Govorov A.O., Liedl T. and Liu N., Reconfigurable 3D plasmonic metamolecules. *Nature Materials* **13** (2014), 862–6.
[38] Song C., Blaber M.G., Zhao G., Zhang P., Fry H.C., Schatz G.C. and Rosi N.L., Tailorable Plasmonic Circular Dichroism Properties of Helical Nanoparticle Superstructures. *Nano Letters* **13** (2013), 3256-61.
[39] Kim Y., Yeom B., Arteaga O., Jo Yoo S., Lee S.-G., Kim J.-G. and Kotov N.A., Reconfigurable chiroptical nanocomposites with chirality transfer from the macro- to the nanoscale. *Nature Materials* **15** (2016), 461-8.
[40] Ma W., Kuang H., Xu L., Ding L., Xu C., Wang L. and Kotov N.A., Attomolar DNA detection with chiral nanorod assemblies. *Nature Communications* **4** (2013), 2689.
[41] Valsami-Jones E. and Lynch I., How safe are nanomaterials? *Science* **350** (2015), 388-9.
[42] Goodman A.M., Cao Y., Urban C., Neumann O., Ayala-Orozco C., Knight M.W., Joshi A., Nordlander P. and Halas N.J., The Surprising in Vivo Instability of Near-IR-Absorbing Hollow Au–Ag Nanoshells. *ACS Nano* **8** (2014), 3222-31.

[43] Karimullah A.S., Jack C., Tullius R., Rotello V.M., Cooke G., Gadegaard N., Barron L.D. and Kadodwala M., Disposable Plasmonics: Plastic Templated Plasmonic Metamaterials with Tunable Chirality. *Advanced Materials* **27** (2015), 5610-6.
[44] Valev V.K., Smisdom N., Silhanek A.V., De Clercq B., Gillijns W., Ameloot M., Moshchalkov V.V. and Verbiest T., Plasmonic Ratchet Wheels: Switching Circular Dichroism by Arranging Chiral Nanostructures. *Nano Letters* **9** (2009), 3945-8.
[45] Liu N., Liu H., Zhu S. and Giessen H., Stereometamaterials. *Nature Photonics* **3** (2009), 157-62.
[46] Zhang S., Zhou J., Park Y.-S., Rho J., Singh R., Nam S., Azad A.K., Chen H.-T., Yin X., Taylor A.J. and Zhang X., Photoinduced handedness switching in terahertz chiral metamolecules. *Nature Communications* **3** (2012), 942.
[47] Gansel J.K., Thiel M., Rill M.S., Decker M., Bade K., Saile V., Von Freymann G., Linden S. and Wegener M., Gold Helix Photonic Metamaterial as Broadband Circular Polarizer. *Science* **325** (2009), 1513-5.
[48] Venables J., Introduction to Surface and Thin Film Processes: Cambridge University Press (2000).
[49] Jeong H.-H., Mark A.G., Lee T.-C., Son K., Chen W., Alarcón-Correa M., Kim I., Schütz G. and Fischer P., Selectable Nanopattern Arrays for Nanolithographic Imprint and Etch-Mask Applications. *Advanced Science* **2** (2015), 1500016.
[50] König H. and Helwig G., Über die Struktur schräg aufgedampfter Schichten und ihr Einfluß auf die Entwicklung submikroskopischer Oberflächenrauhigkeiten. *Optik* **6** (1950), 111-24.
[51] Young N.O. and Kowal J., Optically Active Fluorite Films. *Nature* **183** (1959), 104-5.
[52] Hawkeye M.M. and Brett M.J., Glancing angle deposition: Fabrication, properties, and applications of micro- and nanostructured thin films. *Journal of Vacuum Science & Technology A: Vacuum, Surfaces, and Films* **25** (2007), 1317-35.
[53] First thin film realization of a helicoidal bianisotropic medium. *Journal of Vacuum Science & Technology A: Vacuum, Surfaces, and Films* **13** (1995), 2991-3.
[54] Robbie K., Brett M.J. and Lakhtakia A., Chiral sculptured thin films. *Nature* **384** (1996), 616.
[55] Jensen M.O. and Brett M.J., Periodically structured glancing angle deposition thin films. *IEEE Transactions on Nanotechnology* **4** (2005), 269-77.
[56] Mark A.G., Gibbs J.G., Lee T.-C. and Fischer P., Hybrid nanocolloids with programmed three-dimensional shape and material composition. *Nat Mater* **12** (2013), 802-7.
[57] Glass R., Möller M. and Spatz J.P., Block copolymer micelle nanolithography. *Nanotechnology* **14** (2003), 1153.
[58] Lohmüller T., Aydin D., Schwieder M., Morhard C., Louban I., Pacholski C. and Spatz J.P., Nanopatterning by block copolymer micelle nanolithography and bioinspired applications. *Biointerphases* **6** (2011), MR1-MR12.
[59] Jeong H.-H., Mark A.G., Gibbs J.G., Reindl T., Waizmann U., Weis J. and Fischer P., Shape control in wafer-based aperiodic 3D nanostructures. *Nanotechnology* **25** (2014), 235302.
[60] Singh D.P., Goel P. and Singh J.P., Revisiting the structure zone model for sculptured silver thin films deposited at low substrate temperatures. *Journal of Applied Physics* **112** (2012), 104324.
[61] Movchan B.A. and Demchishin A.V., Investigations of the structure and properties of thick Ni, Ti, W, Al2O3 and ZrO2 vacuum condensates. *Fizika Metallov i Metallovedenie* **28** (1969), 653.
[62] Barna P.B. and Adamik M., Fundamental structure forming phenomena of polycrystalline films and the structure zone models. *Thin Solid Films* **317** (1998), 27-33.
[63] Eslami S., Gibbs J.G., Rechkemmer Y., Van Slageren J., Alarcón-Correa M., Lee T.-C., Mark A.G., Rikken G.L.J.A. and Fischer P., Chiral Nanomagnets. *ACS Photonics* **1** (2014), 1231-6.
[64] Gibbs J.G., Mark A.G., Eslami S. and Fischer P., Plasmonic nanohelix metamaterials with tailorable giant circular dichroism. *Applied Physics Letters* **103** (2013), 213101.
[65] Gibbs J.G. and Fischer P., Active colloidal microdrills. *Chemical Communications* **51** (2015), 4192-5.
[66] Walker D., Kübler M., Morozov K.I., Fischer P. and Leshansky A.M., Optimal Length of Low Reynolds Number Nanopropellers. *Nano Letters* **15** (2015), 4412-6.
[67] Ritchie R.H., Plasma Losses by Fast Electrons in Thin Films. *Physical Review* **106** (1957), 874-81.
[68] Willets K.A. and Van Duyne R.P., Localized Surface Plasmon Resonance Spectroscopy and Sensing. *Annual Review of Physical Chemistry* **58** (2007), 267-97.
[69] Giannini V., Fernández-Domínguez A.I., Heck S.C. and Maier S.A., Plasmonic Nanoantennas: Fundamentals and Their Use in Controlling the Radiative Properties of Nanoemitters. *Chemical Reviews* **111** (2011), 3888-912.
[70] Hoang T.B., Akselrod G.M., Argyropoulos C., Huang J., Smith D.R. and Mikkelsen M.H., Ultrafast spontaneous emission source using plasmonic nanoantennas. *Nature Communications* **6** (2015), 7788.
[71] Stockman M.I., Nanoplasmonic sensing and detection. *Science* **348** (2015), 287-8.
[72] Haes A.J. and Duyne R.P.V., Preliminary studies and potential applications of localized surface plasmon resonance spectroscopy in medical diagnostics. *Expert Review of Molecular Diagnostics* **4** (2004), 527-37.

[73] Mayer K.M. and Hafner J.H., Localized Surface Plasmon Resonance Sensors. *Chemical Reviews* **111** (2011), 3828-57.
[74] Brongersma M.L., Halas N.J. and Nordlander P., Plasmon-induced hot carrier science and technology. *Nature Nanotechnology* **10** (2015), 25-34.
[75] Atwater H.A. and Polman A., Plasmonics for improved photovoltaic devices. *Nature Materials* **9** (2010), 205-13.
[76] Sheldon M.T., Van De Groep J., Brown A.M., Polman A. and Atwater H.A., Plasmoelectric potentials in metal nanostructures. *Science* **346** (2014), 828-31.
[77] Christopher P., Xin H. and Linic S., Visible-light-enhanced catalytic oxidation reactions on plasmonic silver nanostructures. *Nature Chemistry* **3** (2011), 467-72.
[78] Linic S., Christopher P. and Ingram D.B., Plasmonic-metal nanostructures for efficient conversion of solar to chemical energy. *Nature Materials* **10** (2011), 911-21.
[79] Mubeen S., Lee J., Singh N., Kramer S., Stucky G.D. and Moskovits M., An autonomous photosynthetic device in which all charge carriers derive from surface plasmons. *Nature Nanotechnology* **8** (2013), 247-51.
[80] Govorov A.O. and Richardson H.H., Generating heat with metal nanoparticles. *Nano Today* **2** (2007), 30-8.
[81] Fedoruk M., Meixner M., Carretero-Palacios S., Lohmüller T. and Feldmann J., Nanolithography by Plasmonic Heating and Optical Manipulation of Gold Nanoparticles. *ACS Nano* **7** (2013), 7648-53.
[82] Srituravanich W., Fang N., Sun C., Luo Q. and Zhang X., Plasmonic Nanolithography. *Nano Letters* **4** (2004), 1085-8.
[83] Kim S., Jung H., Kim Y., Jang J. and Hahn J.W., Resolution Limit in Plasmonic Lithography for Practical Applications beyond 2x-nm Half Pitch. *Advanced Materials* **24** (2012), OP337-OP44.
[84] Srituravanich W., Pan L., Wang Y., Sun C., Bogy D.B. and Zhang X., Flying plasmonic lens in the near field for high-speed nanolithography. *Nature Nanotechnology* **3** (2008), 733-7.
[85] Stern J.M., Stanfield J., Kabbani W., Hsieh J.-T. and Cadeddu J.A., Selective Prostate Cancer Thermal Ablation With Laser Activated Gold Nanoshells. *The Journal of Urology* **179** (2008), 748-53.
[86] Dickerson E.B., Dreaden E.C., Huang X., El-Sayed I.H., Chu H., Pushpanketh S., Mcdonald J.F. and El-Sayed M.A., Gold nanorod assisted near-infrared plasmonic photothermal therapy (PPTT) of squamous cell carcinoma in mice. *Cancer Letters* **269** (2008), 57-66.
[87] Ndukaife J.C., Kildishev A.V., Nnanna A.G.A., Shalaev V.M., Wereley S.T. and Boltasseva A., Long-range and rapid transport of individual nano-objects by a hybrid electrothermoplasmonic nanotweezer. *Nature Nanotechnology* **11** (2016), 53-9.
[88] De La Rica R. and Stevens M.M., Plasmonic ELISA for the ultrasensitive detection of disease biomarkers with the naked eye. *Nature Nanotechnology* **7** (2012), 821-4.
[89] Lee K.-S. and El-Sayed M.A., Gold and Silver Nanoparticles in Sensing and Imaging: Sensitivity of Plasmon Response to Size, Shape, and Metal Composition. *The Journal of Physical Chemistry B* **110** (2006), 19220-5.
[90] Wiley B.J., Im S.H., Li Z.-Y., Mclellan J., Siekkinen A. and Xia Y., Maneuvering the Surface Plasmon Resonance of Silver Nanostructures through Shape-Controlled Synthesis. *The Journal of Physical Chemistry B* **110** (2006), 15666-75.
[91] Miller M.M. and Lazarides A.A., Sensitivity of Metal Nanoparticle Surface Plasmon Resonance to the Dielectric Environment. *The Journal of Physical Chemistry B* **109** (2005), 21556-65.
[92] Mcpeak K.M., Jayanti S.V., Kress S.J.P., Meyer S., Iotti S., Rossinelli A. and Norris D.J., Plasmonic Films Can Easily Be Better: Rules and Recipes. *ACS Photonics* **2** (2015), 326-33.
[93] Jeong H.-H., Mark A.G., Alarcon-Correa M., Kim I., Oswald P., Lee T.-C. and Fischer P., Dispersion and shape engineered plasmonic nanosensors. *Nature Communications* **7** (2016), 11331.
[94] Knight M.W., King N.S., Liu L., Everitt H.O., Nordlander P. and Halas N.J., Aluminum for Plasmonics. *ACS Nano* **8** (2014), 834-40.
[95] Chen H., Kou X., Yang Z., Ni W. and Wang J., Shape- and Size-Dependent Refractive Index Sensitivity of Gold Nanoparticles. *Langmuir* **24** (2008), 5233-7.
[96] Lounis S.D., Runnerstrom E.L., Llordés A. and Milliron D.J., Defect Chemistry and Plasmon Physics of Colloidal Metal Oxide Nanocrystals. *The Journal of Physical Chemistry Letters* **5** (2014), 1564-74.
[97] Mie G., Contributions to the Optics of Turbid Media: Particularly of Colloidal Metal Solutions: H.M. Stationery Office (1976).
[98] Ogier R., Fang Y., Svedendahl M., Johansson P. and Käll M., Macroscopic Layers of Chiral Plasmonic Nanoparticle Oligomers from Colloidal Lithography. *ACS Photonics* **1** (2014), 1074-81.
[99] Frank B., Yin X., Schäferling M., Zhao J., Hein S.M., Braun P.V. and Giessen H., Large-Area 3D Chiral Plasmonic Structures. *ACS Nano* **7** (2013), 6321-9.

[100] Mcpeak K.M., Van Engers C.D., Blome M., Park J.H., Burger S., Gosálvez M.A., Faridi A., Ries Y.R., Sahu A. and Norris D.J., Complex Chiral Colloids and Surfaces via High-Index Off-Cut Silicon. *Nano Letters* **14** (2014), 2934-40.
[101] Fan Z. and Govorov A.O., Chiral Nanocrystals: Plasmonic Spectra and Circular Dichroism. *Nano Letters* **12** (2012), 3283-9.
[102] Valev V.K., Baumberg J.J., Sibilia C. and Verbiest T., Chirality and Chiroptical Effects in Plasmonic Nanostructures: Fundamentals, Recent Progress, and Outlook. *Advanced Materials* **25** (2013), 2517-34.
[103] Prodan E., Radloff C., Halas N.J. and Nordlander P., A Hybridization Model for the Plasmon Response of Complex Nanostructures. *Science* **302** (2003), 419-22.
[104] Motl N.E., Smith A.F., Desantis C.J. and Skrabalak S.E., Engineering plasmonic metal colloids through composition and structural design. *Chemical Society Reviews* **43** (2014), 3823-34.
[105] Ding T., Sigle D., Zhang L., Mertens J., De Nijs B. and Baumberg J., Controllable Tuning Plasmonic Coupling with Nanoscale Oxidation. *ACS Nano* **9** (2015), 6110-8.
[106] Armelles G., Cebollada A., García-Martín A. and González M.U., Magnetoplasmonics: Combining Magnetic and Plasmonic Functionalities. *Advanced Optical Materials* **1** (2013), 10-35.
[107] Anker J.N., Hall W.P., Lyandres O., Shah N.C., Zhao J. and Van Duyne R.P., Biosensing with plasmonic nanosensors. *Nature Materials* **7** (2008), 442-53.
[108] Yang X., Yang M., Pang B., Vara M. and Xia Y., Gold Nanomaterials at Work in Biomedicine. *Chemical Reviews* (2015),
[109] Jeong H.-H., Mark A.G. and Fischer P., Magnesium plasmonics for UV applications and chiral sensing. *Chemical Communications* **52** (2016), 12179-82.
[110] Maccaferri N., E. Gregorczyk K., De Oliveira T.V.a.G., Kataja M., Van Dijken S., Pirzadeh Z., Dmitriev A., Åkerman J., Knez M. and Vavassori P., Ultrasensitive and label-free molecular-level detection enabled by light phase control in magnetoplasmonic nanoantennas. *Nature Communications* **6** (2015), 6150.
[111] Liu R., Zhou J.-H., Zhou Z.-K., Jiang X., Liu J., Liu G. and Wang X.-H., On-demand shape and size purification of nanoparticle based on surface area. *Nanoscale* **6** (2014), 13145-53.
[112] Nehl C.L., Liao H. and Hafner J.H., Optical Properties of Star-Shaped Gold Nanoparticles. *Nano Letters* **6** (2006), 683-8.
[113] Dondapati S.K., Sau T.K., Hrelescu C., Klar T.A., Stefani F.D. and Feldmann J., Label-free Biosensing Based on Single Gold Nanostars as Plasmonic Transducers. *ACS Nano* **4** (2010), 6318-22.
[114] Mock J.J., Smith D.R. and Schultz S., Local Refractive Index Dependence of Plasmon Resonance Spectra from Individual Nanoparticles. *Nano Letters* **3** (2003), 485-91.
[115] Mcfarland A.D. and Van Duyne R.P., Single Silver Nanoparticles as Real-Time Optical Sensors with Zeptomole Sensitivity. *Nano Letters* **3** (2003), 1057-62.
[116] Sherry L.J., Chang S.-H., Schatz G.C., Van Duyne R.P., Wiley B.J. and Xia Y., Localized Surface Plasmon Resonance Spectroscopy of Single Silver Nanocubes. *Nano Letters* **5** (2005), 2034-8.
[117] Galush W.J., Shelby S.A., Mulvihill M.J., Tao A., Yang P. and Groves J.T., A Nanocube Plasmonic Sensor for Molecular Binding on Membrane Surfaces. *Nano Letters* **9** (2009), 2077-82.
[118] Charles D.E., Aherne D., Gara M., Ledwith D.M., Gun'ko Y.K., Kelly J.M., Blau W.J. and Brennan-Fournet M.E., Versatile Solution Phase Triangular Silver Nanoplates for Highly Sensitive Plasmon Resonance Sensing. *ACS Nano* **4** (2010), 55-64.
[119] Sherry L.J., Jin R., Mirkin C.A., Schatz G.C. and Van Duyne R.P., Localized Surface Plasmon Resonance Spectroscopy of Single Silver Triangular Nanoprisms. *Nano Letters* **6** (2006), 2060-5.
[120] Tam F., Moran C. and Halas N., Geometrical Parameters Controlling Sensitivity of Nanoshell Plasmon Resonances to Changes in Dielectric Environment. *The Journal of Physical Chemistry B* **108** (2004), 17290-4.
[121] Zhou N., Ye C., Polavarapu L. and Xu Q.-H., Controlled preparation of Au/Ag/SnO2 core-shell nanoparticles using a photochemical method and applications in LSPR based sensing. *Nanoscale* **7** (2015), 9025-32.
[122] Sun Y. and Xia Y., Increased Sensitivity of Surface Plasmon Resonance of Gold Nanoshells Compared to That of Gold Solid Colloids in Response to Environmental Changes. *Analytical Chemistry* **74** (2002), 5297-305.
[123] Wang H., Brandl D.W., Le F., Nordlander P. and Halas N.J., Nanorice: A Hybrid Plasmonic Nanostructure. *Nano Letters* **6** (2006), 827-32.
[124] Raschke G., Brogl S., Susha A.S., Rogach A.L., Klar T.A., Feldmann J., Fieres B., Petkov N., Bein T., Nichtl A. and Kürzinger K., Gold Nanoshells Improve Single Nanoparticle Molecular Sensors. *Nano Letters* **4** (2004), 1853-7.
[125] Tullius R., Karimullah A.S., Rodier M., Fitzpatrick B., Gadegaard N., Barron L.D., Rotello V.M., Cooke G., Lapthorn A. and Kadodwala M., "Superchiral" Spectroscopy: Detection of Protein Higher Order Hierarchical Structure with Chiral Plasmonic Nanostructures. *Journal of the American Chemical Society* **137** (2015), 8380-3.

[126] Zhao Y., Askarpour A.N., Sun L., Shi J., Li X. and Alù A., Chirality detection of enantiomers using twisted optical metamaterials. **8** (2017), 14180.
[127] Chang W.-S., Lassiter J.B., Swanglap P., Sobhani H., Khatua S., Nordlander P., Halas N.J. and Link S., A Plasmonic Fano Switch. *Nano Letters* **12** (2012), 4977-82.
[128] Chen H.-T., Padilla W.J., Zide J.M.O., Gossard A.C., Taylor A.J. and Averitt R.D., Active terahertz metamaterial devices. *Nature* **444** (2006), 597-600.
[129] Zhu B., Feng Y., Zhao J., Huang C. and Jiang T., Switchable metamaterial reflector/absorber for different polarized electromagnetic waves. *Applied Physics Letters* **97** (2010), -.
[130] Van Der Zande B.M.I., Koper G.J.M. and Lekkerkerker H.N.W., Alignment of Rod-Shaped Gold Particles by Electric Fields. *The Journal of Physical Chemistry B* **103** (1999), 5754-60.
[131] Sönnichsen C. and Alivisatos A.P., Gold Nanorods as Novel Nonbleaching Plasmon-Based Orientation Sensors for Polarized Single-Particle Microscopy. *Nano Letters* **5** (2004), 301-4.
[132] Khatua S., Chang W.-S., Swanglap P., Olson J. and Link S., Active Modulation of Nanorod Plasmons. *Nano Letters* **11** (2011), 3797-802.
[133] Wang M., Gao C., He L., Lu Q., Zhang J., Tang C., Zorba S. and Yin Y., Magnetic Tuning of Plasmonic Excitation of Gold Nanorods. *Journal of the American Chemical Society* **135** (2013), 15302-5.
[134] Liu Q., Cui Y., Gardner D., Li X., He S. and Smalyukh I.I., Self-Alignment of Plasmonic Gold Nanorods in Reconfigurable Anisotropic Fluids for Tunable Bulk Metamaterial Applications. *Nano Letters* **10** (2010), 1347-53.
[135] Jeong H.-H., Alarcón-Correa M., Mark A.G., Son K., Lee T.-C. and Fischer P., Corrosion-protected hybrid nanoparticles. (Submitted),
[136] Jeong H.-H., Mark A.G., Lee T.-C., Alarcón-Correa M., Eslami S., Qiu T., Gibbs J.G. and Fischer P., Active Nanorheology with Plasmonics. *Nano Letters* **16** (2016), 4887-94.
[137] Waser R. and Aono M., Nanoionics-based resistive switching memories. *Nature Materials* **6** (2007), 833-40.
[138] Yang J.J., Pickett M.D., Li X., Ohlbergdouglas A.A., Stewart D.R. and Williams R.S., Memristive switching mechanism for metal//oxide//metal nanodevices. *Nature Nanotechnology* **3** (2008), 429-33.
[139] Mubeen S., Lee J., Singh N., Kramer S., Stucky G.D. and Moskovits M., An autonomous photosynthetic device in which all charge carriers derive from surface plasmons. *Nat Nano* **8** (2013), 247-51.
[140] Tachibana Y., Vayssieres L. and Durrant J.R., Artificial photosynthesis for solar water-splitting. *Nature Photonics* **6** (2012), 511-8.
[141] Knight M.W., Sobhani H., Nordlander P. and Halas N.J., Photodetection with Active Optical Antennas. *Science* **332** (2011), 702-4.
[142] Bublat T. and Goll D., Influence of dot size and annealing on the magnetic properties of large-area L1[sub 0]-FePt nanopatterns. *Journal of Applied Physics* **110** (2011), 073908-7.
[143] Moritz J., Vinai G., Auffret S. and Dieny B., Two-bit-per-dot patterned media combining in-plane and perpendicular-to-plane magnetized thin films. *Journal of Applied Physics* **109** (2011), 083902-4.
[144] Gupta M.K., Kulkarni D.D., Geryak R., Naik S. and Tsukruk V.V., A Robust and Facile Approach To Assembling Mobile and Highly-Open Unfrustrated Triangular Lattices from Ferromagnetic Nanorods. *Nano Letters* **13** (2012), 36-42.
[145] Pires D., Hedrick J.L., De Silva A., Frommer J., Gotsmann B., Wolf H., Despont M., Duerig U. and Knoll A.W., Nanoscale Three-Dimensional Patterning of Molecular Resists by Scanning Probes. *Science* **328** (2010), 732-5.
[146] Lee H., You S., Pikhitsa P.V., Kim J., Kwon S., Woo C.G. and Choi M., Three-Dimensional Assembly of Nanoparticles from Charged Aerosols. *Nano Letters* **11** (2010), 119-24.
[147] Han D., Pal S., Nangreave J., Deng Z., Liu Y. and Yan H., DNA Origami with Complex Curvatures in Three-Dimensional Space. *Science* **332** (2011), 342-6.
[148] Cho J.-H., Keung M.D., Verellen N., Lagae L., Moshchalkov V.V., Van Dorpe P. and Gracias D.H., Nanoscale Origami for 3D Optics. *Small* **7** (2011), 1943-8.
[149] Ahn B.Y., Shoji D., Hansen C.J., Hong E., Dunand D.C. and Lewis J.A., Printed Origami Structures. *Advanced Materials* **22** (2010), 2251-4.
[150] Lafratta C.N., Fourkas J.T., Baldacchini T. and Farrer R.A., Multiphoton Fabrication. *Angewandte Chemie International Edition* **46** (2007), 6238-58.
[151] Li L., Gattass R.R., Gershgoren E., Hwang H. and Fourkas J.T., Achieving λ/20 Resolution by One-Color Initiation and Deactivation of Polymerization. *Science* **324** (2009), 910-3.
[152] Ahn B.Y., Duoss E.B., Motala M.J., Guo X., Park S.-I., Xiong Y., Yoon J., Nuzzo R.G., Rogers J.A. and Lewis J.A., Omnidirectional Printing of Flexible, Stretchable, and Spanning Silver Microelectrodes. *Science* **323** (2009), 1590-3.

[153] Huang X., Neretina S. and El-Sayed M.A., Gold Nanorods: From Synthesis and Properties to Biological and Biomedical Applications. *Advanced Materials* **21** (2009), 4880-910.
[154] Brett M.J. and Hawkeye M.M., New Materials at a Glance. *Science* **319** (2008), 1192-3.
[155] Steele J. and Brett M., Nanostructure engineering in porous columnar thin films: recent advances. *Journal of Materials Science: Materials in Electronics* **18** (2007), 367-79.
[156] Ghosh A. and Fischer P., Controlled Propulsion of Artificial Magnetic Nanostructured Propellers. *Nano Letters* **9** (2009), 2243-5.
[157] Malac M., Egerton R.F., Brett M.J. and Dick B., Fabrication of submicrometer regular arrays of pillars and helices. *Journal of Vacuum Science & Technology B: Microelectronics and Nanometer Structures* **17** (1999), 2671-4.
[158] Khare C., Fuhrmann B., Leipner H.S., Bauer J. and Rauschenbach B., Optimized growth of Ge nanorod arrays on Si patterns. *Journal of Vacuum Science & Technology A* **29** (2011), -.
[159] Schamel D., Pfeifer M., Gibbs J.G., Miksch B., Mark A.G. and Fischer P., Chiral Colloidal Molecules And Observation of The Propeller Effect. *Journal of the American Chemical Society* **135** (2013), 12353-9.
[160] Ye D.X., Karabacak T., Picu R.C., Wang G.C. and Lu T.M., Uniform Si nanostructures grown by oblique angle deposition with substrate swing rotation. *Nanotechnology* **16** (2005), 1717.
[161] Khare C., Fuhrmann B., Leipner H.S., Bauer J. and Rauschenbach B., Optimized growth of Ge nanorod arrays on Si patterns. *Journal of Vacuum Science & Technology A: Vacuum, Surfaces, and Films* **29** (2011), 051501-5.
[162] Patzig C., Karabacak T., Fuhrmann B. and Rauschenbach B., Glancing angle sputter deposited nanostructures on rotating substrates: Experiments and simulations. *Journal of Applied Physics* **104** (2008), 094318-9.
[163] Dick B., Brett M.J. and Smy T., Controlled growth of periodic pillars by glancing angle deposition. *Journal of Vacuum Science & Technology B: Microelectronics and Nanometer Structures* **21** (2003), 23-8.
[164] Ye D.X., Karabacak T., Lim B.K., Wang G.C. and Lu T.M., Growth of uniformly aligned nanorod arrays by oblique angle deposition with two-phase substrate rotation. *Nanotechnology* **15** (2004), 817.
[165] Summers M.A. and Brett M.J., Optimization of periodic column growth in glancing angle deposition for photonic crystal fabrication. *Nanotechnology* **19** (2008), 415203.
[166] Van Dorp W.F., Van Someren B., Hagen C.W., Kruit P. and Crozier P.A., Approaching the Resolution Limit of Nanometer-Scale Electron Beam-Induced Deposition. *Nano Letters* **5** (2005), 1303-7.
[167] Lukasczyk T., Schirmer M., Steinrück H.-P. and Marbach H., Electron-Beam-Induced Deposition in Ultrahigh Vacuum: Lithographic Fabrication of Clean Iron Nanostructures. *Small* **4** (2008), 841-6.
[168] Kim S., Marelli B., Brenckle M.A., Mitropoulos A.N., Gil E.-S., Tsioris K., Tao H., Kaplan D.L. and Omenetto F.G., All-water-based electron-beam lithography using silk as a resist. *Nature Nanotechnology* **9** (2014), 306-10.
[169] Hu J. and Yu M.-F., Meniscus-Confined Three-Dimensional Electrodeposition for Direct Writing of Wire Bonds. *Science* **329** (2010), 313-6.
[170] Piner R.D., Zhu J., Xu F., Hong S. and Mirkin C.A., "Dip-Pen" Nanolithography. *Science* **283** (1999), 661-3.
[171] Gong J., Lipomi D.J., Deng J., Nie Z., Chen X., Randall N.X., Nair R. and Whitesides G.M., Micro- and Nanopatterning of Inorganic and Polymeric Substrates by Indentation Lithography. *Nano Letters* **10** (2010), 2702-8.
[172] Chai J., Huo F., Zheng Z., Giam L.R., Shim W. and Mirkin C.A., Scanning probe block copolymer lithography. *Proceedings of the National Academy of Sciences* **107** (2010), 20202-6.
[173] Liao X., Brown K.A., Schmucker A.L., Liu G., He S., Shim W. and Mirkin C.A., Desktop nanofabrication with massively multiplexed beam pen lithography. *Nature Communications* **4** (2013), 2103.
[174] Liao W.-S., Cheunkar S., Cao H.H., Bednar H.R., Weiss P.S. and Andrews A.M., Subtractive Patterning via Chemical Lift-Off Lithography. *Science* **337** (2012), 1517-21.
[175] Cho H., Kim J., Park H., Won Bang J., Seop Hyun M., Bae Y., Ha L., Yoon Kim D., Min Kang S., Jung Park T., Seo S., Choi M. and Suh K.-Y., Replication of flexible polymer membranes with geometry-controllable nano-apertures via a hierarchical mould-based dewetting. *Nature Communications* **5** (2014), 3137.
[176] Chou S.Y., Krauss P.R. and Renstrom P.J., Imprint Lithography with 25-Nanometer Resolution. *Science* **272** (1996), 85-7.
[177] Hsu K.H., Schultz P.L., Ferreira P.M. and Fang N.X., Electrochemical Nanoimprinting with Solid-State Superionic Stamps. *Nano Letters* **7** (2007), 446-51.
[178] Shim W., Braunschweig A.B., Liao X., Chai J., Lim J.K., Zheng G. and Mirkin C.A., Hard-tip, soft-spring lithography. *Nature* **469** (2011), 516-20.
[179] Vazquez-Mena O., Villanueva G., Savu V., Sidler K., Van Den Boogaart M.a.F. and Brugger J., Metallic Nanowires by Full Wafer Stencil Lithography. *Nano Letters* **8** (2008), 3675-82.

[180] Huo F., Zheng Z., Zheng G., Giam L.R., Zhang H. and Mirkin C.A., Polymer Pen Lithography. *Science* **321** (2008), 1658-60.
[181] Zhou X., Liu Z., Xie Z., Liu X. and Zheng Z., High-Resolution, Large-Area, Serial Fabrication of 3D Polymer Brush Structures by Parallel Dip-Pen Nanodisplacement Lithography. *Small* **8** (2012), 3568-72.
[182] Hulteen J.C., Treichel D.A., Smith M.T., Duval M.L., Jensen T.R. and Van Duyne R.P., Nanosphere Lithography: Size-Tunable Silver Nanoparticle and Surface Cluster Arrays. *The Journal of Physical Chemistry B* **103** (1999), 3854-63.
[183] Wen T., Booth R.A. and Majetich S.A., Ten-Nanometer Dense Hole Arrays Generated by Nanoparticle Lithography. *Nano Letters* **12** (2012), 5873-8.
[184] Ullrich S., Scheeler S.P., Pacholski C., Spatz J.P. and Kudera S., Formation of Large 2D Arrays of Shape-Controlled Colloidal Nanoparticles at Variable Interparticle Distances. *Particle & Particle Systems Characterization* **30** (2013), 102-8.
[185] Fredriksson H., Alaverdyan Y., Dmitriev A., Langhammer C., Sutherland D.S., Zäch M. and Kasemo B., Hole–Mask Colloidal Lithography. *Advanced Materials* **19** (2007), 4297-302.
[186] Lee T.-C., Alarcón-Correa M., Miksch C., Hahn K., Gibbs J.G. and Fischer P., Self-Propelling Nanomotors in the Presence of Strong Brownian Forces. *Nano Letters* **14** (2014), 2407-12.
[187] Kruss S., Srot V., Van Aken P.A. and Spatz J.P., Au–Ag Hybrid Nanoparticle Patterns of Tunable Size and Density on Glass and Polymeric Supports. *Langmuir* **28** (2011), 1562-8.
[188] Zhao J., Frank B., Neubrech F., Zhang C., Braun P.V. and Giessen H., Hole-mask colloidal nanolithography combined with tilted-angle-rotation evaporation: A versatile method for fabrication of low-cost and large-area complex plasmonic nanostructures and metamaterials. *Beilstein Journal of Nanotechnology* **5** (2014), 577-86.
[189] Larsen G.K., He Y., Ingram W., Lapaquette E.T., Wang J. and Zhao Y., The fabrication of three-dimensional plasmonic chiral structures by dynamic shadowing growth. *Nanoscale* **6** (2014), 9467-76.
[190] Kosiorek A., Kandulski W., Glaczynska H. and Giersig M., Fabrication of Nanoscale Rings, Dots, and Rods by Combining Shadow Nanosphere Lithography and Annealed Polystyrene Nanosphere Masks. *Small* **1** (2005), 439-44.
[191] Jeong H., Pak Y., Hwang Y., Song H., Lee K.H., Ko H.C. and Jung G.Y., Enhancing the Charge Transfer of the Counter Electrode in Dye-Sensitized Solar Cells Using Periodically Aligned Platinum Nanocups. *Small* **8** (2012), 3757-61.
[192] Williams K.R., Gupta K. and Wasilik M., Etch rates for micromachining processing-Part II. *Microelectromechanical Systems, Journal of* **12** (2003), 761-78.
[193] Link S. and El-Sayed M.A., Spectral Properties and Relaxation Dynamics of Surface Plasmon Electronic Oscillations in Gold and Silver Nanodots and Nanorods. *The Journal of Physical Chemistry B* **103** (1999), 8410-26.
[194] Hamaker H.C., The London—van der Waals attraction between spherical particles. *Physica* **4** (1937), 1058-72.
[195] Ray V., Subramanian R., Bhadrachalam P., Ma L.-C., Kim C.-U. and Koh S.J., CMOS-compatible fabrication of room-temperature single-electron devices. *Nat Nano* **3** (2008), 603-8.
[196] Beaudry A.L., Laforge J.M., Tucker R.T., Sorge J.B., Adamski N.L., Li P., Taschuk M.T. and Brett M.J., Directed Branch Growth in Aligned Nanowire Arrays. *Nano Letters* **14** (2014), 1797-803.
[197] Alarcón-Correa M., Lee T.-C. and Fischer P., Dynamic Inclusion Complexes of Metal Nanoparticles Inside Nanocups. *Angewandte Chemie International Edition* **54** (2015), 6730-4.
[198] Geim A.K., Dubonos S.V., Grigorieva I.V., Novoselov K.S., Zhukov A.A. and Shapoval S.Y., Microfabricated adhesive mimicking gecko foot-hair. *Nature Materials* **2** (2003), 461-3.
[199] Lee H., Lee B.P. and Messersmith P.B., A reversible wet/dry adhesive inspired by mussels and geckos. *Nature* **448** (2007), 338-41.
[200] Guo Z., Liu W. and Su B.-L., Superhydrophobic surfaces: From natural to biomimetic to functional. *Journal of Colloid and Interface Science* **353** (2011), 335-55.
[201] Jensen T.R., Malinsky M.D., Haynes C.L. and Van Duyne R.P., Nanosphere Lithography: Tunable Localized Surface Plasmon Resonance Spectra of Silver Nanoparticles. *The Journal of Physical Chemistry B* **104** (2000), 10549-56.
[202] Jeong H.-H., Erdene N., Park J.-H., Jeong D.-H., Lee H.-Y. and Lee S.-K., Real-time label-free immunoassay of interferon-gamma and prostate-specific antigen using a Fiber-Optic Localized Surface Plasmon Resonance sensor. *Biosensors and Bioelectronics* **39** (2013), 346-51.
[203] Jeong H.-H., Erdene N., Lee S.-K., Jeong D.-H. and Park J.-H., Fabrication of fiber-optic localized surface plasmon resonance sensor and its application to detect antibody-antigen reaction of interferon-gamma. *Optical Engineering* **50** (2011), 124405--8.

[204] Jeong H.-H., Erdene N., Park J.-H., Jeong D.-H. and Lee S.-K., Analysis of Fiber-Optic Localized Surface Plasmon Resonance Sensor by Controlling Formation of Gold Nanoparticles and its Bio-Application. *Journal of Nanoscience and Nanotechnology* **12** (2012), 7815-21.
[205] Xu T., Wu Y.-K., Luo X. and Guo L.J., Plasmonic nanoresonators for high-resolution colour filtering and spectral imaging. *Nature Communications* **1** (2010), 59.
[206] Cetin A.E., Coskun A.F., Galarreta B.C., Huang M., Herman D., Ozcan A. and Altug H., Handheld high-throughput plasmonic biosensor using computational on-chip imaging. *Light Sciene & Applications* **3** (2014), e122.
[207] Wang D., Zhu W., Best M.D., Camden J.P. and Crozier K.B., Directional Raman Scattering from Single Molecules in the Feed Gaps of Optical Antennas. *Nano Letters* **13** (2013), 2194-8.
[208] Wu H.-Y., Choi C.J. and Cunningham B.T., Plasmonic Nanogap-Enhanced Raman Scattering Using a Resonant Nanodome Array. *Small* **8** (2012), 2878-85.
[209] Li J.F., Huang Y.F., Ding Y., Yang Z.L., Li S.B., Zhou X.S., Fan F.R., Zhang W., Zhou Z.Y., Wude Y., Ren B., Wang Z.L. and Tian Z.Q., Shell-isolated nanoparticle-enhanced Raman spectroscopy. *Nature* **464** (2010), 392-5.
[210] Norov E., Jeong H.-H., Park J.-H., Lee S.-K. and Jeong D.H., Fiber-Optic Sensor Simultaneously Detecting Localized Surface Plasmon Resonance and Surface-Enhanced Raman Scattering. *Rapid Communication in Photoscience* **2** (2013), 46-51.
[211] Murty K.V.G.K., Venkataramanan M. and Pradeep T., Self-assembled Monolayers of 1,4-Benzenedimethanethiol on Polycrystalline Silver and Gold Films: An Investigation of Structure, Stability, Dynamics, and Reactivity. *Langmuir* **14** (1998), 5446-56.
[212] Wei H. and Xu H., Hot spots in different metal nanostructures for plasmon-enhanced Raman spectroscopy. *Nanoscale* **5** (2013), 10794-805.
[213] Kaesche H., Corrosion of Metals: Physicochemical Principles and Current Problems: Springer (2003).
[214] Elechiguerra J.L., Larios-Lopez L., Liu C., Garcia-Gutierrez D., Camacho-Bragado A. and Yacaman M.J., Corrosion at the Nanoscale: The Case of Silver Nanowires and Nanoparticles. *Chemistry of Materials* **17** (2005), 6042-52.
[215] Gawande M.B., Goswami A., Asefa T., Guo H., Biradar A.V., Peng D.-L., Zboril R. and Varma R.S., Core-shell nanoparticles: synthesis and applications in catalysis and electrocatalysis. *Chemical Society Reviews* **44** (2015), 7540-90.
[216] Ghosh Chaudhuri R. and Paria S., Core/Shell Nanoparticles: Classes, Properties, Synthesis Mechanisms, Characterization, and Applications. *Chemical Reviews* **112** (2012), 2373-433.
[217] Robbie K., Sit J.C. and Brett M.J., Advanced techniques for glancing angle deposition. *Journal of Vacuum Science & Technology B* **16** (1998), 1115-22.
[218] Walker D., Käsdorf B.T., Jeong H.-H., Lieleg O. and Fischer P., Enzymatically active biomimetic micropropellers for the penetration of mucin gels. *Science Advances* **1** (2015), e1500501.
[219] George S.M., Atomic Layer Deposition: An Overview. *Chemical Reviews* **110** (2010), 111-31.
[220] Han X., Liu Y., Jia Z., Chen Y.-C., Wan J., Weadock N., Gaskell K.J., Li T. and Hu L., Atomic-Layer-Deposition Oxide Nanoglue for Sodium Ion Batteries. *Nano Letters* **14** (2014), 139-47.
[221] Weber M.J., Mackus A.J.M., Verheijen M.A., Van Der Marel C. and Kessels W.M.M., Supported Core/Shell Bimetallic Nanoparticles Synthesis by Atomic Layer Deposition. *Chemistry of Materials* **24** (2012), 2973-7.
[222] Venugopalan P.L., Sai R., Chandorkar Y., Basu B., Shivashankar S. and Ghosh A., Conformal Cytocompatible Ferrite Coatings Facilitate the Realization of a Nanovoyager in Human Blood. *Nano Letters* **14** (2014), 1968-75.
[223] Jin Fan H., Knez M., Scholz R., Nielsch K., Pippel E., Hesse D., Zacharias M. and Gosele U., Monocrystalline spinel nanotube fabrication based on the Kirkendall effect. *Nature Materials* **5** (2006), 627-31.
[224] Qin Y., Kim Y., Zhang L., Lee S.-M., Yang R.B., Pan A., Mathwig K., Alexe M., Gösele U. and Knez M., Preparation and Elastic Properties of Helical Nanotubes Obtained by Atomic Layer Deposition with Carbon Nanocoils as Templates. *Small* **6** (2010), 910-4.
[225] Johnson R.W., Hultqvist A. and Bent S.F., A brief review of atomic layer deposition: from fundamentals to applications. *Materials Today* **17** (2014), 236-46.
[226] Pavlov A.A., Nelyubina Y.V., Kats S.V., Penkova L.V., Efimov N.N., Dmitrienko A.O., Vologzhanina A.V., Belov A.S., Voloshin Y.Z. and Novikov V.V., Polymorphism in a Cobalt-Based Single-Ion Magnet Tuning Its Barrier to Magnetization Relaxation. *The Journal of Physical Chemistry Letters* **7** (2016), 4111-6.
[227] Na H.B., Song I.C. and Hyeon T., Inorganic Nanoparticles for MRI Contrast Agents. *Advanced Materials* **21** (2009), 2133-48.
[228] Shin T.-H., Choi Y., Kim S. and Cheon J., Recent advances in magnetic nanoparticle-based multi-modal imaging. *Chemical Society Reviews* **44** (2015), 4501-16.
[229] Grass R.N., Athanassiou E.K. and Stark W.J., Covalently Functionalized Cobalt Nanoparticles as a Platform for Magnetic Separations in Organic Synthesis. *Angewandte Chemie International Edition* **46** (2007), 4909-12.

[230] Hanauer M., Pierrat S., Zins I., Lotz A. and Sönnichsen C., Separation of Nanoparticles by Gel Electrophoresis According to Size and Shape. *Nano Letters* **7** (2007), 2881-5.
[231] Hasenoehrl C., Alexander C.M., Azzarelli N.N. and Dabrowiak J.C., Enhanced detection of gold nanoparticles in agarose gel electrophoresis. *Eelectrophoresis* **33** (2012), 1251-4.
[232] Giljohann D.A., Seferos D.S., Daniel W.L., Massich M.D., Patel P.C. and Mirkin C.A., Gold Nanoparticles for Biology and Medicine. *Angewandte Chemie International Edition* **49** (2010), 3280-94.
[233] Gawande M.B., Goswami A., Felpin F.-X., Asefa T., Huang X., Silva R., Zou X., Zboril R. and Varma R.S., Cu and Cu-Based Nanoparticles: Synthesis and Applications in Catalysis. *Chemical Reviews* **116** (2016), 3722-811.
[234] Mott D., Galkowski J., Wang L., Luo J. and Zhong C.-J., Synthesis of Size-Controlled and Shaped Copper Nanoparticles. *Langmuir* **23** (2007), 5740-5.
[235] Khanna P.K., Gaikwad S., Adhyapak P.V., Singh N. and Marimuthu R., Synthesis and characterization of copper nanoparticles. *Materials Letters* **61** (2007), 4711-4.
[236] Dhas N.A., Raj C.P. and Gedanken A., Synthesis, Characterization, and Properties of Metallic Copper Nanoparticles. *Chemistry of Materials* **10** (1998), 1446-52.
[237] Chowdhury M.H., Ray K., Gray S.K., Pond J. and Lakowicz J.R., Aluminum Nanoparticles as Substrates for Metal-Enhanced Fluorescence in the Ultraviolet for the Label-Free Detection of Biomolecules. *Analytical Chemistry* **81** (2009), 1397-403.
[238] Mcpeak K.M., Van Engers C.D., Bianchi S., Rossinelli A., Poulikakos L.V., Bernard L., Herrmann S., Kim D.K., Burger S., Blome M., Jayanti S.V. and Norris D.J., Ultraviolet Plasmonic Chirality from Colloidal Aluminum Nanoparticles Exhibiting Charge-Selective Protein Detection. *Advanced Materials* **27** (2015), 6244-50.
[239] Maidecchi G., Gonella G., Proietti Zaccaria R., Moroni R., Anghinolfi L., Giglia A., Nannarone S., Mattera L., Dai H.-L., Canepa M. and Bisio F., Deep Ultraviolet Plasmon Resonance in Aluminum Nanoparticle Arrays. *ACS Nano* **7** (2013), 5834-41.
[240] He Y., Zhao Y. and Wu J., The effect of Ti doping on the growth of Mg nanostructures by oblique angle codeposition. *Applied Physics Letters* **92** (2008), 063107.
[241] West P.R., Ishii S., Naik G.V., Emani N.K., Shalaev V.M. and Boltasseva A., Searching for better plasmonic materials. *Laser & Photonics Reviews* **4** (2010), 795-808.
[242] Gu W.Y., Yao H., Vega A.L. and Flagler D., Diffusivity of Ions in Agarose Gels and Intervertebral Disc: Effect of Porosity. *Annals of Biomedical Engineering* **32** (2004), 1710-7.
[243] Du S., Kendall K., Toloueinia P., Mehrabadi Y., Gupta G. and Newton J., Aggregation and adhesion of gold nanoparticles in phosphate buffered saline. *Journal of Nanoparticle Research* **14** (2012), 758.
[244] Homola J., Present and future of surface plasmon resonance biosensors. *Analytical and Bioanalytical Chemistry* **377** (2003), 528-39.
[245] Nagpal P., Lindquist N.C., Oh S.-H. and Norris D.J., Ultrasmooth Patterned Metals for Plasmonics and Metamaterials. *Science* **325** (2009), 594-7.
[246] Brolo A.G., Plasmonics for future biosensors. *Nature Photonics* **6** (2012), 709-13.
[247] Jeong H.-H., Son Y.-J., Kang S.-K., Kim H.-J., Roh H.-J., Erdene N., Park J.-H., Jeong D.-H., Lee H.-Y. and Lee S.-K., Fiber-optic refractive index sensor based on the cone-based round structure. *Sensors Journal, IEEE* **13** (2013), 351-8.
[248] Shen Y., Zhou J., Liu T., Tao Y., Jiang R., Liu M., Xiao G., Zhu J., Zhou Z.-K., Wang X., Jin C. and Wang J., Plasmonic gold mushroom arrays with refractive index sensing figures of merit approaching the theoretical limit. *Nature Communications* **4** (2013), 2381.
[249] Gartia M.R., Hsiao A., Pokhriyal A., Seo S., Kulsharova G., Cunningham B.T., Bond T.C. and Liu G.L., Colorimetric Plasmon Resonance Imaging Using Nano Lycurgus Cup Arrays. *Advanced Optical Materials* **1** (2013), 68-76.
[250] Jin R., Cao Y., Mirkin C.A., Kelly K.L., Schatz G.C. and Zheng J.G., Photoinduced Conversion of Silver Nanospheres to Nanoprisms. *Science* **294** (2001), 1901-3.
[251] Boltasseva A. and Atwater H.A., Low-Loss Plasmonic Metamaterials. *Science* **331** (2011), 290-1.
[252] Chang W.-S., Wen F., Chakraborty D., Su M.-N., Zhang Y., Shuang B., Nordlander P., Sader J.E., Halas N.J. and Link S., Tuning the acoustic frequency of a gold nanodisk through its adhesion layer. *Nature Communications* **6** (2015), 7022.
[253] Choy T.C., Effective Medium Theory: Principles and Applications: Clarendon Press (1999).
[254] Cheng N.-S., Formula for the Viscosity of a Glycerol−Water Mixture. *Industrial & Engineering Chemistry Research* **47** (2008), 3285-8.
[255] Larsen G.K., He Y., Wang J. and Zhao Y., Scalable Fabrication of Composite Ti/Ag Plasmonic Helices: Controlling Morphology and Optical Activity by Tailoring Material Properties. *Advanced Optical Materials* **2** (2014), 245-9.

[256] Kabashin A.V., Evans P., Pastkovsky S., Hendren W., Wurtz G.A., Atkinson R., Pollard R., Podolskiy V.A. and Zayats A.V., Plasmonic nanorod metamaterials for biosensing. *Nature Materials* **8** (2009), 867-71.
[257] Claborn K., Isborn C., Kaminsky W. and Kahr B., Optical Rotation of Achiral Compounds. *Angewandte Chemie International Edition* **47** (2008), 5706-17.
[258] Liu N., Tang M.L., Hentschel M., Giessen H. and Alivisatos A.P., Nanoantenna-enhanced gas sensing in a single tailored nanofocus. *Nature Materials* **10** (2011), 631-6.
[259] Heller W., Remarks on Refractive Index Mixture Rules. *The Journal of Physical Chemistry* **69** (1965), 1123-9.
[260] Kozma I.Z., Krok P. and Riedle E., Direct measurement of the group-velocity mismatch and derivation of the refractive-index dispersion for a variety of solvents in the ultraviolet. *Journal of the Optical Society of America B* **22** (2005), 1479-85.
[261] Hale G.M. and Querry M.R., Optical Constants of Water in the 200-nm to 200-µm Wavelength Region. *Applied Optics* **12** (1973), 555-63.
[262] Sanz J.M., Ortiz D., Alcaraz De La Osa R., Saiz J.M., González F., Brown A.S., Losurdo M., Everitt H.O. and Moreno F., UV Plasmonic Behavior of Various Metal Nanoparticles in the Near- and Far-Field Regimes: Geometry and Substrate Effects. *The Journal of Physical Chemistry C* **117** (2013), 19606-15.
[263] Chen L.-Y., Xu J.-Q., Choi H., Pozuelo M., Ma X., Bhowmick S., Yang J.-M., Mathaudhu S. and Li X.-C., Processing and properties of magnesium containing a dense uniform dispersion of nanoparticles. *Nature* **528** (2015), 539-43.
[264] Sterl F., Strohfeldt N., Walter R., Griessen R., Tittl A. and Giessen H., Magnesium as Novel Material for Active Plasmonics in the Visible Wavelength Range. *Nano Letters* **15** (2015), 7949-55.
[265] Nair G., Singh H.J. and Ghosh A., Tuning the chiro-plasmonic response using high refractive index-dielectric templates. *Journal of Materials Chemistry C* **3** (2015), 6831-5.
[266] Lee S.H., Singh D.P., Sung J.H., Jo M.-H., Kwon K.C., Kim S.Y., Jang H.W. and Kim J.K., Highly photoresponsive and wavelength-selective circularly-polarized-light detector based on metal-oxides hetero-chiral thin film. *Scientific Reports* **6** (2016), 19580.
[267] Deng J., Fu J., Ng J. and Huang Z., Tailorable chiroptical activity of metallic nanospiral arrays. *Nanoscale* **8** (2016), 4504-10.
[268] Xie S., Yang J., Xiao X., Hou Y., Du J., Pang L., Li X. and Gao F., Scalable Fabrication of Quasi-Three-Dimensional Chiral Plasmonic Oligomers Based on Stepwise Colloid Sphere Lithography Technology. *Nanoscale Research Letters* **10** (2015), 1-9.
[269] Singh J.H., Nair G., Ghosh A. and Ghosh A., Wafer scale fabrication of porous three-dimensional plasmonic metamaterials for the visible region: chiral and beyond. *Nanoscale* **5** (2013), 7224-8.
[270] Habteyes T.G., Dhuey S., Wood E., Gargas D., Cabrini S., Schuck P.J., Alivisatos A.P. and Leone S.R., Metallic Adhesion Layer Induced Plasmon Damping and Molecular Linker as a Nondamping Alternative. *ACS Nano* **6** (2012), 5702-9.
[271] Fung Y., Biomechanics: mechanical properties of living tissues: Springer-Verlag (1981).
[272] Krieger I.M. and Dougherty T.J., A Mechanism for Non-Newtonian Flow in Suspensions of Rigid Spheres. *Transactions of The Society of Rheology* **3** (1959), 137-52.
[273] Kersaudy-Kerhoas M. and Sollier E., Micro-scale blood plasma separation: from acoustophoresis to egg-beaters. *Lab on a Chip* **13** (2013), 3323-46.
[274] Késmárky G., Kenyeres P., Rábai M. and Tóth K., Plasma viscosity: A forgotten variable. *Clinical Hemorheology & Microcirculation* **39** (2008), 243-6.
[275] Windberger U., Bartholovitsch A., Plasenzotti R., Korak K.J. and Heinze G., Whole Blood Viscosity, Plasma Viscosity and Erythrocyte Aggregation in Nine Mammalian Species: Reference Values and Comparison of Data. *Experimental Physiology* **88** (2003), 431-40.
[276] Fedosov D.A., Pan W., Caswell B., Gompper G. and Karniadakis G.E., Predicting human blood viscosity in silico. *Proceedings of the National Academy of Sciences* **108** (2011), 11772-7.
[277] Tokarev A., Aprelev A., Zakharov M.N., Korneva G., Gogotsi Y. and Kornev K.G., Multifunctional magnetic rotator for micro and nanorheological studies. *Review of Scientific Instruments* **83** (2012), 065110.
[278] Eric L. and Thomas R.P., The hydrodynamics of swimming microorganisms. *Reports on Progress in Physics* **72** (2009), 096601.
[279] Schamel D., Mark A.G., Gibbs J.G., Miksch C., Morozov K.I., Leshansky A.M. and Fischer P., Nanopropellers and Their Actuation in Complex Viscoelastic Media. *ACS Nano* (2014),
[280] Tuteja A., Mackay M.E., Narayanan S., Asokan S. and Wong M.S., Breakdown of the Continuum Stokes−Einstein Relation for Nanoparticle Diffusion. *Nano Letters* **7** (2007), 1276-81.

[281] Chevry L., Sampathkumar N.K., Cebers A. and Berret J.F., Magnetic wire-based sensors for the microrheology of complex fluids. *Physical Review E* **88** (2013), 062306.
[282] Chiang I.C. and Chen D.H., Synthesis of Monodisperse FeAu Nanoparticles with Tunable Magnetic and Optical Properties. *Advanced Functional Materials* **17** (2007), 1311-6.
[283] Zhou C., Duan X. and Liu N., A plasmonic nanorod that walks on DNA origami. *Nature Communications* **6** (2015), 8102.
[284] Han Y., Alsayed A., Nobili M. and Yodh A.G., Quasi-two-dimensional diffusion of single ellipsoids: Aspect ratio and confinement effects. *Physical Review E* **80** (2009), 011403.
[285] Happel J. and Brenner H., Low Reynolds number hydrodynamics: with special applications to particulate media: Springer Netherlands (1983).
[286] Phatak C., Liu Y., Gulsoy E.B., Schmidt D., Franke-Schubert E. and Petford-Long A., Visualization of the Magnetic Structure of Sculpted Three-Dimensional Cobalt Nanospirals. *Nano Letters* **14** (2014), 759-64.
[287] Berret J.F., Local viscoelasticity of living cells measured by rotational magnetic spectroscopy. *Nature Communications* **7** (2016), 10134.
[288] Colin R., Yan M., Chevry L., Berret J.F. and Abou B., 3D rotational diffusion of micrometric wires using 2D video microscopy. *EPL (Europhysics Letters)* **97** (2012), 30008.
[289] Einstein A., Eine neue Bestimmung der Moleküldimensionen. *Annalen der Physik* **324** (1906), 289-306.
[290] Tenzer S., Docter D., Kuharev J., Musyanovych A., Fetz V., Hecht R., Schlenk F., Fischer D., Kiouptsi K., Reinhardt C., Landfester K., Schild H., Maskos M., Knauer S.K. and Stauber R.H., Rapid formation of plasma protein corona critically affects nanoparticle pathophysiology. *Nature Nanotechnology* **8** (2013), 772-81.
[291] Pino P.D., Pelaz B., Zhang Q., Maffre P., Nienhaus G.U. and Parak W.J., Protein corona formation around nanoparticles - from the past to the future. *Materials Horizons* **1** (2014), 301-13.
[292] Palik E.D., Handbook of Optical Constants of Solids: Elsevier Science (1985).
[293] Draine B.T. and Flatau P.J., Discrete-Dipole Approximation For Scattering Calculations. *Journal of the Optical Society of America A* **11** (1994), 1491-9.
[294] Pelaz B., Alexiou C., Alvarez-Puebla R.A., Alves F., Andrews A.M., Ashraf S., Balogh L.P., Ballerini L., Bestetti A., Brendel C., Bosi S., Carril M., Chan W.C.W., Chen C., Chen X., Chen X., Cheng Z., Cui D., Du J., Dullin C., Escudero A., Feliu N., Gao M., George M., Gogotsi Y., Grünweller A., Gu Z., Halas N.J., Hampp N., Hartmann R.K., Hersam M.C., Hunziker P., Jian J., Jiang X., Jungebluth P., Kadhiresan P., Kataoka K., Khademhosseini A., Kopeček J., Kotov N.A., Krug H.F., Lee D.S., Lehr C.-M., Leong K.W., Liang X.-J., Ling Lim M., Liz-Marzán L.M., Ma X., Macchiarini P., Meng H., Möhwald H., Mulvaney P., Nel A.E., Nie S., Nordlander P., Okano T., Oliveira J., Park T.H., Penner R.M., Prato M., Puntes V., Rotello V.M., Samarakoon A., Schaak R.E., Shen Y., Sjöqvist S., Skirtach A.G., Soliman M.G., Stevens M.M., Sung H.-W., Tang B.Z., Tietze R., Udugama B.N., Vanepps J.S., Weil T., Weiss P.S., Willner I., Wu Y., Yang L., Yue Z., Zhang Q., Zhang Q., Zhang X.-E., Zhao Y., Zhou X. and Parak W.J., Diverse Applications of Nanomedicine. *ACS Nano* (2017),
[295] Jochen W., Jürgen W., Maik H. and Klaus V K., Fabrication of an array of single-electron transistors for a scanning probe microscope sensor. *Nanotechnology* **19** (2008), 375301.
[296] Saiful I.K., Kang L. and Zhen Y., The fabrication of single-electron transistors using dielectrophoretic trapping of individual gold nanoparticles. *Nanotechnology* **21** (2010), 095204.
[297] Nah J., Kumar S.B., Fang H., Chen Y.-Z., Plis E., Chueh Y.-L., Krishna S., Guo J. and Javey A., Quantum Size Effects on the Chemical Sensing Performance of Two-Dimensional Semiconductors. *The Journal of Physical Chemistry C* **116** (2012), 9750-4.
[298] Okada S., Mizukami S., Sakata T., Matsumura Y., Yoshioka Y. and Kikuchi K., Ratiometric MRI Sensors Based on Core–Shell Nanoparticles for Quantitative pH Imaging. *Advanced Materials* **26** (2014), 2989-92.
[299] Chen C., Kang Y., Huo Z., Zhu Z., Huang W., Xin H.L., Snyder J.D., Li D., Herron J.A., Mavrikakis M., Chi M., More K.L., Li Y., Markovic N.M., Somorjai G.A., Yang P. and Stamenkovic V.R., Highly Crystalline Multimetallic Nanoframes with Three-Dimensional Electrocatalytic Surfaces. *Science* **343** (2014), 1339-43.
[300] Hernandez-Fernandez P., Masini F., Mccarthy D.N., Strebel C.E., Friebel D., Deiana D., Malacrida P., Nierhoff A., Bodin A., Wise A.M., Nielsen J.H., Hansen T.W., Nilsson A., Stephensifan E.L. and Chorkendorff I., Mass-selected nanoparticles of PtxY as model catalysts for oxygen electroreduction. *Nature Chemistry* **6** (2014), 732-8.
[301] Wang D., Xin H.L., Hovden R., Wang H., Yu Y., Muller D.A., Disalvo F.J. and Abruña H.D., Structurally ordered intermetallic platinum–cobalt core–shell nanoparticles with enhanced activity and stability as oxygen reduction electrocatalysts. *Nature Materials* **12** (2013), 81-7.
[302] Luo J., Wang L., Mott D., Njoki P.N., Lin Y., He T., Xu Z., Wanjana B.N., Lim I.I.S. and Zhong C.-J., Core/Shell Nanoparticles as Electrocatalysts for Fuel Cell Reactions. *Advanced Materials* **20** (2008), 4342-7.

[303] Tokel O., Inci F. and Demirci U., Advances in Plasmonic Technologies for Point of Care Applications. *Chemical Reviews* **114** (2014), 5728-52.
[304] Kwon K.C., Ryu J.H., Lee J.-H., Lee E.J., Kwon I.C., Kim K. and Lee J., Proteinticle/Gold Core/Shell Nanoparticles for Targeted Cancer Therapy without Nanotoxicity. *Advanced Materials* **26** (2014), 6436-41.
[305] Zijlstra P., Paulo P.M.R. and Orrit M., Optical detection of single non-absorbing molecules using the surface plasmon resonance of a gold nanorod. *Nature Nanotechnology* **7** (2012), 379-82.
[306] He Y., Lawrence K., Ingram W. and Zhao Y., Circular dichroism based refractive index sensing using chiral metamaterials. *Chemical Communications* **52** (2016), 2047-50.
[307] Choi Y., Kang T. and Lee L.P., Plasmon Resonance Energy Transfer (PRET)-based Molecular Imaging of Cytochrome c in Living Cells. *Nano Letters* **9** (2009), 85-90.
[308] Li J., Cushing S.K., Meng F., Senty T.R., Bristow A.D. and Wu N., Plasmon-induced resonance energy transfer for solar energy conversion. *Nature Photonics* **9** (2015), 601-7.
[309] Wei Q., Song H.-M., Leonov A.P., Hale J.A., Oh D., Ong Q.K., Ritchie K. and Wei A., Gyromagnetic Imaging: Dynamic Optical Contrast Using Gold Nanostars with Magnetic Cores. *Journal of the American Chemical Society* **131** (2009), 9728-34.
[310] Buckingham A.D. and Dunn M.B., Optical activity of oriented molecules. *Journal of the Chemical Society A: Inorganic, Physical, Theoretical* (1971), 1988-91.
[311] Brust M., Schaefer C., Doerr R., Pan L., Garcia M., Arratia P.E. and Wagner C., Rheology of Human Blood Plasma: Viscoelastic Versus Newtonian Behavior. *Physical Review Letters* **110** (2013), 078305.

Curriculum Vitae

CONTACT INFORMATION

E-mail: hjeon@is.mpg.de (MPI) / korea323@hotmail.com

PERSONAL INFORMATION

Name: Hyeon-Ho Jeong
Date of birth: 23 March 1985
Nationality: Republic of Korea

EMPLOYMENT HISTORY

- 2017 – present **Postdoc fellowship**, Micro, Nano, and Molecular Systems Laboratory, Max Planck Institute for Intelligent Systems (MPI-IS), Germany
  Supervisor: Prof. Peer Fischer
- 2012 – 2017 **Ph.D. fellowship**, Micro, Nano, and Molecular Systems Laboratory, Max Planck Institute for Intelligent Systems (MPI-IS), Germany
  Supervisor: Prof. Peer Fischer
- 2011 – 2012 **Researcher**, Institute of Radiation Medicine, Seoul National University Medical Research Centre (SNU-MRC), Republic of Korea
  Supervisor: Prof. Ho-Young Lee
- 2010 – 2011 **Graduate research assistant**, Nano and Micro Systems Group, Dankook University (DKU), Republic of Korea
  Supervisor: Prof. Seung-Ki Lee and Prof. Jae-Hyoung Park
- 2009 – 2010 **Undergraduate research assistant**, Nano and Micro Systems Group, DKU, Republic of Korea
  Supervisor: Prof. Seung-Ki Lee

EDUCATION

- 2015 – 2017 **Ph.D.** in Material Science and Engineering (EDMX), and in Molecular Nanoscience and Tech-Nology (MNST), École Polytechnique Fédérale de Lausanne (EPFL), Switzerland
  Advisor: Prof. Peer Fischer and Prof. Francesco Stellacci
- 2010 – 2011 **M.Eng.** in Electronics and Electrical Engineering, DKU, Republic of Korea
  Advisor: Prof. Seung-Ki Lee and Prof. Jae-Hyoung Park
- 2004 – 2010 **B.Eng.** in Electronics and Electrical Engineering, DKU, Republic of Korea
  (2005 – 2007 Korean military service)

AWARDS

- 2017 **EMRS Graduate Student Award** at European Material Research Society (E-MRS) Spring Meeting, Strasbourg, France
- 2016 **MRS Graduate Student Gold Award** at Material Research Society (MRS) Fall Meeting, Boston, USA
- 2012 **Best Paper Award (poster)**, 14th Korean Micro Electro Mechanical Systems (KMEMS) Conference, Jeju, Republic of Korea
- 2011 **Best Paper Award (poster)**, the Information and Control Symposium 2011, Yongin, Republic of Korea

PUBLICATIONS

JOURNALS:

1. Corrosion-protected hybrid nanoparticles, **H.-H. Jeong**, M. Alarcón-Correa, A.G. Mark, K. Son, T.-C. Lee, and P. Fischer (under review)
2. Graphene-Silver Hybrid Devices for Sensitive Photodetection in the Ultraviolet, D. Paria, **H.-H. Jeong**, V. Vadakkumbatt, P. Deshpande, P. Fischer, A. Ghosh, and A. Ghosh (under review)
3. Nanodiamond that swims, J. T. Kim, U. Choudhury, **H.-H. Jeong**, and P. Fischer, ***Advanced Materials*** DOI: 10.1002/adma.201701024 (2017)
4. Magnesium plasmonics for UV applications and chiral sensing, **H.-H. Jeong**, A.G. Mark, and P. Fischer, ***Chemical Communications*** 52, 12179 (2016)
5. Active nanorheology with plasmonics, **H.-H. Jeong**, A.G. Mark, T.-C. Lee, M. Alarcón-Correa, S. Eslami, T. Qiu, J.G. Gibbs, and P. Fischer, ***Nano Letters*** 16, 4887 (2016)
6. Dispersion and shape engineered plasmonic nanosensors, **H.-H. Jeong**, A.G. Mark, M. Alarcón-Correa, I. Kim, P. Oswald, T.-C. Lee, and P. Fischer, ***Nature Communications*** 7, 11331 (2016)
7. Enzymatically active biomimetic micro-propellers for the penetration of mucin gels, D. Walker, B. Käsdorf, **H.-H. Jeong**, O. Lieleg, and P. Fischer, ***Science Advances*** 1, e1500501 (2015)
8. Selectable nanopattern arrays for nanolithographic imprint and etch-mask applications, **H.-H. Jeong**, A.G. Mark, T.-C. Lee, K. Son, W. Chen, M. Alarcón-Correa, I. Kim, G. Schütz, and P. Fischer, ***Advanced Science*** 2, 1500016 (2015) **- Cover article**
9. Shape control in wafer-based aperiodic 3D nanostructures, **H.-H. Jeong**, A.G. Mark, J.G. Gibbs, T. Reindl, U. Waizmann, J. Weis, and P. Fischer, ***Nanotechnology*** 25, 235302 (2014) **- Cover article**
10. Real-time label-free immunoassay of interferon-gamma and prostate-specific antigen using fiber-optic localized surface plasmon resonance sensor, **H.-H. Jeong**, N. Erdene, J.-H. Park, D.H. Jeong, H.-Y. Lee, and S.-K. Lee, ***Biosensors and Bioelectronics*** 39, 346 (2013)
11. Fiber-optic sensor simultaneously detecting localized surface plasmon resonance and surface-enhanced Raman scattering, N. Erdene, **H.-H. Jeong**, J.-H. Park, S.-K. Lee, and D.H. Jeong**, *Rapid Communication in Photoscience*** 2, 46 (2013)
12. Fiber-optic refractive index sensor based on the cone-based round structure, **H.-H. Jeong**, Y.-J. Son, S.-K. Kang, H.-J. Kim, N. Erdene, J.-H. Park, D.-H. Jeong, H.-Y. Lee, and S.-K. Lee**, *IEEE Sensors Journal*** 13, 351 (2013)
13. Analysis of fiber-optic localized surface plasmon resonance sensor by controlling formation of gold nanoparticles and its bio-application, **H.-H. Jeong**, N. Erdene, J.-H. Park, D.-H. Jeong, H.-Y. Lee, and S.-K. Lee, ***Journal of Nanoscience and Nanotechnology*** 12, 7815 (2012)
14. Fabrication of fiber-optic localized surface plasmon resonance sensor and its application to detect antibody-antigen reaction of interferon-gamma, **H.-H. Jeong**, N. Erdene, S.-K. Lee, D.-H. Jeong, and J.-H. Park, ***Optical Engineering*** 50, 124405 (2011)
15. The method of measurement signal processing of biosensor based on optical fiber using reflected localized surface plasmon resonance, **H.-H. Jeong** and S.-K. Lee, ***Journal of Sensor Science and Technology*** 20, 107 (2011)

CONFERENCE PROCEEDINGS:

1. Parallel fabrication of wafer-scale plasmonic metamaterials for nano-optics, S. Eslami, J. G. Gibbs, A. G. Mark, T.-C. Lee, **H.-H. Jeong**, I. Kim, and P. Fischer, ***SPIE Photonics west***, DOI: 10.1117/12.2080098 (2015)
2. 3D nanofabrication on complex seed shapes using glancing angle deposition, **H.-H. Jeong**, A.G. Mark, J.G. Gibbs, and P. Fischer, ***27th IEEE Conference on MEMS***, DOI: 10.1109/MEMSYS.2014.6765670 (2014)

PATENTS:

1. Method for encapsulating a nanostructure, coated nanostructure and use of a coated nanostructure, **H.-H. Jeong**, T.-C. Lee, and P. Fischer, EP 3072582 A1 20160928, European Union (2016) & PCT (pending)
2. Measuring system for biological materials based on Surface Plasmon Scattering and Resonance, **H.-H. Jeong**, S.-K. Lee, D.-H. Jeong, J.-H. Park, H.-Y. Lee, 10-1333482, Republic of Korea (2013)

3. Method for fabricating metal nanostructures using ZnO nanorod and its application, **H.-H. Jeong**, S.-K. Lee, J.-H. Park, S.-H. Jang, D.-H. Jeong, H.-Y. Lee, 10-1303988, Republic of Korea (2013)

PRESENTATIONS: (*PRESENTER)

1. (Oral) Corrosion-protected 3D core-shell nanoparticles, **H.-H. Jeong***, M. Alarcón-Correa, A.G. Mark, T.-C. Lee, and P. Fischer, *2017 European Material Research Society (E-MRS) spring conference*, Strasbourg, France (2017) – **EMRS Graduate student award**
2. (Poster) Chiral plasmonic nanosensors, **H.-H. Jeong***, A.G. Mark, and P. Fischer, *EU-Korea Conference on Science and Technology 2017*, Stockholm, Sweden (2017)
3. (Poster) Corrosion-protected 3D core-shell nanoparticles, **H.-H. Jeong***, M. Alarcón-Correa, A.G. Mark, T.-C. Lee, and P. Fischer, *Conference on Molecular Nanostructures*, Ascona, Switzerland (2017)
4. (Oral) Magnesium plasmonic nanoparticles in water, **H.-H. Jeong**, A.G. Mark, and P. Fischer*, *2017 Material Research Society (MRS) Spring Meetings & Exhibits*, Arizona, USA (2017)
5. (Oral) Nanorheology with Nanopropellers in Biological Fluids, **H.-H. Jeong**, Z. Wu, T. Qiu, D. Walker, A.G. Mark, U. Choudhury, and P. Fischer*, *the 88th Annual Meeting of The Society of Rheology*, Florida, USA (2017)
6. (Oral) Rheology of active colloidal suspensions, U. Choudhury,* D. Singh, T. Qiu, **H.-H. Jeong**, A.G. Mark, and P. Fischer, *the 88th Annual Meeting of The Society of Rheology*, Florida, USA (2017)
7. (Invited seminar talks) Programmable chiral nanocolloids, **H.-H. Jeong***, *at Dankook University (DKU),* Yongin, *Gyeongnam national university of science and technology (GNTECH),* Jinju, and *Electronics and Telecommunications Research Institute (ETRI)*, Daejeon, Republic of Korea (2017)
8. (Oral) Programmable chiral nanocolloids, **H.-H. Jeong***, *2016 Material Research Society (MRS) Fall Meetings & Exhibits*, Boston, USA (2016) – **MRS Graduate Student Gold award**
9. (Oral) Chiral plasmonic nanosensors, **H.-H. Jeong***, A.G. Mark, and P. Fischer, *2016 Material Research Society (MRS) Fall Meetings & Exhibits*, Boston, USA (2016)
10. (Oral) Active Nanorheology with Magnetically Switchable Chiral Plasmonics, A.G. Mark*, **H.-H. Jeong**, T.-C. Lee, M. Alarcon-Correa, S. Eslami, T. Qiu, J.G. Gibbs, P. Fischer, *2016 Material Research Society (MRS) Fall Meetings & Exhibits,* Boston, USA (2016)
11. (Oral) 3D nanomaterials: fabrication and applications, **H.-H. Jeong***, *Conference at the Korean Scientists and Engineers Association in Germany*, Essen, Germany (2016)
12. (Poster) Chiral nanocolloids for sensing applications, **H.-H. Jeong***, A.G. Mark, and P. Fischer, *Workshop on Bio-inspired nanosystems for energy conversion*, Berlin, Germany (2016)
13. (Oral) Molecular optomechanics with plasmons: Backaction at the nanoscale, P. Roelli*, **H.-H. Jeong***, P. Fischer, and T. Kippenberg, *Science day at the Max Planck-EPFL center for molecular nanoscience & technology*, Stuttgart, Germany (2016)
14. (Poster) Nanodiamond-swimmers, U. Choudhury*, J. T. Kim, **H.-H. Jeong**, and P. Fischer, *International Symposium on Micro- and Nanomachines*, Hanover, Germany (2016)
15. (Invited seminar talk) Chiral nanocolloids for sensing applications, **H.-H. Jeong***, *at Dankook University (DKU),* Yongin, Republic of Korea (2016)
16. (Oral) Encapsulated nanocolloids with programmable functions, **H.-H. Jeong***, M. Alarcón-Correa, A.G. Mark, T.-C. Lee, and P. Fischer, *2015 Material Research Society (MRS) Fall Meetings & Exhibits*, Boston, USA (2015)
17. (Oral) Nanodiamond-swimmers, J. T. Kim, U. Choudhury, **H.-H. Jeong**, and P. Fischer*, *2015 Material Research Society (MRS) Fall Meetings & Exhibits*, Boston, USA (2015)
18. (Oral) Molecular optomechanics: Amplification of vibrations in SERS, P. Roelli*, **H.-H. Jeong***, P. Fischer, and T. Kippenberg, *Science day at the Max Planck-EPFL center for molecular nanoscience & technology*, Lausanne, Switzerland (2015)
19. (Poster) Stable hybrid nanocolloids with programmable functions, **H.-H. Jeong***, T.-C. Lee, A. G. Mark, M. Alarcón-Correa, and P. Fischer, *Summer School of the Max-Planck-EPFL Center for Molecular Nanoscience and Technology*, Schloss Ringberg, Germany (2015)

20. (Oral) A novel nanofabrication platform for wafer-scale 3-D metamaterials and active nanomotors, T.-C. Lee*, **H.-H. Jeong**, M. Alarcón-Correa, A.G. Mark, J.G. Gibbs, and P. Fischer, *2015 Recent Appointees in Materials Science Conference (RAMS 2015)*, Coventry, UK (2015)
21. (Invited talk) Chiral metasurfaces, **H.-H. Jeong**, S. Eslami, I. Kim, J. Sachs, M. Alarcón-Correa, T.-C. Lee, J.G. Gibbs, D.P. Singh, A.G. Mark, and P. Fischer*, *36th Progress in Electromagnetics Research Symposium (PIERS)*, Prague, Czech Republic (2015)
22. (Oral) Magnetically switchable chiral plasmonics, A.G. Mark*, **H.-H. Jeong**, T.-C. Lee, M. Alarcón-Correa, S. Eslami, T. Qiu, J.G. Gibbs, and P. Fischer, *Chirality at the nanoscale 2015*, Leuven, Belgium (2015)
23. (Poster) Rapid and selectable method for fabrication of nanopattern master stamp for nanoimprint lithography, K. Son*, **H.-H. Jeong**, A.G. Mark, P. Fischer, and G. Schütz, *Workshop on Micro-contact-Printing and Nanoimprint Lithography*, Dresden, Germany (2015)
24. (Poster) Active colloids as a model for adatom surface diffusion, J. T. Kim, U. Choudhury*, **H.-H. Jeong**, and P. Fischer, *Summer School of the DFG Priority Programme 1726–Microswimmers*, Jülich, Germany (2015)
25. (Oral) Parallel fabrication of wafer-scale plasmonic metamaterials for nano-optics, S. Eslami*, J.G. Gibbs, A.G. Mark, T.-C. Lee, **H.-H. Jeong**, I. Kim, and P. Fischer, *SPIE Photonics West 2015*, Boston, USA (2015)
26. (Poster) Large-area SERS active 3D nanostructured films with multiple hotspots, **H.-H. Jeong***, I. Kim, A.G. Mark, T.-C. Lee, and P. Fischer, *5th International Topical Meeting on Nanophotonics and Metamaterials*, Seefeld, Austria (2015)
27. (Oral) Magneto-chiral plasmonics in hybrid nanostructures, **H.-H. Jeong**, T.-C. Lee, M. Alarcón-Correa, S. Eslami, J.G. Gibbs, C. Miksch, A.G. Mark*, and P. Fischer, *5th International Topical Meeting on Nanophotonics and Metamaterials*, Seefeld, Austria (2015)
28. (Oral) Metal-hybrid nanocolloids for magneto-plasmonics, **H.-H. Jeong**, T.-C. Lee, M. Alarcón-Correa, S. Eslami, J.G. Gibbs, A.G. Mark, C. Miksch, and P. Fischer*, *2014 Material Research Society (MRS) Fall Meetings & Exhibits, Boston*, USA (2014)
29. (Poster) In situ observation of beam-induced assembly of negatively charged gold nanoparticles, M. Alarcón-Correa*, T. Qui, **H.-H. Jeong**, T.-C. Lee, and P. Fischer, *2nd Conference on In-Situ and Correlative Electron Microscopy*, Saarbrücken, Germany (2014)
30. (Oral) Wafer-scale fabrication of 3-D hybrid nanostructures with programmable shape and composition, T.-C. Lee, **H.-H. Jeong***, A.G. Mark, J.G. Gibbs, and P. Fischer, *40th International Conference on Micro and Nano Engineering (MNE)*, Lausanne, Switzerland (2014)
31. (Poster) Large-scale advanced nanopatterning in conjunction with glancing angle deposition, **H.-H. Jeong***, T.-C. Lee, A.G. Mark, J.G. Gibbs, M. Alarcón-Correa, C. Miksch, K. Son, W. Chen, and P. Fischer, *40th International Conference on Micro and Nano Engineering*, Lausanne, Switzerland (2014)
32. (Oral) Large-scale advanced nanopatterning by the combination of block copolymer micelle lithography and glancing angle deposition, **H.-H. Jeong***, T.-C. Lee, A.G. Mark, J.G. Gibbs, M. Alarcón-Correa, C. Miksch, K. Son, W. Chen, and P. Fischer, *7th EU-Korea Conference on Science and Technology 2014*, Vienna, Austria (2014)
33. (Poster) 3D nanofabrication on complex seed shapes using glancing angle deposition, **H.-H. Jeong***, A.G. Mark, J.G. Gibbs, and P. Fischer, *27th IEEE Conference on Micro Electro Mechanical Systems 2014*, San Francisco, USA (2014)
34. (Poster) Fabrication of 3D metal oxide nanostructures by glancing angle deposition, **H.-H. Jeong***, A.G. Mark, J.G. Gibbs, and P. Fischer, *6th EU-Korea Conference on Science and Technology 2013*, Brighton, UK (2013)
35. (Poster) Surface-enhanced Raman scattering (SERS) measurement and real-time label-free immunoassay using Fiber-Optic Localized Surface Plasmon Resonance (FO LSPR) sensor, **H.-H. Jeong***, I.-a. Jeong, N. Erdene, J.-H. Park, D.-H. Jeong, H.-Y. Lee, and S.-K. Lee, *14th Korean conference on Micro Electro Mechanical Systems*, Jeju, Korea (2012) - **Best paper award**
36. (Poster) Design of fiber-optic measurement system to analyze localized surface plasmon resonance (LSPR) signal by gold nanoparticles, H.-J. Kim*, **H.-H. Jeong**, N. Erdene, J.-H. Park, D.-H. Jeong, H.-Y. Lee, and S.-K. Lee, *14th Korean conference on Micro Electro Mechanical Systems*, Jeju, Korea (2012)

37. (Poster) Fabrication of Fiber-optic localized surface plasmon resonance (FO LSPR) sensor using optical fiber tip with cone-based round structure, Y.-J. Son*, **H.-H. Jeong**, N. Erdene, J.-H. Park, D.-H. Jeong, H.-Y. Lee, and S.-K. Lee, *14th Korean conference on Micro Electro Mechanical Systems*, Jeju, Korea (2012)
38. (Poster) Fabrication of biosensor using optical fiber with gold nanoparitlces and design of real-time immunoassay system, **H.-H. Jeong***, N. Erdene, J.-H. Park, D.-H. Jeong, and S.-K. Lee, *the Information and Control Symposium 2011*, Yongin, Korea (2011) - **Best paper award**
39. (Poster) Fabrication of label-free immunosensor based on Fiber-Optic Localized Surface Plasmon Resonance (FO LSPR) and its application, **H.-H. Jeong***, N. Erdene, J.-H. Park, D.-H. Jeong, and S.-K. Lee, *13th Korean conference on Micro Electro Mechanical Systems*, Jeju, Korea (2011)

PROFESSIONAL MEMBERSHIPS

2015 – Present Member, Material Research Society (MRS)
2012 – Present Member, the Korean Scientists and Engineers Association in Germany (VeKNI)